Submarine Fan Systems: Proximal to Distal Reservoir Quality Controls

ABDULWAHAB MUHAMMAD BELLO

How to cite:

BELLO, ABDULWAHAB MUHAMMAD (2021) Submarine Fan Systems: Proximal to Distal Reservoir Quality Controls. Doctoral thesis, Durham University.

Submarine Fan Systems: Proximal to Distal Reservoir Quality Controls

Abdulwahab Muhammad Bello

This thesis is submitted in partial fulfilment of the requirements for the degree
of Doctor of Philosophy at Durham University

Department of Earth Science

Durham University

January 2021

Abstract

Submarine fans and related turbidite systems are important components of continental margins; they contain a stratigraphic record of environmental changes, host large accumulations of oil and gas, and offer potential sites for carbon capture and storage (CCS). The influence of grain size and sediment flux to submarine fans has been recognised as a primary control on the heterogeneity of deep-water facies. Predicting fan depositional facies, changes in clay matrix content from proximal to distal settings, and evaluating the role played by clay coatings on detrital grains are important challenges in the characterizations of submarine fan systems. In this study, a multi-technique approach is applied, including detailed petrography, burial history modelling, SEM, SEM-CL, SEM-EDS mapping, and hydrothermal reactor experiments. Extensive subsurface datasets (well logs, cores, and thin sections) from 13 wells and 191 samples are used from the Paleocene-Eocene Forties Sandstone Member of the Sele Formation, Central North Sea, UK. These data are used to assess the role played by clays (detrital and authigenic), depositional facies, and burial diagenesis in reservoir quality evolution in proximal to distal fan depositional settings. The study reveals that amalgamated sandstones facies of proximal fan of the Forties Sandstone Member have the best reservoir quality due to coarser grain size, less detrital clay matrix, and low ductile grains content (< 5%), whereas the distal fan, mud-prone heterolithic sandstones have the poorest reservoir quality due to finer grain size, high clay matrix, and high ductile grains content (> 5 %). The optimum pore-filling clays volume, which have a deleterious effect on reservoir quality, range from 10-30 %. Furthermore, detrital smectite, which was both inherited and emplaced during sediment dewatering, was the main source of grain-coating chlorite, illite-smectite, and illite. The optimum clay-coating coverage to inhibit quartz cementation ranges from 40 to 50 % (based on the present-day burial depths of 2200 - 3200 m TVDSS) and clay volume of up to 8 %. Average quartz cement volume decreases from 3.62 % in proximal fan to 1.78 % in distal fan settings, presumably due to impact of grain-coating and pore-filling clays. Grain size has no impact on clay-coating coverage, which suggests that the finer-grained distal fan sandstones could have good clay-coating coverage to arrest quartz cementation during burial and chemical compaction depths > 2500 m. Blocky kaolinite and fibrous illite as low as 2 % have been found to have detrimental effect on the sandstones reservoir quality, whereas pore-filling chlorite has a threshold value ranging from 3 to 10 %. A complimentary experimental study using an autoclave-engineers hydrothermal reactor has been undertaken using sand-rich turbidite channel facies samples from the Bute Inlet, British Columbia, Canada. The results demonstrate that the presence of detrital clay is crucial for the formation of authigenic clays. Channelised sand facies with < 1 % detrital clay have poorly-developed coatings coverage (max 47 %) post-experiment. In comparison, lobe facies with 6 % initial detrital clay formed well-developed coatings coverage (max 77 %), with clay volume ranging from 19 to 27 % post-experiment. These results can be used as input parameters for the assessment of reservoir potentials in carbon sequestration and storage, and in hydrocarbon exploration and production.

Declaration

I hereby declare that the work described in this thesis, which I submit for the Degree of Doctor of Philosophy at Durham University, is my own work, except where acknowledgement is made in the text, and that the thesis has not been submitted previously for any degree, diploma or other qualification at this or any other university.

January 2021.

Acknowledgements

In the name of Almighty Allah, the most gracious, the most merciful. All the praises and thanks be to Him for sparing my life to pursue my ambitions, for His blessings upon me and my family, and for making this feat a reality. May His peace and blessings continue to be upon His beloved Messenger, Prophet Muhammad PBUH.

I would like to express my sincere gratitude to my amazing and excellent supervisory team: Stuart Jones, Jon Gluyas, Sanem Acikalin, and Matthieu Cartigny for their guidance, help, and continuous support throughout my PhD programme. Firstly, I would like to thank my supervisor, Dr Stuart Jones for his continuous support, guidance, and advice during my PhD study, and also for his invaluable suggestions and comments on this thesis and manuscripts written. Under his guidance, not only did I learn a lot about the most exciting aspects of sedimentology and sandstones reservoir quality and diagenesis, I have also remarkably improved as a researcher and scientist, thanks to his incredible pieces of advice. I could not have imagined having a better supervisor for my PhD programme. Thank you so much, Stuart. Secondly, I would like to also extend my special appreciation to my co-supervisor Prof Jon Gluyas, for his invaluable comments, discussions, advice, and time. Additionally, without Jon’s generous financial support towards the end of my PhD studies, I could not have overcome many obstacles. Jon, thank you very much and God bless you. My co-supervisors Dr Sanem Acikalin and Dr Matthieu Cartigny are especially thanked for their invaluable suggestions and feedback on my PhD project and written manuscripts, and for providing core and XRD data on the modern-day Bute Inlet sediments, British Columbia, Canada.

My special thanks go to my excellent annual review team, Prof Chris Greenwell and Dr Darren Grocke, for their contributions and constructive reviews. My research has immensely benefited from their wealth of experience, knowledge, and comments.

I would like to thank my amazing wife, Zahrah Abdulghaniy Bello, and my precious son, Muhammad (Amin) for their love, prayers, patience, support, and understanding throughout my PhD programme. I love you so much. To my father, Alhaji Muhammad Bello, I say a big thank you for your care, love, support, and prayers. My sincere gratitude goes to my mother, Hajiya Sa’adatu Shu’aibu, for her moral support and prayers, and for pointing me in the right direction very early in life. My grandmother, Hajiya Kaku is greatly appreciated for her prayers and support. I wish to also thank my father in-law, Barrister Abdulghaniy Bello, and my Mother in-law, Hajiya Jamilah Yahya Ahmed, for their continuous support and prayers.

My special gratitude goes to my siblings Auwal, Hadiza, Zahrah, Sadiya, Abubakar, Zainab, Aminu, Isa, Humaira, and Walid for their love and prayers. I wish to also say a big thank you to my uncle Isa Shuaibu Abbas and brother in-law Suleiman Waziri for their love, prayers, and support. My appreciation goes to my friends Sadiq, Ibrahim, Muhammad, Musa, and Aliyuda for their support and prayers.

My special appreciation goes to the Petroleum Technology Development Fund (PTDF), through the Federal Government of Nigeria, for providing funds for this research project. The project would not have been possible without their generous financial support. Thank you so much, and God bless the Federal Republic of Nigeria.

Mr Ian Chaplin and Miss Sophie Edwards are greatly appreciated for preparation of numerous, high-quality thin sections. I would like to specially thank Leon Bowen and Diana Alvarez-Ruiz for their excellent support and time during my work at the scanning electron microscope laboratory. British Geological Survey and members of staff are greatly acknowledged for providing core data, and I wish to sincerely thank Mr Gary Wilkinson for downloading well data through the UK Common Data Access (CDA). Dr Sean R. O’Neill is appreciated for his help on the use of the PetroMod software. I wish to thank Dr Olakunle J. Oye and Dr Stephan Stricker for their help with point counting software, and for useful discussions and suggestions. Claire McGhee is highly appreciated for her assistance in sampling Bute Inlet cores, and for useful discussions on the Bute submarine fan system.

I am especially grateful to my colleagues Oluwafemi Aro, Dimitrios Charlaftis, and Sudirman for their assistance in core sampling at BGS, conducting hydrothermal reactor experiments, and basin modelling, respectively. Thanks to Nwachukwu Chimaobi, Ahmed Obeid, Nadia Narayan, Timothy Armitage, Maxmillian Franzel, Junjie Liu, Tang Longxun, Natalia Wasielka, Naema Al-Nofeli, and Elizabeth Atar for being very helpful.

Finally, I would like to thank everyone in the in the Department of Earth Science who has contributed in any form towards the success of my PhD programme. THANK YOU ALL.

Table of Contents

List of Figures

List of Tables

Glossary

BSE- Backscattered Electron

BSEM- Backscattered Electron Microscopy

Bbbl- Billion barrels of oil

CL- Cathodoluminescence

EDS- Energy Dispersive X-ray Spectroscopy

SEM- Scanning Electron Microscopy

SIMS- Secondary Ion Mass Spectrometry

1-D- One-dimensional

mD- Millidarcy

m- meter

Km- Kilometre

Ft- Feet

TVDSS- True Vertical Depth Subsea

TVDRSF- Total Vertical Depth Relative to Sea Floor

PPL- Plane Polarized Light

XPL- Cross Polarized Light

XRD- X-ray Diffraction

Chapter 1: Introduction

Chapter 1: Introduction

1.1 Research context

Porosity and permeability are the most important parameters of sandstones reservoir quality (Jiang, 2012; Marchand et al., 2015; Virolle et al., 2019), as they determine the amount of oil and gas a sandstone can store and the rate at which they can be produced. Additionally, while porosity and permeability control the storage capacity and deliverability of hydrocarbon reservoirs (respectively), wettability also plays a vital role in controlling sandstones reservoir quality by affecting the type and amount of fluids to be produced (Grier and Marschall, 1992). An oil-wet reservoir allows the water located in the central portion of the pores to flow through the pore system, whereas a water-wet reservoir allows oil in the central, larger pores to flow through the pore system, restricting the water to the perimeter of the pores. Thus, as hydrocarbon exploration activities move towards more-challenging, poorly-understood deep-water targets, the need to include reservoir quality in pre-drill assessments becomes even more important. More recently, reservoir quality has also been a focus of carbon capture and storage (CCS) projects (Xia and Wilkinson, 2017; Yanzhong et al., 2020), and turbidite sandstones are potential storage sites, which require a comprehensive understanding of their reservoir properties, facies distribution and migration pathways prior to any CO_2 injection. In addition, reservoir porosity and permeability control the efficiency and effectiveness of CO_2 injection into the subsurface geological formation for both CO_2 storage and enhanced hydrocarbon recovery (EOR) (Kordi, 2013; Xia and Wilkinson, 2017). The injected CO_2 can preferentially migrate and distribute via migration pathways that are influenced by reservoir quality variation and heterogeneity. As such, identifying and predicting the reservoir heterogeneities are key for understanding reservoir performance. Accurate characterization and prediction of reservoir quality is crucial throughout the entire “life cycle” of a reservoir, from exploration to field development, for optimum hydrocarbon production strategies (e.g., Bloch, 1991; Kupecz et al., 1997; Sneider, 1990).

Reservoir quality in sandstones is controlled by two main factors: (1) primary depositional parameters, which include sediment composition and texture (e.g., grain size, sorting, and clay content, etc) (e.g., Bell et al., 2018; Huang et al., 2020; Marchand et al., 2015; Stammer, 2014); and (2) diagenetic alterations during burial (Ma et al., 2017; Morad et al., 2010; Oluwadebi et al., 2018). Depositional parameters influence primary reservoir properties and early diagenetic alterations (Porten et al., 2016). Diagenetic alterations, on the other hand, include mechanical compaction, cementation, mineral dissolution and recrystallization, which strongly affect the reservoir quality of siliciclastic rocks. Many studies on deep-water turbidite sandstones have focused on assessing reservoir quality based primarily on depositional parameters alone (e.g., Bell et al., 2018; Lien et al., 2006; Marchand et al., 2015; Porten et al., 2016). Surprisingly, little has been published on the impact of diagenesis on reservoir quality of evolution of the Paleocene deep-water turbidite sandstones of the Central North Sea (e.g., Mansurbeg et al., 2008; Stewart, 1995). Additionally, linking depositional parameters and diagenesis would effectively assess the reservoir quality of the sandstones.

Clean, clay-free sandstones are often thought to form the best reservoir quality; however, they are susceptible to ubiquitous quartz cementation at deeper burial due to chemical compaction (Worden et al., 2020). Sandstones with clay coats, in contrast, can preserve anomalously high porosity at deeper burial by inhibiting the development of quartz overgrowths (Ajdukiewicz and Larese, 2012; Ehrenberg, 1993; Pittman et al., 1992; Stricker and Jones, 2018). Quartz overgrowth is one of the most important cements that significantly reduce porosity and permeability in medium and deeply buried sandstone reservoirs, which severely impedes recoverable hydrocarbon volumes (Bjorlykke and Egeberg, 1993; Bukar, 2013; McBride, 1989; Worden and Morad, 2000). As exploration for oil and gas progresses to even deeper targets in mature basins, the need to understand the controls on the processes of formation of quartz cement, and being able to predict its occurrence, volume and distribution become paramount (Bukar, 2013). The growth of authigenic grain-coating clays during diagenesis has been identified to inhibit quartz cementation in sandstones, thereby preserving reservoir quality (Anjos et al., 2003; Bahlis and De Ros, 2013; Bloch et al., 2002; Dutton et al, 2018; Ehrenberg, 1993; Kordi, 2013; Pittman et al., 1992). Furthermore, occurring as coats on sand grains, grain-coating clays (e.g., chlorite) limit the nucleation area available for quartz cementation by forming a diffusion barrier between the surface of the detrital grain and the pore system, limiting the supply of silica molecules to the detrital grain surface (Ajdukiewicz and Larese, 2012). The mineralogy, thickness, and coverage or completeness of grain coats are reported to have a key control on the ability of clay coats to prevent the formation of quartz cements (Ajdukiewicz and Larese, 2012). In addition to chlorite coatings, grain-coating illite and illite-smectite, although less common, have been reported to preserve porosity and permeability in sandstones (Pittman et al., 1992; Storvoll et al., 2002; Tang et al., 2018; Taylor et al., 2010). The preservation of reservoir quality by clay coatings is assessed by measuring the percentage of detrital grains surface covered by clay coatings using a suitable software package (e.g. Petrog or JMicroVision), and plotting the extent of clay-coat coverage against the volume of quartz cement or porosity and permeability values (e.g. Busch, 2016; Busch et al., 2020).

Higher clay-coating coverage result in higher porosity and permeability values as well as lower quartz cement volumes (Busch et al., 2020; Kordi, 2013).

Consequently, depending on their mode of occurrence, type and abundance in sandstone reservoirs, clay minerals can significantly enhance or degrade reservoir quality (Griffiths et al., 2019, 2018). Whilst grain-coating chlorite and illite, for instance, preserve porosity by preventing the development of pore-filling quartz cement (e.g., Ajdukiewicz and Larese, 2012; Bahlis and de Ros, 2013; Ehrenberg, 1993; Stricker, 2016), pore-filling chlorite and illite can significantly occlude intergranular porosity and reduce reservoir permeability by blocking pore throats, respectively, and hence destroy reservoir quality (Morad et al., 2010; Oluwadebi et al., 2018; Worden et al., 2020; Worden and Morad, 2003). Anomalously high porosity are recorded where grain-coating clays are thick and well-developed (Pittman et al., 1992; Stricker, 2016; Tang et al., 2018). Therefore, understanding the role of grain-coating clays in reservoir quality preservation and pore-filling clays in reservoir quality destruction in siliciclastic reservoirs is crucially important for any hydrocarbon exploration campaigns, especially in poorly-understood, distal-fan heterolithic facies of deep-water turbidite sandstones.

The Paleocene Forties Sandstone Member of the Sele Formation is an important deep-water turbidite reservoir in the Central North Sea, which provides a good case study for understanding the impact of down-fan fining and the role played by clays on reservoir quality evolution of submarine fan turbidite sandstones. Although many studies have discussed the regional depositional history of the Forties Fan system (e.g., Den Hartog Jager et al., 1993; Jennette et al., 2000), a focus on the regional role of clays, particularly grain-coating types, and diagenesis on reservoir quality has received little attention. Most of the secondary studies on the diagenesis of the Forties Sandstone Member have largely focused on the updip Forties and Nelson fields of the Forties Fan system (e.g., Kunka et al., 2003; Whyatt et al., 1992; Wills and Peattie, 1990), and very few downdip areas, such as the Fram discovery (Jones et al., 2015). Thus, as submarine fans are characterized by abrupt change in facies (e.g., Hempton et al., 2005; Marchand et al., 2015) (probably due, in part, to change clay content), the ability to accurately predict the presence of grain-coating clays that could preserve reservoir quality in both proximal and distal fan settings becomes especially important.

However, attempts to understand the formation of grain-coating clays in sandstones are largely based on data from wellbores (e.g., Berger et al., 2009; Hillier, 1994; Lien et al., 2006) and ancient outcrop analogues (e.g., Haile et al., 2019), which might be hampered by insufficient (or clustered) data and mineral alterations due to weathering, respectively. Consequently, to better understand how grain-coating clays are formed, distributed, and transformed in the ancient Forties Fan system, the modern submarine fan sediments from the Bute Inlet, southwestern coast of British Columbia, Canada has been studied alongside those of the Forties Fan system. Additionally, the Bute Inlet would present an excellent opportunity to study controls and processes that may not be present in the ancient Forties system. The Bute system forms the second part of the study and would aim to assess the type, concentrations, coatings coverage of clay minerals. Furthermore, hydrothermal reactor experiments have been performed on the Bute sediments to simulate the formation of grain-coating clays and microquartz for better understanding and prediction of reservoir quality in the ancient Forties system.

The present study, therefore, aims to improve the understanding of the occurrence of porosity-preserving, grain-coating clays in submarine fans sandstones facies using a multi-technique approach.

1.2 Aim of the research

The main aim of the research is to investigate the role played by grain-coating and pore-filling clays, depositional characteristics, sedimentary facies, and diagenesis on reservoir quality evolution of the Paleocene Forties Sandstone Member (Central North Sea) from proximal to distal fan settings. To achieve these, core data covering the proximal to distal Forties Fan system have been collected, and a multi- technique approach and methods have been employed, including scanning electron microscopy, cathodoluminescence, stable isotope analysis, and burial history, to investigate the petrography and diagenesis of the sandstones. The results of the study would provide insights into other poorly-understood submarine fans systems with similar provenance and tectonic settings.

The main objectives of this study are:

- To determine the role of primary depositional facies and diagenesis in controlling reservoir quality of submarine fans and turbidite systems;
- To establish the role played by grain-coating and pore-filling clays in reservoir quality evolution from the submarine fan depositional environment of the Paleocene-Eocene Forties Sandstone Member, Central North Sea, UK;

- To quantify clay-coating coverage on samples from the Forties Sandstone Member, and establish the optimum clay-coating coverage to arrest quartz cementation and preserve enhanced primary porosity; and
- To use hydrothermal reactor experiments to assess the role played by detrital and authigenic clay coatings in samples from a present-day turbidite sand-rich, channelised system in order to provide quantitative data that can be used as inputs for modelling of equivalent systems during mesodiagenesis.

1.3 Techniques and methods used in this research

A multi-technique approach has been employed in this research. The key methods used include:

1.3.1 Sampling and sedimentary facies

Core samples used in this study are from the Paleocene Forties Sandstone Member, Central North Sea, and the modern Bute Inlet, southwestern coast of British Columbia, Canada. The cores have been systematically described and collected based on established facies in proximal, medial, and distal fans settings. Sampling for the Forties Fan system was undertaken based on cores from 13 wells in 7 oil and gas fields, covering a total of 266 m for proximal, medial and distal fan. The core depth intervals were determined and selected based on well completion reports downloaded from UK Common Data Access (CDA) website, and on core images viewed at British Geological Survey (BGS) website prior to the sampling exercise at the BGS core store in Keyworth, Nottingham, UK. For effective coverage, all the sampling points of the Forties Fan system have covered the facies in the proximal, medial, and distal fans. Syringe core samples for the modern Bute Inlet were sub-sampled from box cores, which were collected from proximal to distal Bute Fan system.

1.3.2 Petrography

Thin sections were prepared and used to determine the qualitative and quantitative composition of detrital grains, authigenic minerals, grain size, sorting and optical porosity, and to establish the relative timing of diagenetic events. The thin sections were impregnated with blue epoxy for visible porosity identification, and were examined using a Leica DM2500P standard petrographic microscope. Modal point count analysis (300 counts per thin section) was conducted on the samples in order to determine detrital grains, matrix content, pore-filling and grain-coating cements, and porosity (both primary intergranular and secondary intragranular) using the Petrog software package, developed by Conwy Valley Systems Limited. Grain size distribution was analysed by measuring the long axis of at least 100 randomly selected quartz and fresh feldspar grains for both samples of the Forties Sandstone Member and the Modern Bute Inlet sediments using the Petrog software and ImageJ software.

1.3.3 SEM, SEM-EDS, CL, and EDS phase maps

Selected, diamond-polished thin sections were coated to 30-40 nm with carbon prior to analysis using a Hitachi SU70 scanning electron microscope (SEM) equipped with a backscatter scanning electron detector (BSE) and an energy dispersive X-ray spectrometer (EDS) under acceleration of 12-15 kV. SEM-EDS analysis has been used to study clay mineral types (based on morphology and chemistry) and other diagenetic minerals. To study the origin and extent of quartz overgrowths, and phases of carbonate cementation, Cathode-luminescence (CL) analysis was performed on some selected, polished samples.

In order to quantify sandstones and sediments' framework composition, study clay mineral types and distributions, measure clay- and microquartz-coatings coverage, and complement point count data, SEM-EDS phase maps were acquired and analysed for selected, polished, and carbon-coated thin sections of the Forties Sandstone Member as well all pre- and post-hydrothermal reactor experiments thin sections of the modern-day Bute Inlet. The EDS phase mapping technique is a semi-automated mineralogical tool applied in the identification and quantification of minerals, and it is used on an SEM platform and supported by back-scattered electron/secondary electron (BSE/SE) imaging detectors. The technique has been recognised for scanning a relatively large areas at high resolutions. 2 mm by 2 mm phase maps were acquired on the samples at x150 and x300 magnifications (depending on sample's grain size) for approximately 7-23 hours per sample. The chosen magnification enabled effective visualization and quantification of clays, porosity and other minerals distributions in the samples. The electron beam was accelerated at 15 kV and the sample current was obtained at 0.73nA, with analytical working distance mostly ranging from 14.3 to 15.3 mm. The acquired phase maps were then processed using Oxford's Aztec (v.3.3) software package.

The role of clays in porosity preservation in sandstones has been the focus of many studies (e.g. Busch et al., 2020; Pittman et al., 1992; Stricker and Jones, 2018; Worden et al., 2020). Diagenetic processes during burial such as compaction and cementation could destroy reservoir porosity in sandstones (Grier and Marschall, 1992; Houseknecht, 1987; Lundegard, 1992). Deeply-buried, clay-free sandstones are susceptible to porosity loss due compaction and quartz cementation (Worden et al., 2020). Sandstones with clay coatings, however, could prevent quartz cementation and chemical compaction, thereby preserving porosity (Busch et al., 2020; Charlaftis et al., 2021; Pittman et al., 1992; Stricker and Jones, 2018; Tang et al., 2018). Thus, the use of SEM-EDS phase maps would effectively identify and quantify porosity-preserving clay coatings, thereby improving the understanding of their processes of formation as well as preservation of reservoir quality.

1.3.4 Clay and microquartz coatings thicknesses and coverage

Thicknesses of grain-coating clays and microquartz were measured using the ImageJ software. The measurements were carried out using acquired SEM and/or BSE images. Prior to the thickness measurements, scales were first established and calibrated based on the inscribed scales in imported SEM/BSE images into the ImageJ piece of software. Thicknesses of grain-coating clays or microquartz were then measured from where the coatings are attached to the grain surface to where they terminate, usually into the pore system. The measurements were repeated from different sides of a grain as well as on several grains in order to get a range and an average.

To measure clay- and microquartz-coating coverage on detrital grains, at least 50 quartz grains (for Forties samples) and quartz and unaltered feldspar (albite) grains (for Bute samples), coated by clays and/or microquartz, were measured on montaged SEM/BSE images and high-resolution photomicrographs using the Petrog and JMicrovision software packages based on the methods described by Dutton el. (2018) and Wooldridge et al. (2019) for the ancient Forties sandstones and the modern Bute Inlet samples, respectively.

1.3.5 Stable isotope analysis

Stable carbon and oxygen isotopes of carbonate-cemented samples of the Forties Sandstone Member were studied in order to establish the likely sources of the carbonate cements, and to determine the formation water temperatures at which the cements precipitated. The analysis was conducted at the Stable Isotope Laboratory of the Earth Science Department at Durham University (UK). Before the analysis, samples with a single, dominant carbonate cement type (e.g., calcite or dolomite) in the sandstones were selected based on their volume percentages from the modal point count data. Eighteen (18) sandstones samples with variable amounts of carbonate cements, consisting of calcite (both ferroan and non-ferroan), dolomite, and siderite, were gently disaggregated with a hammer and subsequently crushed into powder (< 200 mesh) in a mortar, and at least 3 mg of the cement were obtained for each sample. Based on carbonate cements types, each sample was weighed out to give a CO_2 signal of 12mV and was reacted with 99 % ortho-phosphoric acid for 2 hours at 70 °C. The resultant gas mix of helium and CO_2 was then separated and analysed via a Thermo Fisher Scientific Gasbench II interfaced with a Thermo Fisher Scientific MAT 253 gas source mass spectrometer for isotopic analysis. Data are reported in standard delta notation as per mil (‰) relative to Vienna Pee Dee Belemnite (V-PDB). In order to calculate paleotemperatures, $\delta^{18}O_{\text{V-PDB}}$ values of carbonate cements were converted to $\delta^{18}O_{\text{SMOW}}$ using the equation $\delta^{18}O_{\text{SMOW}} = 1.03091 \times \delta^{18}O_{\text{V-PDB}} + 30.91$ (Coplen et al., 1983).

1.3.6 1-D Burial history modelling

Schlumberger's PetroMod (V.2015) software was used to construct 1-D basin modelling plots in order to determine burial and thermal history of the Forties Sandstone Member in the proximal and distal fan settings. Two wells (Nelson11-6 and Blane-03a-1; Figure 3.3A & B) were selected to represent proximal and distal fan, respectively, and to show the differences in burial and thermal histories between the proximal and distal fan settings. The burial history models were constructed using the present-day stratigraphy from well-completion reports, well logs lithology and lithological descriptions of stratigraphic units, and wirelinel-log derived bottom-hole-temperature (BHT) data. BHT corrections were applied using the method developed by Waples et al. (2004). Paleo-basement heat flow model and paleo-surface temperature history were adopted from Swarbrick et al. (2000).

1.3.7 Hydrothermal reactor experiments

Hydrothermal reactor experiments were performed on proximal and distal fan samples of Bute Inlet sediments in order to simulate diagenesis and synthesize grain-coating clays and microquartz, and to test the assumption that the growth of clays and microquartz coatings on sand grains inhibits the development of authigenic quartz and albite overgrowths. About 5g of the sediments and silica gel each were used for the experiments. The experiments were conducted with and without silica gel in the reactor, and the samples were heated to 250 °C in a 0.1 M Na_2CO_3 solution for 3 days (72 hours) at water vapour pressure. The experiments were carried out under strictly closed conditions in the reactor, with subsequent cooling to room temperature after each next run.

1.4 Thesis outline

1.4.1 Chapter I: Introduction

Chapter I sets the context and scope for the current study. It provides the starting out hypothesis and justifications for the research and the chosen methodologies. A multi-dimensional approach has been employed to test the hypothesis, with a view to linking depositional characteristics and diagenesis to reservoir quality, and evaluating the significance of clays on reservoir quality of submarine fans' heterolithic facies.

1.4.2 Chapter II: Submarine fans depositional systems and reservoir quality: a review

Chapter II reviews submarine fans depositional systems in terms of their sediment gravity flow processes, turbidite deposits, and sand-rich and mud/sand-rich submarine fan models. The chapter also reviews the literature on the role of grain-coating and pore-filling clays in reservoir quality evolution of turbidite sandstones reservoirs, and the role played by provenance in determining submarine fans' framework composition, diagenesis, and reservoir quality. This provides a background for understanding how grain-coating clays inhibit quartz cementation and preserve reservoir quality in submarine fans' depositional facies. The chapter forms the basis for Chapters 3, 4 and 5, and will contribute to papers intended at the end of the chapters.

1.4.3 Chapter III: Role played by clay content in controlling reservoir quality: Forties Sandstone Member, Central Graben, North Sea

This chapter focuses on evaluating the role played by grain-coating and pore-filling clays, depositional characteristics (grain size, sorting, and clay content), sedimentary facies, and diagenesis in reservoir quality evolution of the Paleocene Forties submarine fan sandstones (Central North Sea) from proximal to distal fan settings, with a view to linking depositional characteristics and diagenesis and to establish the percentage of clay-coating coverage required to inhibit quartz cementation and, thus, preserve reservoir quality in the sandstones. The chapter has been written in a journal article format entitled "Role played by clay content in controlling reservoir quality of submarine fan systems, Forties Sandstones, Central Graben, North Sea", and has been published in Journal of Marine and Petroleum Geology.

1.4.4 Chapter IV: Importance of grain-coating clays for porosity preservation

This chapter is aimed at understanding the origin and role of grain-coating clays in reservoir quality evolution of the Forties Sandstone Member. The chapter also focuses on investigating the control factors of relatively high-porosity and high-permeability zones in supposedly low-porosity and low-permeability heterolithic facies in turbidite sandstones. This would give insights into the reservoir potentials of the medial to distal fan heterolithic facies. Thus, the chapter evaluates the origin, conditions of precipitation, and effectiveness of grain-coating clays in preventing quartz cementation and preserving porosity. The chapter has also been written in a paper format and will be submitted to Journal of Petroleum Geoscience.

1.4.5 Chapter V: Experimental diagenesis using a present-day submarine turbidite sands

This chapter focuses on hydrothermal reactor experiments to simulate diagenesis in turbidite sandstones by using the modern-day sediments from Bute Inlet, southwestern coast of British Columbia, Canada. The experiments, which were performed with and without silica gel in the reactor, used quartz, plagioclase (albite), K-feldspar, and mica as the main framework grains. Selected samples were heated to 250 °C for 72 hours (at water vapour pressure). The chapter aims to evaluate the role of precursor clay coatings on detrital grains, their transformations, and measure the extent of clay-coating coverage on sand grains. This would compare the results of the experimental diagenesis to those of the natural, Palaeocene Forties Sandstone Member of UK North Sea, and evaluate the role played by clays and new cements in submarine fans sandstones from proximal to distal fan settings, which would provide quantitative data that can be used as inputs for modelling. The chapter has been written in a paper format and will be submitted to a suitable journal such as Journal of Chemical Geology.

1.4.6 Chapter VI: Summary and future work

This chapter elaborates on the general summary of the preceding chapters, implications for other deep-water systems, summary and conclusions for the whole work, and some suggestions for future work

1.5 Paper Status and Author Contributions

1.5.1 Paper published

- **Bello**, A. M., Jones, S., Gluyas, J., Acikalin, S. and Cartigny, M. (2021). Role played by clay content in controlling reservoir quality of submarine fan systems, Forties Sandstones, Central Graben, North Sea. Marine and Petroleum Geology, 128, pp. 1-23.

1.5.2 Manuscripts in Preparation

- **Bello**, A. M., Charlaftis, D., Jones, S., Gluyas, J., Acikalin, S. and Cartigny, M. Experimental diagenesis using a present-day submarine turbidite sands (*to be submitted Journal of Chemical Geology*).
- **Bello**, A. M., Jones, S., Gluyas, J., Acikalin, S. and Cartigny, M. Importance of grain-coating clays for porosity preservation (*to be submitted Journal of Petroleum Geoscience*).

Chapter 2: Submarine fans depositional systems and reservoir quality: a review

Chapter 2: Submarine fans depositional systems and reservoir quality: a review

2.1 Summary

Over the past decades, submarine gravity-flow deposits and submarine flows have become increasingly important as sites of carbon sequestration and storage, and as hydrocarbon reservoirs (Kroeger et al., 2019; Leithold et al., 2016; Talling, 2013 and many others). The sedimentary processes by which the depositional facies were deposited often control the primary petrophysical properties of sandstones (i.e., depositional reservoir quality), depositional architecture, and sediment composition and texture (grain size and sorting) and thus have a strong impact on eogenetic and mesogenetic alterations (Bjørlykke, 2014; Mansurbeg et al., 2008; Morad et al., 2010). The spatial and temporal evolution of flow processes deposit different bed-types, which are associated with different sub-environments. A significant challenge for appraisal of submarine fans during burial diagenesis, is the heterogeneity of the sandstones that may be dramatically altered due to complex diagenetic processes. These can especially be the case with submarine fan depositional systems, where a mix of sand-rich, heterolithic, and mud-rich facies can exist in close proximity to each other. These facies characteristics can make reservoir quality prediction in the subsurface particularly challenging. This chapter will review submarine fans depositional systems in terms of their sediment gravity flow processes, turbidite deposits, sand-rich and mud/sand-rich submarine fan models, role of clays in reservoir quality evolution of submarine fan sandstones, and the role of provenance in submarine fans sandstones framework composition, thereby giving an insight into the role played by depositional characteristics and facies, grain-coating and pore-filling clays, and diagenesis on reservoir quality of submarine fan systems.

2.2 Introduction

Submarine fans are defined as bodies of sediment accumulations on continental slopes and basin floors, deposited by sediment gravity flow processes in deep-water environments (Posamentier et al., 1991; Shanmugam, 1997a; Shanmugam and Moiola, 1988). They are mainly formed during sea level lowstand system tracts, which have been divided into two components: the lowstand fan and lowstand wedge (e.g., slope fans) (Posamentier et al., 1991). Deposited on the basin floor, the lowstand fans are formed during periods of relative sea level fall, whereas the lowstand wedge, deposited on the slope, are formed during subsequent periods of relative sea level standstill and slow rise (Posamentier, et al., 1991). The shapes and geometries of submarine fans largely depend on the grain size and composition of material supplied (gravel, sand, or mud), basin configurations, and tectonic settings (Reading and Richards, 1994; Shanmugam and Moiola, 1988).

Turbidite sandstone reservoirs of submarine fan systems are among the largest hydrocarbon reservoir targets around the world, with estimated 58 billion barrels of oil equivalent from 18 basins on six continents (Weimer and Pettingill, 2007; Pettingil and Weimer, 2002). Turbidite sandstones have been interpreted to have some of the best high-rate, high-ultimate-recoveries sandstone reservoirs in deep-water settings, making them economically significant (Weimer and Slatt, 2004). Although deep-water turbidite reservoirs have continued to produce significant volume of hydrocarbons, reservoir quality and prediction continue to be critical risks factors for current and future production strategies. As such, the influence of diagenesis in clastic turbidite reservoirs is relatively poorly understood and believed to be mostly mediated by marine pore waters (Mansurbeg et al., 2008). In addition, turbidite sandstones are characterized by reservoir heterogeneity influenced by rapid variation in sedimentary facies, and proximal to distal fan change in clay content (e.g., Collins et al., 2015; Hempton et al., 2005).

In this chapter, therefore, submarine fan depositional systems in terms of sediment gravity flow processes, submarine fan deposits, models of submarine fans, origin and types of clay minerals in submarine fans and their influence on reservoir quality, and the role of provenance on framework composition and reservoir quality of turbidites sandstones will be reviewed.

2.3 Sediment gravity flows

Sediment gravity flows are the most important processes by which submarine fans are developed (Covault, 2011; Lowe, 1979; Middleton and Hampton, 1973). Four types of sediment gravity flow processes have been recognized based on sediment-support mechanism (Middleton and Hampton, 1973): turbidity current, debris flows, grain flows, and fluidized sediment flows (Figure 2.1). This classification scheme, however, has been modified to incorporate blocky submarine slides and slumps, which have been identified and described from several deep-water deposits (Booth, 1979; Keller et al., 1979; Moore, 1977). Each of these processes are characterized by different sediment support mechanism and allow for segregation into distinct classes (Figure 2.1). Nevertheless, due to the role of liquefaction, internal pore pressure, and water content, it is difficult to observe clearly under natural conditions the class distinction of the submarine gravity flow processes (Klein, 1982; Lowe, 1976). Therefore, the understanding of the evolution of sediment gravity flows largely depends on interpreted data from sedimentary records, laboratory-based experiments, and numerical modelling (Cartigny et al., 2014; Salles et al., 2008; Stammer, 2014; Talling et al., 2012).

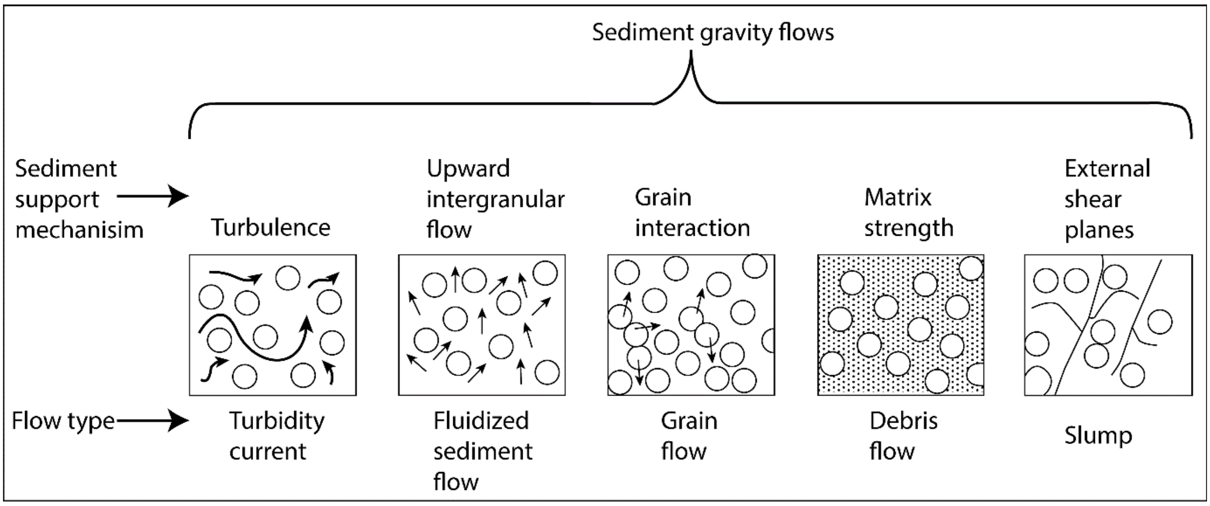

Figure 2.1. Classification of sediment gravity flow processes based on dominant sediment support mechanism (modified after Middleton and Hampton, 1973).

2.3.1 Turbidity currents

Turbidity current is a density-driven flow in which the sediment is supported by fluid turbulence and moves downslope by gravitational acceleration (Klein, 1982; Middleton and Hampton, 1973) (Figure 2.2). The flows are initiated by slope failure, or transition from one sediment gravity flow to another (Figure 2.2). They erode and form submarine canyons and then channelize into submarine fans, spreading as thin sheets where the flows are unconfined (Stammer, 2014). Deposition by turbidity currents occurs when there is sudden slope reduction and decrease in turbulence (Figure 2.2). Turbidity currents and associated debris flows are the two most important types of sediment gravity flows that form submarine fan deposits (Shanmugam and Moiola, 1988).

2.3.2 Fluidized flow

In fluidized flows, the sediment support mechanism is upward escaping fluid, which causes expansion of a sediment bed (Covault, 2011; Klein, 1982; Middleton and Hampton, 1973)(Figure 2.1). Thus, during the flow, both the fluid and the grains move upward. The sediments are kept afloat by excess interstitial pore pressure and become resistant to fluid injection when they are densely packed (Klein, 1982). Particles transported by this process include clay, silt and sand, and the liquefied beds commonly exhibit water-escape structures and lensoid laminations due to pore-pressure loss (Middleton and Hampton, 1973).

2.3.3 Grain flow

The sediment in grain flow is supported by gain-grain collisions (Covault, 2011)(Figure 2.1). Upward, dispersive stresses act on grains within grain flows due to grain-grain interactions. The dispersive stress is proportional to the shear stress transmitted between grains, which supports the grains within flows (Klein, 1982). These flows are typical of the upper parts of submarine canyons, and are strong enough to erode canyons (Shanmugam, 1997a).

2.3.4 Debris flows

These are gravity flows in which large grains and gravels are supported by a mixture of interstitial fluid and fine-grained sediment, with a finite yield strength (Middleton and Hampton, 1973)(Figure 2.1). Debris flows are characterized by dispersive pressure and, probably, turbulence, with matrix strength and buoyancy as the main sediment support mechanism. Deposition occurs when the driving gravitational stress decreases below the strength of the debris, causing freezing (Lowe, 1982; Middleton and Hampton, 1973).

2.4 Relationship between sediment gravity flows

Submarine gravity flows may undergo transformations from their onset to deposition on submarine fans (Covault, 2011; Fisher, 1983). Debris flow, for instance, can, with increasing fluid content, transition to a fluidized flow. Similarly, with rapid water loss, the reverse could also occur (Klein, 1982). Furthermore, shelf-edge sediment failure could initiate slumping, which could transform into turbidity currents as fluid content and turbulence increase downslope (Covault, 2011)(Figure 2.2). Additionally, sediment gravity flows and their transformations can be significantly influenced by seafloor topography (Hempton et al., 2005; Kneller and McCaffrey, 1999), and no intermediate stage is required for the transition to occur. The mechanism of sediment transport, thus, is controlled by rapid fluctuations in water content at a given time (Klein, 1982).

2.5 Deep-water depositional products

Deep-water deposits are formed by sediment gravity flow processes, and they include slides, slumps, turbidites, and debrites (Covault, 2011; Middleton and Hampton, 1973; Shanmugam, 2000) (Figure 2.2). Slides commonly consists of large blocks of lithified or semi-lithified deposits on continental slopes (Klein, 1982; Reading, 1996) (Figure 2.2A), or regions of salt-induced highs (Hempton et al., 2005). Slump are terrigenous or pelagic material, which break up into large blocks during transport downslope by mass movement processes (Boggs, 2006; Covault, 2011) (Figure 2.2B), and they largely exhibit complex internal deformation. Turbidity currents and debris flows, unlike slides and slumps, are characterized by higher degree of internal deformation (Covault, 2011; Middleton and Hampton, 1973) (Figure 2.2C & D). The downslope, sediment gravity flows occur due to density difference between the gravity flow and ambient water (Klein, 1982). Furthermore, the excess density could be attributed to temperature contrast between water layers, difference in salinity between two water layers, and rapid influx of sediments in suspension (Biju-Duval, 2002). Turbidity currents and debris flows are the two most important types of sediment gravity flows that form submarine fan deposits (Shanmugam, 2000; Shanmugam and Moiola, 1988).

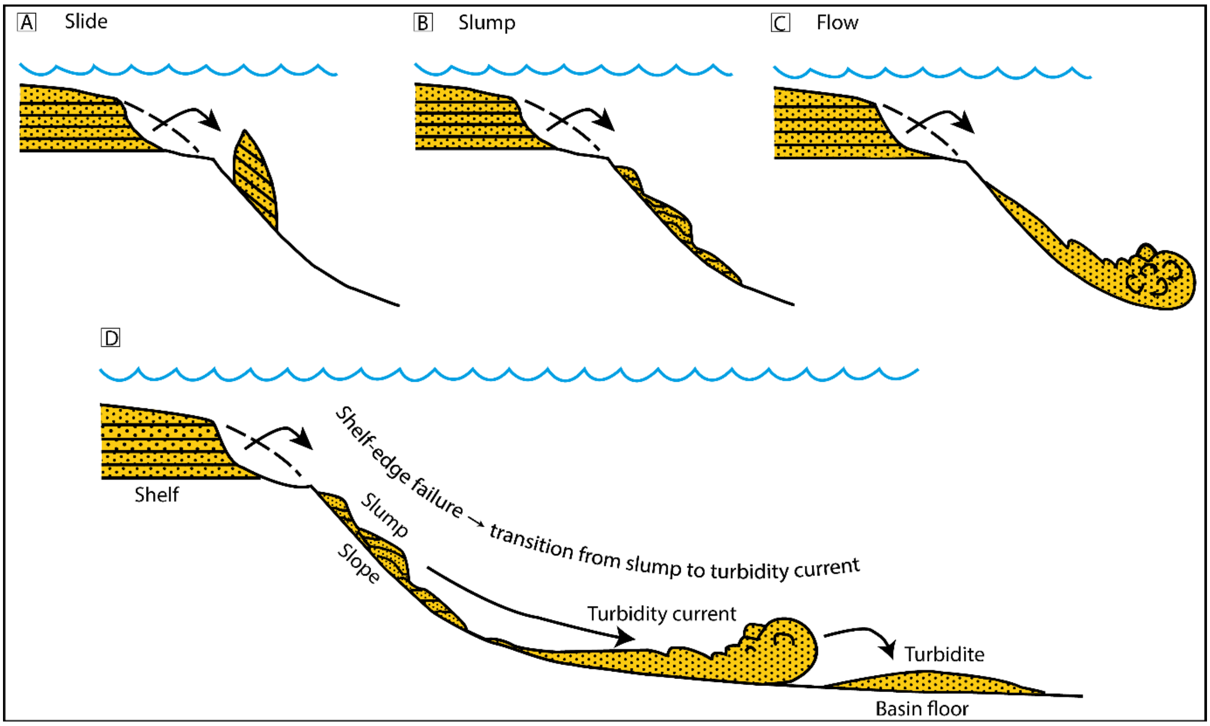

Figure 2.2. (A-C) Classification of submarine mass movements, which are generally distinguished based upon the degree of internal deformation. (D) Initiation of submarine movement mass movement resulting from shelf-edge sediment failure, accompanied by transformation from slumping to turbidity current processes and deposits. The decrease in clay/mud content, among other factors, increases flow turbulence, thereby converting, for instance, slump into turbidity currents and vice versa (modified after Covault, 2011).

2.5.1 Turbidite sandstones

A turbidite is a product of a single depositional event from a turbidity current (Figure 2.2D). They are deposited in the lower part of submarine canyons and extend farther seaward as cone-shaped fans and deep-water channels (Boggs, 2006). Turbidites are characterized by graded bedding in which the sediment grain size fines upward, indicating deposition from a waning turbidity current (Shanmugam, 2000; Shanmugam and Moiola, 1988) (Figure 2.3).

Although there are several lithofacies models for deep-water, sediment gravity flow deposits, the well-known and the most widely used include: the Bouma sequence (Bouma, 1962) (Figure 2.3), which is based on fining upward sequence; the Lowe model (Lowe, 1982), which is based on high- and low-density turbidites; the fluxo-turbidites model, which assumes deposition from composite sediment gravity flows and include turbidity currents, debris flows, grain flows, and liquefied sediment flows (Górska, 2019); and the hybrid event beds model (Houghton et al., 2009), which depicts the transition from non-cohesive to a cohesive flow behaviour. In this chapter, however, the Bouma sequence will be discussed only.

2.5.1.1 The Bouma sequence

Thick, massive sandstones of **Facies A** (Figure 2.3) division are usually identified as: (i) amalgamated deposits of high-density turbidity currents (Collins et al., 2015; Górska, 2019; Hempton et al., 2005) and (ii) deposits formed from massive freezing of debris flows (Talling et al., 2012). Normal grading is common and interpreted to have formed due to rapid fallout from suspension in a turbulent, high density turbidity currents (Lowe, 1982).

Horizontally laminated sandstones of the **Facies B** (Figure 2.3) division were interpreted as deposits of low-density turbidity current (Lowe, 1982), associated with low sedimentation rates. It has recently been established, however, that the parallel lamination in the facies might be formed at the lowest part of high-density turbidity currents (Leclair and Arnott, 2005).

The ripple laminated sandstones of **Facies C** interval (Figure 2.3) are considered as deposits of traction processes under the lower flow regime. Their formation might be attributed to turbidity currents (Shanmugam, 1997b), deep-water bottom currents (Shanmugam et al., 1993) and/or sediment bed-loading. The ripple cross lamination associated with the facies are indicative of deposition from low-density turbidity currents (Talling et al., 2012).

The parallel laminated siltstone/mudstone of **Facies D** interval (Figure 2.3) suggests a weak, lower flow regime traction process, which leads to the formation of the individual laminae (Lowe, 1982). The laminated mudstones are thought to indicate a transition to an overlying hemipelagic and pelagic sedimentation (Lowe, 1982), which form massive mudstones of the **Facies E** division of the Bouma sequence, and indicate settlement from suspension (Figure 2.3).

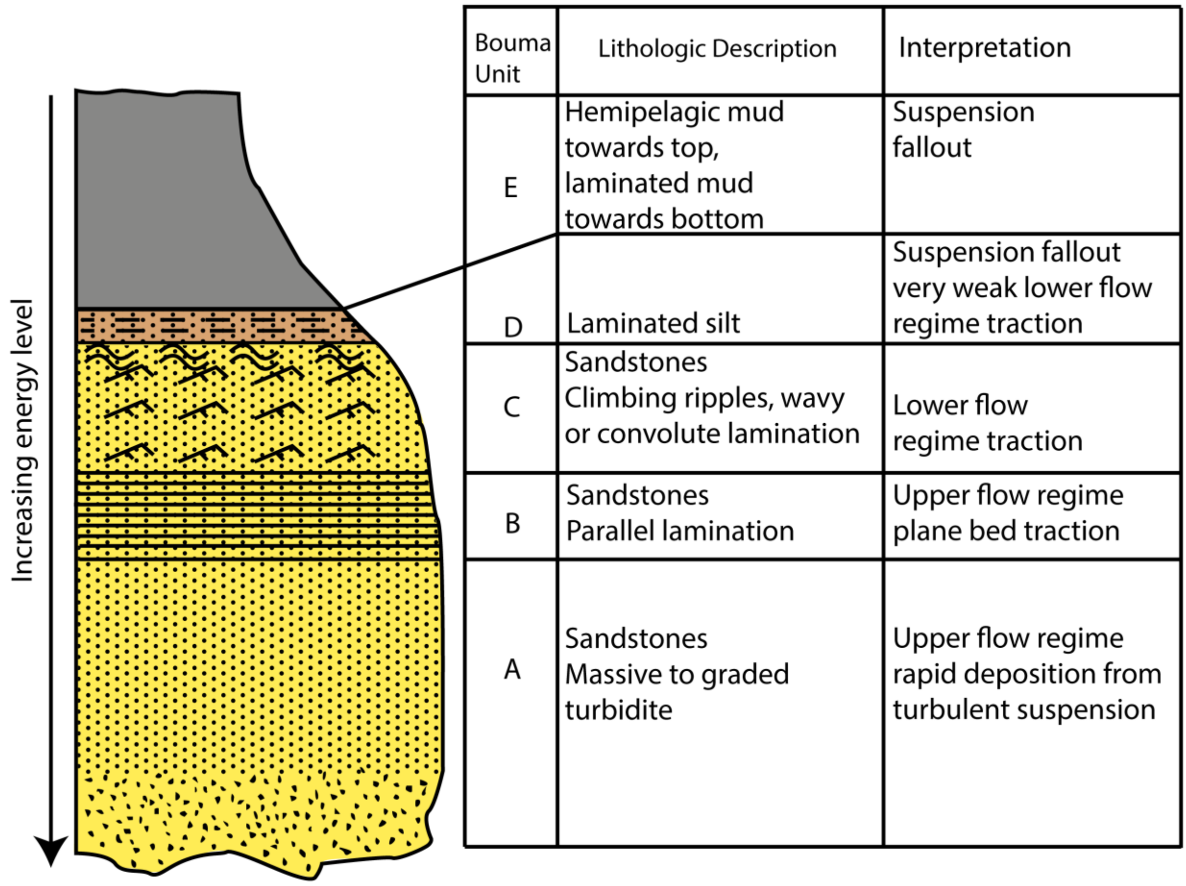

Bouma Unit	Lithologic Description	Interpretation
E	Hemipelagic mud towards top, laminated mud towards bottom	Suspension fallout
D	Laminated silt	Suspension fallout very weak lower flow regime traction
C	Sandstones Climbing ripples, wavy or convolute lamination	Lower flow regime traction
B	Sandstones Parallel lamination	Upper flow regime plane bed traction
A	Sandstones Massive to graded turbidite	Upper flow regime rapid deposition from turbulent suspension

Figure 2.3. Sedimentary log for the classic Bouma Sequence, showing lithologies, sedimentary structures, and interpretation of the depositional mechanisms (modified after Bouma, 1962).

2.6 Submarine fan models

Submarine fans systems have been classified based on modern and ancient fans (Jacka et al., 1968; Mutti and Ricci Lucchi, 1972; Normark, 1970), attached and detached lobes (Mutti and Ricci Lucchi, 1975, 1972), highly- and poorly-efficient fans (Johns and Mutti, 1981; Mutti, 1979; Ricci Lucchi, 1981), and transverse and longitudinal fans (Dickinson and Seely, 1979; Underwood and Bachman, 1982). However, Shanmugam and Moiola (1988), for instance, pointed out that Mutti (1979)'s classification of fan systems based on their efficiency to transport sand alone, is impractical. This is because of the fact that a single fan can possess the features of both 'highly-efficient' and 'poorly-efficient' systems, indicating that sand can be transported over long and short distance, respectively. Consequently, having recognized the need to develop all-encompassing models of submarine fans systems, because the existing models are too simple to take into account the complexities in the interpretation of petroleum-rich turbidite reservoirs, Reading and Richards (1994) developed submarine fan models based on grain sizes, composition of materials supplied (e.g., gravel, sand, or mud), sediment feeder type, and delivery processes, which are more widely used today. The models would significantly help in predicting and evaluating the possible geometry and facies characteristics of deep-water siliciclastic systems.

Based on the criteria stated above, Reading and Richards (1994) have proposed four representative models of submarine fans systems: gravel-rich systems, sand-rich systems, mud/sand-rich systems, and mud-rich systems. However, for the purpose of this study, and because of their relevance to several other submarine fans systems around the world, focus will be based on the sand-rich and mud/sand-rich systems, as they are characterized by high and moderate sand/mud ratio (respectively), with generally higher depositional porosity. Furthermore, they offer suitable sites for studying the role of clay minerals on reservoir quality evolution of turbidite sandstones.

2.6.1 Sand-rich submarine fans

Sand-rich submarine fans systems have more than 70 % of sandy material in the whole deposits, and typically tend to be moderate in size, with a radius of less than 50 km (Reading and Richards, 1994). The classic examples of the sand-rich fan systems include the Cengio fan system, Northwest Italy (Cazzola et al., 1985); the Jurassic Magnus and Miller fans, North Sea (De'Ath and Schuyleman, 1981; Garland, 1993); the Eocene Frigg and Paleocene Forties fans, North Sea (Den Hartog Jager et al., 1993; Heritier et al., 1979), etc. The systems tend to be radial rather than lobate in shape, and are fed by proximal, sand-rich shelf, where the sand material gets sorted by waves, tides, and storms (Nichols, 2009; Shanmugam and Moiola, 1988). The sand materials are delivered into the basin by high-density turbidity currents via shelf-incised canyons (Figure 2.4) and/or shelf failure (Reading and Richards, 1994). The sand-rich fan systems have been recognized as 'poorly-efficient' because of their inability to transport sand far into the basin (Mutti, 1979). In addition, they are characterized by low-sinuosity, unconfined braided channels, which repeatedly switch over the fans due to the absence of levees. Thus, deposition consists of amalgamated sandstones of channels and lobes, and because they are poorly efficient, the transition to fine-grained sheet deposits of the lower fan area tends to be abrupt (Nichols, 2009; Reading and Richards, 1994).

Supplied by a proximal source, the sandstones of sand-rich submarine fans systems are likely to preserve their detrital clay coats inherited from continental shelf, having travelled short distance from the shelf (e.g., Bahlis and de Ros, 2013; Yezerski and Shumaker, 2018). Consequently, the coatings are unlikely to suffer intense abrasion during transport. The sands, therefore, would preserve reservoir quality, if well coated by clays, by preventing quartz cementation during deep burial.

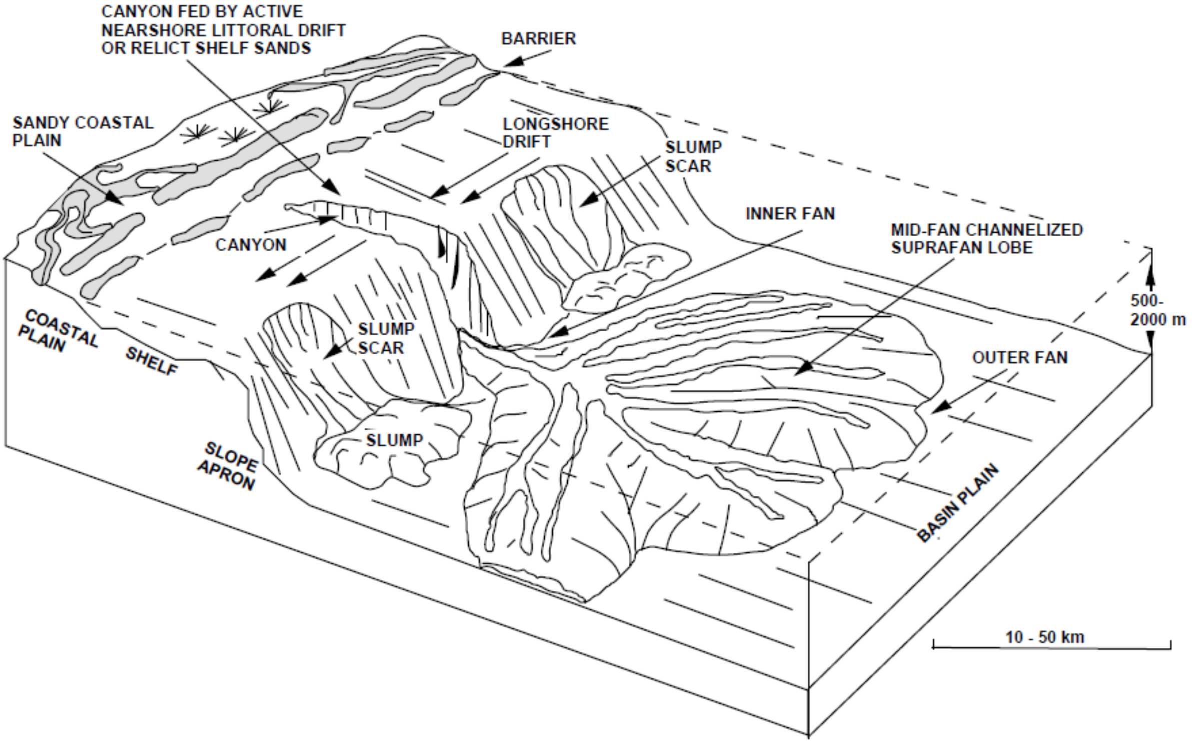

Figure 2.4. Depositional model for a point-source, sand-rich submarine fan system, showing sand dominance and lobate-shaped fan. Sand is supplied from shelf and coastal areas and transported into deep-water through canyons (from Reading and Richards, 1994).

2.6.2 Mud/sand-rich submarine fans

Many classic submarine fans are represented by mud/sand-rich fans (e.g., Normark, 1970; Piper and Normark, 1983; Shanmugam and Moiola, 1991; Walker, 1978). They, among others, include the Delgada Fan, offshore Northern California; the Hecho Fan, South-Central Pyrenees, Spain; and the Navy Fan, Pacific Ocean. The mud/sand-rich fan systems occur where a river/delta system supplies large volumes of both sandy and muddy material, with a typical sand percentage ranging from 30 to 70 % for the whole system (Nichols, 2009; Reading and Richards, 1994). The systems, which are lobate in shape rather than elongate, have been described as moderate, with typical radii ranging between 10 km and 450 km (Reading, 1996; Reading and Richards, 1994). They are characterized by low gradient, distal source, and are 'highly efficient', transporting sand material over a long distance (Mutti, 1979). Mud/sand-rich fans are commonly fed by a mixed mud/sand delta, coastline, and/or sediment-rich continental shelf incised by a canyon (Reading and Richards, 1994) (Figure 2.5). Deposits of the mud/sand-rich fan systems consists of high-density, coarse-grained turbidite sandstones in the channel and low-density currents, muddy channel abandonment facies, while the lobe deposits are variable in composition, consisting of both high- and low-density turbidite sandstones (Marchand et al., 2015; Nichols, 2009).

The formation of detrital, grain-coating clay minerals in deep-water turbidite sandstones has been linked to the distance of transport the sediments have travelled (Bahlis and de Ros, 2013; Yezerski and Shumaker, 2018). The mud/sand-rich fan systems are largely fed by river delta through deeply incised canyons that extend up to delta fronts (Burke, 1972; Reading and Richards, 1994; Shanmugam, 1997a), suggesting that deep-water density currents, generated by oversteepening, storm and wave actions, earthquakes, increased salinity and lowered temperature, subject the sediments to a long distance of transport, which pervasively abrades their detrital, grain-coating. Should the abraded sediments undergo deep-burial, consequently, they might be cemented by ubiquitous quartz overgrowths due to lack of coatings. Shelf-break and shelf-canyon fed deep-water mud/sand-rich systems, however, are likely to have shelf-inherited detrital clay coats because of relatively shorter distance of transport, which could potentially inhibit quartz cementation at deep burial. Additionally, the relatively long channels associated with such systems could emplace detrital clay coats during sediment dewatering (Housenknecht and Ross, 1992; Porten et al., 2019), which could be preserve reservoir quality in deeply buried turbidite sandstones.

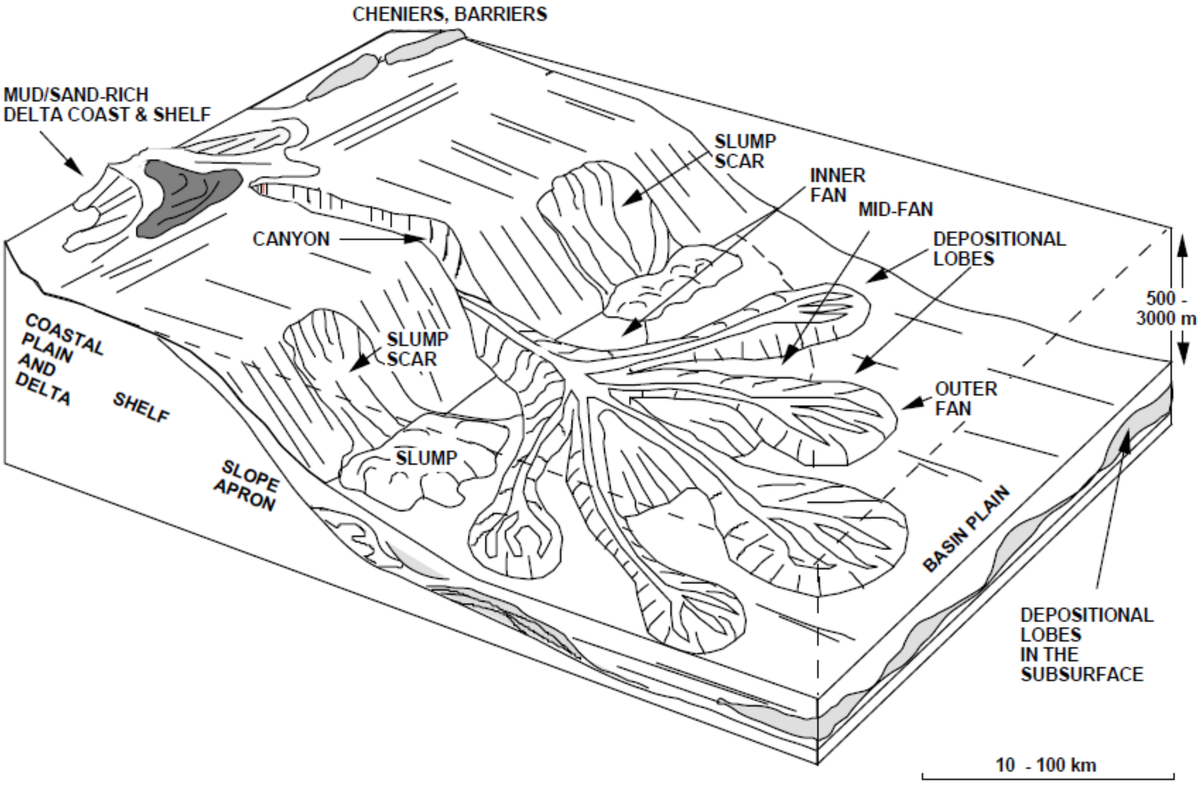

Figure 2.5. Depositional model for a point-source, mud/sand-rich submarine fan, showing a mixture of sand and mud, and showing how lobes build further out as the turbidites travel far distances. The fan is fed by a mixed-load delta, a coastline, or a sediment-rich shelf, incised by a canyon (from Reading and Richards, 1994).

2.7 Role of clay minerals in sandstones

Porosity, permeability, and wettability are the most important parameters of sandstones reservoir quality (Jiang, 2012; Marchand et al., 2015; Grier and Marschall, 1992), as they determine the type and amount of reservoir fluids a rock can contain and the rate at which they can be produced. The occurrence of clay minerals in sandstones reservoirs has significant impact upon reservoir porosity and permeability (Griffiths et al., 2018), the two parameters upon which reservoir quality is effectively evaluated. Depending on their mode of occurrence, type and abundance in sandstone reservoirs, clay minerals can degrade or enhance reservoir quality (Griffiths et al., 2019). Pore-filling illite, for instance, significantly reduces reservoir permeability by blocking pore throats (Morad et al., 2010; Oluwadebi et al., 2018; Worden and Morad, 2003), whilst grain-coating chlorite preserves porosity by inhibiting the development of pore-filling quartz cement (Ajdukiewicz and Larese, 2012; Bahlis and De Ros, 2013; Ehrenberg, 1993; Griffiths et al., 2018; Stricker et al., 2016; Stricker and Jones, 2018; Wooldridge et al., 2018). Anomalously high porosity are recorded where grain-coating clays are thick and well-developed (Pittman et al., 1992; Stricker, 2016; Tang et al., 2018). However, poorly prepared thin-sections and polished SEM samples are often identified by their oversized porosities, detrital grains being pulled out or intergranular clays and carbonate cements being removed, thereby resulting in the overestimation of both intergranular and intragranular thin-section porosities and, thus, reservoir quality. Such samples are either reprepared or excluded from point counting. Table 2.1 shows some reported porosity-preserving, grain-coating clays (consisting of chlorite, illite-smectite, and illite) in turbidite sandstone reservoirs around the world, with their preserved porosity values. The mineralogy and coverage or completeness of grain coats have been reported to play a crucial role in controlling the ability of clay coats to inhibit the formation of quartz cements (Ajdukiewicz and Larese, 2012). The optimum amount of grain-coating clays to prevent quartz cementation and, thus, preserve porosity in sandstones is variable. Studies of the Berea Sandstone and the Tuscaloosa Formation, for instance, have shown the optimum clay coat volume (to preserve porosity) is in the range of 4–7% and 5–12%, respectively (Pittman et al., 1992). However, a relatively minor amount of clay, as little as 1–2% of the rock volume, are reported to have formed well-developed coats on individual sand grains (Bloch et al., 2002). Therefore, although they are often considered to have detrimental effect on reservoir quality (because they enhance compaction and block pore throats), the occurrence of clay minerals in sandstones does not always signify to reduce reservoir quality, as grain-coating clays have positive impact on reservoir quality by arresting quartz cementation.

The origin of clay minerals in sandstones, including grain-coating clays, can be detrital and/or authigenic (diagenetic) (McKinley et al., 2003; Porten et al., 2019; Worden et al., 2020; Worden and Morad, 2003). Detrital clay coatings are emplaced in sandstones during mechanical infiltration (Kordi, 2013; Matlack et al., 1989), bioturbation (Taylor and Goldring, 1993), sediment dewatering (Houseknecht and Ross, 1992; Porten et al., 2019), and biofilms (Wooldridge et al., 2017). The type of detrital grain-coating clays emplaced in sandstones is influenced by depositional environment, weathering, and climate (McKinley et al., 2003; Worden et al., 2020). Smectites, for example, tend to form in depositional environment close to the sediments provenance (although they occur in turbidites) (Figure 2.6), and in arid climatic condition, which ensures less availability of water for chemical weathering (McKinley et al., 2003). Chlorite, on the other hand, tends to form in deltaic and shallow marine environments where intense chemical weathering occurs (Worden et al., 2020). Detrital clays undergo transformation during burial diagenesis to form other clay minerals. Smectite, for instance, depending on its composition, transform into chlorite or illite, often via a mixed-layer chlorite/smectite or illite/smectite, respectively (Bahlis and de Ros, 2013; McKinley et al., 2003; Worden et al., 2020; Worden and Morad, 2003) (Figure 2.7). Furthermore, authigenic clays can be transformed to other clays that are stable under high temperature conditions. For example, vermiform, low-temperature kaolinite transforms to either blocky, higher-temperature dickite or fibrous illite (Lanson et al., 1996; Morad et al., 1994; Worden and Morad, 2003) (Figure 2.7). Additionally, detrital grains such as K-feldspar and lithic fragment transfrom into diagenetic illite and chlorite, respectively (Chen et al., 2011; Kordi, 2013; Worden and Morad, 2003).

Table 2.1. Selection of turbidite reservoirs with grain-coating chlorite, illite-smectite, and illite reported in the literature, with information on country, basin name, formation, age, reference, coating type, burial depth, and porosity.

Country	**Basin Name**	**Formation**	**Age**	**Reference**	**Coating Type**	**Burial Depth (m)**	**Porosity (%)**
Brazil	Santos Basin	Itajaí-Açu Formation	Upper Cretaceous	(Anjos et al., 2003)	Chlorite	4000-5000	25
Norway	Vøring Basin	Springar Formation	Upper Cretaceous	(Porten et al., 2019)	Illite	2600-3800	24
UK	Faroe-Shetland Basin	Sullum Formation and Vaila Formation	Early to Middle Paleocene	(Friis et al., 2014)	Chlorite	3500-3600	
US	Arkoma Basin	Atoka Formation	Lower to Middle Pennsylvanian	(Houseknecht and Ross, 1992)	Chlorite, Illite/smectite, and Illite		5 to 20

2.7.1 Smectites

Smectites have been recognized as chemically complex group of clay minerals that, unlike other clay minerals like chlorite and illite, are poorly documented in sandstone reservoirs (McKinley et al., 2003). Nevertheless, they are crucially important in sandstones as they represent up to 25 % of clay-cemented sandstones, thereby significantly impacting sandstones their reservoir quality (Primmer et al., 1997). Smectite acts as pathways through which other clay minerals such as chlorite and illite are formed during diagenesis (Morad et al., 2010; Worden and Morad, 2003) (Figure 2.7). Pore-filling smectites have a detrimental effect on reservoir quality, despite having significant but ineffective micro-porosity. Detrital, grain-coating smectites (Figure 2.8), in contrast, have positive impact on sandstones reservoir quality, for they serve as precursors for grain-coating chlorite and illite, which inhibit the development of quartz cementation (Pittman et al., 1992). Smectites, like other clay minerals, can be both detrital and authigenic (Huggett, 1996; Weibel, 1999). Detrital smectites consists of weathering products of surficial soils, igneous rocks, and volcaniclastic sedimentary rocks, whereas early, diagenetic smectite results from authigenic processes during shallow-burial, eodiagenesis, including alterations of detrital lithic fragments (McKinley et al., 2003). Unlike in mudstones where smectites are inherited directly from primary sediment (Niu and Ishida, 2000), the smectites in sandstones are emplaced through bioturbation, infiltration, soft sediment deformation, and authigenesis in formation water (Jeans, 1989).

2.7.1.1 Chemistry of smectites

Smectites, like chlorite and illite, are 2:1 phyllosilicates characterized by 2 tetrahedral sheets surrounding one octahedral sheet, and have a general formula of $(0.5Ca,Na)_{0.7}(Al,Mg,Fe)_4(SiAl)_8O_{20}(OH)_4 \text{ x } nH_2O$ (Altaner, 1978). The tetrahedral sheets are dominated by Si and Al, whereas the octahedral sheets are occupied by metal hydroxides such as $Al_2(OH)_6$, $Mg_3(OH)_6$, and $Fe_3(OH)_6$. Smectites have been classified as dioctahedral (e.g., montmorillonite), in which the octahedral sheets are occupied mainly by trivalent cations such as Al^{3+} or Fe^{3+}; and trioctahedral (e.g., saponite), in which the octahedral sheets are occupied mainly by divalent cations such as Fe^{2+} and Mg^{2+} (Brigatti et al., 2013). Dioctahedral smectites, thus, tend to be Al-rich, whilst the trioctahedral smectites tend to be Fe-Mg rich (McKinley et al., 2003). In smectites, the interlayer cations, typically consisting of Ca^{2+}, Mg^{2+}, or Na^+, are variably hydrated, resulting in the swelling characteristic of smectites (Huggett, 2015; Worden and Morad, 2003). As smectite expands, an interlayer cation can be replaced by another cation, resulting in higher cation exchange capacities in comparison to non-expanding clays minerals.

2.7.1.2 Origin of smectites

The occurrence of smectites in sandstones is controlled by both depositional and diagenetic factors. Primary, depositional smectites are incorporated into sediment transported from a nearby source terrain characterized by less advanced weathering and mineralogically immature sediments, favouring the formation of smectites in preference to other clays (McKinley et al., 2003; Ruffell et al., 2002). These conditions are typical of arid and high-relief regions where weathering cannot proceed into an advanced stage due to insufficient water and poor drainage. Thus, the removal and transport of aqueous weathering material is inhibited, which prevents advanced (chemical) weathering. The type of smectites formed are influenced by the lithology of the source terrain. Dioctahedral smectites originate from weathering of acid and intermediate igneous rocks and silicic metamorphic rocks, whereas trioctahedral smectites are formed from the weathering of more mafic-rich, basaltic and volcaniclastic rocks, and lithic sandstones

(McKinley et al., 2003). In addition, the breakdown of alkali feldspars and plagioclase due to weathering often result in the formation of pseudomorphic dioctahedral smectite (Aoudjit et al., 1995). The weathering of Fe-Mg-rich minerals such as biotite and pyroxene, in contrast, results in the formation of pseudomorphic trioctahedral smectites (Chang et al., 1986; McKinley et al., 2003).

The depositional environments that favour the formation of detrital smectite include alluvial, fluvial, aeolian, lacustrine, and deep-marine fans (McKinley et al., 2003) (Figure 2.6). Although smectitic clays in turbidite sandstones are not emplaced through sediment ingestion and excretion (biofilm) mechanism, the process is common in fluvial and deltaic sediments (Worden *et al.* 2020), resulting in the transport of biofilm-emplaced sediments from fluvial and deltaic depositional environments to deep-water settings during periods of low sea level. The occurrence of detrital smectites in turbidite sandstones is influenced by highly-fluctuating, turbulent energy conditions (coupled with rapid sedimentation) where clay- and sand-sized materials are mixed together during transport, or because the smectites are finer grained than other clays (with particle size ranging from 0.9 µm to <0.1 µm) and hence can be transported further downslope (into deep water) before settling out of suspension during quiescent periods (Bjørlykke, 2014; McKinley et al., 2003). Thus, high-energy environments such as delta and shallow marine are unlikely to form smectites (Figure 2.6), due to the actions of waves and tidal currents that winnow out clay-size material from sand- and silt-size material (Lynch, 1996).

In arid conditions, under which smectites are formed, the ability to lose cations is impeded by the lack of water and advanced weathering, thereby increasing the mineralogical immaturity as well as the chances of preserving smectites. Warm and humid climate, in contrast, speed up chemical weathering and (hence) facilitates the loss of cations (e.g., Na, K, Ca, Mg, etc.), which limits the preservation potentials of smectites and enhances the preferential formation of kaolinite and illite over smectites (McKinley et al., 2003).

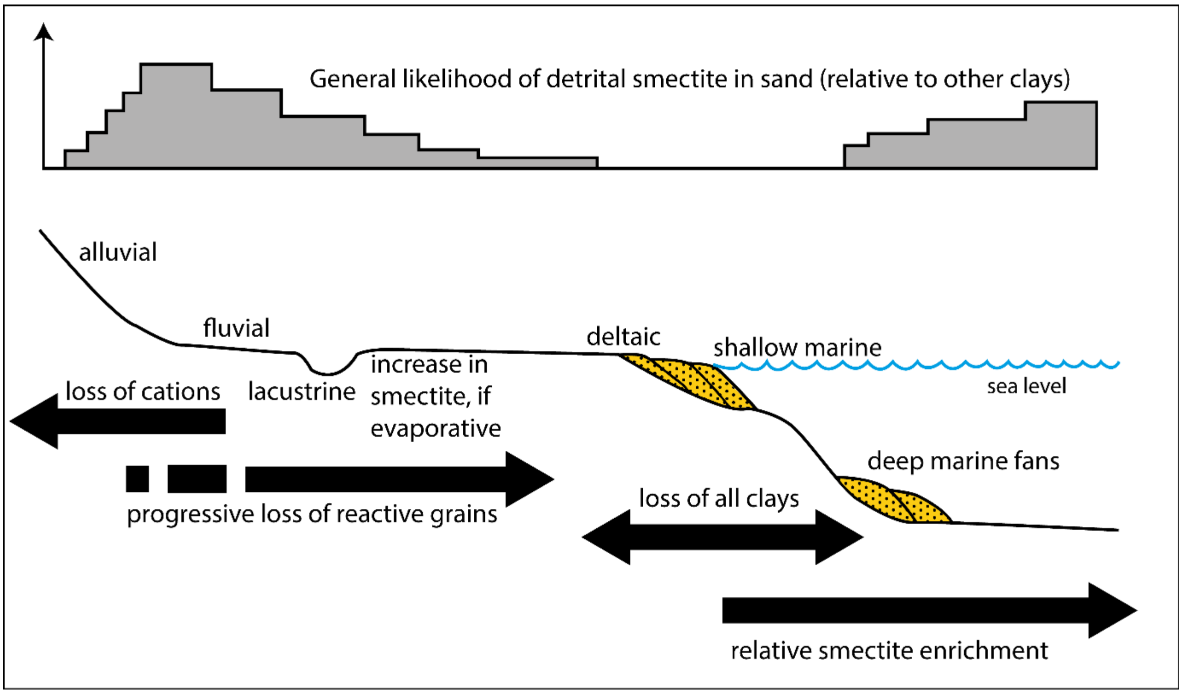

Figure 2.6. Relative abundance of detrital smectite in sandstones from various depositional environment. Supply of smectite may be influenced by geology of hinterland (provenance), paleoclimate of hinterland, and depositional environments. The diagram highlights depositional environments favourable for the formation of smectite, and assumes that no significant changes in sediment provenance or paleoclimatic conditions have occurred during deposition (modified after McKinley et al., 2003).

2.7.1.3 Transformation of smectite to other clay minerals

Early diagenetic smectites are formed from dissolution of detrital plagioclase and lithic grains in plagioclase-rich sandstones and litharenites, respectively (Ryu and Niem, 1999). The smectite enrichment of ocean basin sediments has been interpreted to have resulted from *in situ* transformation and recrystallization of terrigenous clay components (Thiry and Jacquin, 1993). Smectites transform to illite, chlorite, and via mixed layer clays (McKinley et al., 2003; Worden and Morad, 2003) (Figure 2.7). Dioctahedral smectites tend to transform to illite, and the conversion requires aqueous Al and K to occur, which could be sourced from dissolution of K-feldspar. If the reaction proceeds, the amount of K-feldspar and smectite will decrease with depth, and the lack of Al and K, thus, suggests an increase in stability of smectites in the sandstone reservoirs. Illitization of smectites is, therefore, more likely to occur in arkoses than in quartz arenites (95 % quartz). Furthermore, depending on the lithology (whether sandstones or mudstones), and on the overall permeability and connectivity in sandstones, an overpressure may develop as a result of the illitization of smectite, as water is a by-product of the reaction (Lynch, 1997). The transformation of smectites to other clays is often accompanied by precipitation of quartz and/or carbonate cements (McKinley et al., 2003). For instance, as dioctahedral smectite transforms into illite, Na, Ca, Mg, or Fe are released, and if bicarbonate is present in the formation water, the released metal cations would react with the bicarbonate to form carbonate cements (e.g., siderite and dolomite) (Worden et al., 2020).

Trioctahedral smectites, on the other hand, tend to convert to chlorite, with the addition of Fe, Mg and water (Chang et al., 1986). Chloritization of smectite, like illitization, also leads to precipitation of quartz cement, as Al/Si ratio of the clay mineral increases during the transformation, but with even more quartz cement precipitation compared to illitization (McKinley et al., 2003). Similarly, due to the release of Na, and Ca (and possibly Mg), chloritization may lead to the precipitation of carbonate cements should bicarbonate be present in the formation water. The stability of smectite depends on ambient temperature and geochemical environment. While dioctahedral smectite transforms to form a mixed-layer illite-smectite at relatively lower temperature (60-80 ℃) , trioctahedral smectite persists to higher temperature (70-90 ℃) (Worden and Morad, 2003).

The transformation of smectites to either chlorite or illite occurs through mixed-layer stage (Worden and Morad, 2003). Mixed-layer smectites consists of smectite/ illite (S/I), illite/smectite (I/S), smectite/chlorite (S/C), and chlorite/smectite (C/S) (McKinley et al., 2003; Morad et al., 2010; Worden and Morad, 2003). The transformations commonly start at shallow depths and continues into deeper burial diagenesis. In the Triassic sandstones of Skagerrak Formation Denmark, for instance, the transformation of smectite into smectite/illite occurred at shallow depths and at relatively low temperature (47-68 °C) (Weibel, 1999).

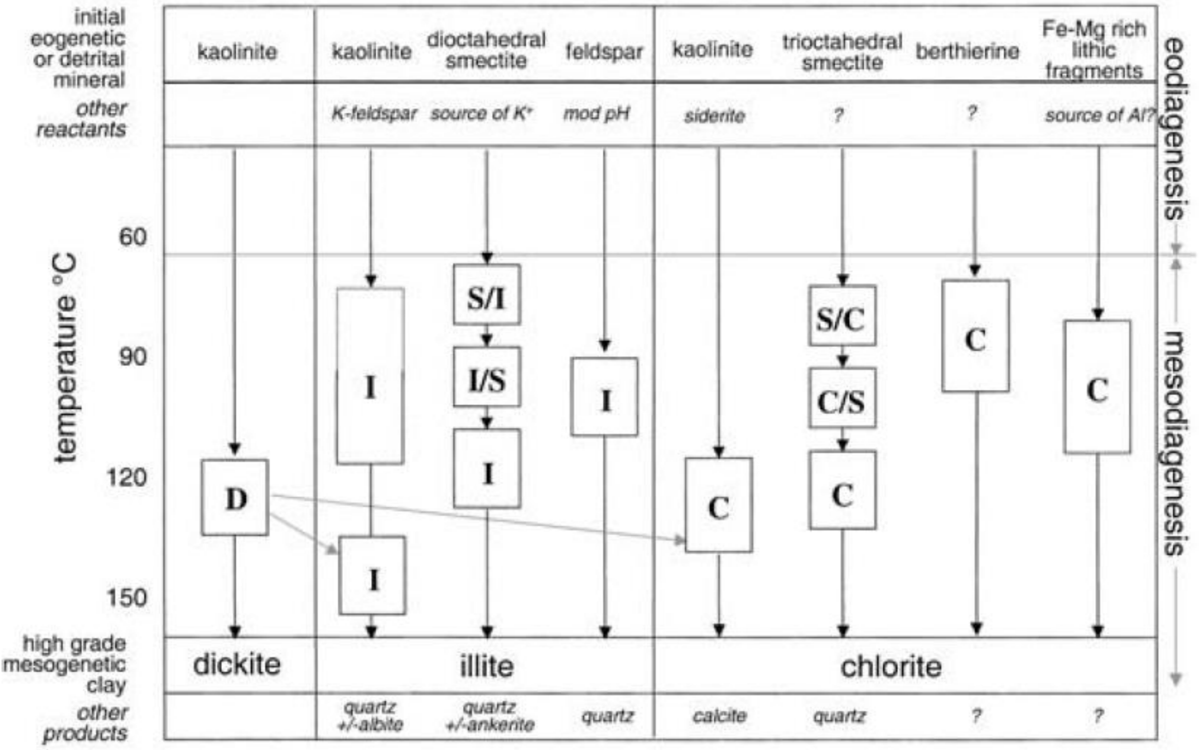

Figure 2.7. Common mesogenetic pathways for clay minerals in sandstones, where D is dickite, S is smectite, I is illite and C is chlorite, from Worden and Morad (2003). Randomly interstratified mixed-layer clay minerals are named according to the types of layers involved, with the most abundant layer type listed first: S/I is mixed-layer smectite–illite dominated by smectite; I/S is the same mineral mixture dominated by illite. The same naming rules apply for interlayered smectite–chlorite. High-grade diagenesis leads to dickite, illite and chlorite clay minerals in sandstones. Kaolinite forms predominantly during eodiagenesis and can be cannibalized to form dickite, illite or even chlorite during mesodiagenesis. Illite forms by at least three main routes during mesodiagenesis. Although it can be a detrital clay (following incomplete weathering), it does not form during eodiagenesis. Chlorite also seems to be unlikely to form during eodiagenesis and forms by at least four main pathways.

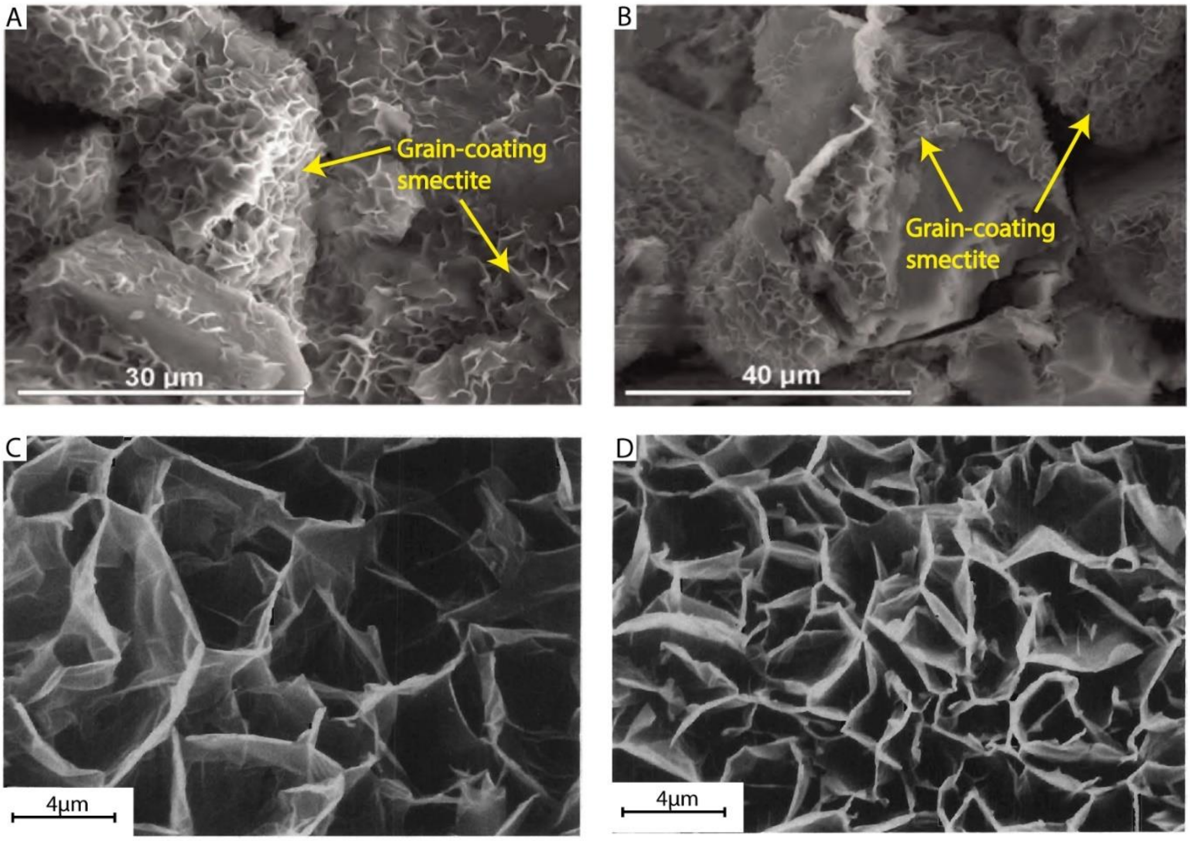

Figure 2.8 (A-B) SEM images showing grain-coating smectite (from Fesharaki et al., 2007). (C-D) SEM images showing grain-coating smectite (from Pittman et al., 1992).

2.7.2 Mixed-layer clays

Mixed-layer clays are important group of clay minerals with complex structure and intermediate composition between end-members (Brigatti et al., 2013) (Figure 2.9). Mixed-layer clay minerals occur in a single structure, often with high- and low-temperature end-members (Środoń, 1999). The mixed-layer clay species consists of smectite/illite, illite/smectite (Figure 2.7), smectite/chlorite, chlorite/smectite, chlorite/kaolinite, chlorite/ illite, illite/kaolinite, kaolinite/smectite, and dickite/kaolinite (Brigatti et al., 2013; Worden and Morad, 2003). They represent ongoing transformation stages between low- and high-temperature clay minerals, and their coatings can be present in sandstones reservoirs, indicating an incomplete or an ongoing transformation of low-temperature clays (Figure 2.7). The mixed-layer illite/smectite chlorite/ illite species are the most widely studied among the mixed-layer clays (Ajdukiewicz et al., 2010; Brigatti et al., 2013; Chen et al., 2011) There is, however, less information on chlorite/smectite than on illite/smectite. Mixed-layer illite/smectite occurs as both grain coating clays, which could prevent quartz cementation, (Figure 2.9A), and as pore-filling cement, which degrades reservoir quality (Figure 2.9B).

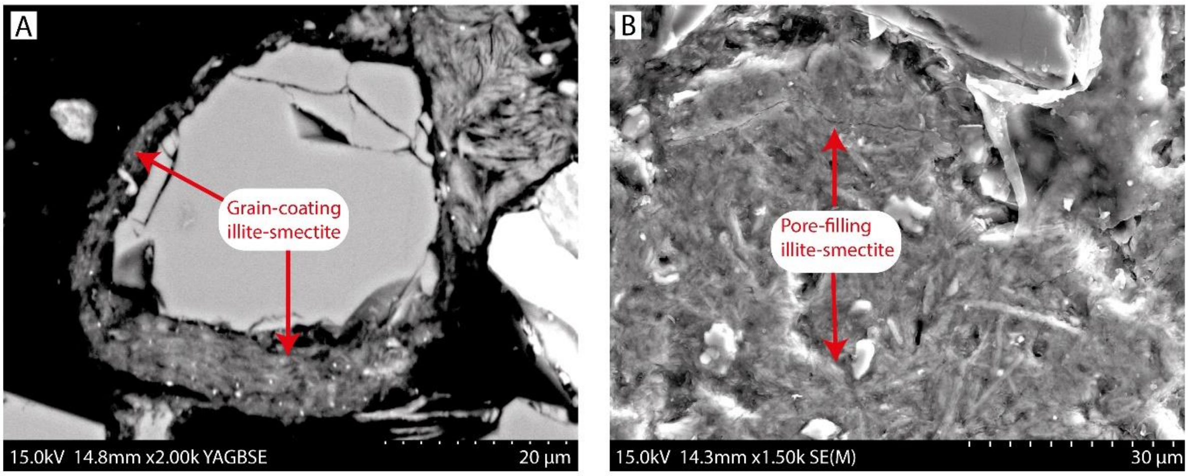

Figure 2.9 BSEM images showing examples of mixed-layer, grain-coating, and pore-filling clays within the studied Forties Sandstone Member. (A) BSEM image of grain-coating, mixed-layer illite/smectite preventing quartz cementation and preserving porosity. Blane field, well 30/03a-1, 3097 m TVDSS; (B) SEM image showing mixed-layer, pore-filling illite/smectite, destroying intergranular porosity. Blane field, well 30/03a-1, 3096 m.

2.7.3 Chlorite

Chlorite is an important clay mineral that has been widely reported for porosity preservation in sandstone reservoirs (Ajdukiewicz and Lander, 2010; Bahlis and de Ros, 2013; Ehrenberg, 1993; Pittman et al., 1992; Stricker and Jones, 2018; Worden et al., 2020) . Grain-coating chlorites prevent quartz cementation in deeply buried reservoirs (Chen et al., 2011; Dutton et al 2018) (Figure 2.10A). The coatings cover detrital quartz grain surfaces, reducing the nucleation area for precipitation of quartz cement (Ehrenberg, 1993; Heald and Larese, 1974; Pittman et al., 1992). Clean, well-sorted sandstones which lack detrital or authigenic clay coats are susceptible to extensive quartz cementation during deep burial (> 80 to 100 °C) (Worden et al., 2020) (e.g., Figure 2.10A), thereby decreasing porosity and permeability of the sandstones. Consequently, contrary to the common belief that clay-free sandstones have the best reservoir quality, sandstones with small amount of clay (in the form of chlorite coatings) can have far better reservoir quality than those that lack grain-coating chlorites (Bloch et al., 2002). Grain-coating chlorites in sandstones have been linked to compaction (Fisher et al., 2000; Worden et al., 2020), which is divided into mechanical and chemical end members (Lundegard, 1992), and chlorite coats have been identified to prevent chemical compaction (Worden et al., 2020). Mechanical compaction involves grain rearrangement, bending, rotation, fracturing, and ductile deformation (Lundegard, 1992; Worden et al., 2000), whereas chemical compaction involves the dissolution of minerals at grain-grain contacts due to effective stress during burial (Bjorlykke et al., 1986) and due to tectonic processes (Worden et al., 2018).

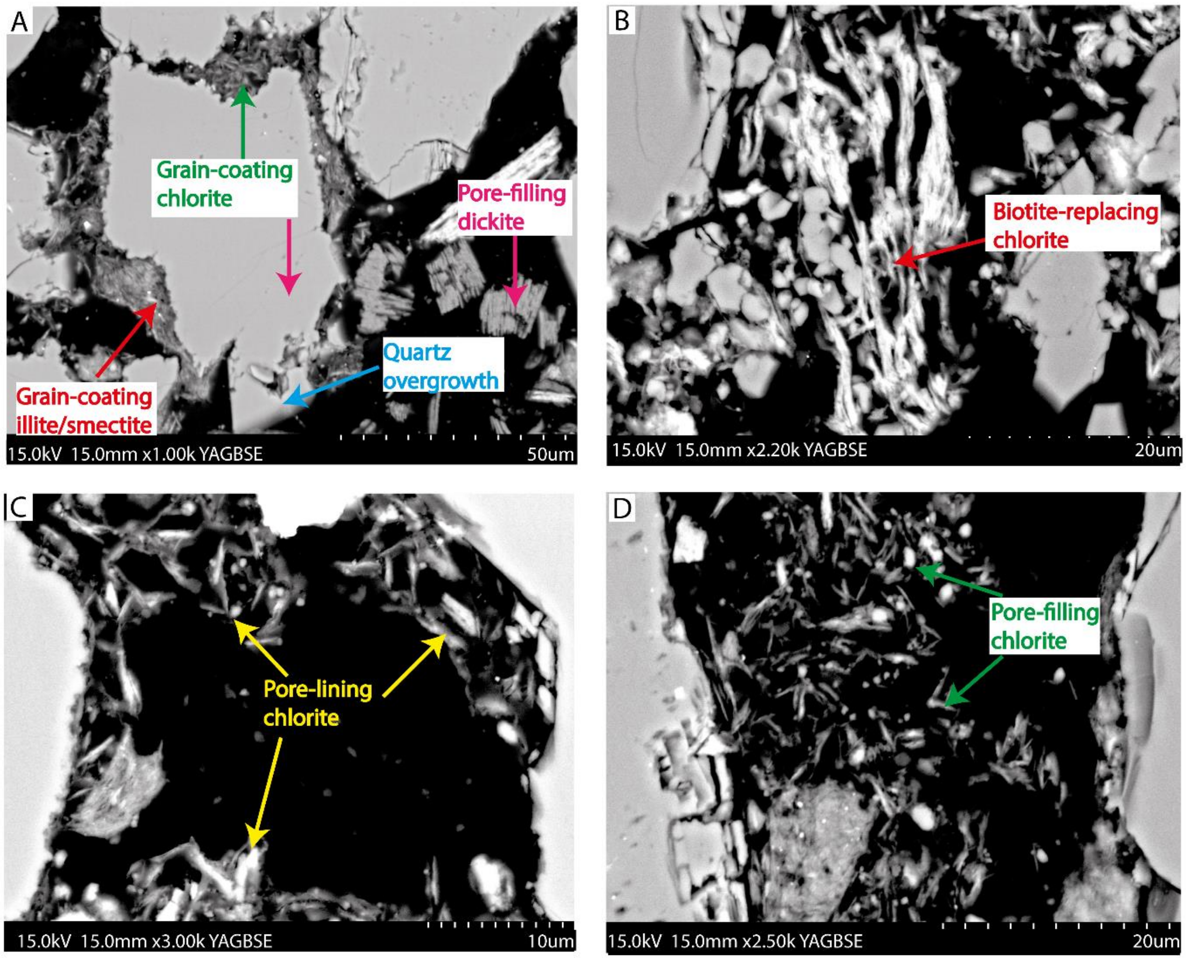

Figure 2.10. BSEM images showing of examples grain-coating, grain-replacing, pore-lining, and pore-filling chlorite in the studied Forties Sandstone Member. (A) BSEM image of grain-coating chlorite and mixed-layer illite smectite, preventing quartz cementation and preserving porosity. Notice the development of a quartz overgrowth where the grain-coating clays are absent. Everest field, well 22/14a-2, 2616 m TVDSS; (B) BSEM image showing chlorite replacing dissolved mica. Pierce field, well 23/27-5, 2733.75 m TVDSS.; (C) (B) BSEM image of pore-lining chlorite, preserving porosity. Everest field, well 22/14a-2, 2616 m TVDSS; (D) BSEM image showing pore-filling chlorite, destroying intergranular porosity. Everest field, well 22/14a-2, 2616 m TVDSS.

2.7.3.1 Chlorite chemistry

Chlorite is an Fe- and Mg-rich group of aluminosilicate clay minerals, with a general chemical formula of $(Fe^{2+},Fe^{3+}, Mg \text{ or } Al)_{4-6}(Si,Al)_4O_{10}(OH,O)_8$ (Worden et al., 2020). Based on the generalized chemical formula, chlorites are characterized by a wide range of compositional variations due to ionic or elemental substitutions (e.g., Fe^{2+} substituting for Mg^{2+}). Structurally, chlorite is a layered hydrous phyllosilicate with repeating tetrahedrally-coordinated Si-O layers, represented as T, connected by H-bonds to octahedrally-coordinated Al-O, Fe-O or Mg-O, represented as O, (Moore and Reynolds Jr., 1997) (Figure 2.11). The chlorite group is thus a three-layer tetrahedral-octahedral-tetrahedral (T-O-T) clay minerals, with a 2:1 structure (Worden et al., 2020) (Figure 2.11). Their structure is stable at high temperatures owing to the positively charged octahedral sheets filling the interlayers (Huggett, 2015). Chlorites can be: trioctahedral in both sheets, i.e., where both the 2:1 octahedral sheets and the interlayer are trioctahedral; dioctahedral, where both the 2:1 octahedral sheets and the interlayer are dioctahedral (Bailey, 1980; Brigatti et al., 2013; Huggett, 2015). Additionally, di-trioctahedral chlorites are also common, where the 2:1 octahedral sheet is octahedral, and the interlayer sheet is trioctahedral. The reverse, tri-dioctahedral chlorites, are, however, unknown (Huggett, 2015).

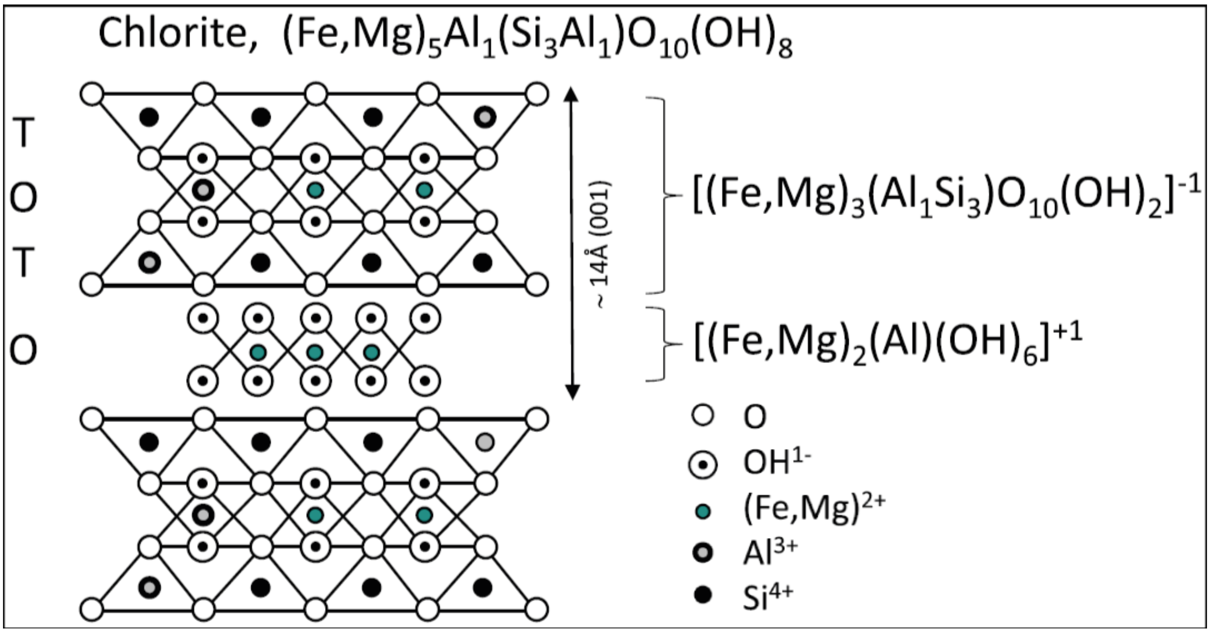

Figure 2.11. Crystal chemistry of chlorite (adopted from Worden et al. 2020).

2.7.3.2 Origin of chlorites

The origin of chlorites in sandstones may be either detrital or authigenic (Dowey et al., 2017; Worden et al., 2020). Owing to its relative chemical stability and slow weathering, detrital chlorites occur in sandstones as components of lithic grains, mineral grains (individual chlorite crystals), silt- and clay-sized interstitial matrix, and detrital coats, (Griffiths et al., 2019). Detrital chlorite which constitutes part of sand grains have been divided into allogenic and autogenic grains (Worden et al., 2020). Allogenic chlorites are transported from the hinterland to the sedimentary environment as metamorphic and/or volcanic rock fragments, which constitute key ingredients for authigenic chlorite (Anjos et al., 2003; Chen et al., 2011). Chlorite-bearing lithics and biotite tend to be relatively chemically stable and more likely to be transported with sands. The allogenic, chlorite-rich grains are susceptible to ductile deformation during compaction, forming chlorite pseudomatrix (Worden et al., 2020). Autogenic chlorites, in contrast, are formed within the sedimentary environment as concentric layers of Fe-rich chloritic clays in ooids, and are peculiar to estuarine-deltaic, chlorite-coated sandstones (Ehrenberg, 1993; Gould et al., 2010). Furthermore, Fe from fine material (e.g., FeO) gets dissolved in fluvial waters and deposited in river water- seawater mixing zone (Boyle et al., 1977). Consequently, due to the river water-seawater mixing, Fe is localised in estuaries and deltas (Ehrenberg, 1993), suggesting the preferential formation of chlorite in deltaic and estuarine depositional environments. Detrital silt- and clay-sized interstitial clays are emplaced in sands through infiltration, soft sediment deformation (e.g., sediment dewatering) (Dowey et al., 2017; Porten et al., 2019). Detrital chlorite coats infiltrate sandstones and are attached to detrital sand grains (Griffiths et al., 2018; Wooldridge et al., 2019b). They are also emplaced through dewatering (Porten et al., 2019). In modern sediments, detrital coats consist of a wide range of phyllosilicate clay minerals including berthierine, chlorite, illite, kaolinite, smectite, and other Fe-rich clays (Daneshvar and Worden, 2017; Ehrenberg, 1993). The detrital coats are often bound to the surface of sand grains by biofilms, generated through the activities of diatoms (Wooldridge et al., 2017).

Authigenic chlorite comprises grain-coating (Figure 2.10A), grain-replacing (Figure 2.10B), clay-replacing, pore-lining (Figure 2.10C), or pore-filling cements (Figure 2.10D). Authigenic chlorite coats may develop on earlier formed detrital coats during burial (Wooldridge et al., 2019b), and commonly form perpendicular to the detrital coats (Kordi, 2013; Worden et al., 2020). Furthermore, authigenic chlorite coats are formed from alteration of detrital clays (e.g., smectite) (Bahlis and de Ros, 2013; Shaw and Conybeare, 2003) and mineral grains (e.g., mica and lithic rock fragments) (Kordi, 2013).

Grain-replacing chlorite are formed when Fe-Mg-Al rich detrital grains such as volcanic rock fragments, biotite, tourmaline, hornblende etc., undergo partial to complete alteration or replacement by chlorite (Chen et al., 2011; Worden et al., 2020). The concentration of Fe-bearing heavy minerals (e.g., tourmaline, ilmenite, haematite, etc.), for example, tend to decrease during deep-burial diagenesis (Walderhaug and Porten, 2007), which liberates the Fe for incorporation into chlorite. Grain-replacive chlorites grow directly on altered detrital grains (Figure 2.10B), which commonly show signs of dissolution.

Clay-replacing chlorite develop due to transformation of pre-existing detrital or authigenic clays, such as smectite to chlorite, kaolinite to chlorite, berthierine to chlorite, and odinite to chlorite (Bahlis and Ros, 2013; Chen et al., 2011; Ehrenberg, 1993; Morad et al., 2010; Taylor et al., 2010; Worden et al., 2020; Worden and Morad, 2003). The transformation of the precursor clays to chlorite starts during burial at depths of 2-3 km and at temperatures between 60-100 °C (Ehrenberg, 1993; Worden and Morad, 2003). Berthierine and odinite, for instance, are transformed to an Fe-rich chlorite (chamosite) during burial (Hillier, 1994; Morad et al., 2010). In addition, kaolinite is transformed to chlorite in an Fe- and Mg-rich environment with increasing burial depth and temperature (Moraes and De Ros, 1992); the transformation has been reported to occur at depths of 3500 to 4500 m at temperature ranging from 165 to 200 °C (Boles and Franks, 1979). Carbonate cements such as siderite and ankerite have been reported to react with kaolinite and illite by mineral replacement to form chlorite (Curtis et al., 1985; Smith and Ehrenberg, 1989; Worden and Morad, 2003).

Authigenic chlorite can also occur as pore-filling clay (Berger et al., 2009) (Figure 2.10D), which is detrimental to reservoir quality by reducing intergranular porosity. The origin of pore-filling chlorite can be enigmatic due to multiple, potential sources (Worden et al., 2020). Some grain-coating chlorite grow into pore-filling chlorite if they are thickly developed, reducing pore throats and lowering reservoir quality.

2.7.4 Kaolinite

Kaolinite is one of the most widely reported clay minerals in sandstone reservoirs (e.g., Bjørlykke, 2014; Marfil et al., 2003; Morad et al., 2010, 1994; Stewart, 1995). The origin of kaolinite has been largely attributed to authigenesis, occurring mainly as pore-filling cement (Figure 2.12A), but also as grain replacements (Figure 2.12B) (Marfil et al., 2003; Milliken, 2003). Detrital kaolinite, however, can occur in sandstones, having been recycled from uplifted, weathered sandstones. Two forms of kaolinite have been identified in the Jurassic reservoirs of the North Sea based on petrographic studies (Osborne et al., 1994): (i) early diagenetic vermiform kaolinite, formed from dissolution of feldspar and mica detrital grains (e.g., Figure 2.12B), and (ii) late-diagenetic, blocky kaolinite (dickite) (e.g., Figure 2.12C), formed during deep-burial diagenesis and organic matter maturation.

2.7.4.1 Chemistry of kaolinite

Kaolinites, which have a general chemical formula of $Al_2Si_2O_5(OH)_4$, are 1:1 clay minerals, consisting of one tetrahedral layer linked to one octahedral layer with no interlayer cations (Worden and Morad, 2003). A kaolinite layer/structure has no electrical charge and, thus, low to no interlayer cations (e.g. Ca^{2+}, Na^{+}, or K^{+}). Consequently, unlike smectite, for instance, which is characterized by exchangeable interlayer cations and swells, kaolinite has a relatively low ion exchange capacity, resulting in its non-swelling character. The term kaolin has been applied to kaolinite and/or dickite (Marfil et al., 2003). While kaolinite is the low-temperature form of kaolin, dickite is thought to be the high-temperature form. Additionally, kaolinite forms pseudohexagonal plates that commonly exhibit book- or worm-like habit, whereas dickite forms small, rhombic crystals (Worden and Morad, 2003).

2.7.4.2 Origin of kaolinite

The origin of pore-filling and grain-replacive kaolinite in sandstones (Figure 2.12A & B) can be attributed to wide range of conditions of formation: (i) at shallow depth (< 1000 m) during eodiagenesis by meteoric influx; (ii) during subaerial exposure and/or uplift (telodiagenesis); and (iii) at deeper burial depths (2-4 km) during mesodiagenesis due to acidic pore fluid generated from thermal maturation of organic matter in source rocks (Curtis, 1983; Surdam et al., 1989). Vermicular, pore-filling and grain-replacing kaolinite can develop from any of the above conditions. In turbidite sandstones, however, the pore-filling and grain-replacing kaolinite (Figure 2.12A & B) develop during shallow burial due to meteoric flushing during sea level lowstands (Mansurbeg, 2007; Mansurbeg et al., 2012, 2008; Stewart, 1995).

Kaolinite tends to form under humid climatic conditions in continental sands due to the action of low-Ph, acidic, and meteoric pore water on detrital grains such as feldspars, mica, rock fragments (Emery et al., 1990; Weibel et al., 2017). In addition, large areas of continental shelf sediments become subaerially exposed during forced regression and sea level lowstands, causing significant meteoric recharge. Thus, meteoric head migrates basinward, which leads to the flushing of shallow marine sediments and, occasionally, deep-sea turbidites (Den Hartog Jager et al., 1993; Stewart, 1995; Worden and Morad, 2003).

The amount and distribution pattern of kaolinite formed in sandstones largely depends on the amount of unstable silicate grains (e.g., feldspars, mica, mud intraclasts, etc), annual precipitation, and rate of fluid flow in the sands (Worden and Morad, 2003). Humid conditions supply greater amounts of meteoric water, especially to high permeability sediments, which results in significant eogenetic grain dissolution and precipitation of authigenic kaolinite. Albite and calcic plagioclase, which are more susceptible to kaolinitization than K-feldspar, undergo dissolution in the presence of meteoric pore fluid, resulting in the formation of kaolinite. As such, Na and Ca are released into the pore fluid, and the availability of Ca in the pore fluid leads to the precipitation of calcite cement, if there is sufficient bicarbonate (Worden et al., 2020; Worden and Morad, 2003).

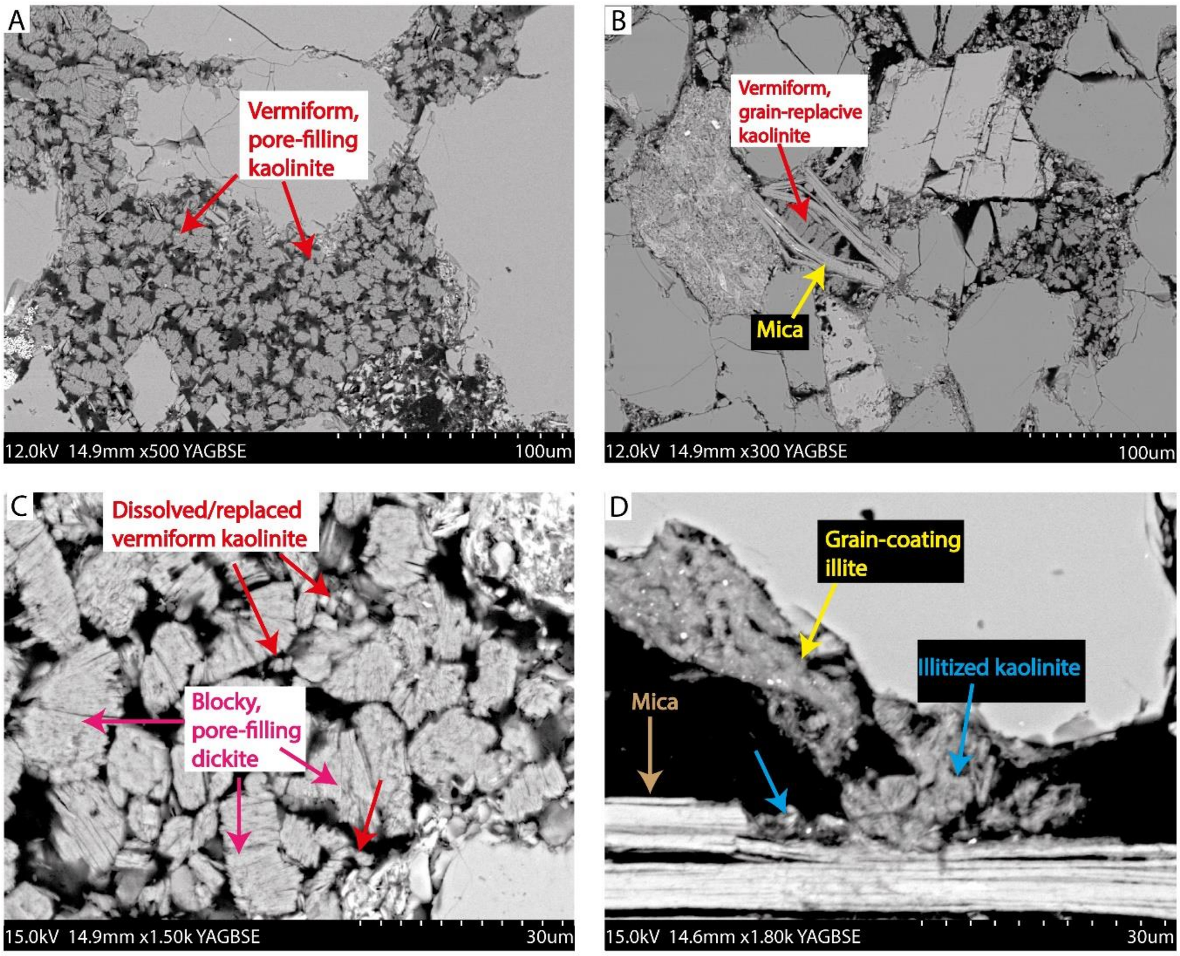

Figure 2.12. BSEM images showing examples pore-filling, grain-replacing, grain-coating, and clays-replacing clays in the studied Forties Sandstone Member. (A) BSEM image of pore-filling, vermiform kaolinite, destroying intergranular porosity. Pierce field, well 23/27-5, 2729.5 m TVDSS; (B) BSEM image showing grain-replacing, vermiform kaolinite, destroying secondary intragranular porosity in partly dissolved mica. Pierce field, well 23/27-5, 2729.5 m TVDSS (C) BSEM image of blocky, pore-filling dickite, replacing dissolved kaolinite and destroying intergranular porosity. Pierce field, well 23/27-5, 2729.5 m TVDSS; (D) BSEM image showing illitized kaolinite from a dissolving mica grain. Nelson field, well 22/11-6, 2218.64 m TVDSS.

2.7.4.3 Transformation of kaolin to dickite, illite and chlorite

Due to increasing burial depth and temperature (2-3 km; 70-90 °C), eogenetic, thin, pseudohexagonal, and vermiform kaolinite is progressively transformed to and/or replaced by thick, well-developed crystals of dickite (Marfil et al., 2003; Morad et al., 1994; Worden and Morad, 2003) (Figure 2.12C). This is evident by the growth of monoclinic, blocky dickite between pervasively dissolved pseudohexagonal, vermiform kaolinite remnants (Figure

2.12C). However, like smectite to illite transformation, the conversion of kaolinite to dickite has been suggested to proceed over a prolonged period of time (Marfil et al., 2003), and in rocks characterized by high porosity and permeability (Lanson et al., 1996) . Similarly, Ehrenberg et al. (1993) and Morad et al. (1994) pointed out that the conversion of kaolinite to dickite is influenced by the starting material, with the vermiform kaolinite formed from feldspar dissolution being more reactive than those from mica dissolution. The transformation can, nonetheless, be inhibited in sandstones that are oil-saturated, highly compacted, and pervasively cemented (Worden and Morad, 2003). The conversion of kaolinite to dickite is probably enhanced by an increase in acidic pore waters, which is corroborated by concomitant dissolution of unstable silicate grains (e.g., feldspars) and precipitation of carbonate cements (Worden and Morad, 2003). Given the substantial burial depths at which dickites are formed, it is unlikely that meteoric-water influx leads to their formation. Instead, it has been linked to organic acids and/or source-rock-derived CO_2 (Morad et al., 1994).

The transformation of kaolinite into illite (Figure 2.12D) takes place during deep-burial, mesodiagenesis at temperatures greater than 70 °C, but becomes ubiquitous at temperatures greater than 130 °C (Worden and Morad, 2003). Detrital K-feldspar and kaolinite seem to be generally unstable together, based on equilibrium thermodynamic models, and their coexistence at relatively shallow burial depth has been attributed to low temperature and slow reaction rates (Bjorlykke and Aagaard, 1992). At high temperature, however, they react to form illite, with quartz as by-product which occur as discrete crystals or as overgrowths on detrital quartz grains (Worden and Morad, 2003). Authigenic illite forms from both grain-replacive and pore-filling kaolinite (Marfil et al., 2003). The illitization of kaolinite occurs in the presence of K^+ (which might be sourced from K-feldspar) during mesodiagenesis at temperature above 120 °C (Bjørlykke et al., 1995). Low K-feldspar content, consequently, would result in less precipitation of illite and more precipitation of dickite from kaolinite. In the absence of kaolinite, K-feldspar converts to illite if there is source of low-Ph, acidic pore fluid (Platt, 1993), probably from maturation of source rocks (Surdam et al., 1989). The dissolution of K-feldspar produces potassium and silica, which diffuse and then precipitate to form illite and quartz, respectively (Thyne et al., 2001).

Kaolinite can transform into chlorite with an increasing burial depth and temperature (3.5-4.5 km; 165-200 °C) and in an environment that is Fe- and Mg-rich (Chen et al., 2011; Boles and Franks, 1979; Moraes and De Ros, 1992). The Fe and Mg could be derived from carbonate cements such as dolomite, ankerite, ferroan calcite, and siderite. However, the transformation has been reported to have occurred at depths of about 2.5 km (100 °C) in the Triassic red-bed sandstones of Lunde Formation, offshore Norway (Worden and Morad, 2003), with the Fe having been derived from the reduction of iron oxides (Curtis et al., 1985). Dickite and illite, in contrast, are less sensitive to chloritization than kaolinite.

2.7.5 Illite

Illite, like chlorite, kaolinite, and smectite, is one of the most abundant clay minerals in sandstone reservoirs (Lanson et al., 1996; Lanson et al., 2002; Oluwadebi et al., 2018; Weibel et al., 2020; Worden and Morad, 2003). However, illite, like kaolinite, is mainly diagenetic in origin (Lanson et al., 1996; Pittman et al., 1992), occurring largely as grain coats on detrital grains (Figure 2.13A &B). Grain-coating illite inhibits the development of authigenic quartz overgrowths, thereby preserving reservoir quality in deeply buried sandstones. In addition, illite occurs as grain-replacive cement, replacing partially or pervasively dissolved, unstable feldspar and mica grains (e.g., Figure 2.13B); as replacement of kaolinite (Figure 2.13C); and as pore-filling cement (Figure 2.13D), which fills intergranular pores and block pore throats, reducing reservoir permeability (Bjorlykke and Aagaard, 1992; Oluwadebi et al., 2018).

Illite is a dioctahedral 2:1 layered sheet silicate mineral, with a general formula of $K_{1.5-1.0}Al_4[Si_{6.5-7.0}Al_{1.5-1.0}O_{20}](OH)_4$ (Deer et al., 1992). Structurally, the illite consists of an octahedral layer sandwiched by two inward-pointing tetrahedral layers (Figure 2.14).

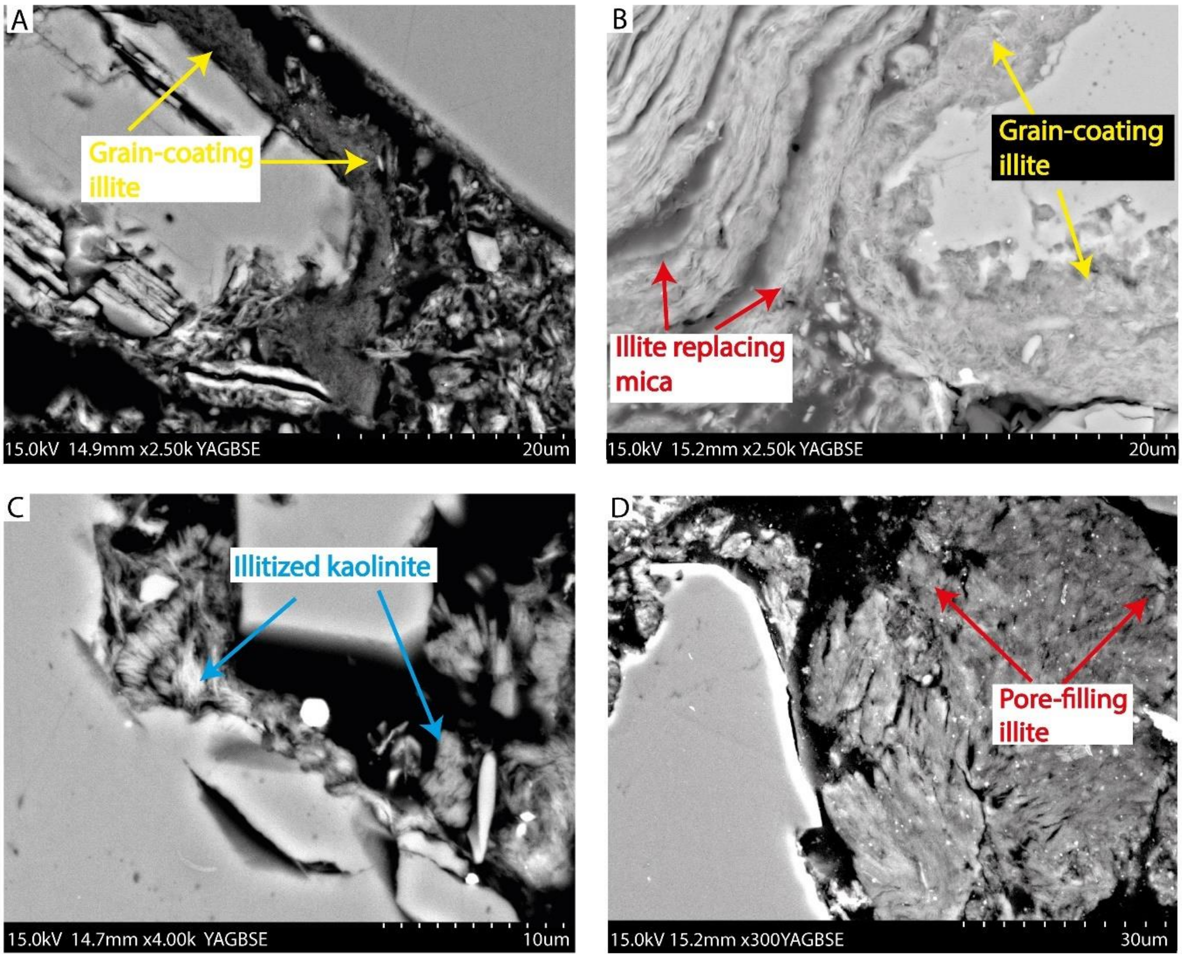

Figure 2.13. BSEM images showing examples grain-coating, kaolinite-replacing, and pore-filling illite in the studied Forties Sandstone Member. (A) BSEM image of grain-coating illite relatively preserving porosity. Pierce field, well 23/27-5, 2729.50 m; (B) BSEM image showing grain-replacing, and grain-coating illite. Blane field, well 30/03a-1, 3096 m TVDSS (C) BSEM image showing vermiform kaolinite being replaced by illite. Blane field, well 30/03a-1, 3096 m TVDSS; (D) BSEM image showing pore-filling illite destroying intergranular porosity. Nelson field, well 22/11-6, 2218.64 m TVDSS.

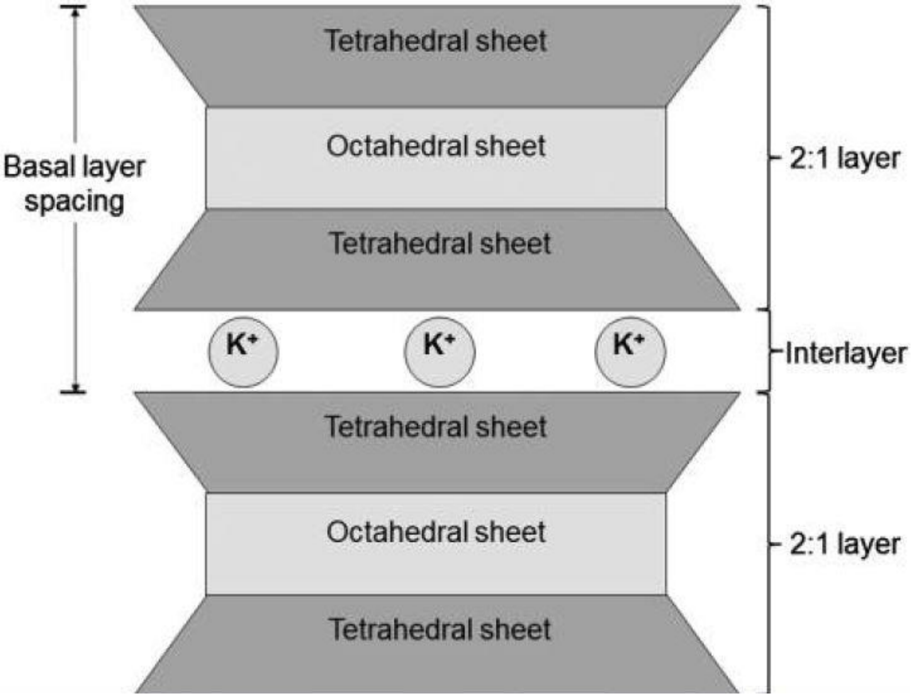

Figure 2.14. Crystal structure of illite (adopted from Sayers and den Boer, 2016).

2.7.5.1 Transformation of kaolin and smectite to illite

Three mechanisms have been linked to the formation of illite in sandstones reservoirs: replacement of kaolinite (Figure 2.13C), replacement of K-feldspar, and illitization of smectites. The conversion of kaolinite to illite commences at temperature 70 °C (Worden and Morad, 2003), but is more prevalent at higher temperature above 120 °C, usually between 120 and 140 °C (Bjørlykke et al., 1995; Lanson et al., 2002). The conversion requires K^+, which is often derived from K-feldspar, and is more prevalent in arkoses than in quartz arenites. However, owing to its highly ordered structure, dickite is less susceptible to illitization (Morad et al., 1994). The illitization of kaolinite is detrimental to reservoir quality, especially reservoir permeability. This is because the illite retains the pore-filling character of the replaced kaolinite, thereby blocking pore throats (Deer et al., 1992; Lanson et al., 2002). Additionally, the process releases silica as by-product, which precipitates as quartz cement. Thick, grain-coating illite develops into pore-filling illite which reduces sandstones reservoir quality (Figure 2.13A & B).

Illitization of smectite takes place with increasing burial depths and temperature (Worden and Morad, 2003). The origin of smectites in siliciclastic reservoirs can be both detrital and diagenetic (McKinley et al., 2003). Characterized, typically, by low Al/Si ratio and contained Ca, Fe, and Mg, dioctahedral smectite converts to illite through a mixed-layer illite/smectite (Worden and Morad, 2003). The transformation has been reported to occur via two routes: first, the process conserves silica and requires a source of Al to proceed; second, the process conserves Al and produce excess silica, probably as quartz cement. During the transformation of smectite to illite, to maintain charge balance, the tetrahedral sites require a loss of silicon at the expense of Al, and the interlayer sites require a gain of K at the expense of water. Consequently, the process releases silica, which precipitate as quartz cement. Additionally, the released water could help in generating overpressure in the reservoirs (Lynch, 1997). Formed at temperature below 90 °C, diagenetic illites have a minor component of smectite within them as remnants of the original clay, probably smectite (Burley and MacQuaker, 1992). The illitization of smectites releases cations such as Mg^{2+}, Fe^{2+}, Na^{+}, and Ca^{2+}, which could be used for subsequent diagenetic processes in adjacent lithologies (e.g., precipitation of carbonate cements and albitization of feldspars) (Worden et al., 2020; Worden and Morad, 2003).

2.8 Microquartz coatings

The occurrence of grain-coating, microcrystalline quartz on detrital grains has been recognized as an effective mechanism for porosity preservation in deeply-buried sandstones reservoirs by inhibiting the development syntaxial, porosity-occluding macroquartz cement (e.g., Aase et al., 1996; French et al., 2012; French and Worden, 2013; Weibel et al., 2010) (Figure 2.15A, B & C). Numerous oil fields sandstones characterized by grain-coating, microcrystalline quartz have been identified to have anomalously high porosity due to the inhibition of quartz overgrowths development (French et al., 2012). Microcrystalline quartz ranges in size from 1 to 10 µm, and are not in optical crystallographic continuity with detrital quartz grains (Aase et al., 1996; French and Worden, 2013). Because of their crystal size, the microcrystalline quartz are difficult to identify using standard thin-section light microscopy. Instead, their crystallography and growth mechanism are better studied using a range of techniques, including scanning electron microscopy (SEM), electron backscatter diffraction (EBSD), transmission electron microscopy (TEM), and cathodoluminescence (CL) (French and Worden, 2013).

Microcrystalline quartz is commonly associated with sandstones rich in biogenic silica (e.g., sponge spicules) (Aase and Walderhaug, 2005; Hendry and Trewin, 1995), and develops at temperature of about 50 °C (Vagle et al., 1995), indicating formation at shallow depth. The optical discontinuity between microcrystalline quartz and the host, detrital quartz grain ensures porosity preservation due to the fact that the fastest growth axis, known as c-axis, of the microcrystalline quartz is oriented parallel to the host grain surface, and not directed into the pore, thereby preventing the development of macroquartz overgrowths and hence preserving porosity (French and Worden, 2013). Therefore, well-developed, randomly-oriented microquartz crystals, typically less than 10 µm in length, prevent the overgrowth of optically continuous quartz cement on detrital quartz, leading to anomalous preservation of intergranular porosity in deeply-buried sandstones. The effectiveness of microcrystalline quartz coatings in porosity preservation, as with chlorite and illite coatings, depends on coatings completeness or coverage (Stricker, 2016). Macroquartz develops where there is a break in coatings, occluding porosity and lowering reservoir quality. Due to its tendency to precipitate rapidly from a silica-saturated pore fluid and often at lower temperature, the microcrystalline quartz preserve porosity during burial. Experimental simulation of diagenesis in a hydrothermal reactor on modern sediments (this study) using silica crystals has shown that microcrystalline quartz precipitates as both grain-coating and pore-filling cements (Figure 2.15B, C &D).

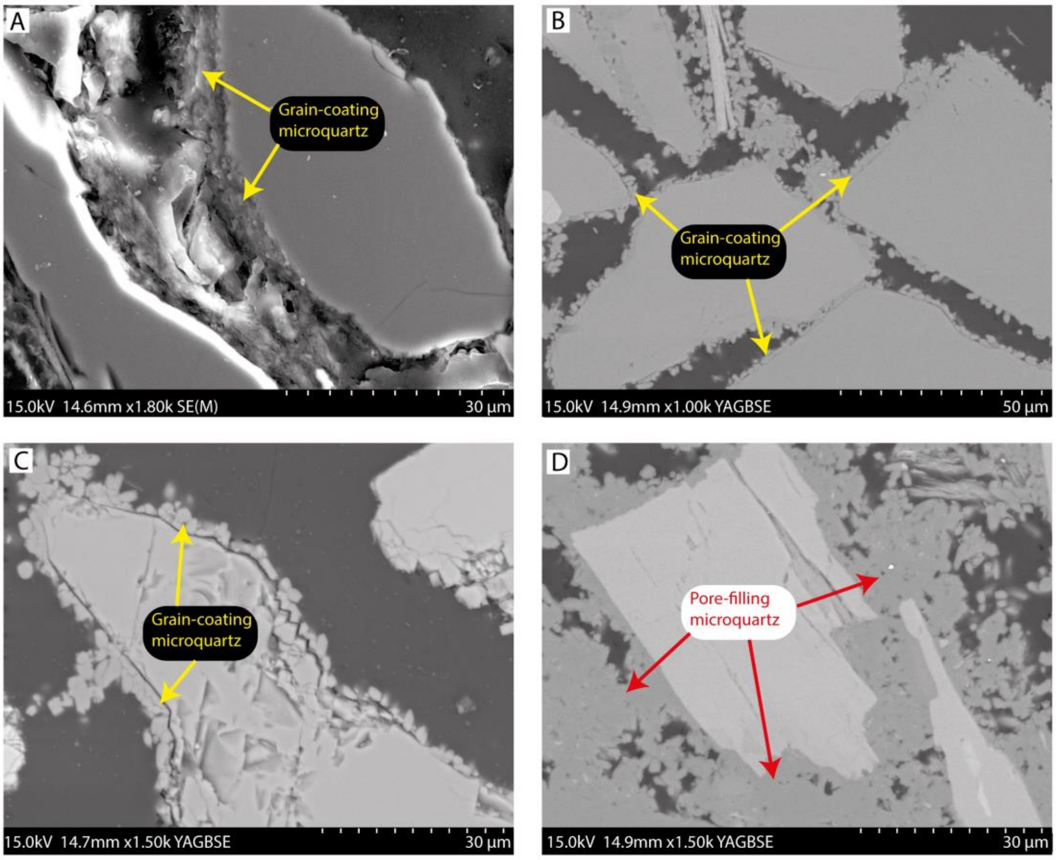

Figure 2.15. SEM/BSEM images showing examples grain-coating and pore-filling microcrystalline quartz in the studied Forties Sandstone Member and the Modern Bute Inlet sediments. (A) SEM image showing grain-coating microcrystalline quartz. Blane field, well 30/03a-1, 3096 m; (B) BSEM image showing grain-coating, microcrystalline quartz on detrital quartz grains. Bute Inlet, station 036; (C) BSEM image showing grain-coating microcrystalline quartz on detrital feldspar grain. Bute Inlet, station 036; (D) BSEM image showing pore-filling microcrystalline quartz, destroying intergranular porosity. Bute Inlet, station 036.

2.9 Linking turbidite sandstones provenance with framework composition and diagenesis

The choice of the turbidite/submarine fan to study mainly depends on the objectives of the study. However, for our study, the study area (the Forties Fan) was chosen because it is a sand-rich system, characterized by extensive submarine channels where the role of clay minerals on reservoir quality can be effectively evaluated. Sandstones framework compositions largely reflect tectonic settings and rock types in the hinterland (Dickinson and Suczek, 1979; Mansurbeg, 2007; Shanmugam and Moiola, 1988). The Forties and Frigg fans are passive margin submarine fans turbidite sandstones, whose sediments were derived from the uplifted basement rocks and recycled Triassic clastics of the Scottish Highlands and the East Shetland Platform areas (Den Hartog Jager et al., 1993; Heritier et al., 1979; Kilhams et al., 2013; Morton et al., 1993). The Forties and Frigg fans systems have been classified as restricted, sand-rich basin floor fans (Den Hartog Jager et al., 1993), and such fans are characterized by proximal source, steep gradient, and narrow shelf (Shanmugam and Moiola, 1988). The framework composition is of profound significance in controlling the spatial and temporal distribution of diagenetic products and reservoir quality evolution in turbidite sandstones (Mansurbeg, 2007; Mansurbeg et al., 2009, 2008). Turbidite sandstones from the passive margin settings have quartz-feldspar dominated framework grains, and are derived mainly from uplifted granitic and gneissic basement rocks, whilst sandstones from the active margin settings are rich in ductile lithic grains and are mainly derived from carbonate-mudstone dominated sedimentary rocks and low-grade metamorphic rocks (Mansurbeg, 2007; Mansurbeg et al., 2009). Being from passive margin settings, the studied Forties Sandstone Member is characterized by quartz-rich, arkosic and subarkosic compositions (*sensu* Folk, 1980 classification scheme). Their quartz/feldspar-rich compositions make them mechanically stable but chemically unstable during burial diagenesis. While the detrital quartz grains make the sandstones mechanically stable and resistant to compaction, the detrital feldspars are chemically unstable and, thus, are susceptible to dissolution and kaolinitization, which might enhance and destroy reservoir quality, respectively. Additionally, the lack of abundant lithic and carbonate fragments in the sandstones has enhanced their mechanical stability during compaction. Turbidite sandstones of active margin settings, on the other hand, lose porosity due to mechanical compaction and cementation as a result of ductile-rich framework grains, carbonate cements, and quartz cementation (Mansurbeg, 2007). Furthermore, the influence of meteoric influx on diagenesis of turbidite sandstones of the active margin settings is limited due to the fact that porosity and permeability are lost during shallow burial because of the impact of mechanical compaction, and the presence of abundant carbonate cements and carbonate fragments might weaken the action of meteoric water on the sandstone. Meteoric influx in the passive margin turbidite sandstones, therefore, is more likely to cause dissolution of unstable framework grains such as feldspar, mica, and mudclasts, enhancing reservoir quality of the sandstones.

Chapter 3: Role played by clay content in controlling reservoir quality: Forties Sandstone Member, Central Graben, North Sea

---

This chapter has been published in the Journal of Marine and Petroleum Geology (https://doi.org/10.1016/j.marpetgeo.2021.105058)

Chapter 3: Role played by clay content in controlling reservoir quality of Forties Sandstone Member, Central Graben, North Sea

3.1 Summary

Proximal to distal fan change in grain size, clay matrix content, and grain-coating clays have been identified as key contributing factors for reservoir quality evolution of submarine fan turbidite sandstones. This study evaluated the role played by grain-coating and pore-filling clays, depositional facies, and diagenesis in reservoir quality evolution of the Paleocene Forties submarine fan sandstones (Central North Sea) from proximal to distal fan settings. To help provide a comprehensive understanding of the role played by of pore-filling and grain-coating clays to destroy and preserve reservoir quality, respectively, in turbidite sandstones, we have used a multi-technique approach including petrography, burial history, scanning electron microscopy, and stable isotopes analysis. Results of the study show that reservoir quality is influenced by both depositional facies and diagenesis. The proximal-fan, amalgamated sandstones facies have the best reservoir quality due to coarser grain size, lower pore-filling clays, and lower amount of ductile grains. In contrast, the distal-fan, mud-prone heterolithic facies have the poorest reservoir quality due to finer grain size, higher pore-filling clays, and higher amount of ductile grains. Pore-filling clays between 10 and 30 % per total rock volume have a deleterious effect on reservoir quality, reducing porosities and permeabilities to generally < 10 % and < 1 mD, respectively. Based on the relatively shallow, present-day burial depths of the studied Forties Sandstone Member (2200-3100 m TVDSS), the percentage of clay-coating coverage to significantly inhibit quartz cementation ranges from 40 to 50 %, (which was measured on detrital quartz grains using JMicroVision software package), corresponding to grain-coating clay volume of up to 8 %. Detrital, grain-coating smectites, probably inherited from the shelf/continental environments and/or emplaced through sediment dewatering, have transformed into chlorite, illite, and illite-smectite. Calcite and siderite, where well-developed, have arrested mechanical compaction and also occluded porosity, thereby rapidly degrading reservoir quality in the submarine fan reservoir facies; however, their dissolution by acidic pore fluids could potentially create secondary intergranular porosity, enhancing reservoir quality of the sandstones. Evidence presented demonstrates that, high quality reservoir sandstones that deviate from normal porosity-depth trends for submarine fans sandstones can be attributed to facies changes (composition and grain size) with a complex interplay of mechanical compaction, detrital clays and authigenic clay coatings inhibiting quartz cement precipitation.

3.2 Introduction

Understanding of the distribution of diagenetic processes and products is of major importance for the characterisation of quality and overall heterogeneity of clastic reservoirs (Ma et al., 2017; Morad et al., 2010, 2000). In general, the influence of diagenesis in clastic turbidite reservoirs is relatively poorly understood and believed to be mostly mediated by marine pore waters (Bjorlykke and Aagaard, 1992; Dutton, 2008; Mansurbeg et al., 2008). In the past decades, offshore hydrocarbon exploration has been increasingly concentrated in marine turbidite sandstone reservoirs (e.g., Bahlis and de Ros, 2013; Chudi et al., 2016; Marchand et al., 2015; Porten et al., 2019, 2016). More recently, the need to better understand reservoir quality has become paramount for carbon capture and storage (CCS) projects, where turbidite sandstones are potential storage sites that require a comprehensive understanding of the reservoir properties, facies distribution and migration pathways prior to any CO_2 injection (Xia and Wilkinson, 2017).

The Paleocene turbidite sandstones of the Central North Sea contain about half of the total recoverable oil reserves within the region (2.99 Bbbbl), with estimated reserves of approximately 6.01 Bbbl (Brennand et al., 2009). Therefore, quantitative evaluation of sandstones reservoir quality is crucial for understanding of reserve estimations and development of continued hydrocarbon production strategies (Chen et al., 2019; Marchand et al., 2015; Morad et al., 2010). Reservoir quality is strongly influenced by depositional parameters (e.g., primary sediment composition, grain size, sorting, and clay content, which constitute depositional facies) (Bell et al., 2018; Marchand et al., 2015; Porten et al., 2016; Stammer, 2014) and diagenetic alterations (Morad et al., 2010; Oluwadebi et al., 2018). Depositional parameters commonly have a significant impact on primary reservoir porosity and permeability and on early diagenetic processes (Porten et al., 2016). Diagenetic processes, which include mechanical compaction, cementation mineral dissolution, and recrystallization, can extensively affect the reservoir quality of sandstones. Numerous studies have focused on establishing the link between depositional sand quality [defined by Ehrenberg, (1997) as combined impact of primary sediment composition, texture, and early diagenetic alterations, influenced by depositional environment controls on reservoir quality] and reservoir quality in deep-water turbidite sandstones (Bell et al., 2018; Lien et al., 2006; Marchand et al., 2015). Surprisingly, little has been published on the impact of diagenesis on reservoir quality evolution of the Paleocene deep-water turbidite sandstones of the Central North Sea (e.g., Mansurbeg et al., 2008; Stewart, 1995).

The Paleocene Forties turbidite sandstones are characterized by rapid variation in sedimentary facies, influenced by topography of older formations and salt-induced highs, causing significant variation in clay content from proximal to distal fan (Collins et al., 2015; Hempton et al., 2005). The variation in clay content is common even within the same sedimentary facies, thereby affecting the reservoir quality of the sandstones. Clay minerals have been widely recognised to play a key role in diagenesis and reservoir quality of sandstones (Houseknecht and Ross, 1992; Stricker and Jones, 2018; Taylor et al., 2010). The amount, mode of occurrence and distribution patterns of clay minerals strongly influence sandstones reservoir porosity and permeability (Worden and Morad, 2003) . Quartz-rich sandstones which are clay-poor often lose significant intergranular porosity at deeper burial depths due to quartz cementation (Porten et al., 2016). Conversely, quartz-rich, clay-coated sandstones preserve porosity at deeper burial depths by inhibiting quartz cementation (Stricker, 2016; Stricker et al., 2016; Stricker and Jones, 2018). Grain-coating clay minerals such as chlorite and illite/illite-smectite can significantly enhance and preserve porosity in deeply buried sandstone reservoirs by reducing the nucleation sites available for the development of authigenic quartz cements on detrital quartz grains (Dos Anjos et al., 2000; Ehrenberg, 1993; Stricker et al., 2016; Tang et al., 2018). Porosity can be at least 10% higher than anticipated where grain-coating clays are well-developed on detrital grains (Wooldridge et al., 2017). However, pore-filling detrital and authigenic clays can destroy reservoir quality by occluding intergranular pores and bridging pore-throats (e.g., Oluwadebi et al., 2018).

In this study, we investigate the effect of pore-filling and grain-coating clays on deep-water sandstones porosity and permeability evolution from Forties Sandstone Member, Central Graben, North Sea. Specific research objectives include: (1) establishing role of primary depositional characteristics, involving grain size and clay content, on reservoir for reservoir quality evolution of the Forties turbidite sandstones; (2) investigating the role of diagenesis and grain-coating clays on reservoir quality of the sandstones; and (3) determining the percentage of clay-coating coverage to arrest quartz cementation and preserve reservoir quality in the sandstones.

3.3 Geological background of the Forties Fan

The Upper Paleocene Forties Sandstone Member of the Sele Formation has been recognised as a deep-water submarine fan system, hosting a significant number of producing fields in the North Sea Central Graben, including the Forties, Everest, Nelson, Pierce, Lomond and Mirren

(Hempton et al., 2005) (Figure 3.1). The Forties Fan system developed in response to the accumulation of clastic deltaic and shelf sediments, and it is situated to the north and west of the main depocenter (Bowman, 1998; Scott et al., 2010; Whyatt et al., 1992). Thermal doming associated with the Early Paleocene rifting of the Greenland and European plates initiated the uplift (up to 2 km) of Scottish Highlands and East Shetland platforms (Den Hartog Jager et al., 1993), causing more than 800 m drop in the relative sea level and a 90 km basinward regression (Davis et al., 2009). This led to intensified erosion of the uplifted igneous, metamorphic, and meta-sedimentary hinterland and the subsequent accumulation of extensive deltaic and shallow marine sediments on the basin margin. The resulting high sedimentation rates and steep basin margins created unstable delta fronts with frequent slope failures, delivering large volumes of sediments into the basin by a combination of turbidity currents and debris flows processes along the main NW-SE graben axes (Charles and Ryzhikov, 2015). A regional study by Kilhams et al., 2014 based on 3D seismic data has shown that there are two principal sediment routes into the Central Graben: the NW to SE oriented axial system along the graben, and the west to east trending lateral systems crosscutting the axial system (Figure 3.1). The primary NW-SE sediment route, which was sourced in the Outer Moray Firth, forms the axial Forties Fan and serves as the principal reservoirs to the Forties, Everest, Nelson, Montrose, Arbroath, Arran, Pierce, and Blane fields (Figure 3.1). The secondary lateral fans systems, sourced from the west, form the reservoirs in some fields, including Bittern, and Gannet, and also extend as far east as Merganser and Scoter fields in the Central Graben (Hempton et al., 2005) (Figure 3.1). The distribution of the Sele Formation gravity flows were primarily controlled by local reactivation of the Palaeozoic and Mesozoic faults due to uplift (Eldrett et al., 2015), local-scale bathymetric relief at diapir crests (Davis et al., 2009; Davison et al., 2000; Hempton *et al.,* 2005), and relief associated with the deposition of the earlier, Danian–Selendian-aged Maureen and Lista Formations (Mudge, 2015). Figure 3.1B shows GR logs demonstrating reservoir lithologies, sand thicknesses in some selected wells, and change in grain size from proximal to distal fan of the axial Forties Fan.

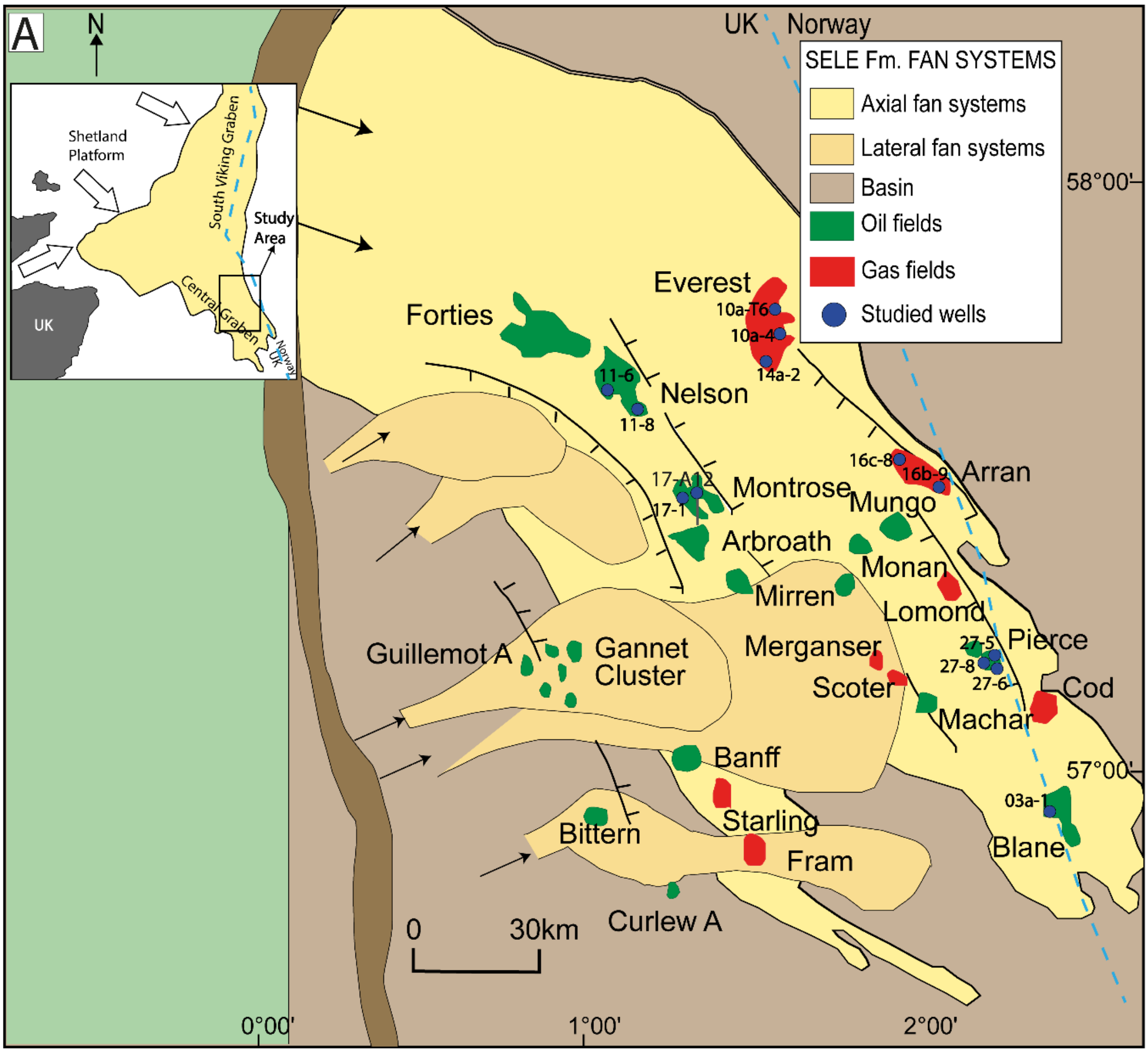
A
N
Shetland Platform
South Viking Graben
Study Area
Central Graben
UK
Norway
UK
UK
Norway
SELE Fm. FAN SYSTEMS
Axial fan systems
Lateral fan systems
Basin
Oil fields
Gas fields
Studied wells
58°00'
57°00'
0°00'
1°00'
2°00'
0
30km
Forties
Everest
10a-T6
10a-4
14a-2
11-6
11-8
Nelson
16c-8
16b-9
Arran
17-A12
17-1
Montrose
Mungo
Arbroath
Monan
Mirren
Lomond
27-5
Pierce
27-8
27-6
Cod
Guillemot A
Gannet
Cluster
Merganser
Scoter
Machar
Banff
03a-1
Bittern
Starling
Fram
Blane
Curlew A

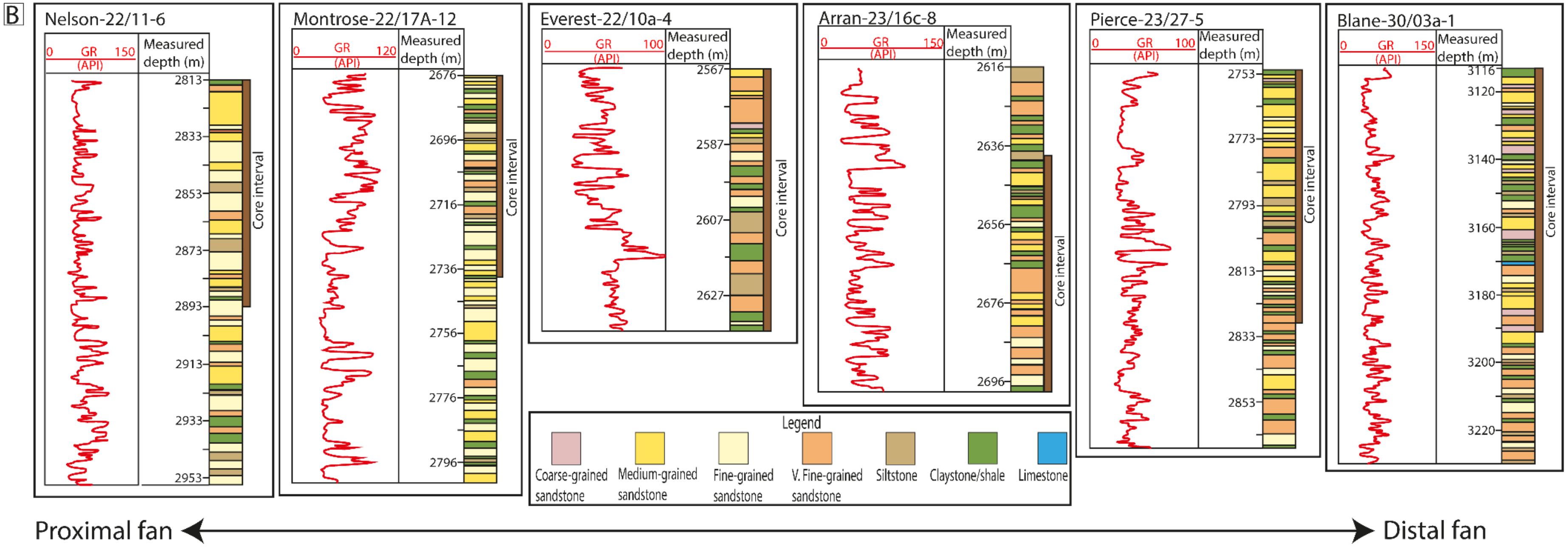

Figure 3.1. (A) Regional map of the Forties submarine fan system. The figure shows the distribution of the main fan (NW-SE) and location of the wells sampled for this study (modified from Hempton et al., 2005). (B) GR logs showing reservoir lithologies and thicknesses in some selected wells from proximal to distal fan used in the study.

3.4 Stratigraphy

The lithostratigraphic framework of the Palaeogene Central North Sea has been well established by Deegan and Scull (1977), and further refined using biostratigraphic techniques (Knox and Holloway, 1992; Neal, 1996; Vining et al., 1993) and seismic reflection data (Eldrett et al., 2015). Three major depositional cycles of deep-water sedimentation occurred in the Central North Sea during the Paleocene to Early Eocene (Kilhams et al., 2014), with each cycle representing a period of relative sea level lowstand, which enabled routing of sediments from the shelf to the basin floor (Jennette et al., 2000). The earliest stratigraphic units are the Maureen Sandstone Member of the Maureen Formation (c. 63 to c. 59.8 Ma) (Figure 3.2). The Maureen and the overlying Lista Formations constitute the first and second deep-water depositional cycles, respectively. The two formations constitute the Montrose Group (Mudge and Copestake, 1993). Stratigraphically lying above the Montrose Group is the Moray Group, which consists of the Sele Formation (c. 56.8–54 Ma) and the Balder Formation (Figure 3.2), and constitutes the third depositional cycle. Sedimentation during the Sele deposition was dominated by submarine fan systems and/or phases of submarine fan systems that covered a large part of the Central Graben.

The depositional architecture and facies distribution are interpreted to have been influenced by basin configuration, palaeo-topographic highs, and salt diapirs (Den Hartog Jager et al., 1993; Hempton et al., 2005; Scott et al., 2010). The Forties Fan system is a restricted, sand-rich fan within the Central Graben, forming an elongate depositional system that lacks classical ‘fan’ morphology (Scott et al., 2010). The palaeo-highs and highs developed by salt diapirs constrained and funnelled flows from proximal to distal fan, resulting in channelization and slumping (Eldrett et al., 2015), with channels and channels facies often persisting to the fringes of the fan system (Collins et al., 2015; Kessler et al., 1980; Thompson and Butcher, 1990). Salt withdrawal in medial to distal fan settings (e.g., Pierce field) decreased and captured sediment gravity flows (Scott et al., 2010), confining and depositing sediments in a mini-basin fill and spill fashion. Deposits close to the diapirs might be muddier due to slumping, which could serve as baffles and barriers to flow (Hempton et al., 2005).

Although the biostratigraphic analysis of the Sele Formation is characterised by limited faunal abundance and diversity due to high sedimentation rates and basin restriction, four distinct sandstone members have been identified within the formation based on palynology (Eldrett et al., 2015). These include the Forties, Bittern, Cromarty and Gannet Sandstone Members

(Figure 3.2), which widely represent discrete fan systems or phases of fan deposition. Restricted to the Central Graben, the Forties Sandstone Member of the Sele Formation is the most areally extensive (300 km by 100 km) and thickest discrete fan (over 200 m) (Eldrett et al., 2015; Hempton et al., 2005). The sandstone member has been described as the product of relatively rapid deposition of a mixed sand and mud sequence by turbidity currents and hemipelagic mud (Collins et al., 2015; Jones et al., 2015). By the end of the Paleocene, a regional, basinal mudstone of the Sele Formation was deposited in response to a sea level rise. These fine-grained sediments act as a regional seal to the Forties Sandstones reservoirs (Whyatt et al., 1992). This study focuses on the proximal through to distal parts of the axial Forties Fan (Figure 3.1), which is equivalent to the Forties Sandstone Member, dominated by channels and submarine fan lobes.

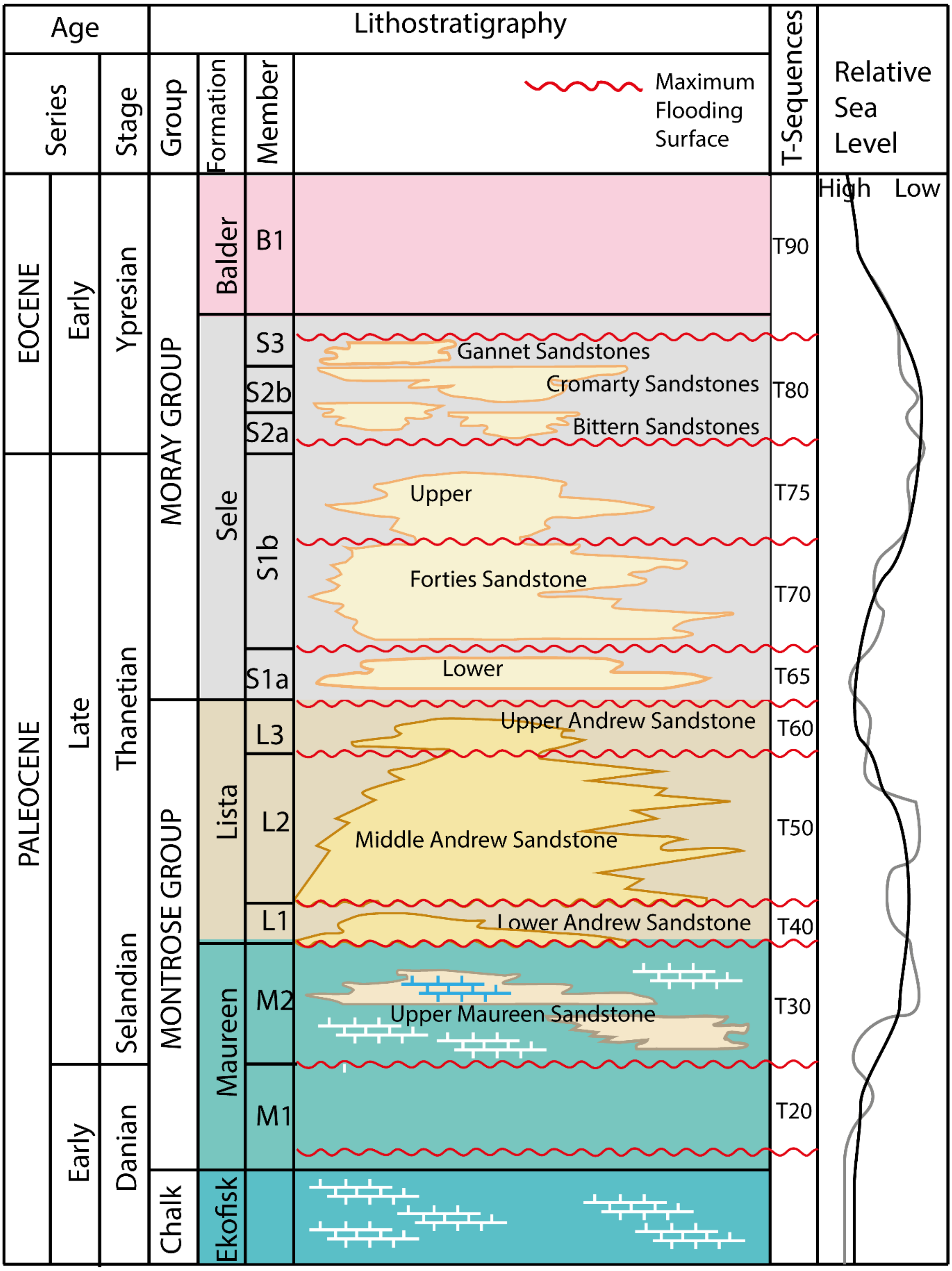

Figure 3.2. Regional stratigraphic chart for the Paleogene Central Graben (modified from Charles and Ryzhikov, 2015). The main focus of the study is the Upper Forties Sandstone Member (T-70 and T-75). The sequences represent periods of sustained clastic sediment input into the basin from the shelf, which are marked by maximum flooding surfaces (MFS).

3.5 Samples and methodology

3.5.1 Sedimentary facies

In this study, we established sedimentary facies based on core descriptions, and we examined a total of 266 m of cores at British Geological Survey (BGS), which were originally taken and from thirteen (13) wells in six oil and gas fields from the proximal to distal parts of the axial Forties Fan system, UK Central North Sea (Figure 3.1) . The results of the sedimentary core descriptions are presented in Table 3.1.

3.5.2 Petrography and stable isotope analysis

A total of one hundred and ninety-one (191) representative sandstone core samples of the Forties Sandstone Member were collected for analysis. The samples were collected based on sedimentary characteristics to identify key facies variations from proximal to distal fan settings. Each sample was impregnated with blue epoxy for identification of porosity and stained with alizarin red and potassium ferricyanide for carbonate cement identification. The samples were examined using a Leica DM2500P standard petrographic microscope. Modal point count analysis using 300 counts per thin section was conducted on all the samples in order to determine the percentage of detrital grains, clay matrix content, pore-filling and grain-coating cements, and porosity (both primary intergranular and secondary intragranular). Grain size and sorting were determined by measuring the long and short axes of 100 grains per thin section using the Petrog software and then calculating the average value for each sample.

For detailed analysis of sandstone microstructure, clay mineral composition, morphology and distribution, selected diamond-polished, carbon-coated thin sections were studied using a Hitachi SU70 scanning electron microscope (SEM) equipped with a backscatter electron detector (BSE) and an energy dispersive X-ray spectra (EDS) under acceleration of 12-15 kV.

Stable isotope analysis for carbon and oxygen isotopes were conducted on 18 sandstone samples with variable amounts of carbonate cements, consisting of calcite (ferroan and non-ferroan), dolomite, and siderite. Based on carbonate content, bulk samples were powdered (< 200 mesh), and each sample was weighed out to give a CO_2 signal of 12mV, and was reacted with 99% ortho-phosphoric acid for 2 hours at 70°C. The resultant gas mix of helium and CO_2 was then separated and analysed via a Thermo Fisher Scientific Gasbench II interfaced with a Thermo Fisher Scientific MAT 253 gas source mass spectrometer for isotopic analysis. Duplicate analysis of 3 samples yielded a precision of <± 0.1 ‰ for both $\delta^{13}C$ and $\delta^{18}O$, with one sample having a slightly higher standard deviation of ± 0.2 for $\delta^{13}C$. All standards yielded an analytical reproducibility of <± 0.1 ‰ standard deviation for both $\delta^{13}C$ and $\delta^{18}O$. All values have been normalised to the accepted values of +2.49‰VPDB and -46.6‰VPDB for $\delta^{13}C$, and -2.40‰VPDB and -26.70‰VPDB for $\delta^{18}O$, for both IAEA-CO-1 and LSVEC respectively. Data are reported in standard delta notation as per mil (‰) relative to Vienna Pee Dee Belemnite (V-PDB).

Porosity and permeability (poroperm) datasets for a total of one hundred and thirty-one (167) core samples were supplied by UK common data access (CDA). Measurements for porosity and permeability were carried out by operators of the studied oil and gas fields, the results of which were subsequently supplied to UK CDA. Additionally, the samples used in the study were in close proximity to where the measurements were undertaken, usually < 0.5 ft (15 cm). Porosity measurements were made using helium in a Boyle's Law porosimeter to give grain volume. Air permeability measurements were conducted using oxygen-free nitrogen as the flowing fluid with the plug mounted in a Hassler cell under a routine confining pressure of 200 psi.

3.5.3 Clay-coating coverage measurements

Clay-coating coverage was measured on 50 selected thin sections using the JMicrovision (v. 1.3.3) software. The samples were selected based on high and low volume of grain-coating chlorite and illite/illite-smectite determined from thin-section point counts. Volume of grain-coating clays in the samples range from 0.30 to 10.70 % of the whole rock volume, averaging 4.63 %. Clay-coating coverage was measured on at least 50 randomly selected quartz grains in each thin section using montaged SEM/BSE images and high-resolution photomicrographs as used by Wooldridge et al. (2019) and Dutton et al (2018), respectively. The measurements were carried out based on the procedure described by Dutton et al (2018).

3.5.4 One-dimensional burial history modelling

1-D basin modelling was carried out using Schlumberger's PetroMod (V.2015) software in order to determine the burial and thermal history of the Forties Sandstone Member in the proximal and distal fan. Two wells (Nelson11-6 and Blane-03a-1) were selected to represent proximal and distal fan, and to show the differences in burial and thermal history between the proximal and distal fan (Figure 3.3). The one-dimensional burial models were constructed using input data from well completion reports provided by the UK CDA. The data include the present-day well stratigraphy, formations lithologic descriptions, and wireline-logging-derived bottom hole temperatures (BHT). BHT corrections were applied using the equation and method developed by Waples et al. (2004). The BHT correction is mainly based on time since end of mud circulation (TSC) and, to a smaller degree, on depth. Information on TSC, surface temperature, measured log temperature, and measurement depth are inputted into the equation and then the corrected temperature is calculated. Paleo-basement heat flow model and paleo-surface temperature history have been adopted from Swarbrick et al. (2000).

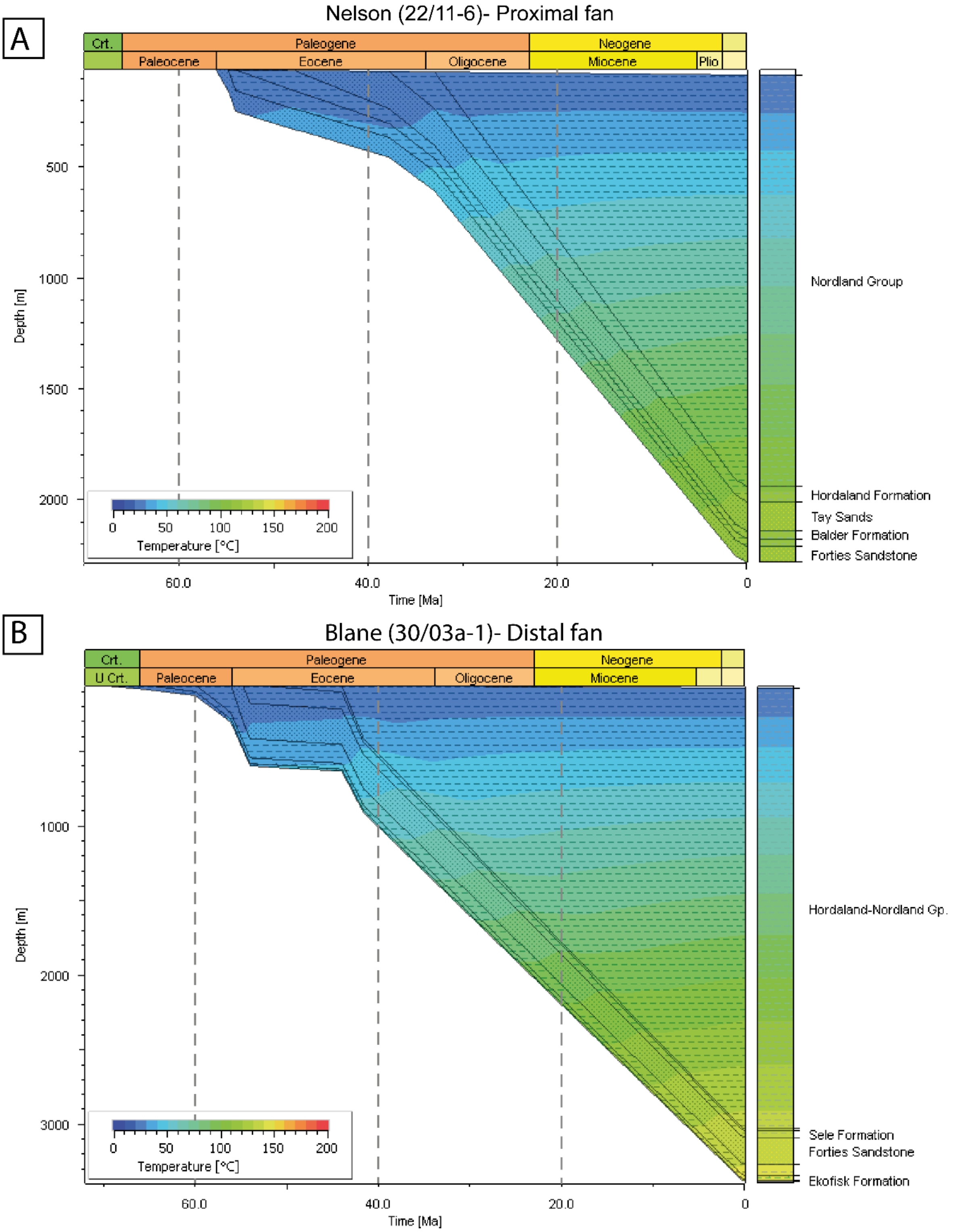

Figure 3.3. Burial and thermal history plots for the Forties Sandstone Member. (A) Proximal fan (Nelson field). In the Nelson field, the sandstones were deposited faster have spent relatively shorter time in the mechanical compaction domain (< 500 m) than in the Blane field in (B); (B) Distal fan (Blane field). See Figure 3.1 for location of fields.

3.6 Results and interpretations

3.6.1 Sedimentary lithofacies

A detailed core study of the Forties Sandstone Member, which comprises of cores from proximal to distal Forties Fan settings, has been undertaken (e.g. Figures 3.4 & 3.5) in order to understand the distribution of reservoir facies and key reservoir quality controls, and to effectively evaluate the role of clays on reservoir quality evolution of the sandstones. Based on the core observations, 7 main core lithofacies and 3 sub-facies were identified using a depositional, process-based facies scheme (Figure 3.4A-I). The subdivision is mainly due to minor differences in depositional processes within the main facies. The facies consist of thick, massive sandstones (Figure 3.4A), massive, dewatered sandstones (Figure 3.4B), massive interbedded sandstones (Figure 3.4C), parallel laminated sandstones (Figure 3.4D), wavy laminated sandstones (Figure 3.4E), slump sandstones (Figure 3.4F), sand injections (Figure 4G), laminated mudstones (Figure 3.4H), and massive, hemipelagic mudstones (Figure 3.4I). Table 3.1 shows the description of the facies grain size, bed thicknesses, main features, depositional processes, and environments of deposition. The facies classification was informed by our understanding of the Bouma turbidite facies by Bouma (1962), and the low- and high-density turbidites by Lowe (1982).

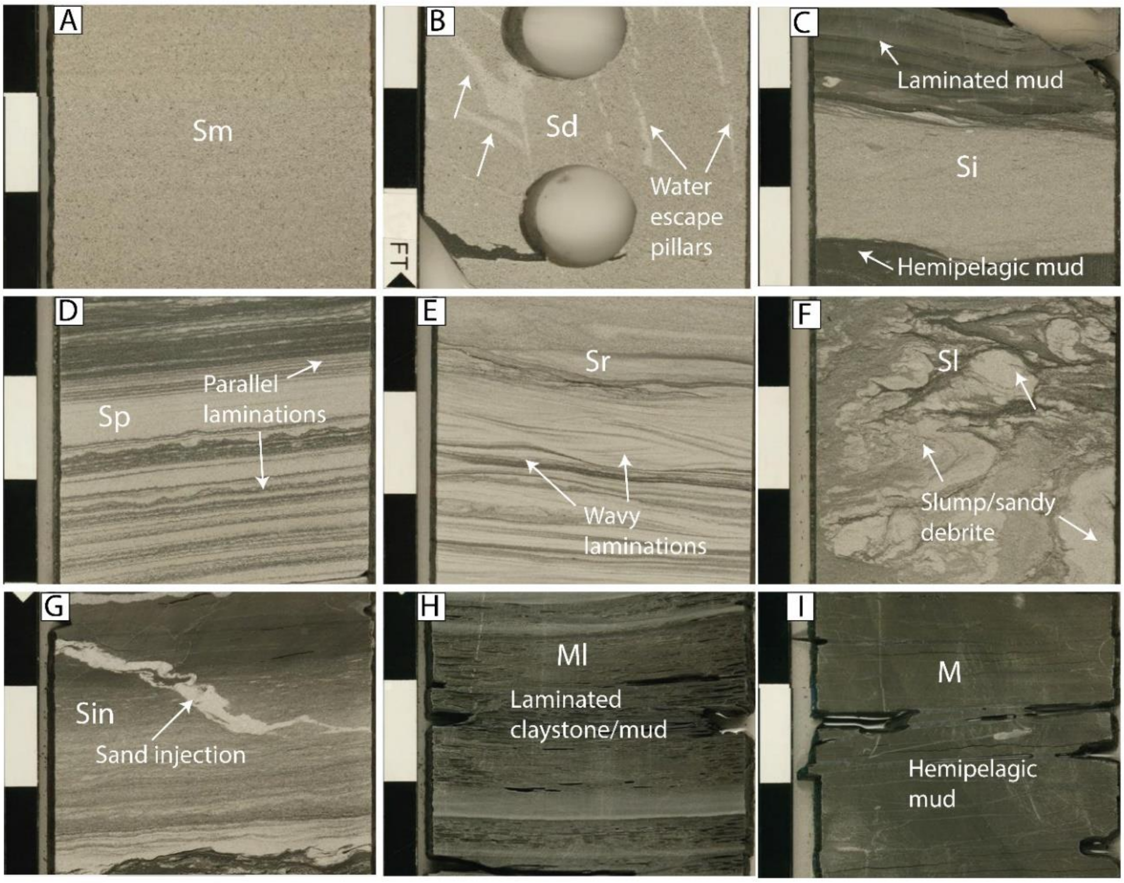

Figure 3.4. Sedimentary core lithofacies scheme established for the study. (A) Massive sandstones (Sma) facies. (B) Massive, dewatered sandstones facies (Sd). (C) Massive, interbedded sandstones facies (Si). (D) Parallel laminated sandstones facies (Sp). (E) Wavy, ripple laminated sandstones facies (Sr). (F) Slump facies (Sl). (G) Sand injections facies (Sin). (H) Laminated mudstones facies (Ml). (I) Massive, hemipelagic mudstones facies (M). Note: black and white scale = 0.3 ft (~ 9 cm).

Table 3.1. Sedimentary facies classification, description, and interpretation of predominant processes and depositional environments.

Facies	**Subfacies**	**Grain size**	**Bed thickness (cm)**	**Description**	**Interpretation**	**Depositional environments**
Sm: Massive sandstones	St: Thick structureless sandstones	Fine-medium	12-60	Clean, structureless sandstones, often with water escape pipes. Bed bases might be sharp or undulating and might contain mudclasts.	High-density turbidity currents (Lowe, 1982), probably confined in submarine channels.	Channel (axis), channel-lobe transition zone, lobe-axis.
	Sd: Dewatered sandstones	Fine-medium	6-30	Dewatered sandstones, characterized by vertical to subvertical water escape pillars. Gradational or sharp bases and tops.	High-density turbidity currents (Lien et al., 2006).	Channel (axis), channel-lobe transition zone, lobe-axis.
	Si: Interbedded massive sandstones	Fine	5-24	Clean sandstones with interbedded mudstone. The interbedded mudstones can be laminated or massive. Sharp or gradational bed bases and tops.	The sandstones are products of high-density turbidity currents, but with less frequency (Lien et al., 2006).	Channel (margin), channel-lobe transition zone, lobe (off-axis, fringe).
Sp: Parallel laminated sandstones		Very fine-fine	5-10	Relatively clean sandstones with planar laminations. No dewatering structures. Sharp and/or gradational bed bases.	The lamination represents deposition from tractional currents, below a dilute turbidity currents (Walker and Martinsen, 1999).	Channel (axis, margin), lobe (axis, off-axis).
Sr: Wavy, ripple laminated sandstones		Very fine-fine	3-9	This facies occurs in close association with Sp facies, with packages largely having gradational tops.	Deposition from tractional flows, formed from the settlement of grains from a waning turbidity current (Górska, 2019).	Channel (axis, margin), lobe (axis, off-axis).

Sl: Slumps		Very fine	6-24	Deformed sandstones or mudstones that are often < 1 m thick and lack internal sedimentary structures. Gradational to sharp bases and tops.	Products of deposition around unstable levees (Lien et al., 2006), salt-induced slopes, or indicate a transition to debris flows (Stanley, 1982).	Channel (axis, margin), oversteepened slope, channel-lobe transition zone.
Sin: Sand injections		Very fine-silt/mudstone	3-9	Sub-horizontal to subvertical sandstones injections, and commonly occurs in mudstones. Sharp bases and tops.	Liquefaction and remobilization of sands (Hiscott, 1979).	Channel (axis), lobe (axis).
Ml and Mh: Laminated mudstones and hemipelagic mudstones			<10-34 and 9-15 (respectively)	Laminated to massive mudstones. Rare sand injections. Sharp and often gradational bases and tops.	Transition into hemipelagic sedimentation and/or product of hemipelagic suspension fallout (Górska, 2019).	Channel (margin, abandonment), channel-lobe transition, lobe fringe, basinal mudstone.

3.6.2 Lithofacies associations

Core lithofacies were grouped into 3 predominant depositional facies associations (Figure 3.5) and interpreted based on depositional environments and architectural elements in the Forties submarine fan system (e.g., submarine fan channel, lobe, lobe fringe). The established facies associations is based upon the previous interpretations of the Forties Fan's architectural elements and depositional facies schemes of Collins et al. (2015) and Kunka et al. (2003) for proximal to distal fan settings.

3.6.2.1 Amalgamated sandstone facies association

This facies association, which form 44 % of the studied cores, are characterized by the presence of amalgamated surfaces between beds, commonly identified by shifts in grain size and minor scour surfaces that form relatively homogeneous sand packages. Dark, minor rip-up clasts of silty claystone are commonly incorporated into the basal sections of the sandstone beds, which can serve as baffles to fluid flow.

Although the individual beds are generally homogeneous, they occasionally exhibit a subtle upward-fining profile. Individual bed thickness typically ranges between 0.6 and 1 m, while the composite amalgamated sandstone bodies in the Nelson Field are up to 6 m thick. Amalgamated sandstone deposits exhibit high net to gross, with a total sandstone thickness exceeding 20 m in the Nelson field areas (e.g., Figure 3.5A). The GR log curve of single channel sandbody exhibits box-shaped appearance in the Nelson field (Figure 3.1B) These facies associations are capped by lower-energy, channel abandonment facies consisting of thinly bedded turbidites (Sp), slumps (Sl) and muddy debris flows deposits or abandonment claystone/shale.

The massive, amalgamated sandstones facies associations are interpreted as products of high-density turbidity currents, probably confined to submarine channels, in which sediments are supported by buoyancy, grain collisions and fluid turbulence (Lowe, 1982; Talling et al., 2012). They are deposited from rapid fallout of sediments from confined high-density flows, and because of the high suspended load fallout rates, the sediments had insufficient time to be reworked by traction currents on the beds, which result in massive sand deposition (Middleton and Hampton, 1973; Talling et al., 2012). The rapid deposition of sand from a turbulent flow leads to entrapment of abundant fluids between sand grains, and during the early stages of bed compaction (due to the deposition of the overlying parts of the same bed), the entrapped excess pore fluid escaped and formed water escape pipes (Figure 3.4B) (Lien et al., 2006). The amalgamated sandstones facies associations, therefore, are suggested to be deposited in submarine channel and proximal lobe (Huang et al., 2020; Porten et al., 2016).

3.6.2.2 Sand-prone heterolithic facies association

Forming 24 % of the studied cores, the sand-prone heterolithic facies association comprises massive (and often dewatered) fine to medium-grained sandstones, interbedded with siltstones and mudstones (Figure 3.5B). The silts and mudstones interbeds could serve as baffles (where thin) and barriers (where thick) to flow. The sandstones are similar to those of the amalgamated sandstone facies, with decreased bed thicknesses and increased mud content. The facies are typically less well-sorted than the amalgamated sandstone facies, and are mainly fine grained (Figure 3.5B). The sand-prone heterolithic deposits are characterized by moderate-to-high net to gross (Figure 3.1B; Arran-23/16c-8), with laminated argillaceous deposits forming bed tops and discrete interbeds with the massive sandstones (Figure 3.5B). The argillaceous bed tops and interbeds mostly form gradational and sharp-based contacts with the underlying massive, dewatered sandstones, respectively.

The sandstone beds range in thickness from 0.15 m to *c.* 0.7 m, with an average of 0.4 m. The interbedded argillaceous sandstones, shale drapes, and silty mudstones range from 0.1 to 0.3 m. The argillaceous sandstones contain injection and slump features and mud clasts.

The massive sandstones in these facies are interpreted predominantly as deposits of high-density turbidity currents that are overlain by, or grade into, linked debrites (Haughton et al., 2003; Talling et al., 2004), whereas the finer-grained rippled or parallel-laminated bed tops were interpreted as products of low-density turbidity currents (Lowe, 1982; Talling et al., 2012), with localized turbidite and/or hemipelagic shale drapes. The massive sandstone beds represent individual depositional units, separated by low-energy bed tops, which markedly indicate the interbedded nature of the non-amalgamated sandstones (Collins et al., 2015).

These facies have been interpreted to have been deposited in the lobe off-axis depositional environment (Bell et al., 2018; Huang et al., 2020), and the transition from massive, amalgamated sandstones to non-amalgamated sandstones could occur within a single depositional lobe, both laterally lobe off-axis and longitudinally down-flow (Collins et al., 2015). Their abundance decreases from proximal to distal fan.

3.6.2.3 Mud-prone heterolithic facies association

The mud-prone heterolithic facies association, which forms 25 % of the total studied cores, predominantly consists of mudstones, silty mudstones, siltstones, and very fine- to medium-grained sandstones (Figure 3.5C). They are thinly bedded, very fine- to fine-grained, parallel- and ripple-laminated sandstones, with slump deposits also observed (Figure 3.5C). However, unlike in the amalgamated sandstones and sand-prone heterolithic facies associations, the massive, relatively clean sandstones in the mud-prone heterolithic facies association is much lower in thickness, with even the thickest units being less than 0.5 m. Furthermore, discrete sand beds are characterized by sharp, non-erosional bases and gradational bed tops (Figure 3.5C). The slump deposits in this facies could serve as baffles, whereas the thick mudstones could serve as barriers to fluid flow.

The massive sandstones in this facies association are interpreted here as deposits of high-density turbidity which transform into, or are sharply overlain by, linked debrites, although with relatively lower energy than the massive sandstones of the preceding facies associations. The laminated, heterolithic sandstones, which might be locally slumped and deformed, were formed by low-density turbidity currents, and are equivalent to the type 7 event beds of Davis et al. (2009). Although the likely origin of the silt-mud lamination in this heterolithic packages is somewhat poorly understood, the planar lamination is thought to have formed by a process that sorts silt and very fine sand from mud (Talling et al., 2012). In addition, the parallel laminated siltstone/mudstone interval suggests a weak, lower flow regime traction process, which leads to the formation of the individual laminae (Lowe, 1982). The laminated siltstones, therefore, indicate deposition from a relatively weak and dilute turbidity current that might be comparable to the Td subdivision of Bouma (1962) or TE-1 subdivision of Talling et al. (2012). The laminated mudstones, on the other hand, are thought to indicate a transition to an overlying hemipelagic and pelagic sedimentation (Lowe, 1982), which form massive mudstones of the equivalent to the Te subdivision of the Bouma (1962), and indicate sediment settlement from suspension.

Overall, the mud-prone heterolithic facies abundance increases from proximal to distal fan, and are thought to have been deposited in a lobe off-axis and lobe margin areas, on the margins of the coeval depositional fairway (Bell et al., 2018; Collins et al., 2015; Huang et al., 2020).

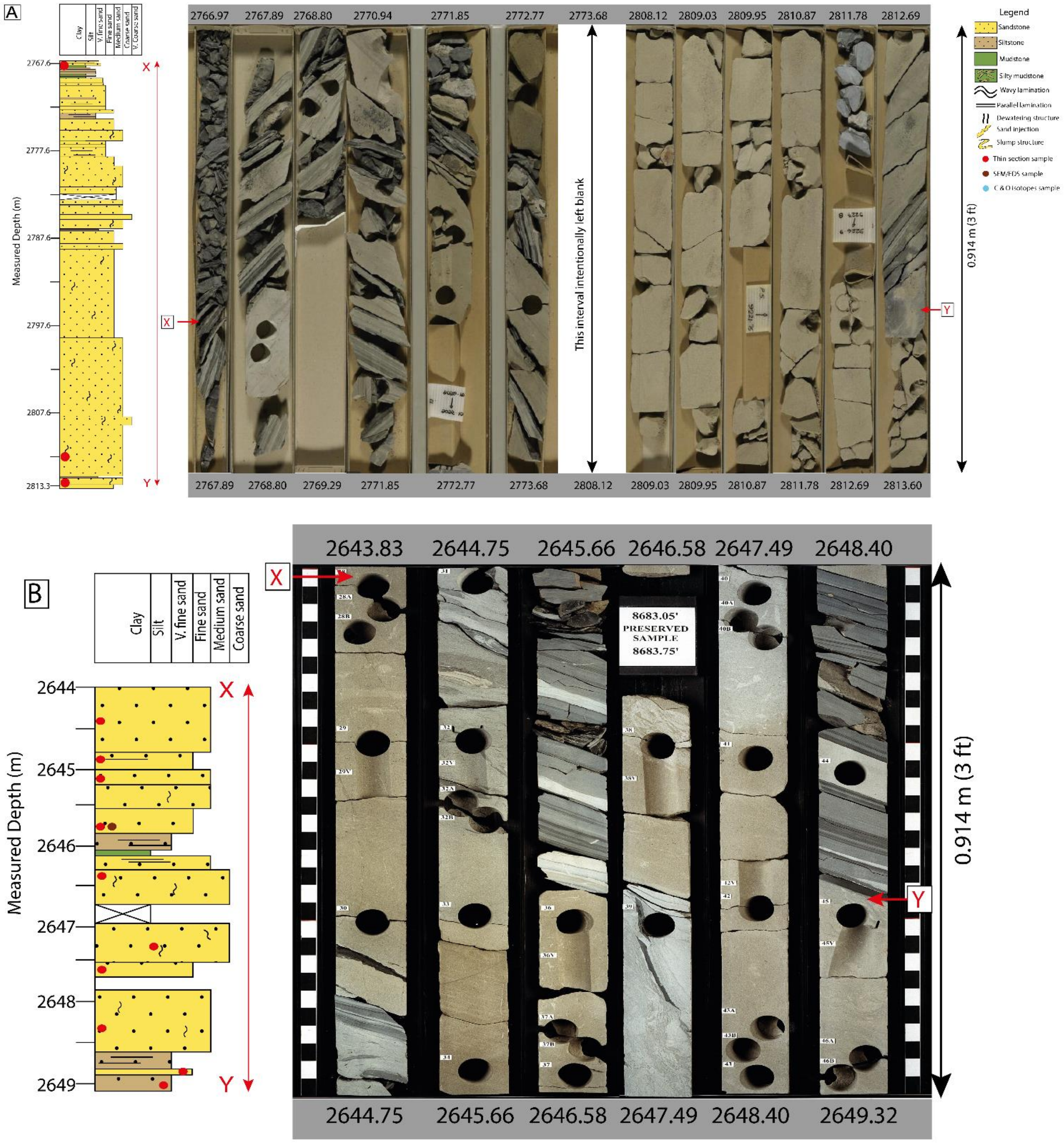
A
Clay
Silt
V. fine sand
Fine sand
Medium sand
Coarse sand
V. Coarse sand
Measured Depth (m)
2767.6
2777.6
2787.6
2797.6
2807.6
2813.3
X
Y
2766.97
2767.89
2768.80
2770.94
2771.85
2772.77
2773.68
2808.12
2809.03
2809.95
2810.87
2811.78
2812.69
This interval intentionally left blank
2767.89
2768.80
2769.29
2771.85
2772.77
2773.68
2808.12
2809.03
2809.95
2810.87
2811.78
2812.69
2813.60
0.914 m (3 ft)
Legend
Sandstone
Siltstone
Mudstone
Silty mudstone
Wavy lamination
Parallel lamination
Dewatering structure
Sand injection
Slump structure
Thin section sample
SEM/EDS sample
C & O isotopes sample
B
Clay
Silt
V. fine sand
Fine sand
Medium sand
Coarse sand
Measured Depth (m)
2644
2645
2646
2647
2648
2649
X
Y
2643.83
2644.75
2645.66
2646.58
2647.49
2648.40
8683.05'
PRESERVED
SAMPLE
8683.75'
2644.75
2645.66
2646.58
2647.49
2648.40
2649.32
0.914 m (3 ft)

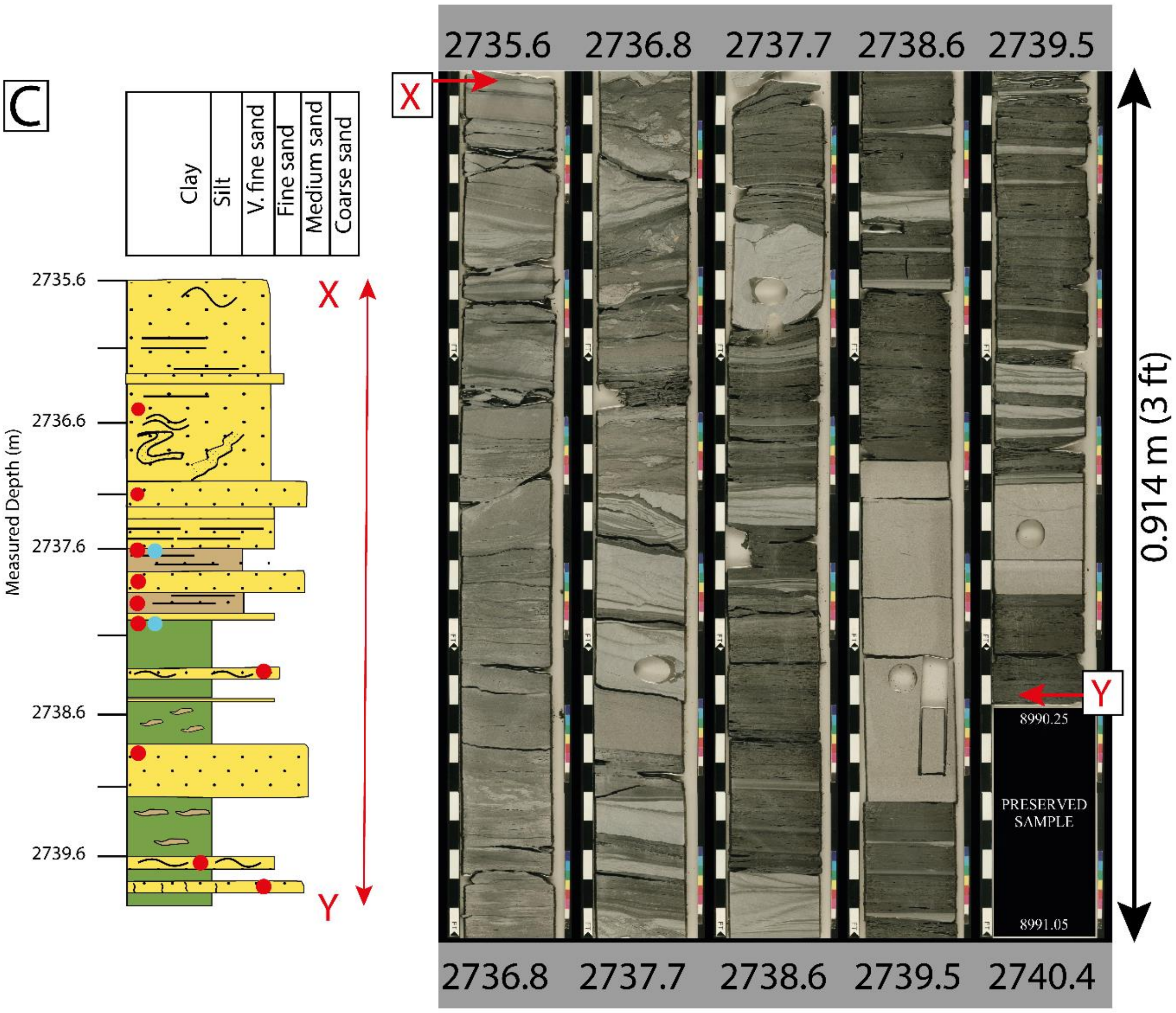

Figure 3.5. Example sedimentary logs for the three key facies and lithofacies associations as established in this study. (A) Amalgamated sandstones facies is dominated by stacked massive sandstones up to ~20 m thick; (B) Sand-prone heterolithic facies. The sandstones are similar to those in (A), but are interbedded with mudstones and siltstones. Sand bed thickness is substantially less than the facies in (A) and typically < 1 m thick; (C) Mud-prone heterolithic facies. In contrast, the mud-prone heterolithic facies comprises mainly mudstones, siltstones, and interbedded sandstones up to a maximum of 0.5 m thick and typically below standard logging tool resolution.

3.6.3 Petrology

3.6.3.1 Sandstone composition

The Forties Sandstone Member mainly consists of arkose to subarkose and rarely lithic arkose sandstones (Figure 3.6A). The average, present-day framework composition of the sandstones is $Q_{69.2}F_{27.2}R_{3.6}$. Quartz grains are mainly monocrystalline, whereas polycrystalline quartz, which also doubles up as a rock fragment, occurs as trace to up to 6 %. Microcline and orthoclase are the two types of detrital potassium feldspars present. Overall, potassium feldspar predominates over plagioclase feldspar. The rock fragments consist of metamorphic, polycrystalline quartz, mudclasts, and volcanic rock fragment. The detrital mica occurs in variable amounts, with biotite dominating over muscovite. Accessory minerals consist of glauconite and heavy minerals (e.g., rutile). The detrital clay matrix is composed of smectitic, mixed-layer clays (mainly illite-smectite), with moderately high birefringence and greenish to brown in colour (Figure 3.6B, C & D) (Shaw and Conybeare, 2003; Ulmer-Scholle et al., 2015). These smectitic clays also occur as grain coatings (Figure 3.6E). Grain-coating illite-smectite has moderately high birefringence and greenish to brown in (Figure 3.6E) (Ulmer-Scholle et al., 2015), whereas chlorite has yellow birefringence, which was interpreted elsewhere to have replaced smectite (Bahlis and de Ros, 2013).

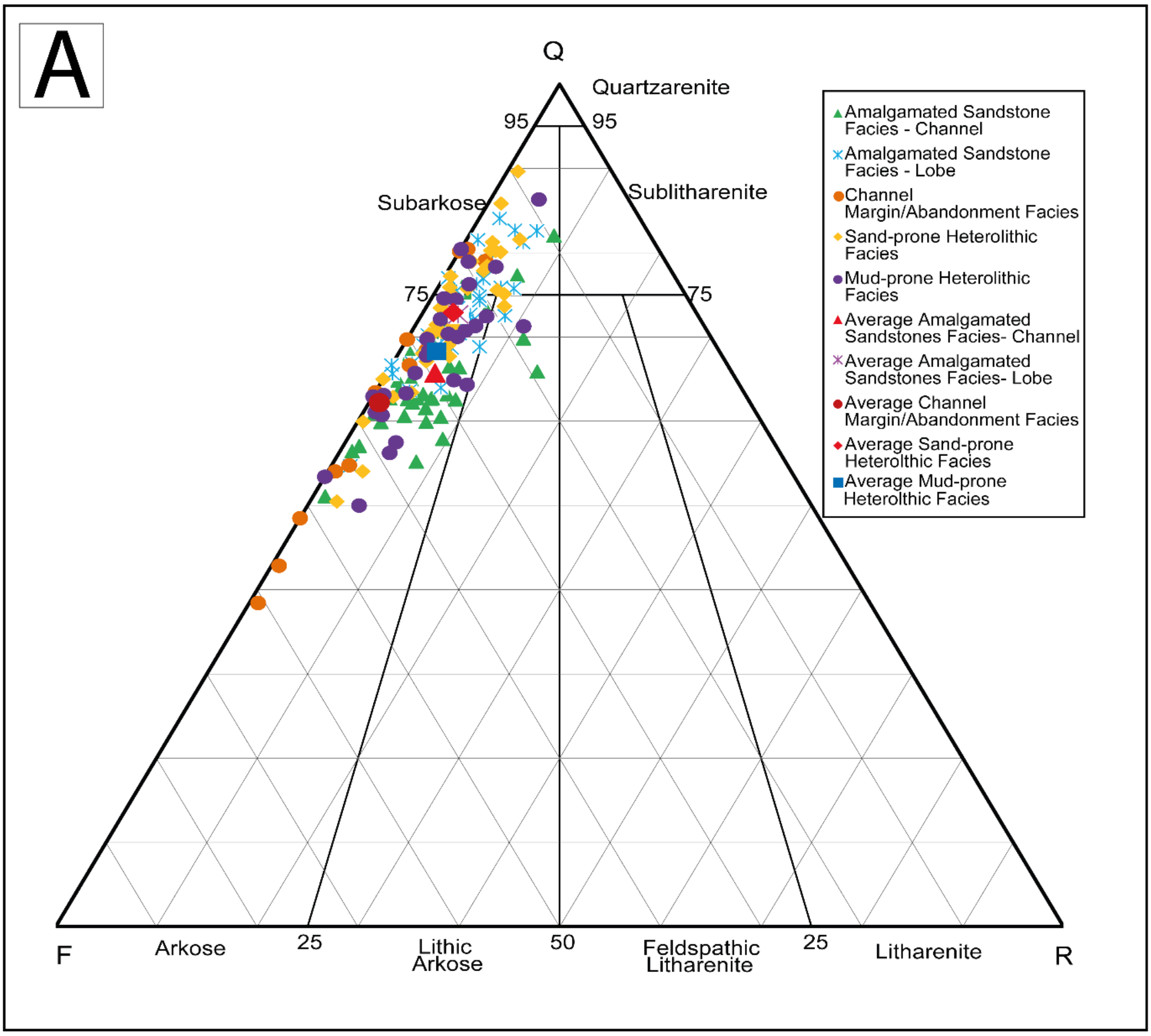
A
Q
Quartzarenite
95
95
Subarkose
Sublitharenite
75
75
▲ Amalgamated Sandstone Facies - Channel
✳ Amalgamated Sandstone Facies - Lobe
● Channel Margin/Abandonment Facies
◆ Sand-prone Heterolithic Facies
● Mud-prone Heterolithic Facies
▲ Average Amalgamated Sandstones Facies- Channel
✳ Average Amalgamated Sandstones Facies- Lobe
● Average Channel Margin/Abandonment Facies
◆ Average Sand-prone Heterolthic Facies
■ Average Mud-prone Heterolthic Facies
F
Arkose
25
Lithic Arkose
50
Feldspathic Litharenite
25
Litharenite
R

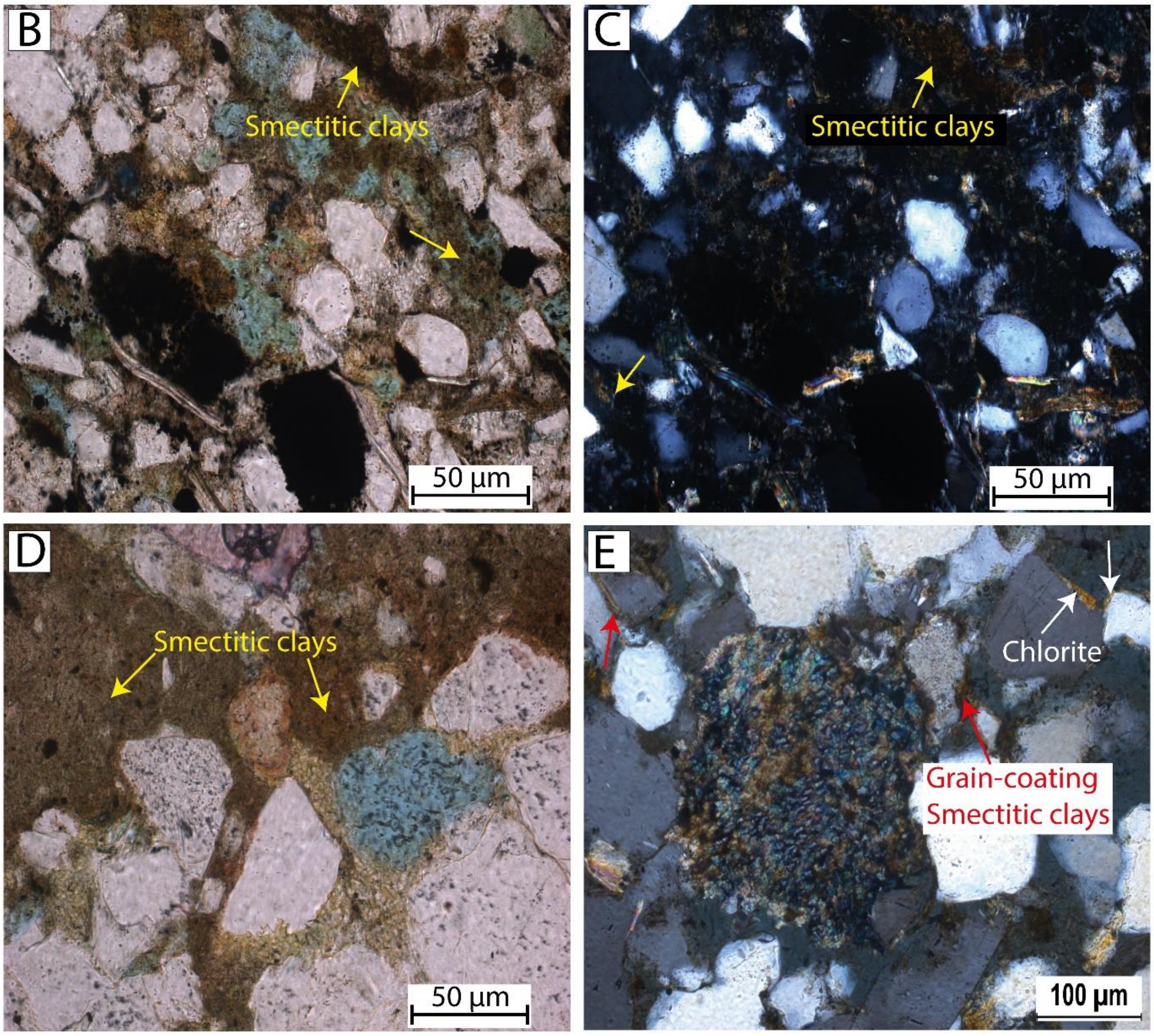

Figure 3.6. (A) QFR plot (after Folk, 1980) showing the compositional mineralogy of the Forties Sandstones Member for all the wells used in this study. Most of the sandstones are arkosic to subarkosic with a smaller proportion represented by lithic arkoses. (B) PPL photomicrograph of moderately high refringence, greenish to brown smectitic clay matrix filling intergranular porosity. Pierce field, well 23/27-5, 2728.26 m TVDSS; (C) XPL image of (B); (D) Greenish to brown, smectitic detrital clay matrix destroying intergranular porosity. Pierce field, well 23/27-5, 2728.26 m TVDSS; (E) XPL photomicrograph of grain coating chlorite from smectite (with yellow birefringence; white arrows) and greenish to brown grain-coating illite-smectite (red arrow). Blane Field, well 30/03a-1, 3097 m TVDSS.[PPL= plane polarized light; XPL= cross polarized light].

3.6.4 Grain size and clay content

Based on core observations and thin sections study, variations in grain size and clay content were observed among all the studied samples of the established reservoir facies associations from proximal to distal fan. Amalgamated sandstones facies, from submarine channels and proximal lobes, are fine- to medium-grained (mean grain size 0.25 mm) (e.g., Figure 3.7A), with less detrital clay matrix that ranges from 0.3 to 28 % (av. 7 %). Figure 3.7A shows a representative sedimentary core log for the amalgamated sandstones facies in well 22/11-8 (Nelson field), with vertical mean grain size profile (Figure 3.7B), mud content (Figure 3.7C), and samples of thin-section photomicrographs (Figure 3.7D & E). Samples with finer grain size (Figure 3.7B) have higher pore-filling, detrital clay content (Figure 3.7C & D), whereas samples with coarser grain size have less pore-filling, detrital clay content (e.g., Figure 3.7E).

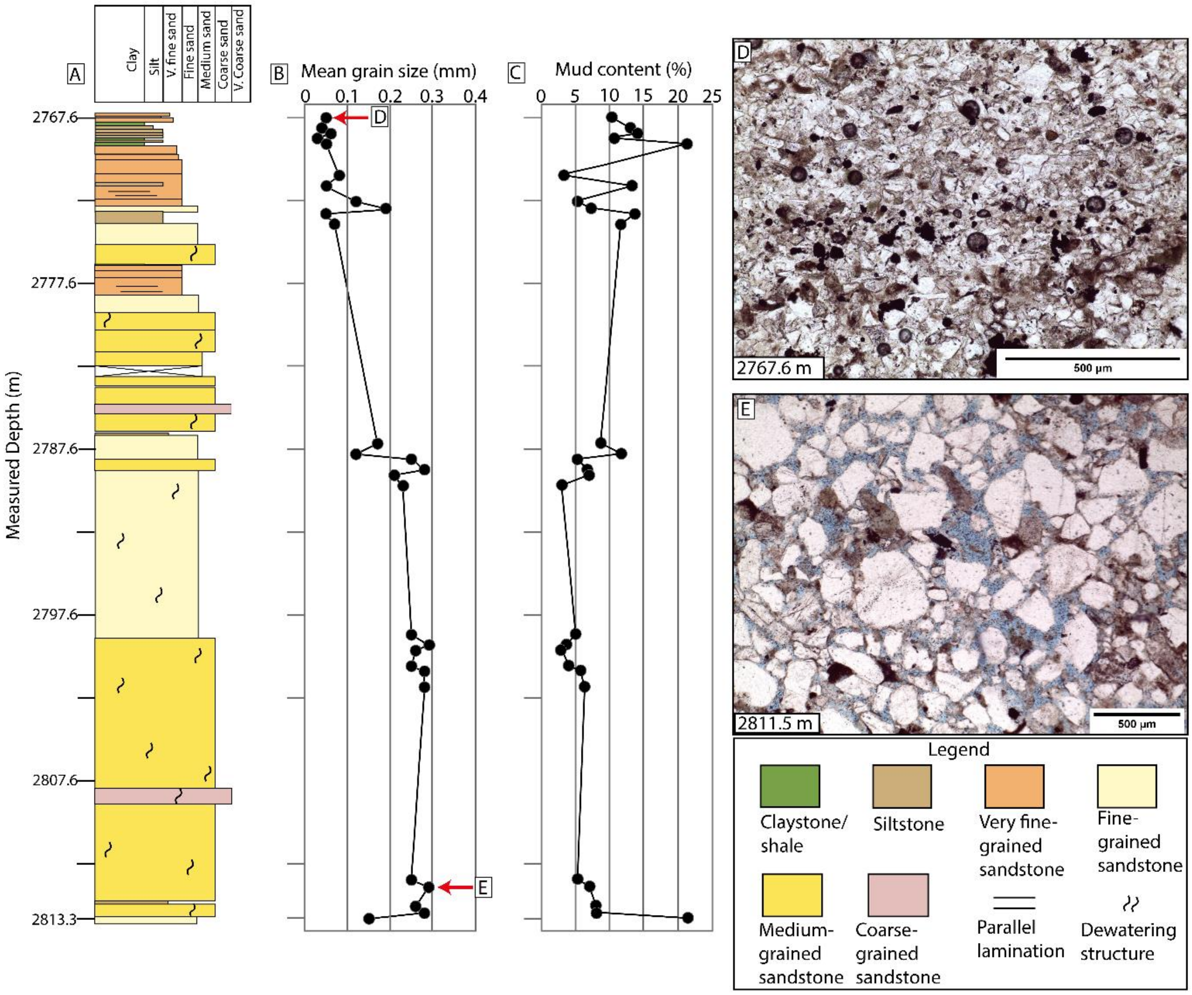

Figure 3.7. (A) Sedimentary log demonstrating amalgamated sandstones facies in well 22/11-8 (Nelson field); (B-C) Vertical variations in mean grain size and mud content determined by petrographic point counting, respectively. The vertical changes show that a decrease in grain size leads to an increase in detrital mud content and vice versa; (D-E) Thin-section photomicrographs showing finer and coarser grain size for amalgamated sandstones facies association, respectively.

The minor channel margin facies association are coarse silt to fine sand (mean grain size 0.10 mm), with detrital clay matrix ranging from 3.3 to 21.5 % (average 12 %)

Sand-prone heterolithic facies are predominantly fine grained (average grain size 0.19 mm) (e.g., Figures 3.5B & 3.8A), with clay matrix content ranging from 5 to 27 % (average 11.5

%). A representative sedimentary core log for sand-prone heterolithic facies association in well 23/16c-8 (Arran field) (Figure 3.8A) shows that, a decrease in grain size (Figure 3.8B) leads to an increase in pore-filling detrital clay content (Figure 3.8C & D). A coarser grain size has lesser clay content (Figure 3.8E).

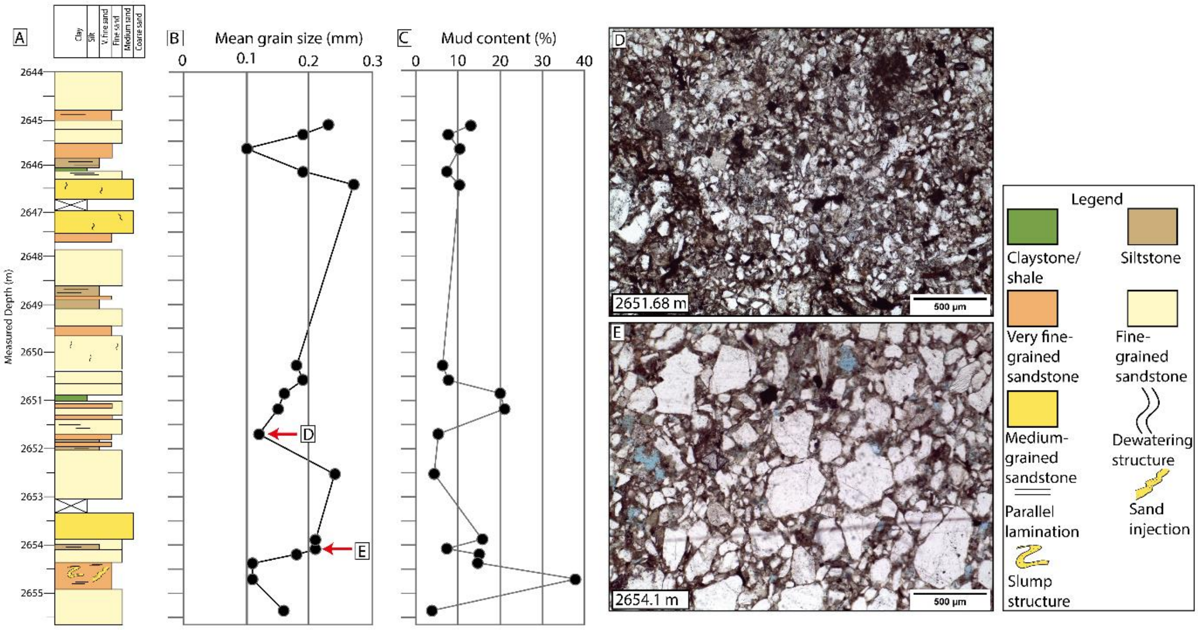

Figure 3.8. (A) Sedimentary log demonstrating sand-prone heterolithic facies in well 23/16c-8 (Arran field); (B-C) Vertical variations in mean grain size and mud content determined by petrographic point counting, respectively. The vertical changes show that a decrease in grain size leads to an increase in detrital mud content and vice versa; (D-E) Thin-section photomicrographs showing finer and coarser grain size for sand-prone heterolithic facies association, respectively.

Mud-prone heterolithic facies associations are very fine- to medium-grained (average grain size 0.17 mm), and are interbedded with mudstones, silty mudstones, and siltstones (e.g., Figures 3.5C & 3.9A). Vertical mean grain size and mud content profiles (Figure 3.9B & C) show that there is an increase in pore-filling clay matrix with a decrease in grain size (Figure 3.9D) and vice versa (e.g., Figure 3.9E). This facies association is characterized by abundant, greenish-brown clay matrix (e.g., Figure 3.9D), ranging from 0.3 to 44 % (average 15 %).

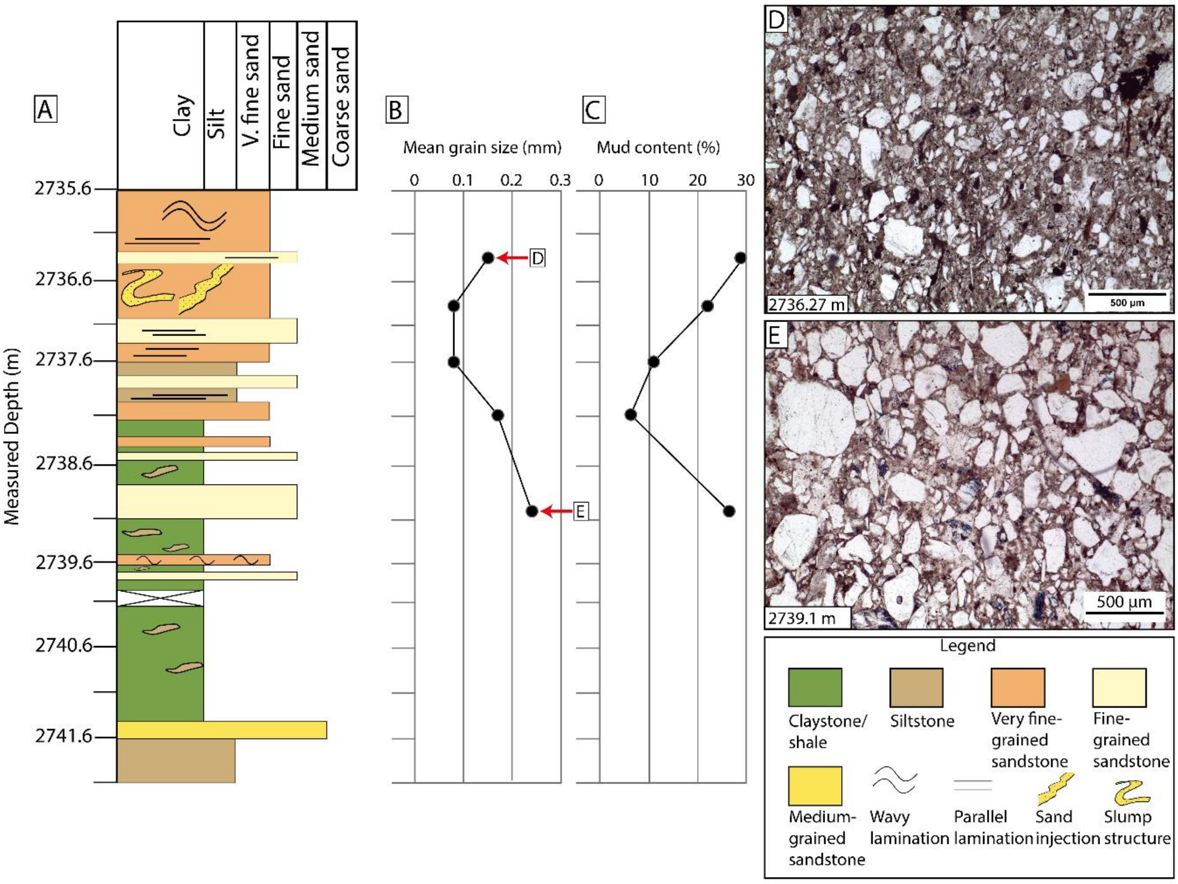

Figure 3.9. (A) Sedimentary log showing mud-prone heterolithic facies in well 23/16b-9 (Arran field); (B-C) Vertical variations in mean grain size and mud content determined by petrographic point counting, respectively. The vertical changes show that a decrease in grain size leads to an increase in detrital mud content and vice versa; (D-E) Thin-section photomicrographs showing finer and coarser grain size for mud-prone heterolithic facies association, respectively.

A plot of detrital, pore-filling clay content against mean grain size (Figure 3.10A) shows that, there is an increase in clay content with decreasing grain size from proximal to distal Forties Fan system. Additionally, ductile grain contents, consisting of mica and mudclasts, have been found to increase with decreasing grain size from proximal to distal fan (Figure 3.10B).

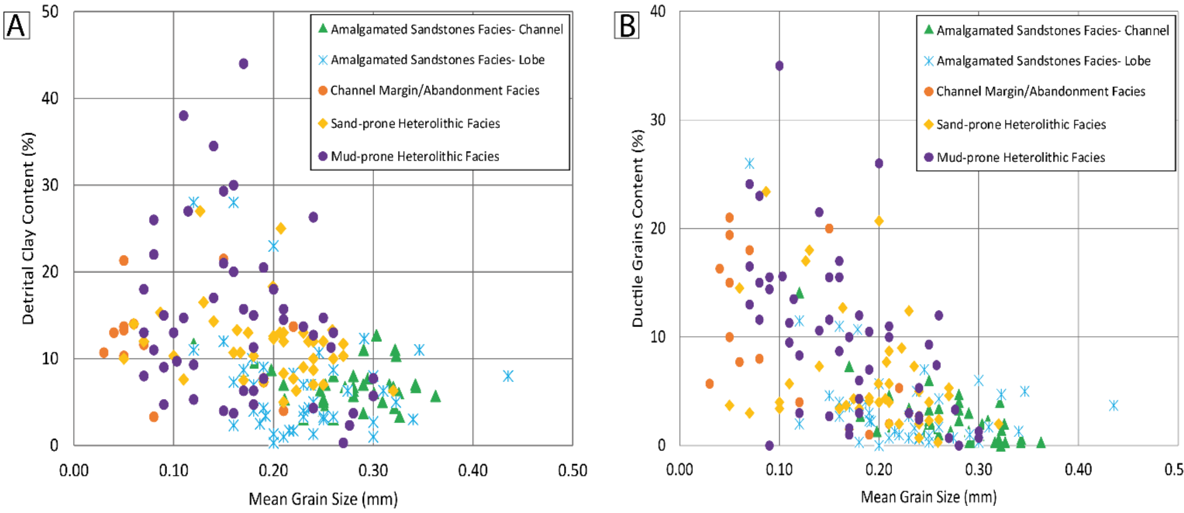

Figure 3.10. Relationship between mean grain size and detrital clay matrix showing that the coarser-grained, proximal-fan sandstones have low detrital clay matrix, and the finer-grained, distal-fan sandstones have higher detrital clay matrix; (B) Plot of ductile grains contents (mica and mudclasts) against mean-grain size showing that, the coarser-grained, proximal-fan sandstones have low ductile grains content (and thus less mechanical compaction), and finer-grained, distal-fan sandstones have higher ductile grains content (and hence higher impact of mechanical compaction).

3.6.5 Diagenetic processes, alterations and products

The diagenetic processes affecting the Forties Sandstone Member include mechanical compaction, cementation (clay minerals, quartz overgrowth, carbonate cements), dissolution and replacement of unstable detrital grains by clay minerals, pyrite, and carbonate cements.

3.6.5.1 Mechanical compaction

The extent of compaction in the Forties Sandstone Member was assessed based on burial history plots (Figure 3.3A & B), petrographic observations of grain contacts, grains rearrangements and fracturing, ductile deformation of grains (mica, mudclasts, and rock fragments), extent of carbonate cementation, and establishing the degree of porosity loss by compaction (COPL) and cementation (CEPL) using the method of Lundegard, 1992 (Figure 3.11). The burial history plots of the Forties Sandstone Member (Figure 3.3) illustrate that the sandstones were deposited faster and spent a relatively shorter residence time in mechanical compaction domain (<500 m) in the proximal fan (Nelson/11-6; Figure 3.3A) than in the distal fan (Blane/03a-1; Figure 3.3B). The effect of mechanical compaction is more intense in the sandstones with higher amount of ductile grains (e.g., Figures 3.10B & 3.12A) in the distal fan than in the proximal fan. Additionally, petrographic observations show that grain fracturing due to compaction are common in feldspar and quartz grains (Figure 3.12B). In contrast, samples with extensive, early carbonate cements (Figure 3.12C) show less impact of mechanical compaction on porosity loss than samples with little or no carbonate cements (e.g. Figure 3.12A). In these samples, however, porosity is lost by cementation than by compaction (Figure 3.12C).

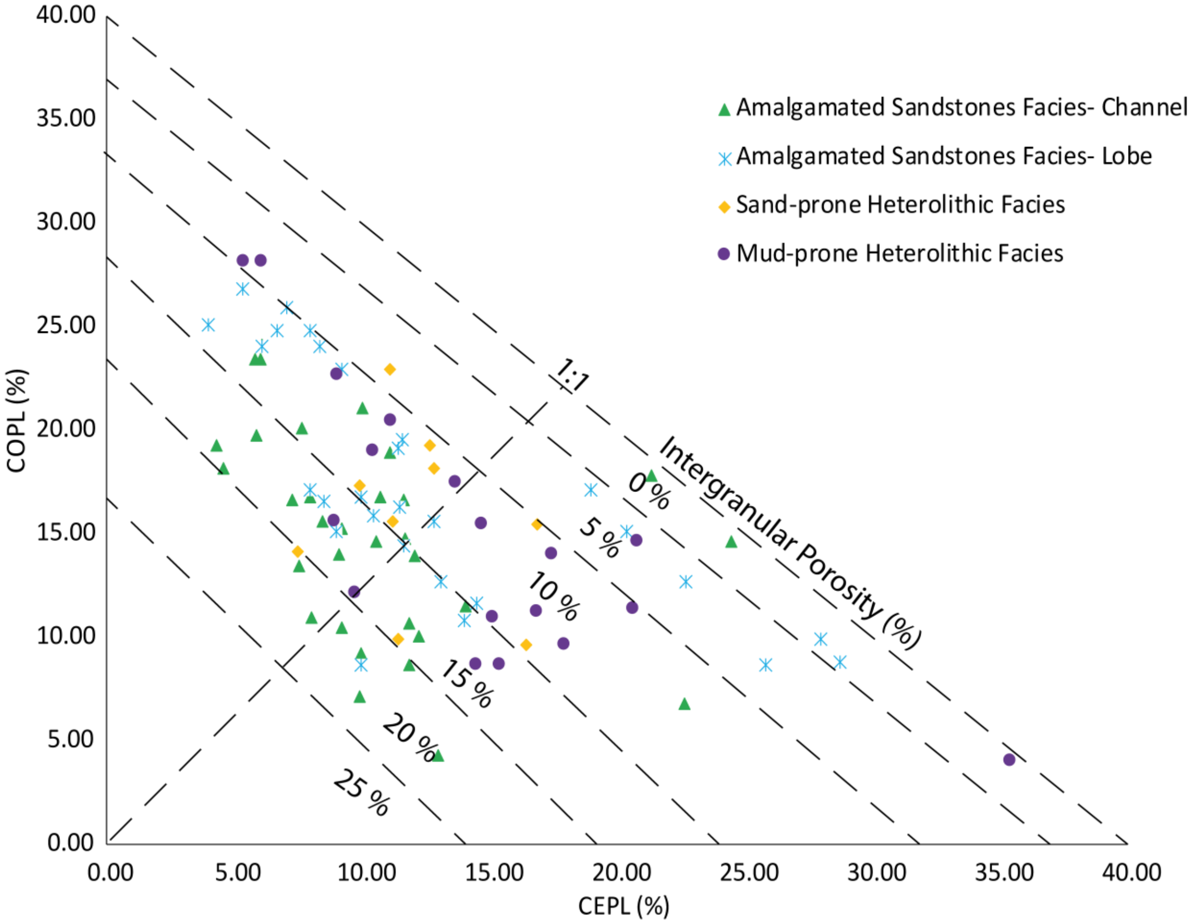

Figure 3.11. Plot of compactional porosity loss (COPL) against cementational porosity loss (CEPL) for the Forties Sandstone Member (calculated after Lundegard, 1992). The plot shows that more porosity is lost due to compaction than due to cementation.

Calculation of porosity loss by compaction and by cementation was performed by calculating the intergranular volume (IGV), using the method of Paxton et al. (2002). One major source of uncertainty in the calculation of porosity loss by compaction and by cementation is the initial depositional porosity of the sediments, with high estimated initial porosity resulting in high calculated compactional porosity loss (Lundegard, 1992). In addition, the initial depositional porosity of sediments has been liked to sorting, with very well- to well-sorted sands having depositional porosities > 40 % Pryor (1973). The studied Forties sandstones, however, are moderately to well sorted, and the initial depositional porosities of 36 and 43 % have been reported in the literature (Allsop, 1994; Whyatt et al., 1992). Consequently, an average of 40

% initial depositional porosity was used. The plot of porosity loss due to compaction against porosity loss due to cementation is shown in Figure 3.11. The plot demonstrates that porosity loss is primarily driven by compaction than by cementation.

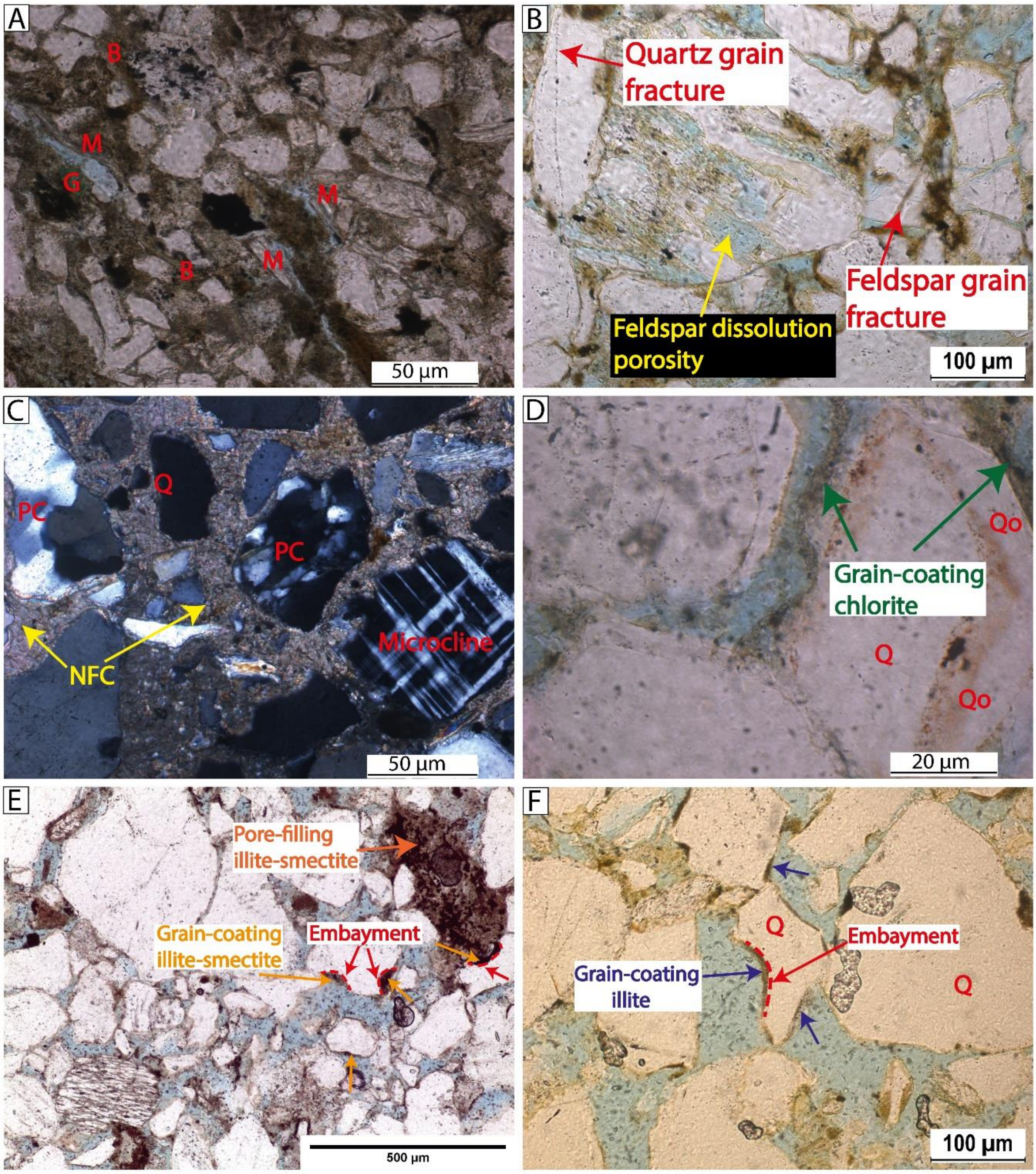

Figure 3.12. Thin-section photomicrographs illustrating the examples of compaction, cementation, and dissolution for the Forties Sandstone Member. (A) Increased compaction due to high detrital clay matrix and abundant ductile biotite and muscovite grains. Pierce field, well 23/27-5, 2726.74 m TVDSS; (B) Grain fracturing due to compaction, and development of secondary intragranular porosity due to feldspar dissolution. Blane field, well 30/03a-1, 3097 m TVDSS; (C) Less mechanical compaction due to floating grains in an early, non-ferroan calcite (yellow arrows). Pierce field, well 23/27-8, 2479.85 m TVDSS; (D) Grain-coating chlorite postdating quartz cementation. Arran field, well 23/16c-8, 2580.74 m TVDSS; (E)

Thick, inherited grain-coating illite-smectite in a grain embayment (which is resistant to abrasion during transport) and thin clay coats outside the embayment. Nelson field, well 22/11-8, 2608.17 m TVDSS. (F) Well-developed grain-coating illite (blue arrow) preserved in embayment. Nelson field, well 22/11-6, 2216.59 m TVDSS. [B= biotite; G=glauconite; M= muscovite; NFC= non-ferroan calcite; PC= polycrystalline quartz; Q=quartz; Qo= quartz overgrowth].

3.6.5.2 Clay minerals

Clay minerals are the most abundant diagenetic minerals in the studied sandstones. Petrographic observations, SEM morphological characteristics and EDS analyses of the clay minerals indicate four types of clays in the sandstones: chlorite (Figures 3.12D and 3.13A), kaolinite, pore-filling, mixed layer illite/smectite (Figures 3.6B-E & 3.12E), grain-coating illite/smectite-illite (Figure 3.12E), and illite (Figure 3.12F). The grain-coating illite/illite-smectite appear to be thick and continuous on the concave surfaces of grains, which are called embayments (Figures 3.12E & F and 3.13A). Such grains with embayments are thought to have inherited clay coats from shelf, transitional or continental environments, and are resistant to abrasion during transport (Bahlis and de Ros, 2013).

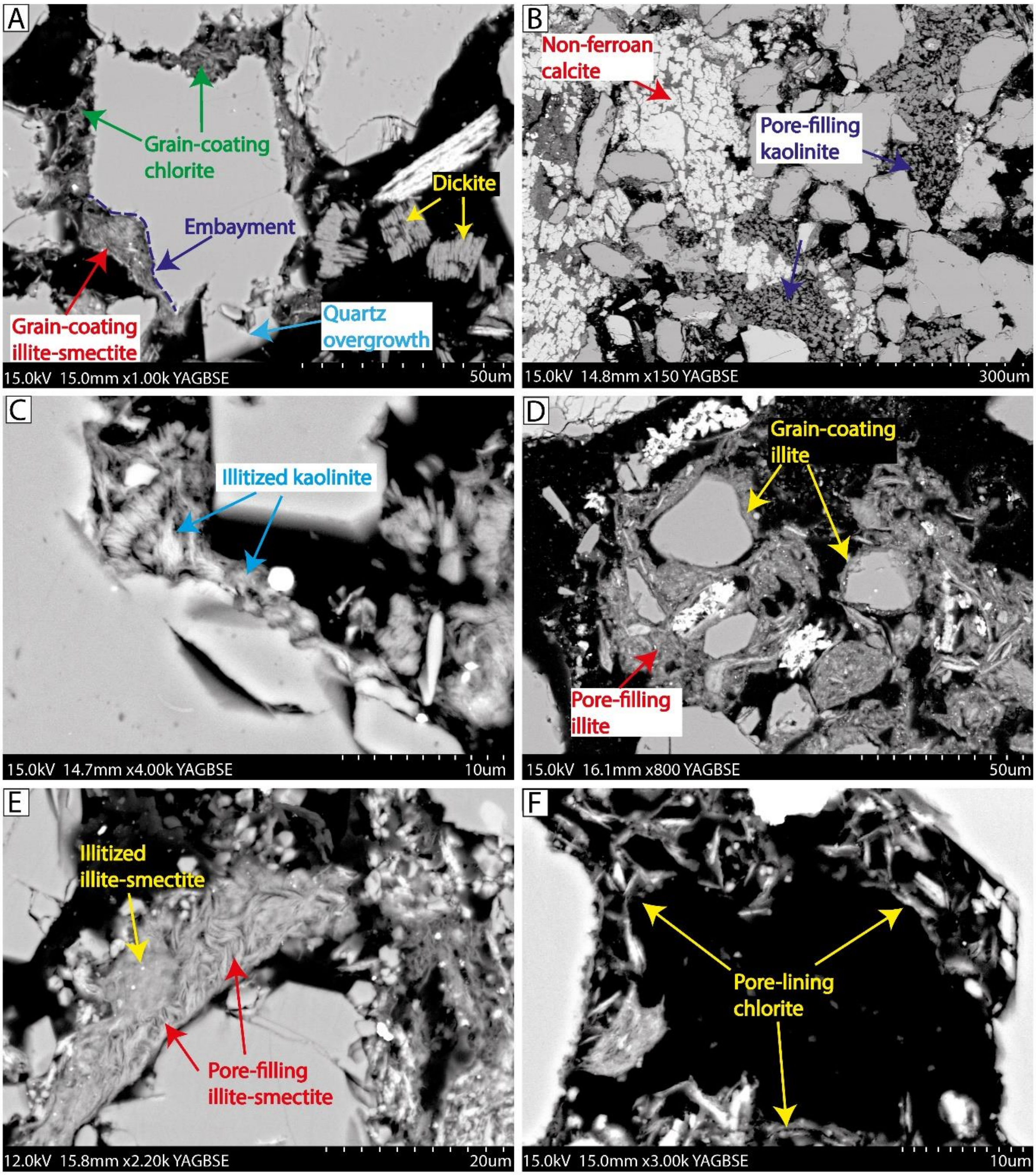

Figure 3.13. BSEM images showing examples of grain-coating, pore-filling, cement-replacing, pore-lining clays and carbonate cements in the studied Forties Sandstone Member. (A) BSEM image of grain-coating chlorite and illite-smectite preventing quartz cementation, and where the clays are absent, quartz cement develops. Everest field, well 22/14a-2, 2616 m TVDSS; (B) BSEM image of pore-filling kaolinite and calcite destroying intergranular macroporosity. Nelson field, well 22/11-6, 2206.45 m TVDSS; (C) BSEM image showing kaolinite being replaced by illite. Blane field, well 30/03a-1, 3096 m TVDSS; (D) BSEM image showing grain-coating and pore-filling illite cements. Nelson field, well 22/11-6, 2218.64 m TVDSS; (E) BSEM image showing illite-smectite being replaced by illite. Pierce field, well 23/27-5, 2733.75 m TVDSS; (F) BSEM image showing pore-lining chlorite. Everest field, well 22/14a-2, 2616 m TVDSS.

Authigenic kaolinite, which is identified by its vermicular or booklet form (Figure 3.13B), occurs as both grain-replacive and pore-filling cement. Vermicular kaolinite ranged in diameter from 2µm to 20 µm and the booklets ranged in length from 3µm to 22 µm. Grain-replacive kaolinite occurs as replacement of unstable, dissolved feldspar and mica grains, whereas pore-filling kaolinite precipitate adjacent to leached feldspar and mica grains (i.e. in open pores). Occasionally, the kaolinite transforms into illite (Figure 3.13C), or changes to its blocky, higher-temperature form (dickite) at depth (Figure 3.13A). Although the kaolinites have abundant microporosity, pore-filling kaolinites cause significant reduction in reservoir macroporosity (Figure 3.13B).

Authigenic illite occurs as fibrous and hair-like crystal aggregates. The illite present in the sandstones commonly occurs as grain-coating (2µm to 12 µm) (e.g., Figures 3.12F & 3.13D), pore-filling (Figure 3.13D), as replacement of kaolinite (Figure 3.13C) and dissolved feldspar and mica grains. The percentage of illite increases with burial depth probably because of the transformation of kaolinite to illite and illite-smectite to illite.

Mixed layer illite/smectite (I/S) mainly occur as pore-filling cement (2µm to 10 µm) (Figure 3.13E) and are commonly replaced by illite (Figure 3.13E). Percentages of I/S decrease with depth, possibly due to transformation to illite and/or chlorite.

Authigenic chlorite is observed as grain-coating (2µm to 10 µm) (e.g., Figure 3.13A), pore-lining (Figure 3.13F), pore-filling, and grain-replacive cement. In many samples, petrographic and SEM observations suggest that authigenic chlorite seems to have formed after the first phase of quartz cementation (e.g., Figure 3.12D), and that subsequent phase(s) of quartz overgrowths have been impeded by grain-coating chlorite or illite/illite-smectite. SEM observations shows that, where grain-coating chlorite/illite-smectite are absent on quartz grains, quartz overgrowths develop, thereby destroying porosity (e.g., Figure 3.13A). Pore-lining chlorite precipitated parallel to detrital grains (Figure 3.13F). Occasionally, thick, well-developed pore-lining chlorite transforms into pore-filing chlorite (Figure 3.13F).

3.6.5.3 Variation of clay minerals with depth

Plots of authigenic and detrital clays that are pore-filling (per total rock volume) vary significantly with depth (Figure 3.14A-D). Authigenic, pore-filling kaolinite content generally decreases with depth (Figure 3.14A), presumably due to its conversion to illite with increasing temperature. Conversely, authigenic, pore-filling illite increases with depth (Figure 3.14B), probably due to the conversion of kaolinite and smectite/illite-smectite to illite. Detrital, pore-filling illite-smectite increases and then decreases with depth (Figure 3.14C), probably due to decrease in energy of flows and its subsequent conversion to illite, respectively. Authigenic, pore-filling chlorite increases and then decreases with depth (Figure 3.14D), presumably because trioctahedral smectite has been exhausted and or dioctahedral smectite content, which forms illite, is higher in the sandstones.

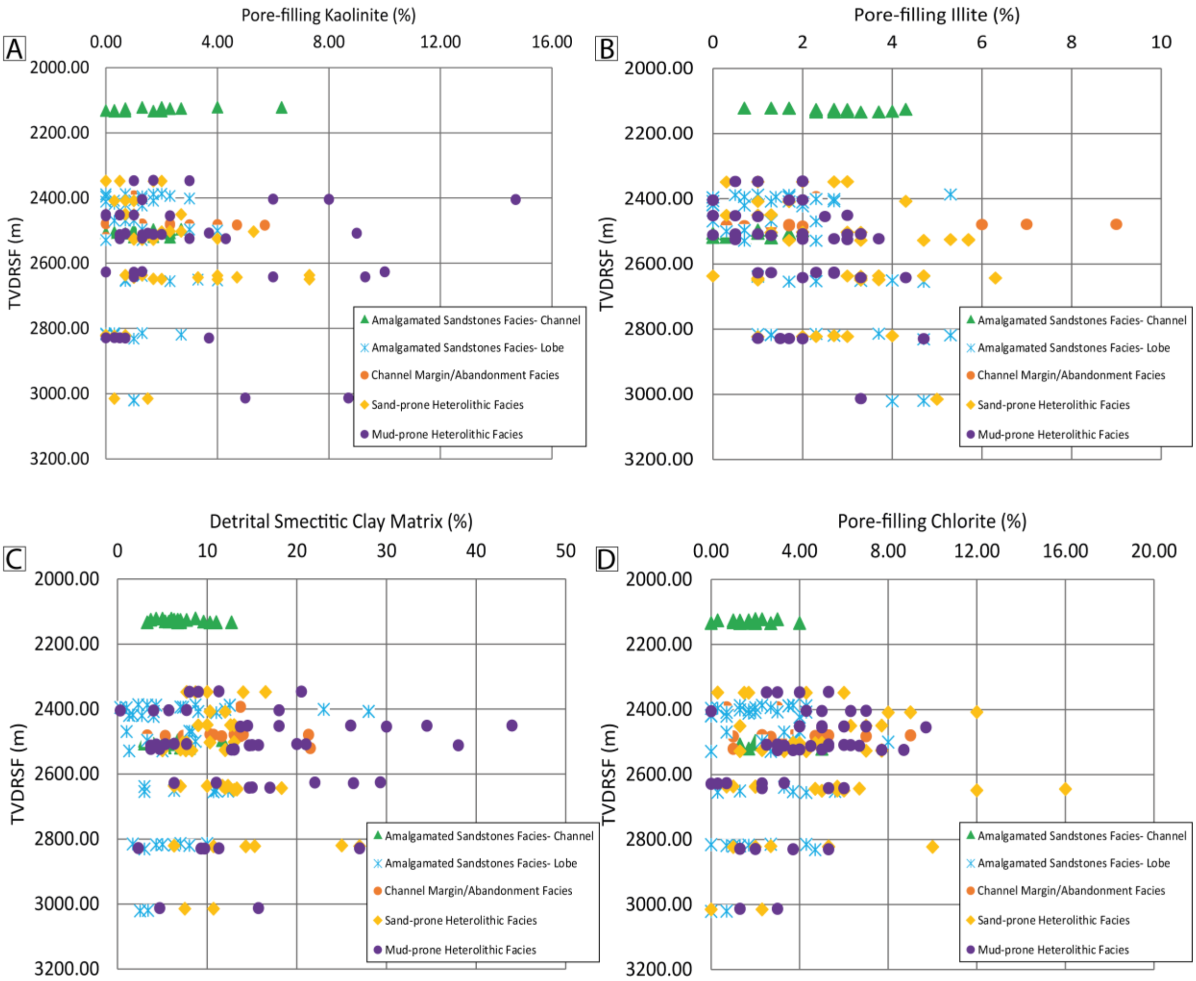

Figure 3.14. Variation in pore-filling clays with depth. (A) Plot of authigenic, pore-filling kaolinite against depth for proximal to distal fan facies. The kaolinite generally decreases with an increase in depth, probably due to its illitization (see Figure 3.13C); (B) Plot of pore-filling illite with depth showing an increase in illite content with depth, presumably due to illitization of kaolinite and smectite (see Figure 3.13C & E); (C) Plot of detrital smectitic clay matrix against depth, indicating an increase and then decrease in the matrix content with depth, probably due to its replacement by illite and chlorite; (D) Plot of authigenic, pore-filling chlorite against depth. However, the intergranular chlorite generally decreases with depth in the facies, probably because the illitization of smectite matrix occurs in preference to chloritization of smectite matrix. [TVDRSF = total vertical depth relative to sea floor].

3.6.5.4 Carbonate cements

Carbonate cements (mainly calcite and siderite) are the second most abundant cements in the studied sandstones. Pore-filling carbonate cements include non-ferroan calcite, ferroan calcite, siderite, and some dolomite.

Non-ferroan calcite occurs as patchy (Figure 3.15A) and as blocky, poikilotopic (Figure 3.12C) cement. The blocky calcite, which commonly occurs near mudstone-sandstone contacts, are early cements (due to floating grains) (Figure 3.12C) and commonly show evidence of pervasive dissolution, and the resulting porosity are either fairly connected and well-preserved or are completely filled by later ferroan calcite (Figure 3.15B).

Ferroan calcite occurs as patchy, pore-filling cement or as replacement of pervasively dissolved non-ferroan calcite and feldspar grains (Figure 3.15B). The cement commonly precipitates where non-ferroan calcite had dissolved, and also engulfs (thus postdates) quartz overgrowths.

Authigenic siderite commonly occurs in loosely packed sandstones as scattered rhombs (Figure 3.15C) and are commonly associated with dolomite and/or pyrite. Siderite is also found in the vicinity of dissolved mica grains, which probably serve as the principal source of Fe required for their formation (Mansurbeg et al., 2008). The cement commonly undergoes dissolution, with secondary intergranular porosity generation (Figure 3.15C), probably due to influx of acidic pore fluids.

Dolomite occurs as pore-filling cement and as replacement of dissolved, detrital mica grains, filling dissolution pores. They occur in close association with siderite and pyrite.

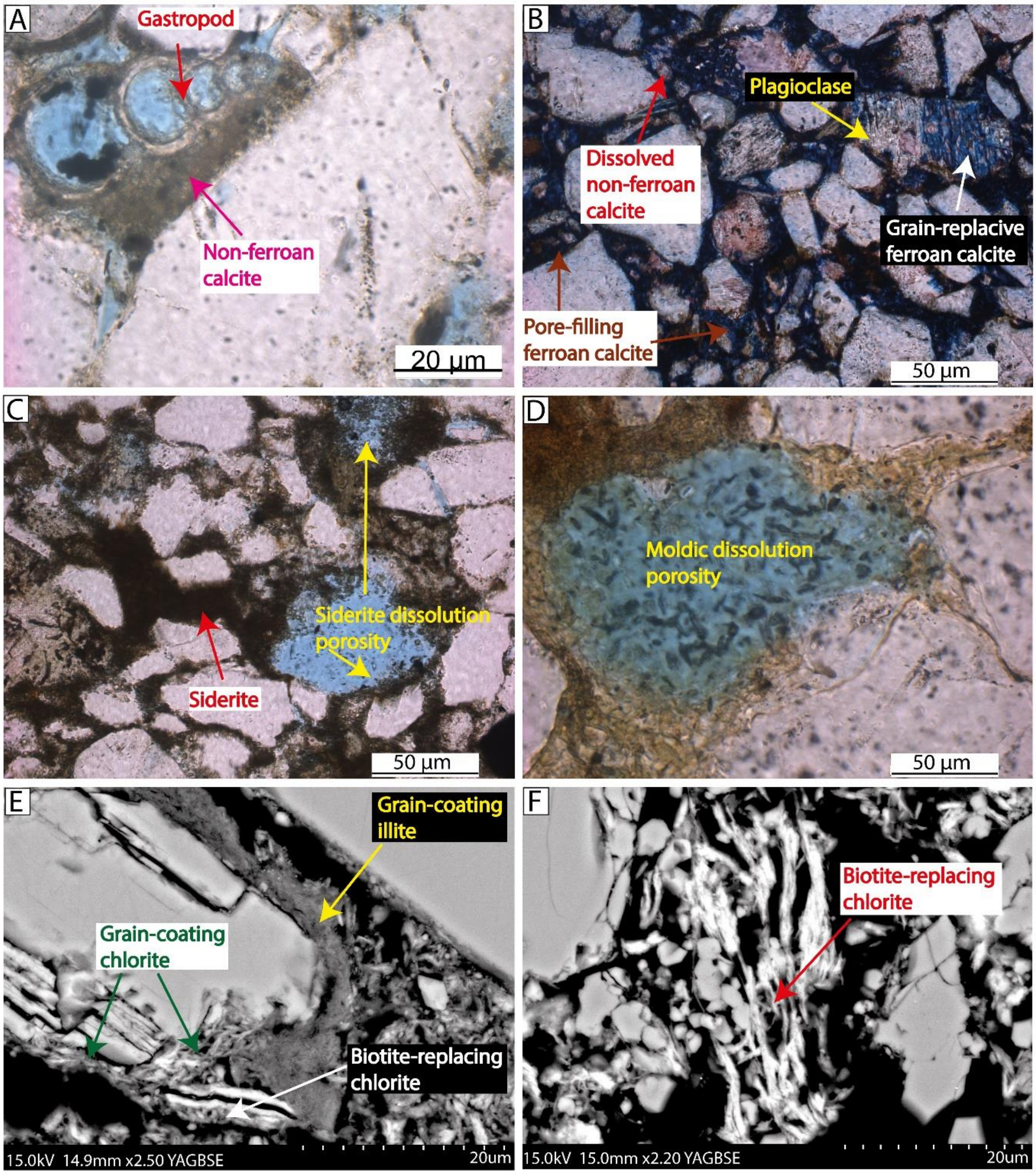

Figure 3.15. Dissolution, cementation, and mineral replacement. (A) Secondary intragranular porosity (blue) within dissolved gastropod chambers, and precipitation of patchy non-ferroan calcite adjacent to the gastropod shell. Everest field, well 22/10a-T6, 2476.5 m TVDSS; (B) Thin-section photomicrograph showing late ferroan calcite replacing dissolved plagioclase feldspar and non-ferroan calcite cement. Pierce field, well 23/27-8, 2479.55 m TVDSS; (C) Thin-section photomicrograph showing dissolved siderite cement, creating secondary intergranular porosity. Pierce field, well 23/27-6, 2900.48 m TVDSS; (D) Formation of moldic porosity due to feldspar dissolution. Pierce field, well 23/27-5, 2728.26 m TVDSS; (E) BSEM image of grain-coating chlorite and illite cements occurring on the same grain, indicating precipitation under similar diagenetic conditions. The image also shows the development of grain-coating illite into pore-filling illite. Pierce field, well 23/27-5, 2729.48 m TVDSS; (F) BSEM image showing chlorite replacing dissolved mica. Pierce field, well 23/27-5, 2733.75 m TVDSS.

3.6.5.5 Quartz cement

Quartz overgrowths occur as euhedral and syntaxial overgrowths around quartz grains (e.g., Figures 3.12D & 3.13A). In the sandstones, the quartz cements occur as partial to complete cover around detrital quartz grains, and either partially or pervasively fills primary intergranular porosity. Under petrographic light microscope, the boundary between a quartz overgrowth and a detrital quartz grain is usually delineated by dust rim (Figure 3.12D) or thin clay coatings. It has been observed that quartz overgrowths are more abundant or well developed in sandstones with clean quartz grain surfaces compared to those characterised by the presence of grain-coating clays.

3.6.5.6 Mineral dissolution

Dissolution of feldspars, mica, and carbonate cements has resulted in the formation of secondary porosity in most of the sandstones, notably in the amalgamated sandstones facies (Figure 3.12B). Analysed samples show partial to complete dissolution of K-feldspar and plagioclase grains, resulting in the formation of secondary intragranular porosity. In addition, the feldspars often undergo complete dissolution, forming moldic, open pores (Figure 3.15D). Authigenic chlorite, kaolinite, ferroan and non-ferroan calcites, illite, and pyrite have, in some samples, precipitated in feldspars and micas that had undergone partial and/or complete dissolution. Mica grains undergo dissolution to form both grain-coating (Figure 3.15E) and grain-replacive (Figure 3.15F) chlorite. Dissolution of carbonate bioclasts and cements is common and results in the development of open pores that are either well-preserved (e.g., Figure 3.15A & C) or later filled by late authigenic cements (such as ferroan calcite) (Figure 3.15B).

3.6.6 Clay-coating coverage

The percentage of grain-coating chlorite and illite/illite-smectite coverage on detrital quartz grains was measured on 50 randomly selected quartz grains in 50 Forties Sandstone samples, based on the established facies schemes. Average clay-coating coverage in the selected samples ranges from 18 to 61 %, averaging 38 %. Plots of average clay-coating coverage show positive correlation with both helium and optical porosity and permeability (Figure 3.16A & B), as well as good inverse correlation with the volume of quartz overgrowths (Figure 3.16C). Figure 3.16A indicates that optical, thin-section porosity has much better positive correlation with clay-coating coverage than helium porosity does. This is because the latter takes into account micro- and macro-porosity and fracture porosity, whereas the former considers macro, intergranular porosity alone. Sandstones with > 40 % clay-coating coverage retain higher porosity and permeability values (Figure 3.16A & B). Similarly, sandstone samples with > 40 % clay-coating coverage have low quartz cement volume (Figure 3.16C), which corresponds to clay-coat volume of up to 8 % (Figure 3.16D). A good, positive correlation, however, exists between clay-coating coverage and volume of grain-coating chlorite and illite/illite-smectite (Figure 3.16D).

Based on Figure 3.16C, there is seemingly lack of an excellent negative correlation between quartz cement volume and clay-coating coverage in some samples. From the plot, it has been observed that, while some samples have low quartz cements volume (< 2%) despite having low clay-coating coverage (< 40 %) (blue circle on the plot), others have relatively high quartz cement (≥ 6 %) despite having high clay-coating coverage (> 40 %) (purple circle on the plot). This is probably because in the former, the samples are characterized by high pore-filling clay matrix, which is also effective in preventing quartz cementation as it covers the surface area of grains (Porten et al., 2019; Shaw and Conybeare, 2003). In the latter samples, on the other hand, grain-coating clays have formed after the formation of quartz cement (e.g., Figure 3.12D); nonetheless, the clay coats would arrest further quartz cementation in such sandstones.

In general, the stronger correlation between clay-coating coverage and porosity and permeability (Figure 3.16A & B) may partly be due to the combination effect of depositional facies and primary depositional character and diagenesis are having on reservoir quality.

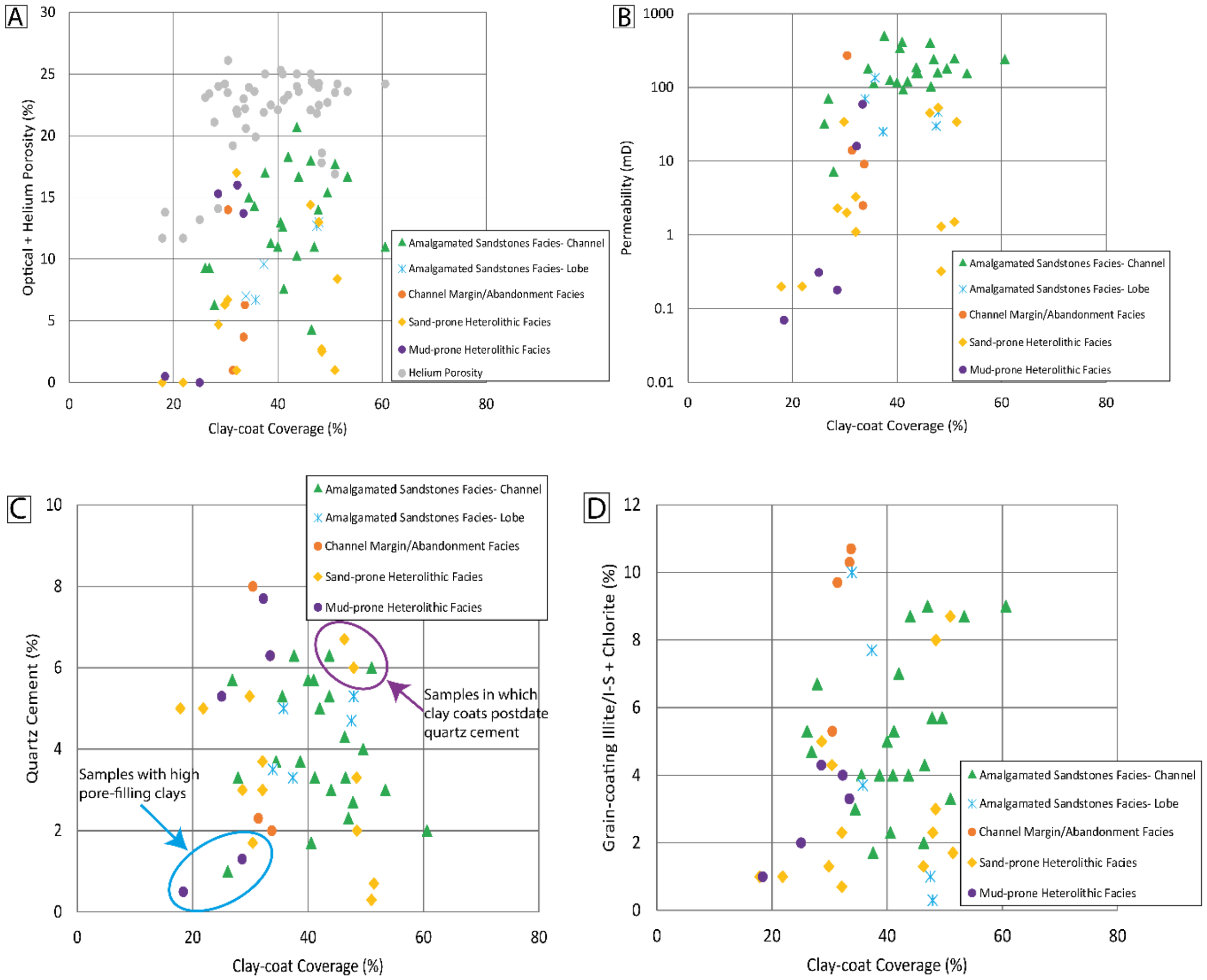

Figure 3.16. Role played by clay coat-coverage on porosity, permeability, quartz cement, and volume of grain-coating clays in the Forties Sandstone Member. (A) Plot of optical and helium porosity against clay-coating coverage showing a positive correlation. The higher the clay-coating coverage, the higher the porosity; (B) Plot of permeability against clay-coating coverage showing a positive correlation. Higher permeability values are recorded with increasing clay-coating coverage; (C) Plot of quartz cement against clay-coating coverage, indicating an inverse correlation. The plot suggests that clay-coating coverage >40 % is required to significantly arrest quartz cementation; (D) Plot of volume of grain-coating clays against clay-coating coverage showing a positive correlation. High clay-coating coverage largely correspond to high volume of grain-coating clays.

3.6.7 Carbonate cement geochemistry

Stable carbon and oxygen isotopes analysis was conducted on carbonate cements, which include ferroan and non-ferroan calcites, siderite, and dolomite. Results of the analysis are shown in Table 3.2. Carbon and oxygen isotopes values can be used to establish the sources of carbon for carbonate cements (Ma et al., 2017; Mao et al., 2019; Stewart, 1995). The δ ^{13}C values for the carbonate cements range from -21.12 ‰ to +9.48 ‰, averaging -7.04 ‰ (Table

3.2). This indicates a wide range of sources for carbon, which include organic and inorganic sources (Figure 3.17). A previous research has indicated a number of multiple sources of carbon for carbonate cements of the Paleocene to Early Eocene turbidite sandstones, Central North Sea (Stewart, 1995). These include meteoric flushing, bacterial sulphate reduction, dissolution of detrital carbonate shells, anaerobic hydrocarbon oxidation, thermal decarboxylation, and fermentation. Based on the carbon isotope values, non-ferroan calcites cements were sourced from mixed meteoric input and/or carbonate bioclasts (Figure 3.17), whereas ferroan calcite were mainly derived from thermal decarboxylation. The decarboxylation is presumably due to the influx of late acidic pore fluids in the sandstones, and is interpreted to have been influenced by proximity to heat-conducting salt diapirs and/or due to vertical transfer of fluid by leak-off from overpressured, deeply-buried Jurassic reservoirs through faults created by salt domes (Darby et al., 1996; Stewart, 1995; Stewart et al., 2000). The carbon isotope values for dolomite and siderite indicate that the cements might have been derived from fermentation and/or recrystallization of bioclastic carbonates (Figure 3.17).

Table 3.2. Stable carbon and oxygen isotopes data for carbonate cements.

Field/Well	**Depth (m)**	**Carbonate cement type**	**$\delta^{13}C$ VPDB**	**$\delta^{18}O$ VPDB**	**$\delta^{18}O$ SMOW (Calculated, ‰)**
Nelson/22/11-6	2206.45	Non-Ferroan Calcite	-8.66	-12.18	18.35
Nelson/22/11-6	2210.41	Non-Ferroan Calcite	-2.32	-6.54	24.16
Nelson/22/11-6	2211.02	Non-Ferroan Calcite	-3.98	-8.82	21.82
Nelson/22/11-6	2211.02	Non-Ferroan Calcite	-4.30	-8.96	21.68
Montrose/22/17-A12	2496.31	Non-Ferroan Calcite	-7.38	-11.94	18.60
Arran/23/16b-9	2710.28	Non-Ferroan Calcite	-4.12	-10.23	20.36

Everest/22/10a-4	2538.07	Non-Ferroan Calcite	-7.22	-13.27	17.23
Everest/22/10a-T6	2499.97	Non-Ferroan Calcite	-5.63	-13.55	16.94
Pierce/23/27-5	2726.74	Non-Ferroan Calcite	-2.47	-4.99	25.77
Pierce/23/27-5	2727.05	Non-Ferroan Calcite	-5.70	-9.07	21.56
Pierce/23/27-5	2727.05	Non-Ferroan Calcite	-5.66	-9.06	21.57
Pierce/23/27-8	2477.11	Non-Ferroan Calcite	-7.78	-12.09	18.45
Montrose/22/17-1	2510.33	Feroan Calcite	-19.04	-10.67	19.91
Montrose/22/17-1	2510.03	Feroan Calcite	-21.12	-8.62	22.02
Montrose/22/17-1	2508.05	Feroan Calcite	-20.45	-8.82	21.82
Arran/23/16b-9	2710.89	Feroan Calcite	-8.53	-13.10	17.41
Montrose/22/17-1	2508.5	Feroan Calcite	-20.40	-8.79	21.84
Pierce/23/27-8	2479.55	Siderite	9.48	-9.30	21.33
Everest/22/10a-4	2537.46	Siderite	0.26	-5.88	24.85
Everest/22/10a-4	2556.97	Dolomite	0.59	-6.25	24.46
Everest/22/14a-2	2620	Dolomite	-3.40	-5.99	24.73

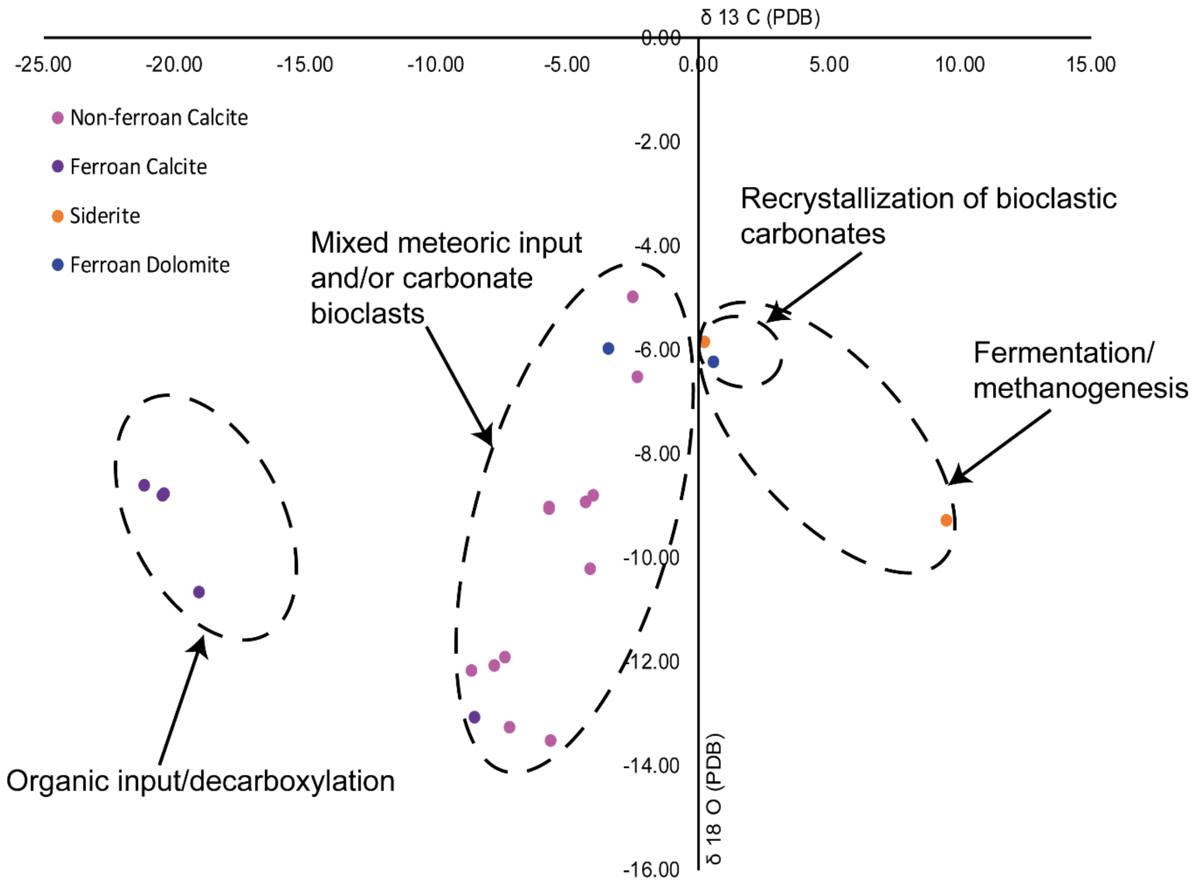

Figure 3.17. Scatterplot of delta ^{13}C carbon and delta ^{18}O oxygen isotopic compositions showing the various sources of carbon for precipitation of carbonate cements in the Forties Sandstone Member. The plot shows that mixed meteoric and carbonate bioclasts are the main sources of carbon for the cements.

3.7 Discussion

3.7.1 Impact of depositional processes on reservoir quality

Our study shows that depositional processes exert a key control on the distribution of sedimentary facies, grain size, and clay content, which result in spatial variation in reservoir quality of submarine fan deposits (Bell et al., 2018; Marchand et al., 2015; Porten et al., 2016; Stammer, 2014). The studied Forties Sandstone Member have porosity ranging from 1.9 to 28.4 % and permeability ranging from 0.01 to 500 mD (Figure 3.18A), which generally decrease with an increase in depth (Figure 3.18B & C). A multi-technique approach involving core description, measured petrophysical properties, and petrographic observations employed in this study has shown that the proximal fan, amalgamated sandstones channel facies have the best reservoir quality because of the larger grain size (Figures 3.18, 3.19A & B), lowest pore-filling clays (Figures 3.10A, 3.19C & D), lowest amount of ductiles (Figure 3.10B), the lowest total amount of cements (Figure 3.19E & F), which lead to higher porosities and permeabilities (Figure 3.18A). The distal fan, mud-prone heterolithic facies have the poorest reservoir quality due to the finer grain size (Figure 3.19A & B), highest pore-filling clays (Figures 3.10A, 3.19C & D), highest amount of ductiles (Figure 3.10B), and highest of total amount of cements (Figure 3.19E & F), which lead to lower porosities and permeabilities (Figure 3.18A). Total pore-filling clays between 10 and 30 % have a deleterious effect on reservoir quality, reducing porosities and permeabilities to generally < 10 % and < 1 mD, respectively (Figure 3.19C &D). Based on the porosity and permeability values stated above and some overlaps in the data points in Figure 3.18A, considerable reservoir heterogeneity exists even within the same depositional facies. The amalgamated sandstones facies of turbidite channel are the most homogeneous among the different turbidite zones, in which the sandstones have similar grain size, thickness, and net to gross. The sand- and mud-prone heterolithic facies, in contrast, have varying grain size, thickness, and net to gross, probably due to the impact of paleohighs on sediment gravity flows. Additionally, the reservoir heterogeneity is presumably due to variations in detrital compositions and diagenetic evolution pathways. The depositional facies are characterized by variations detrital smectitic clays matrix and authigenic kaolinite, which have abundant microporosity that contribute to helium porosity. Furthermore, the overlap in porosity and permeability values among the facies can be attributed to variations in intragranular and moldic pores which are isolated and contribute to total porosity but little (if any) to the sandstones permeability. However, generally, porosities and permeabilities decrease with increasing depths (Figure 3.18B & C).

Overall, the decrease in sandstones thickness (N:G) (Figure 3.1B), degree of sandstone amalgamation, and increase in clay content from proximal to distal fan (Figure 3.10A and 3.19C & D) show that the amalgamated sandstones facies have the highest connectivity and, hence, the best reservoir quality. The rapid decrease in grain size and increase in clay content from sand-prone heterolithic facies to mud-prone heterolithic facies (Figure 3.19A & B) result in the deterioration of reservoir quality, indicating that the mud-prone heterolithic facies are unlikely to form a significant/good quality hydrocarbon reservoir (Figure 3.19A & B) (Bell et al., 2018; Fildani et al., 2018).

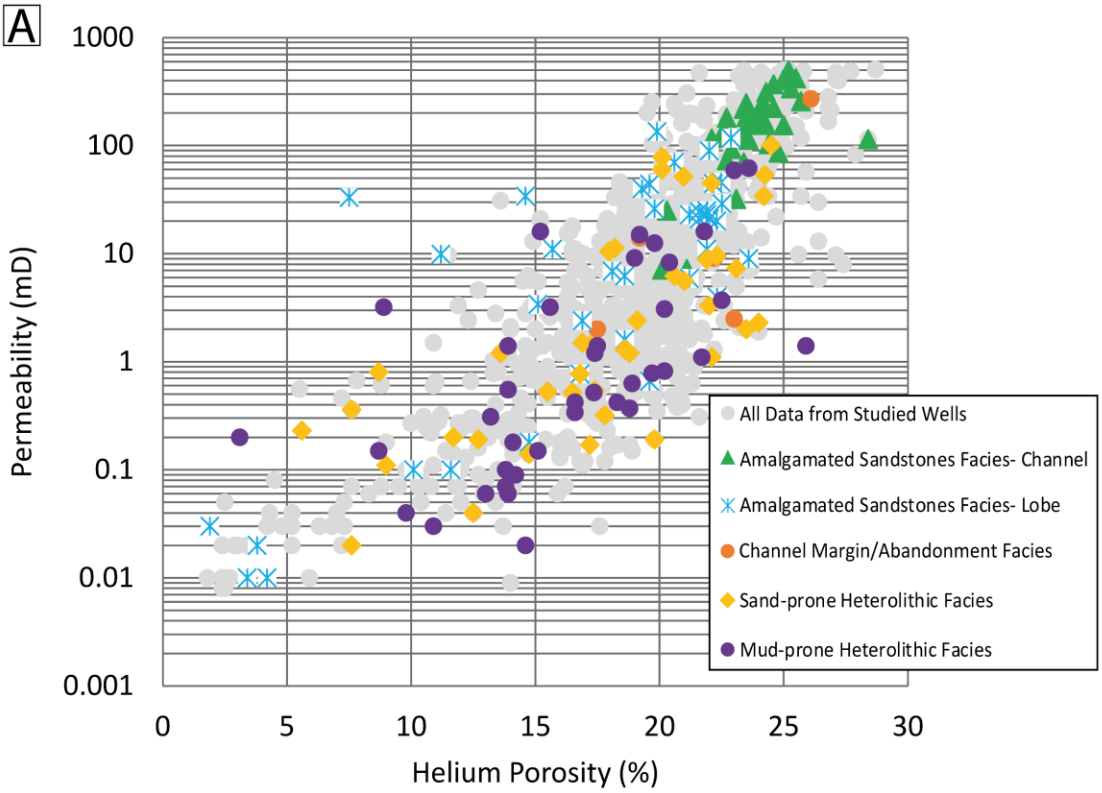
A
Permeability (mD)
1000
100
10
1
0.1
0.01
0.001
0
5
10
15
20
25
30
Helium Porosity (%)
All Data from Studied Wells
Amalgamated Sandstones Facies- Channel
Amalgamated Sandstones Facies- Lobe
Channel Margin/Abandonment Facies
Sand-prone Heterolithic Facies
Mud-prone Heterolithic Facies


B
Helium Porosity (%)
0
5
10
15
20
25
30
TVDRSF (m)
2000.00
2200.00
2400.00
2600.00
2800.00
3000.00
3200.00
All Data from Studied Wells
Amalgamated Sandstones Facies- Channel
Amalgamated Sandstones Facies- Lobe
Channel Margin/Abandonment Facies
Sand-prone Heterolithic Facies
Mud-prone Heterolithic Facies

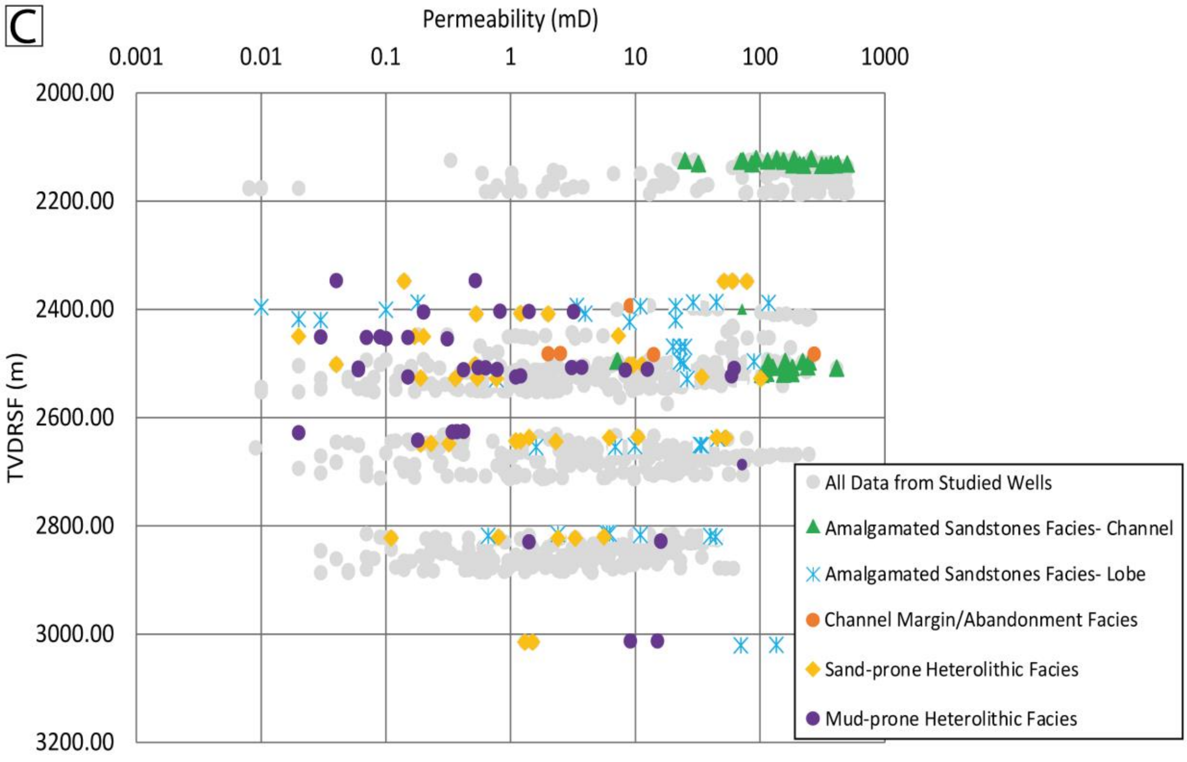

Figure 3.18. (A) Plot of core permeability against core porosity for the studied Forties sandstone reservoirs. The higher permeabilities in the 10 to > 100 mD range and porosities > 20 % are predominantly for the proximal amalgamated sandstones facies. This compares markedly to the sand-prone and mud-prone heterolithic facies where permeabilities can be > 0.1 mD and porosities frequently > 10 %. The overlaps in the data points is presumably due to variations in detrital smectitic clays matrix and authigenic kaolinite, which have abundant microporosity that contribute to helium porosity, and due to variations in intragranular and moldic pores, which are isolated and contribute to total porosity but little (if any) to the sandstones permeability. (B) Plot of helium porosity against depth, showing a general decrease in porosity with depth. (C) Plot of permeability against depth, showing a general decrease in permeability (by up to two orders of magnitude) with depth. This is due increase in pore-filling clays, total cements, and compaction from proximal to distal fan.

Sediments undergo textural and compositional segregation during transport in turbidity currents based on competency and capacity of flows, resulting in fan-scale spatial variations in reservoir quality (Kane et al., 2017; Kuenen and Sengupta, 1970; Marchand et al., 2015). An experimental study of turbidity currents by Stammer (2014) shows that particles are spatially fractionated based on grain density and grain shape, which result in large-scale spatial variations in the texture and composition of the deposits. During sediment transport from submarine channel to lobe axis and lobe off axis settings, coarser grain sediments fraction settle first at the base of high-density turbidity flows in the channel and lobe axis areas, whereas the finer-grained, less-dense fractions remain in the flows and are progressively deposited in the lobe off-axis depositional settings (Huang et al., 2020; Marchand et al., 2015). In this study, textural and petrographic data have indicated that turbidity flows have segregated particles by both grain size and composition (Figure 3.10A & B), and have had a significant impact on their reservoir quality. Ductile grains content, consisting of mica grains and mudclasts, are preferentially higher in lower-energy deposits of channel margin and lobe margin/fringe, and increase with decreasing grain size (Figure 3.10B) and enhance mechanical compaction. This is similar to the findings of the study of the Paleogene deep-water reservoirs of the US Gulf of Mexico (Marchand et al., 2015).

It has been observed that pore-filling detrital clay matrix have more deleterious impact on reservoir permeability than on porosity (Figure 3.19C & D). This is partly because pore-filling chlorite and illite, probably produced from the diagenetic alteration of mixed-layer detrital smectite, have abundant microporosity that make up the measured, helium porosity (Bahlis and de Ros, 2013). Consequently, this explains, in part, why porosity is relatively high despite the high pore-filling effect of the illite-smectite clay matrix in the heterolithic facies.

Therefore, the proximal to distal fan changes in original sediments as well as lithofacies associations identified from channel to lobe fringe areas in the Forties Fan system suggests a gradual transformation of turbidity currents from high-density, non-cohesive flows to low-density, cohesive/muddy debris flows. The flow transformation normally occurs at a transition zone in middle fan channel-lobe areas (Ito, 2008). As turbidity currents move downslope, they erode and incorporate muddy fines, leading to subsequent suppression of turbulence and the conversion of turbulent flows into laminar flows (Ito, 2008; Kane et al., 2017; Talling et al., 2012; Baker and Baas, 2020).

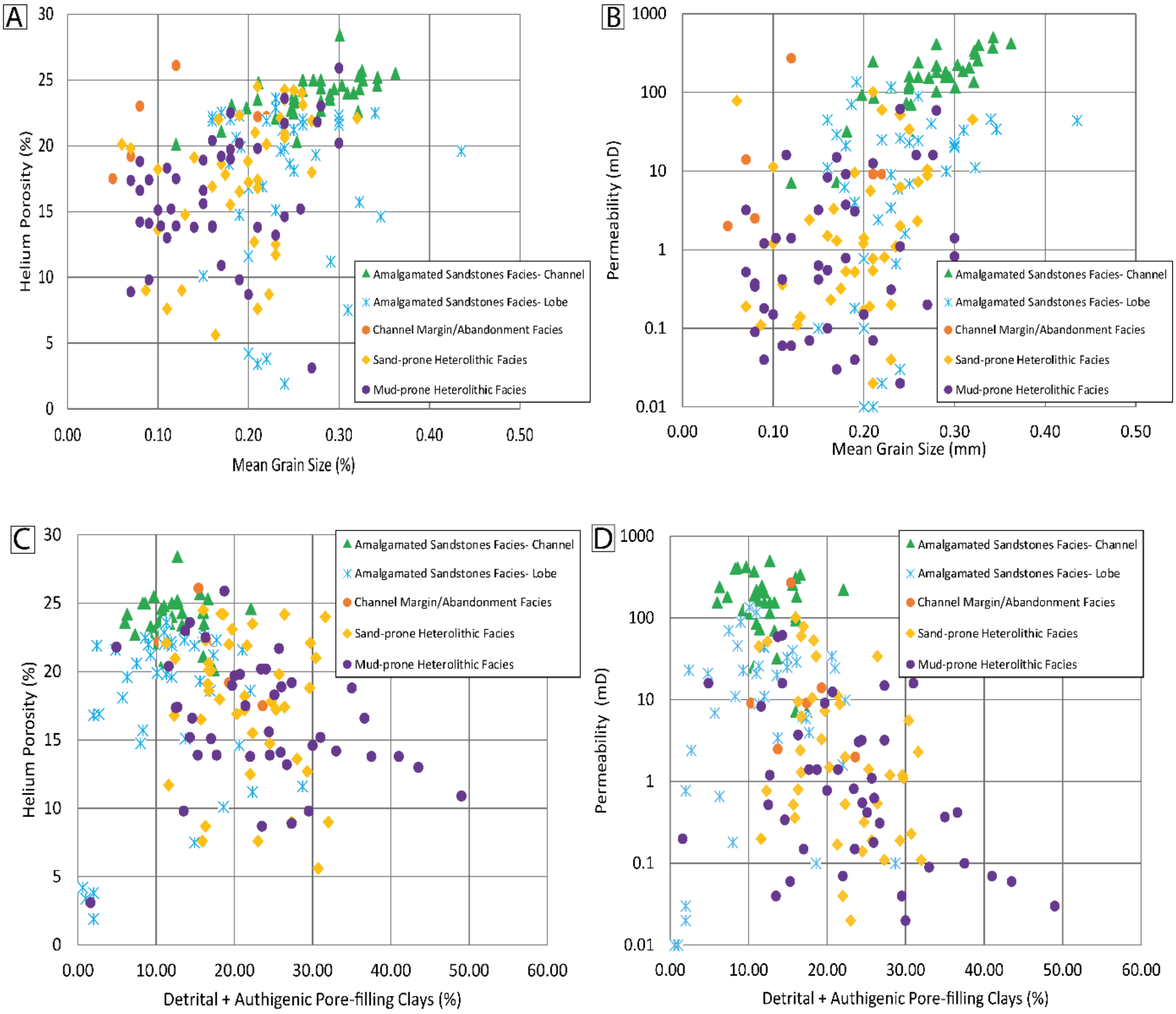
A
Helium Porosity (%)
30
25
20
15
10
5
0
0.00
0.10
0.20
0.30
0.40
0.50
Mean Grain Size (%)
Amalgamated Sandstones Facies- Channel
Amalgamated Sandstones Facies- Lobe
Channel Margin/Abandonment Facies
Sand-prone Heterolithic Facies
Mud-prone Heterolithic Facies
B
Permeability (mD)
1000
100
10
1
0.1
0.01
0.00
0.10
0.20
0.30
0.40
0.50
Mean Grain Size (mm)
Amalgamated Sandstones Facies- Channel
Amalgamated Sandstones Facies- Lobe
Channel Margin/Abandonment Facies
Sand-prone Heterolithic Facies
Mud-prone Heterolithic Facies
C
Helium Porosity (%)
30
25
20
15
10
5
0
0.00
10.00
20.00
30.00
40.00
50.00
60.00
Detrital + Authigenic Pore-filling Clays (%)
Amalgamated Sandstones Facies- Channel
Amalgamated Sandstones Facies- Lobe
Channel Margin/Abandonment Facies
Sand-prone Heterolithic Facies
Mud-prone Heterolithic Facies
D
Permeability (mD)
1000
100
10
1
0.1
0.01
0.00
10.00
20.00
30.00
40.00
50.00
60.00
Detrital + Authigenic Pore-filling Clays (%)
Amalgamated Sandstones Facies- Channel
Amalgamated Sandstones Facies- Lobe
Channel Margin/Abandonment Facies
Sand-prone Heterolithic Facies
Mud-prone Heterolithic Facies

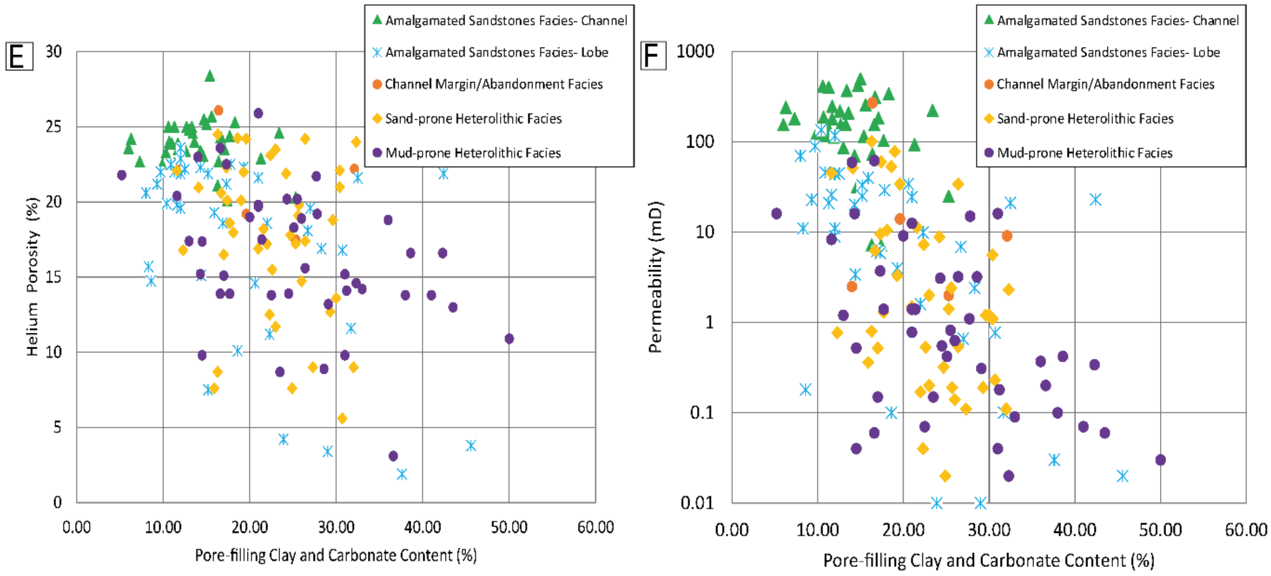

Figure 3.19. Impact of grain size, clay content, and total cements on reservoir properties of the Forties Sandstone Member. (A) Plot of core porosity against mean grain size. Porosity increases with increasing grain size; (B) Plot of core permeability against mean grain size. Reservoir permeability increases with increasing grain size; (C) Plot of helium porosity against pore-filling detrital and authigenic clays. High pore-filling clays lower porosity, but they have more deleterious effect on permeability; (D) Plot of core permeability against pore-filling detrital and authigenic clays. Permeability is significantly lowered with increasing pore-filling clays; (E) Plot of helium porosity against total pore-filling clays and carbonate cements. The higher the cements, the lower the porosity; (F) Plot of core permeability against total pore-filling clays and carbonate cements. Permeability significantly decreases with increasing total clays and carbonate cements.

3.7.2 Role of provenance, depositional processes, and diagenetic alterations on grain-coating clays and coats coverage

The Forties Sandstone is interpreted to have been sourced from the basement and Triassic sandstones to the NW (Kilhams et al., 2014), and their quartz/feldspar-rich compositions make them mechanically stable but chemically unstable during burial diagenesis. While the detrital quartz grains make the sandstones mechanically stable and resistant to compaction, the detrital feldspars are chemically unstable and, thus, are susceptible to dissolution and kaolinitization, which might enhance and destroy reservoir quality, respectively. Additionally, the lack of abundant lithic and carbonate fragments in the sandstones has enhanced their mechanical stability during compaction. Furthermore, during their residence time on the shelf, the sandstones might have developed clay coatings, which have undergone less intense abrasion because of their close proximity to the shelf, typical of sand-rich fans.

Clay-coating coverage in the studied Forties Sandstone Member has been observed to vary with depositional facies, which in turn are controlled by depositional environments. Amalgamated sandstones facies (channel) have an average clay-coating coverage that ranges from 26 to 61 %; amalgamated sandstones facies (proximal lobe) from 34 to 48 %; channel margin/abandonment facies from 30 to 34 %; sand-prone heterolithic facies from 18 to 51; and mud-prone heterolithic facies from 18 to 33; %. However, with the exception of the mud-prone heterolithic facies, which have grain-coating clay volume ranging from 1 to 4 %, the other facies have similar total volume of grain-coating chlorite and illite/illite smectite, ranging from 0.3 to 10.7 %.

The occurrence of grain-coating clays in deep-water sandstones can be linked to provenance, depositional processes, and diagenetic processes (Bahlis and de Ros, 2013; Porten et al., 2019; Yezerski and Shumaker, 2018). Depositional and diagenetic processes can significantly influence the amount of clay-coating coverage on detrital grains in deep-water turbidite sandstones. Sand grains can develop precursor clay coats in continental, transitional or shallow marine/shelf environments before being transported to deep-water environments (Bahlis and de Ros, 2013; Yezerski and Shumaker, 2018). These precursor clay coats can be partially or pervasively abraded during transport to deep-water environments. The convex surfaces of such grains with inherited clay coats, therefore, are characterized by discontinuous clay coats, probably due to abrasion (Figure 3.12E & F). The concave parts of the grains, on the other hand, which are called as embayments or indentations, may preserve precursor clay coats because they are less likely to be abraded during transport (Bahlis and de Ros, 2013) (Figure 3.12E & F). Thus, deep-water depositional environments like submarine channels and proximal lobes, which are not far from the shelf edge, could potentially have more sand grains with inherited clay coats (e.g., Figures 3.12E & F and 3.13A) than the ones deposited further in distal fan settings.

Furthermore, grain-coating clays are emplaced in sediments of deep-water channels and proximal lobes (Houseknecht and Ross, 1992; Porten et al., 2019), and occasionally in lobe axis sediments (Collins et al., 2015) during sediment dewatering (e.g., Figure 3.4B). Sediments deposition in subaqueous environments are characterized by fluid trapping within intergranular pore space, and the fluids are expelled during sediment consolidation, impacting variably on grain fabric (Porten et al., 2019). Grain size and clay matrix content significantly control fluid flow through porous sands (Fraser, 1935), and fluids move faster in sands with coarser grain size and less clay content than in finer-grained, clay-rich sands. This implies that sands with coarser grain size and higher permeability are more likely to have more grain-coating clays emplaced through dewatering under favourable conditions than finer-grained, low-permeability sands. Consequently, characterized by inherited clay coats and coats emplaced during dewatering, the amalgamated sandstones facies have the highest clay-coating coverage in the studied sandstones. In addition, the observed illitization of kaolinites (Figure 3.13C) in this facies might have also contributed to higher clay-coating coverage.

In the channel margin/abandonment facies, the relatively low clay-coating coverage is due to the abundant pore-filling detrital clay matrix, which covers surface area of grains and destroy porosity. In this facies, although there is presence of inherited grain-coating clays, they are less abundant compared to the preceding facies. This is probably due to the position of the facies with respect to channel axis, in which the sand grains might have been abraded.

Two main possible sources of grain-coating clays have been observed in sand-prone heterolithic facies association: sediment dewatering and alteration of biotite grains (e.g., Figure 3.15E). Like in the amalgamated sandstones facies association, sediment dewatering features in form of vertical to sub-vertical pillars occur in the sand-prone heterolithic facies, although they are scattered and less abundant. Additionally, partial to pervasive alterations of detrital biotite grains have contributed to the formation of grain-coating chlorite (e.g., Figure 3.15E). The fractionation and segregation by turbidity flows based on grain density and composition during flows might have led to a relative increase in detrital mica content in this facies association in comparison to amalgamated sandstone facies association (Figure 3.10B). With the increase in burial temperature from proximal to distal fan (Figure 3.3A & B), the alteration of mica (biotite) to form chlorite (Figure 3.15F) is likely to occur if there is a source of acidic pore fluid to enhance dissolution/alteration.

The mud-prone heterolithic facies association have the least clay-coating coverage, which ranges from 18 to 33 %. The absence of sediment dewatering features as well as paucity of inherited, precursor coats in this facies association might have contributed to the observed low clay-coating coverage. Alteration of biotite grains, nonetheless, might have contributed to the formation of grain-coating clays. In addition, the observed sand injection features (Figure 3.4G) in the mud-prone heterolithic facies indicate communication between sandy and muddy beds and, thus, pore-fluid exchange between the sandy and muddy layers. Consequently, dissolved ingredients required for the formation of grain-coating clays could be transported from the muddy to sandy layers. The interbedded mudstones, however, could act as baffles (where thin) and barriers (where thick) to sandstones.

3.7.3 Implications of clay coats on reservoir quality

The main grain-coating clays, consisting of chlorite, illite, and illite-smectite, identified in this study suggest detrital origin, which were emplaced during sediment dewatering and those that might have been inherited from continental, transitional or shallow marine/shelf environments. Petrographic evidence suggests that the clay coats were originally from smectites, which, depending on the smectite compositions, were transformed to chlorite and illite (e.g., Figure 3.13E), often via a mixed-layer illite-smectite or chlorite-smectite. Furthermore, detrital clay coats have been reported to serve as potential precursors to authigenic clay coats in several deeply-buried sandstone reservoirs (Ajdukiewicz and Larese, 2012; Bloch et al., 2002; Worden and Morad, 2003). The inherited, precursor clay coats might be discontinuous at the time of sediment deposition due to the impact of abrasion during transport (Yezerski and Shumaker, 2018); however, an experimental study by Aagaard et al. (2000) replicating burial diagenesis shows that discontinuous detrital-clay coats develop into complete authigenic-clay coats. In addition, sands with discontinuous clay coats would require a minor clay volume of 1 to 2 % of the rock volume to transform and coat significant surface area of sand with clays that are capable of inhibiting quartz cementation in deeply buried reservoirs (Bloch et al., 2002). Therefore, discontinuous, inherited or dewatering-emplaced clay coats on deep-water sand grains could potentially transform into complete coats at deeper burial, thereby inhibiting the development of quartz cements and, hence, preserving reservoir quality.

Being able to understand and accurately predict quartz cementation is crucially important for pre-drill porosity prediction in quartz-rich sandstones that have undergone deep-burial, high-temperature diagenesis (Bukar, 2013; Porten et al., 2019). The amount of quartz cement formed in sandstones is determined by the temperature history of the sandstone, the amount of nucleation surface area available for quartz cementation, and the presence of dissolved silica in the sandstone (Walderhaug, 1994, 2000; Walderhaug, 1996; Walderhaug and BjØrkum, 2003).

Quartz cementation rate in sandstones increases exponentially with increasing temperature, resulting in a significant decrease in porosity at a given depth in a basin characterized by a higher heat flow (Walderhaug, 1996). This implies that quartz-rich sandstones in basins with high present or past heat flows are more prone to quartz cementation. Burial and temperature history plots for the Nelson field (proximal fan; Figure 3.3A) and Blane field (distal fan; Figure 3.3B) indicate that, while the former attained a temperature of 120 ˚C during the Late Miocene to present, the latter attained a temperature of 130 °C during the same period, indicating that the Forties Sandstone Member in both wells is in the quartz cementation domain. However, the observed low volume of quartz cements in both wells (max 6.3 % of rock volume) could be attributed to the relatively shallow burial depths, short residence times in the quartz cementation domains, or the moderately good clay-coating coverage. The observed dissolution of feldspars and the evidence of the conversion of smectite to illite/chlorite, which are thought to supply silica as by-products (Worden and Morad, 2003), indicate the likely presence of silica in the system, but has been relatively inhibited from precipitating as quartz cements by the good clay-coating coverage.

Our study demonstrates that clay-coating coverage of 40 to 50 % on detrital grain surfaces might be sufficient to preserve reservoir quality and inhibit quartz cementation at the present-day burial depth of Forties Sandstone Member (Figure 3.16C), which corresponds to grain-coating clays volume of up to 8 % (Figure 3.16D). Furthermore, Figure 3.16C shows that the relatively low clay-coating coverage and yet low quartz cement volume observed in some samples is probably due to the impact of pore-filling clays, which are also effective in arresting quartz cementation. Therefore, this partly explains the relatively low quartz cement in the distal fan facies despite the relatively deeper burial, higher temperature and smaller grain size. Additionally, it has been observed that sandstones with moderately good clay-coating coverage of up to 50 % have high porosity and permeability (Figure 3.16A & B), and samples with low percentage of clay-coating coverage have low porosity and permeability.

3.7.4 Implications for proximal to distal fields

The proximal-fan, updip areas, primarily consisting of Nelson-Montrose fields (Figure 1A) and represented by amalgamated sandstones facies association, have the highest degree of channelization, reservoir thickness (Figures 3.1B & 3.5A), net to gross (65 % in Nelson field)(Hempton et al., 2005), sand bed thickness (Figures 3.1B & 3.5A), larger grain size (Figures 3.10A and 3.19A & B), higher permeabilities (Figure 3.18A), and lowest pore-filling clays (Figures 3.10A and 3.19C & D), implying that they have the best reservoir quality. The distal-fan, downdip areas, mainly consisting of Arran, Pierce, and Blane fields (Figure 1A) and represented by heterolithic facies, are characterized by the lowest degree of channelization (comprising lobe and sheet sands), reservoir thickness, net to gross (58 % in Pierce field) (Hempton et al., 2005), sand bed thickness (Figures 3.1B and 3.5B & C), smaller grain size (Figures 3.10A and 3.19A & B), lower permeabilities (Figure 3.18A), and pore-filling clays

(Figures 3.10A and 3.19C & D), suggesting poorer reservoir quality. In addition to having excellent primary depositional factors like larger grain size, lack of fines, and presence of sand amalgamation, the amalgamated sandstones have the best reservoir quality because they are buried shallower than the mud-prone heterolithic facies (Figure 3.18B & C), which have finer grain size, higher amount of fines, and lack sand amalgamation. Although the down-dip areas are generally characterized by lower net to gross due to the predominance lobe and sheet deposits, the overlapping of lobes and sheets deposits has been interpreted to have enhanced reservoir connectivity in the sandstones (Hempton et al., 2005). However, because the deposits of the down-dip areas are strongly influenced by salt-induced highs (e.g., Collins et al., 2015; Hempton et al., 2005; Jones et al., 2015), the instability created due to salts diapirism resulted in mixing and generation of slumps, debrites, and sand injections facies (e.g., Figure 3.5C), developing baffles to fluid flow in the reservoirs (e.g., Figures 3.1B & 3.5C).

The combined impact of paleotopographic highs and salt diapirs has affected the depositional architecture, depositional facies, diagenesis and reservoir quality of the Forties Sandstone Member (Hempton et al., 2005; Scott et al., 2010). The Forties Sandstone Member is said to have been deposited in the lows between paleotopographic highs of Lista Formation, forming extensive channels that often extend to the margins of the fan (e.g., Den Hartog Jager et al., 1993; Kessler et al., 1980; Scott et al., 2010) (Figure 3.20A). In the Pierce Field area, for instance, the relief created on underlying mass transport deposits and that generated by rising salt diapirs, which pierce through the Paleocene deposits, cause flows to speed up and lead to the creation and infilling of channels (Figure 3.20B), with deposition of coarser material in an otherwise overall distal part of the fan. (Eldrett et al., 2015; Scott et al., 2010). These channels formed high-density turbidity currents deposits, and served as conduits for meteoric water transport from proximal to distal fan settings. This is corroborated by the presence of kaolinite in medial to distal fan deposits (Figure 3.14A), suggesting that meteoric flushing might have caused feldspar dissolution and the subsequent formation of kaolinite. Furthermore, the channel deposits could have grain-coating clays emplaced due to sediment dewatering, resulting in the formation of clay coats that would impede quartz cementation. In the lobe-dominated settings, however, where sediment gravity flows become unrestricted and where the rising diapirs are not high enough to pierce through the reservoirs, the resultant turbidite beds thin, widen, and dome-up over the diapir, with increasing shale interbeds and argillaceous sandstones and mudstones (Figure 3.20C) (Eldrett et al., 2015). The shale interbeds and mudstones can act as baffles and barriers to fluid flow (Figure 3.20C), resulting in vertical compartmentalization of the reservoirs. In addition, the movement of salt diapirs has been reported lead to ponding and confinement sediments in salt withdrawal areas (e.g., Pierce field) (Scott et al., 2010), and the associated muddier and slump deposits could also act as baffles and barriers to fluid flow.

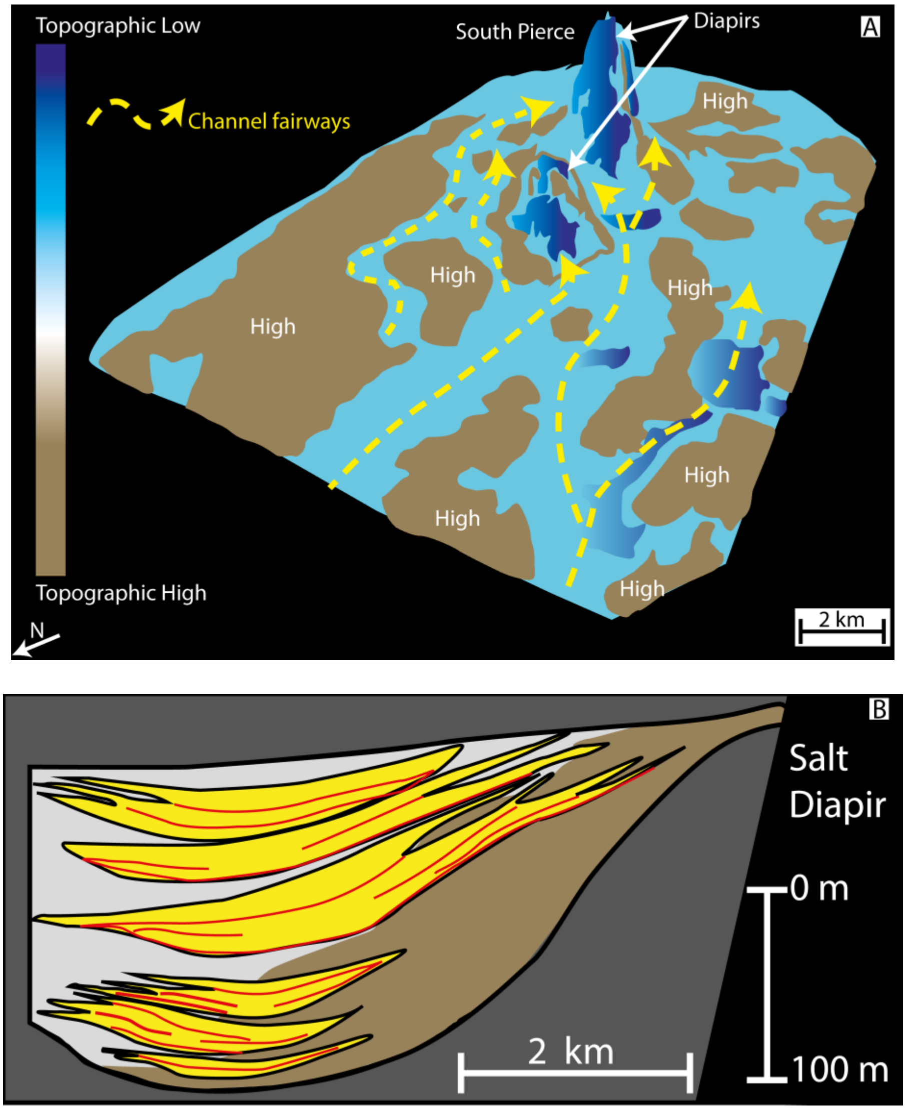

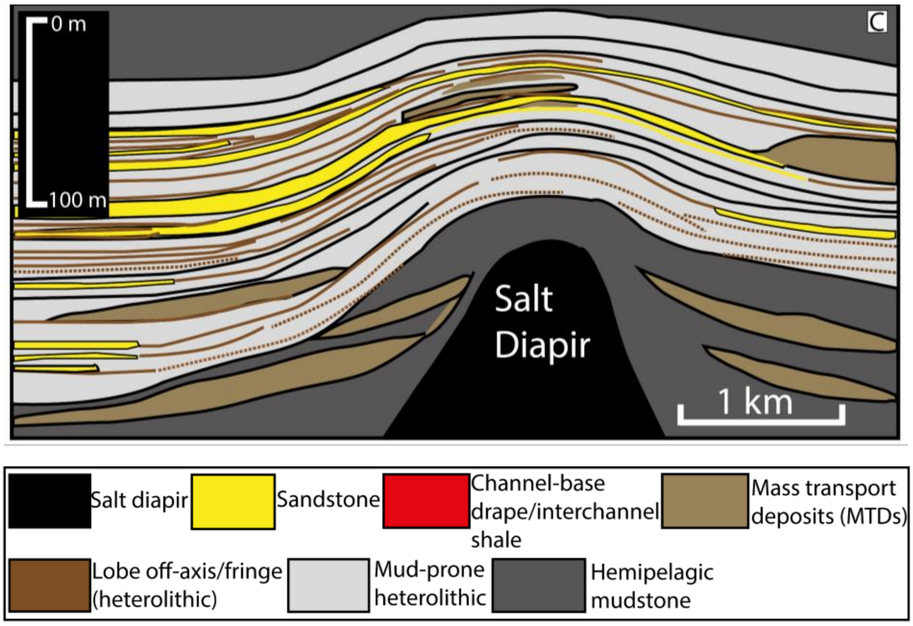

Figure 3.20. (A) The Forties Sandstone Member isochrones on a 3D representation of the Lower Forties (T65) showing areas of paleotopographic highs and sediment fairways through the Pierce area (modified from Scott et al. 2010). (B) Conceptual model of sandbody architecture of the Forties reservoirs in channel-dominated areas of salt diapirs (modified after Eldrett et al. 2015). (C) Conceptual model of sandbody architecture of the Forties reservoirs in lobe-dominated areas of salt diapirs.

3.7.5 Diagenetic and reservoir quality evolution

Diagenetic and reservoir quality in the Forties Sandstone Member is controlled by depositional facies. Figure 3.21 shows schematic model summarizing the various diagenetic processes and products in the Forties Sandstone Member. The diagenetic alterations have been identified based on shallow (eodiagenesis, which occur at temperatures < 70 ˚C) and deep-burial (mesodiagenesis, which occur at temperatures < 70 ˚C) environments (Morad et al., 2010). They include: (1) mechanical compaction, which of consists of grain rearrangement, fracturing and formation of pseudomatrix, which started during shallow burial and continued into deep burial. (2) early dissolution and kaolinitization of feldspar, mica, and mudclasts during shallow burial, which block pore throat and lower permeability. The kaolinite is commonly replaced by illite (Figure 3.13C), and transformation of kaolinite is said to occur at a temperature of 120 ˚C (Bjørlykke et al., 1995; Worden and Morad, 2003) in the presence of K^+, commonly from dissolved K-feldspar. The percentage of kaolinite decreases with depth (Figure 3.14A), probably due to its illitization, leading to an increase in illite content with depth (Figure 3.14B). Based on the burial history plot (Figure 3.3), although the proximal fan area has entered the temperature window (120 °C) for illitization of kaolinite (Figure 3.3A), the illitization of kaolinite might be higher in the distal fan area probably due to longer residence time and higher temperature (130 °C) (Figure 3.3B), and this might have contributed to higher illite content in medial to distal fan facies (Figure 3.14B). (3) formation of detrital, grain-coating smectites, which are inherited from shelf/continental environments and/or emplaced during dewatering, seem to have retarded quartz cementation (Figure 3.16C). These smectitic clay coats undergo transformation to form chlorite, illite, and illite-smectite during burial diagenesis (Figure 3.20). Grain-coating chlorite was formed after the first phase of quartz cementation, but has impeded the subsequent phase(s) of quartz overgrowths in the sandstones (Figure 3.21). In addition, detrital, pore-filling smectitic clays are replaced by illite (e.g., Figure 3.13E) and chlorite, which result in the decrease in detrital smectitic matrix with depth (Figure 3.14C) and increase in intergranular illite (Figure 3.14B) and an initial increase then decrease in intergranular chlorite content (Figure 3.14D). (4) Precipitation of carbonate cement, which consists of non-ferroan calcite, siderite, and dolomite, reduces reservoir quality, causing reservoir heterogeneity in the sandstones. The early carbonate cements occur mainly as intergranular pore-filling cements, and their dissolution creates secondary intergranular porosity, which is readily available for the precipitation of late carbonate cement (e.g., late ferroan calcite; Figure 3.15B). Additionally, the remnants of the dissolved non-ferroan calcite provides Ca required for the precipitation of the late ferroan calcite (e.g., Figure 3.15B). The origin of the late acidic pore fluids that led to the dissolution of early carbonate cements and the precipitation of the late ferroan calcite in the Paleocene deep-water sandstones of the Central North Sea can be attributed to decarboxylation (Stewart, 1995; Stewart et al., 2000), which is associated with the maturation of organic source rocks (Hendry et al., 2000; Ma et al., 2016). Results of the stable isotope analysis for carbon (-20 to -19 PDB; Figure 3.17) corroborate the decarboxylation origin of the late ferroan calcite in the sandstones. The decarboxylation has been interpreted to be influenced by proximity to heat-conducting salt diapirs and/or due to vertical transfer of fluid by leak-off from overpressured, deeply-buried Jurassic reservoirs through faults created by salt domes (Darby et al., 1996; Stewart, 1995; Stewart et al., 2000). Although the early, well-developed carbonate cements destroy intergranular porosity and arrest mechanical compaction in the Forties sandstones (e.g., Figure 3.12C), their dissolution can significantly enhance secondary intergranular porosity (e.g. Figure 3.15C), thereby improving reservoir quality, especially if they are not filled by late ferroan calcite. (5) Dissolution of feldspar, mica, rock fragments, and carbonate cements has considerably enhanced porosity and permeability of the sandstones. While the dissolution of unstable grains is often accompanied by the precipitation of pore-filling kaolinite and chlorite thereby reducing reservoir quality, grain-coating chlorite (and illite/illite-smectite) have impeded quartz cementation and enhanced reservoir quality in the sandstones.

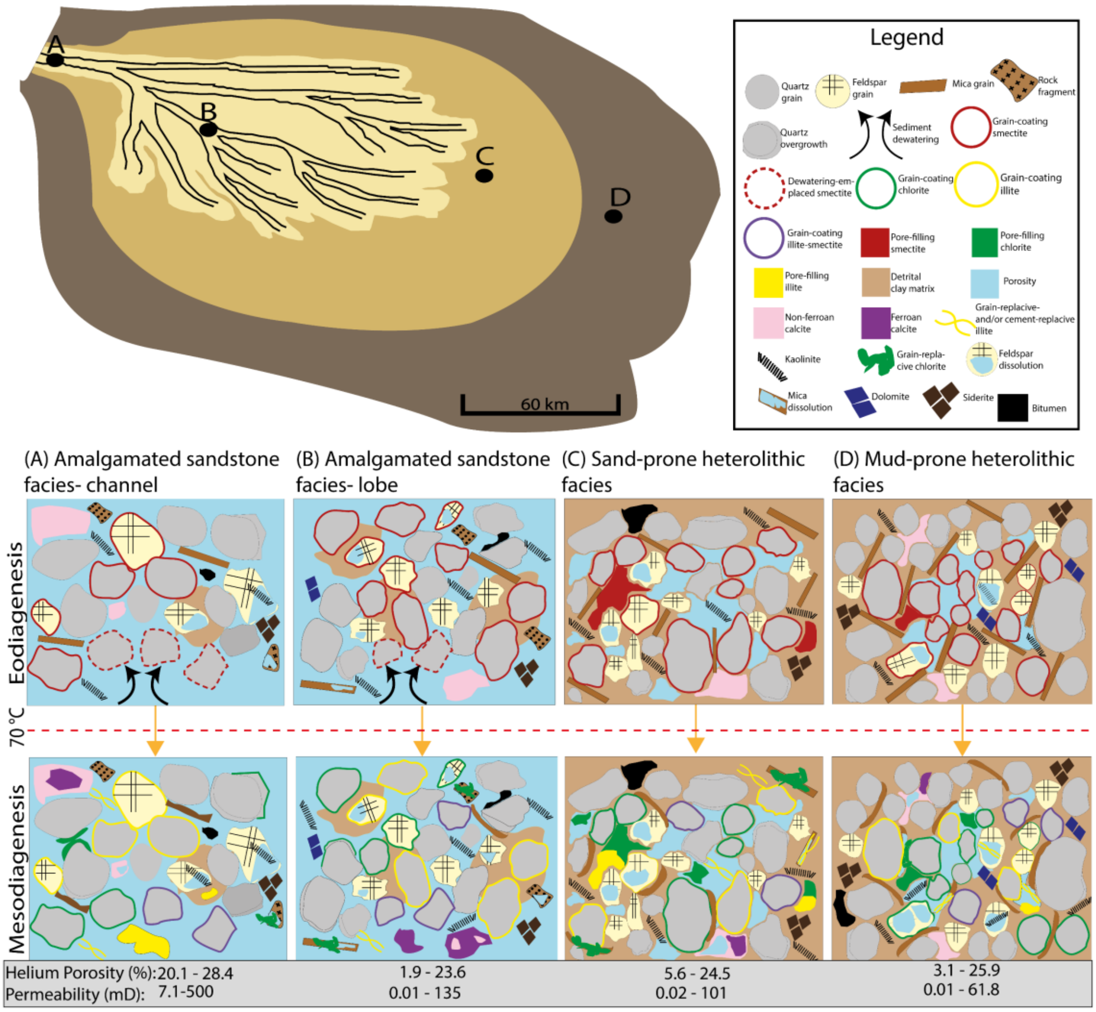

Figure 3.21. Schematic conceptual model for the facies control and diagenesis of the Forties Sandstone Member reservoir quality evolution. The model shows the types of diagenetic alterations and products that have affected the reservoir quality of the Forties Sandstone Member.

3.8 Conclusions

Establishing the link between depositional facies with diagenetic processes in sandstone reservoirs is crucial for understanding their controls on reservoir quality evolution. This is exemplified by the Tertiary, deep-sea turbidite sandstones of the Forties Member of Sele Formation, North Sea Central Graben. This study found that:

- The Forties Sandstone Member are very fine- to medium-grained, poorly- to moderately well-sorted, mainly arkose to subarkose, and deposited in submarine fan settings. The sandstones have considerable reservoir heterogeneity due to variations in facies and mud content, with a wide range of porosity from 1.9 to 28.4 % and permeability from 0.01 to 500 mD.

- Three main lithofacies associations were identified based on depositional environments and core description: (1) amalgamated sandstones facies (channel and proximal lobe), (2) sand-prone heterolithic facies (lobe off-axis), (3) mud-prone heterolithic facies (lobe margin/fringe),

- The proximal fan, amalgamated sandstones facies have the best reservoir quality due to coarser grain size, lower detrital clays, and lower ductile grains content. The distal fan, mud-prone facies have the poorest reservoir quality due to finer grain size, higher detrital clays, and higher ductile grains content. Total pore-filling clays between 10 and 30 % have a deleterious effect on reservoir quality, reducing porosities and permeabilities to generally < 10 % and < 1 mD, respectively.

- Diagenetic alterations of the Forties Sandstone Member have been achieved during early and late diagenesis. Key diagenetic processes and alterations include mechanical compaction, formation of smectite (and illite/smectite), kaolinite, illite, chlorite and quartz overgrowth, calcite (ferroan and non-ferroan). Minor diagenetic alterations include dissolution of feldspar, mica and carbonate cement cements and precipitation of dolomite and pyrite.

- Measurements of grain-coating clays, consisting of chlorite and illite/illite-smectite, coverage have shown that the clay-coating coverage to arrest quartz cementation and preserve reservoir quality at the present-day burial depths of Forties Sandstone Member (2200-3100 m TVDSS) ranges from 40 to 50 %, corresponding to the volume of grain-coating clays of up to 8 %. The clay coats have relatively maintained reservoir quality in both the amalgamated and heterolithic sandstones facies by inhibiting the development of quartz cementation. Macroporosity and permeability are preserved in the reservoir facies due to the grain-coating clays.

Chapter 4: Importance of grain-coating clays for porosity preservation

---

This chapter has been written in a manuscript format, and will be submitted to Journal of Petroleum Geoscience.

4.1 Summary

Turbidite sandstones of the Forties Sandstone Member were deposited in a sand-rich submarine fan system, and act as important deep-water hydrocarbon reservoirs for several fields in the North Sea Central Graben. Clay minerals, particularly grain-coating type, have played a vital role in the reservoir quality evolution of the Forties Sandstone Member. Evaluating the role of clay minerals in turbidite sandstones will significantly improve the understanding of the occurrence of relatively high-porosity and high-permeability zones in low-porosity and low-permeability heterolithic facies in submarine fans sandstones. This study employed a multi-technique approach to understand the origin of grain-coating clay minerals and assess their role in reservoir quality evolution of the sandstones by incorporating core studies, petrography, electron microscopy, and EDS mapping. Results of the study indicate that depositional facies and diagenesis control the reservoir quality of the sandstones. Grain-coating chlorite and illite/illite-smectite, originally from smectites inherited as coats and/or emplaced during sediment dewatering, seem to have inhibited the formation of ubiquitous, pore-occluding quartz cementation, with the required clay-coating coverage to inhibit quartz cementation ranging from 40-50 %. Grain size has been found to have no impact on clay-coating coverage in the sandstones, which suggests that the smaller grain-sized medial to distal fan heterolithic facies could potentially have good clay-coating coverage. Quartz cement generally decreases in volume from proximal (av. 3.62 %) to distal (av. 1.78 %) fan due to the role of grain-coating and pore-filling clays, resulting in an increase in reservoir potentials of the medial to distal fan heterolithic facies. Authigenic, pore-filling kaolinite and illite as low as 2 % have could affect the reservoir quality of the sandstones due to their often blocky and fibrous habits (respectively), occluding porosity and bridging pore throats. However, pore-filling authigenic chlorite has a threshold value of 3-10 % in order to have significant impact on reservoir quality. Although mechanical compaction is the main driver for porosity loss, sandstones with total grain-coating clays volume ranging from 6-11 % have suffered less impact of mechanical compaction, resulting in higher intergranular volume. Carbonate cements have had a minor impact on reservoir quality of the sandstones, except where their total volume ranges from 20-40 %; nevertheless, they have arrested mechanical compaction and have the potential to form excellent reservoirs should they undergo dissolution due to acidic pore fluids.

4.2 Introduction

Clay mineral coatings on sand grains are widely reported for preservation of anomalously high porosity in deeply buried sandstones reservoirs, by arresting the development of ubiquitous, porosity-occluding quartz overgrowths (e.g. Ajdukiewicz and Larese, 2012; Anjos et al., 2003; Bloch et al., 2002; Busch, 2016; Busch et al., 2020; Ehrenberg, 1993). Pore-filling quartz overgrowth is an important diagenetic cement that exerts a strong control on reservoir quality of deeply buried quartzose sandstones, which are susceptible to chemical compaction. Grain-coating chlorite and illite have been recognized to preserve porosity by reducing the nucleation area available for the precipitation of quartz overgrowths on detrital quartz grains (Ehrenberg, 1993; Pittman et al., 1992). Studies have shown that the effectiveness of grain-coating clays in inhibiting quartz cementation depends on their mineralogy, thickness, and coverage (or completeness) of coatings on sand grains (Ajdukiewicz and Larese, 2012; Lander et al., 2008).

The term “clay coat” comprises clays of both detrital and diagenetic origins. Detrital clay coats either form during or soon after deposition of sand grains, commonly through mechanical infiltration (Dowey et al., 2017; Matlack et al., 1989). The occurrence of detrital clay coats in deep-water turbidite sandstones has been linked to two main origins and processes: (1) detrital clay coats inherited from continental, deltaic, and/or shallow marine/shelf environments, which are transported to deep-water settings (Bahlis and de Ros, 2013; Yezerski and Shumaker, 2018). (2) clay coats emplaced by sediment dewatering (Housenknecht and Ross, 1992; Porten et al., 2019). Furthermore, clay coats can form in sandstones through the diagenetic, thermally-driven transformation of precursor detrital clay coatings (e.g., smectite), or those formed *in situ* from alteration of detrital grains (e.g., volcanic rock fragment, mica) (Berger et al., 2009; Wise et al., 2001; Worden et al., 2020; Worden and Morad, 2003). The clay coats cover detrital grains, with varying thicknesses and percentage of coverage (Busch et al., 2020; Kordi, 2013). In addition, they coat intergranular and moldic pores (Bahlis and de Ros, 2013).

Turbidite sandstones of proximal submarine fans are commonly targeted for hydrocarbon explorations in preference to the heterolithic sandstones commonly associated with the medial and distal fans. Additionally, the heterolithic sandstones are thought to make poor quality reservoirs due to abundance of pore-filling clays and smaller grain size that are characterized by larger surface area per volume, requiring a large volume of authigenic clays to form complete clay coatings on sand grains. The proximal-fan, clay-free sandstones, however, are highly susceptible to quartz cementation during deep burial diagenesis if they lack clay coats that inhibit the development of quartz cementation (Mansurbeg, 2007). Moreover, coarser sand grains have been reported to be more likely to suffer the impact of abrasion during transport, which might remove their clay coatings, than finer sand grains (Ajdukiewicz et al., 2010). Consequently, in order to be able to predict high reservoir quality in turbidite sandstones, there is a need to understand the origin and occurrence of grain-coating clays in deep-water turbidite facies, including the medial to distal fan heterolithic sandstones facies. This will reveal their reservoir quality potentials, thereby providing useful insights into hydrocarbon exploration, carbon capture and storage and potential geothermal systems. This study aims to use the Forties Sandstone Member, Central North Sea to evaluate the role of heterolithic facies and diagenesis in reservoir quality evolution of turbidite sandstones reservoirs. Specific research objectives are to: (1) understand the origin of clay coatings and their impact on reservoir quality evolution of the Forties Sandstone Member; (2) quantitatively measure the extent of clay-coating coverage around detrital quartz grains using JMicroVision software package following the method described by Dutton et al. (2018), and establish their role in inhibiting quartz cementation and reservoir quality preservation in the sandstones; and (3) establish the link between grain size and clay-coating coverage in the Forties sandstones.

4.3 Geological setting and stratigraphy

The Paleocene Forties Sandstone Member of the Sele Formation is a turbidite sandstone deposited in a series of overlapping submarine fans in the Central North Sea (Bowman, 1998; Hempton et al., 2005; Vining et al., 1993) (Figure 4.1). The turbidite sandstones of the Sele Formation have been divided into two major systems: (1) the primary, NW-SE-trending sediment dispersal system, which measures ca. 300 km by 100 km (Hempton et al., 2005); and (2) the E-W-trending lateral fans (Collins et al., 2015; Hempton et al., 2005; Jones et al., 2015) (Figure 4.1). Sourced from the Outer Moray Firth, the NW-SE sediment route constitutes the axial Forties Fan, which is the main focus of this study, and forms the major reservoir to the Forties, Everest, Nelson, Montrose, Arbroath, Arran, Pierce, and Blane fields (Hempton et al., 2005; Jennette et al., 2000) (Figure 4.1). The secondary lateral fans systems were sourced from the west and serve as the main the reservoirs in fields such as the Bittern, and Gannet, and also extend as far east as Merganser and Scoter fields in the Central Graben (Hempton et al., 2005) (Figure 4.1).

The Early Paleocene rifting of the Greenland and European plates, which was associated with thermal doming, uplifted the Scottish Highlands up to 2 km (Den Hartog Jager et al., 1993), causing more than 800 m fall in relative sea level and basinward regression (up to 90 km)

(Davis et al., 2009). This resulted in intensified erosion of the uplifted igneous, metamorphic, and meta-sedimentary hinterland, accumulating extensive deltaic and shallow marine sediments on the basin margin. Unstable delta fronts were created owing to high sedimentation rates and steep basin margins, transporting large volumes of sediments into the basin by sediment gravity flows along the major NW-SE graben axes (Charles and Ryzhikov, 2015). Consequently, the Forties Fan system developed as a product of transport of accumulated clastic deltaic and shelf sediments into deep-water setting by gravity flows (Bowman, 1998; Scott, et al., 2010; Whyatt et al., 1992).

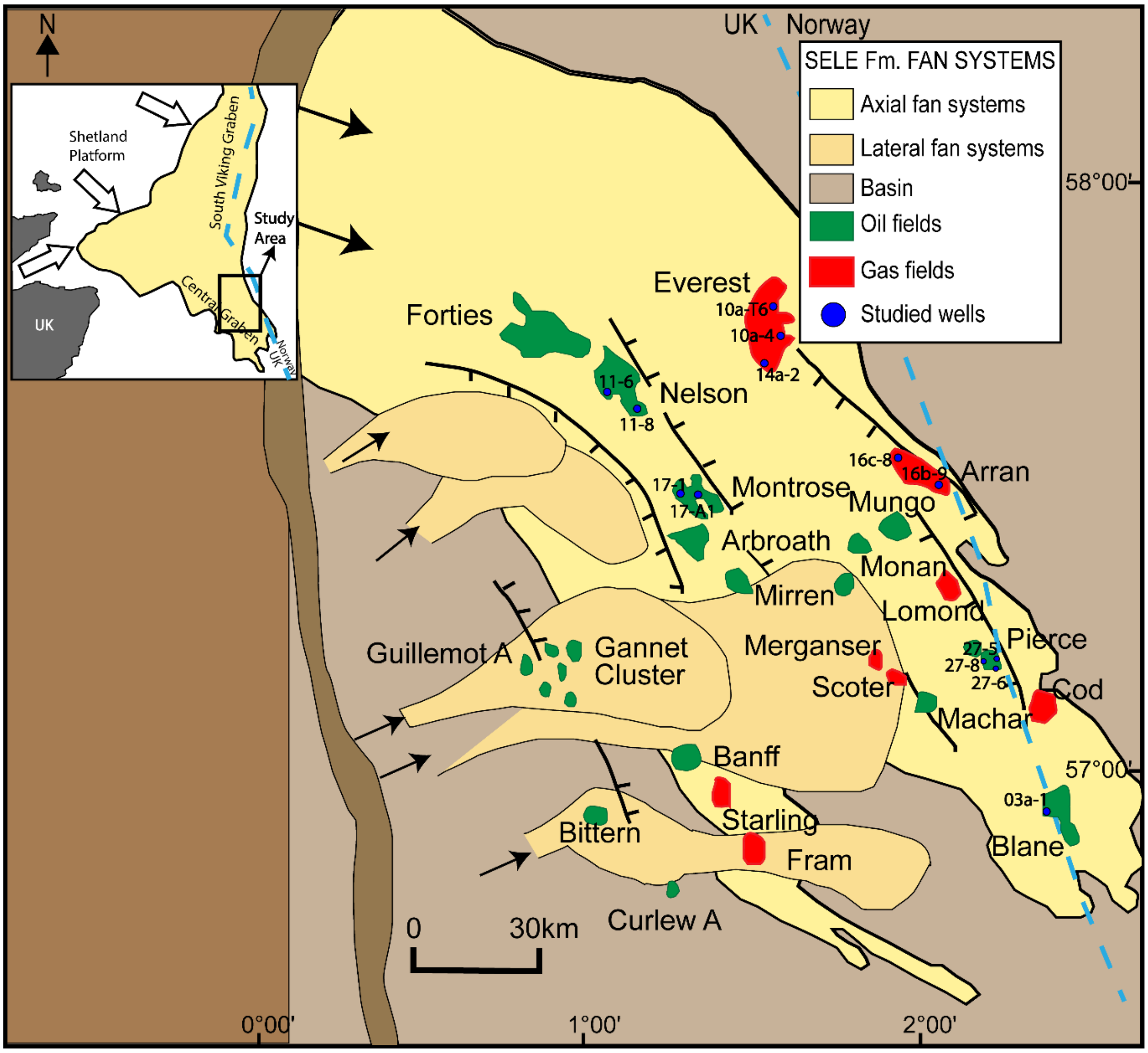

Figure 4.1. Regional map of the Forties Fan system showing locations of the studied wells (modified from Hempton et al., 2005).

Deegan and Scull, (1977) established the lithostratigraphic framework for the Palaeogene Central North Sea, and was reviewed further using biostratigraphic techniques (Knox and Holloway, 1992; Neal, 1996; Vining et al., 1993), and seismic reflection data and additional well data (Eldrett et al., 2015). Based on the periods of relative sea level falls, three major depositional cycles of deep-water sedimentation have occurred in the Central North Sea during the Paleocene to Early Eocene (Kilhams et al., 2014), and each cycle represents a period of sediments routing from the shelf to the basin floor due to the relative sea level lowstand (Jennette et al., 2000). The first depositional cycle consists of the Maureen Sandstone Member of the Maureen Formation (63-59.8 Ma) and the Lista Sandstone Member of the Lista Formation (56.8–59.8 Ma) (Figure 4.2), which constitute the first and second deep-water depositional cycles, respectively. The two formations have been named as the Montrose Group (Mudge and Copestake, 1993). The Montrose group is overlain by the Moray Group, which forms the third depositional cycle, consisting of the Sele Formation (56.8–54 Ma) and Balder Formation (Figure 4.2). The Forties Sandstone Member of the Sele Formation is a thick, discrete fan turbidite sandstone (over 200m) and areally extensive (ca. 300 km by 100 km) (Eldrett et al., 2015; Hempton et al., 2005). A regional, basinal mudstone of the Sele Formation (Figure 4.2) was deposited at the end of the Paleocene in response to a sea level rise. These mudstones act as regional seal for the Forties Sandstones reservoirs (Whyatt et al., 1992). The axial, NW-SE Forties Fan, dominated by channels and submarine fan lobes, forms the main focus of the present study (Figure 4.1).

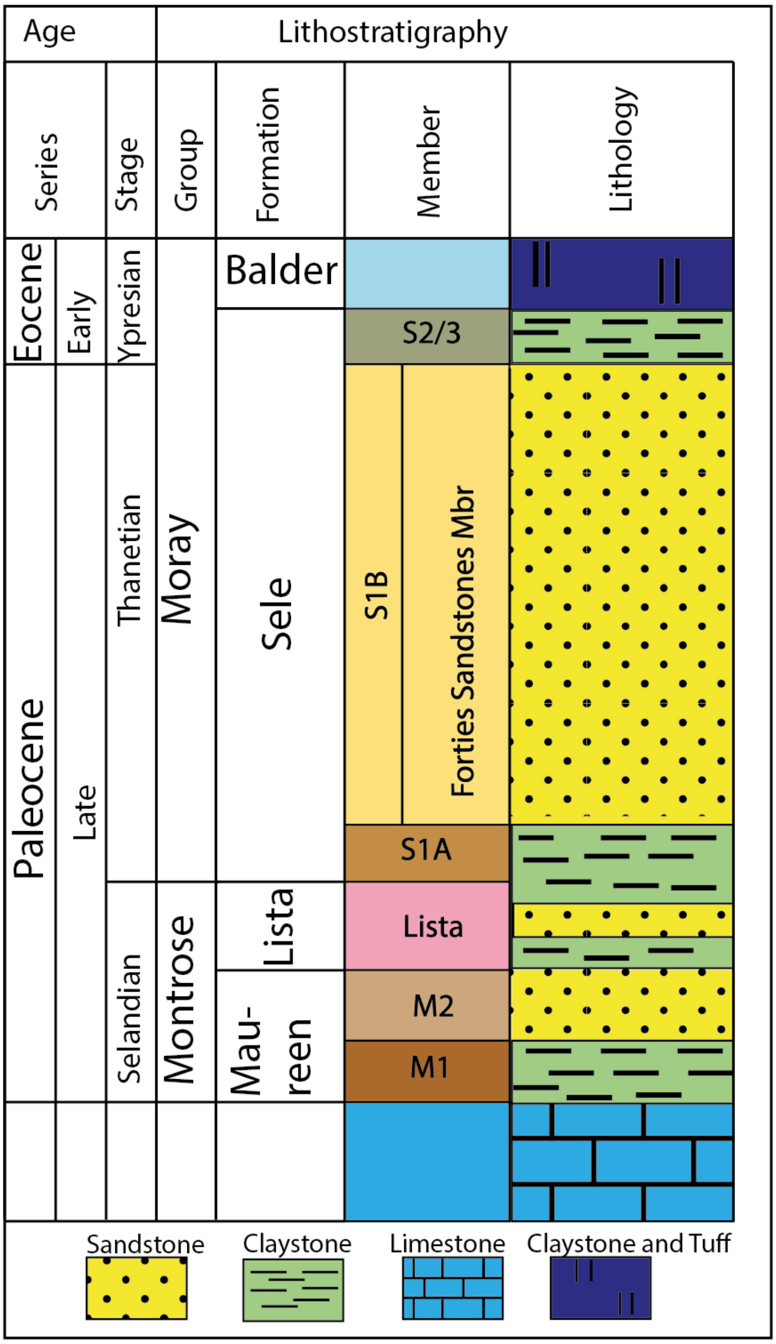

Figure 4.2. Stratigraphic chart for the Paleocene and Early Eocene formations, Central Graben, North Sea. The main focus of the study is the Forties Sandstone Member of the Sele Formation.

4.4 Methodology

One hundred and ninety-one (191) representative sandstone core samples of the Forties Sandstone Member were collected for petrographic analysis from thirteen (13) wells in six oil and gas fields of the axial Forties Fan system (Figure 4.1). A total of 266 m of cores were studied. Core samples were collected based on sedimentary lithofacies characteristics to identify changes in facies from proximal to distal Forties Fan system. Thin sections were prepared, impregnated with blue epoxy for identification of porosity, and stained with alizarin red and potassium ferrycyanide for carbonate cements identification. They were then studied using a Leica DM2500P standard petrographic microscope. Point count analysis was carried out using the Petrog software package based on 300 counts per thin section, and the process was repeated on all the samples in order to determine percentage of detrital grains, matrix content, pore-filling and grain-coating cements, and primary and secondary porosity.

Selected, polished, and carbon-coated thin sections were studied using a Hitachi SU70 scanning electron microscope (SEM) equipped with backscatter (BSE) and an energy dispersive X-ray spectrometer (EDS) for detailed analysis of sandstone microstructure, clay mineral composition, morphology and distribution. The analysis was conducted under acceleration of 12-15 kV. To further study clay mineral distribution and quartz overgrowths in 3D, 10 rock chips were studied using a Hitachi TM1000 scanning electron microscope.

Three polished and carbon-coated thin sections were selected for SEM-EDS mapping and analysis. The EDS phase mapping was conducted to visualize the distribution of minerals within the selected samples, with emphasis on clay minerals distribution, and also to complement the point count data. The maps also facilitated measurements of clay-coating coverage. Used on an SEM platform and supported by back-scattered electron/secondary electron (BSE/SE) imaging detectors, the EDS phase mapping technique is a semi-automated mineralogical tool used in the identification and quantification of minerals. The tool has an advantage of scanning relatively large areas at high resolutions, and 2 mm by 2 mm phase maps were acquired on each of the samples at 300x magnification for approximately 23 hours per sample. The chosen magnification enabled the effective visualization and quantification of clays and other minerals distributions in the samples. The electron beam was accelerated at 15 kV and the sample current was obtained at 0.73nA, with analytical working distance mostly ranging from 14.3 to 15.6 mm. The acquired phase maps were then processed using Oxford's Aztec (v.3.3) piece of software.

Measurements of the percentages of clay-coating coverage were conducted on 50 selected thin sections with known volumes of grain-coating chlorite, illite/illite-smectite, and quartz cement using the JMicrovision (v.1.3.3) software package based on the methodology described by Dutton et al. (2018). The selected samples were based on the established facies associations in section 4.5.1, with the details of the samples shown in Appendix I. Additionally, the samples were selected based on higher and lower volume of grain-coating clays and quartz cement determined from thin-section point counts. Clay-coating coverage was measured on 50 quartz grains per thin section using imported, high-resolution photomicrographs into the software. For each quartz grain, we measured the grain circumference, the lengths of any parts of the grain that are in contact with other grains (and hence not available for clay coatings and/or quartz cement to develop), and then the lengths of clay coatings on the grain surface. Clay-coating coverage was then calculated as: (sum of clay-coated lengths)/(grain circumference – sum of grain-contact lengths) (Dutton et al. 2018).

Cathode-luminescence (CL) analysis was performed on selected polished thin sections in order to determine the origin (detrital and/or authigenic) and extent of quartz cement, and to establish different phases (where available) of quartz cement development.

Porosity and permeability (poroperm) datasets for a total of one hundred and sixty-seven (167) sampled cores were obtained from UK common data access (CDA). While porosity measurements were conducted using helium in a Boyle’s Law porosimeter to give grain volume, air permeability measurements were carried out using oxygen-free nitrogen as the flowing fluid with the plug mounted in a Hassler cell under a routine confining pressure of 200 psi.

Stable isotope analysis for carbon and oxygen isotopes were conducted on 18 sandstones samples (and 3 duplicates) with variable amounts of carbonate cements, consisting of calcite (ferroan and non-ferroan), dolomite, and siderite. Based on carbonate content, bulk samples were powdered (< 200 mesh) and each sample was weighed out to give a CO_2 signal of 12mV, and was then reacted with 99% ortho-phosphoric acid for 2 hours at 70°C. The resultant gas mix of helium and CO_2 was then separated and analysed via a Thermo Fisher Scientific Gasbench II interfaced with a Thermo Fisher Scientific MAT 253 gas source mass spectrometer for isotopic analysis. Data are reported in standard delta notation as per mil (‰) relative to Vienna Pee Dee Belemnite (V-PDB).

4.5 Results

4.5.1 Lithofacies description

Four lithofacies for the Forties Sandstone Member have been established based on lithological characteristics and depositional environments (Figure 4.3A, B & C). The facies detailed description and inferred depositional processes are summarized in Table 4.1.

Proximal-fan, amalgamated sandstones facies (Figure 4.3A). These facies have been interpreted as products of high-density turbidity currents (Lien et al., 2006; Porten et al., 2016). They are characterized by massive stacked and predominantly medium-grained sandstones (Figures 4.3A & 4.4A), often with dewatering structures. The facies are several metres thick and fine-upward, and are capped by silty graded tops or laminated mudstones, indicating the end of depositional events (Figure 4.3A). They are associated with channel and proximal lobe depositional environments.

Sand-prone heterolithic facies (Figure 4.3B). This consists of interbedded sandstones, siltstones, and mudstones. The sandstones are similar to those of the amalgamated sandstones facies in lithological characteristics, but with increased silt and mud content and decreased sand thickness. These facies are mainly fine-grained (Figure 4.4A), and represent lobe off-axis depositional environments. In addition, they have been interpreted as products of low-density turbidity currents, with occasional high-density flows (Bell et al., 2018; Lien et al., 2006).

Mud-prone heterolithic facies (Figure 4.3C). These facies largely consist of siltstones, mudstones, with thinly interbedded sandstones, commonly less than 1 m thick. Mud content significantly increases with decrease in grain size and sandstones thickness. The sandstones are very fine- to medium-grained (Figure 4.4A). The facies represent lobe margin and/or lobe fringe depositional environments, and are predominantly products of low-density turbidity currents (Bell et al., 2018).

Mudstones facies. These are essentially non-reservoir facies, consisting of dark-grey mudstone and silty laminate mudstones, with rare, thin sandstones. The facies are the same as the mudstones of the mud-prone heterolithic facies (Figure 4.3C), which represent products of suspension fallout and muddy turbidity currents, indicating low-energy channel abandonment/margin, inter-channel, interlobe, and lobe fringe depositional environments.

Table 4.1. Description and interpretation of principal lithofacies of the Forties Sandstone Member.

Facies code	**Facies**	**Description**	**Interpreted flow type**	**Associated depositional environment**
AA	Amalgamated sandstone	Clean, stacked massive sandstone, fine-medium grained, moderately to well sorted, structureless with occasional de-watering (water escape) structures.	High-density turbidity current.	Turbidite channel and proximal lobe.
SH	Sand-prone heterolithic	Sand-rich, fine-grained argillaceous sandstone, moderately sorted, interbedded with thin laminated siltstone/mudstones. Some parallel and ripple laminations preserved. Some minor soft sediment deformation structures also preserved.	High- and low-density turbidity currents/.	Lobe off-axis.
MH	Mud-prone Heterolithic	Argillaceous silty sandstones, very fine- to fine-grained sandstones, moderately to poorly sorted, mostly rippled and interbedded with laminated and silty mudstones.	Low-density turbidity current.	Lobe margin/fringe.
M	Mudstone	Hemipelagic mudstone.	Suspension fallout (hemipelagic) and debris flow.	Channel abandonment/margin, inter-channel, interlobe, and lobe fringe.

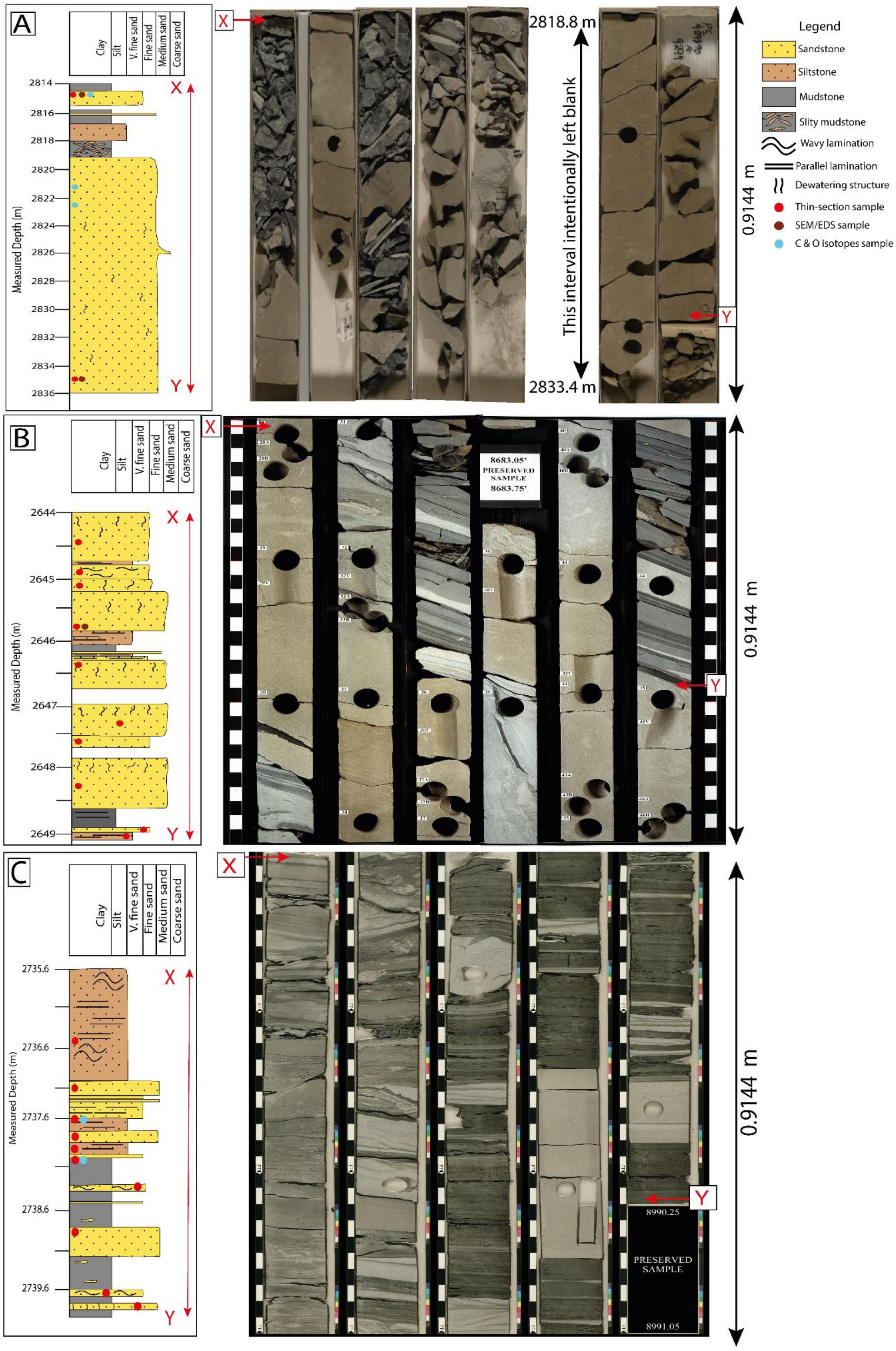

Figure 4.3. Graphic sedimentary logs samples and illustrative core photographs of principal lithofacies of the Forties Sandstone Member used in the study. (A) Amalgamated sandstones facies consisting of stacked sandstones, with a total thickness reaching up to 20 m. Nelson field, well 22/11-6; (B) Sand-prone heterolithic facies, consisting of massive sandstones similar to those in (A) (albeit thinner) and increased silt and mud content. Arran field, well 23/16c-8; (C) Mud-prone heterolithic facies. This facies mainly comprises interbedded mudstones, siltstones, and sandstones, with the sandstones thickness commonly less than 1 m. Arran field, well 23/16b-9.

4.5.2 Grain size, porosity, and permeability

The sandstones grain size vary from medium silt to medium-grained sandstones, with predominance of fine to medium grain size (Figure 4.4A). Mean grain size for all samples ranges from 0.03 to 0.44 mm (average 0.2 mm).

Petrographic observations and SEM analysis of thin-section samples revealed two types of porosity: primary (intergranular) and secondary (intragranular) porosity. Point count data indicates that the primary, optical porosity ranges from 0 to 26 %, averaging 6.48 % (for all samples analysed), and commonly decreases with an increase in depth. Secondary intragranular, feldspar-dissolution porosity ranges from 0 to 5.5 %, averaging 1.16 %. Pore-filling non-ferroan calcite, dolomite, and siderite are partially to completely dissolved, creating secondary intergranular porosity. Total carbonate dissolution porosity ranges from 0 to 5 %, averaging 0.04 %. Helium porosity data, on the other hand, indicates that the porosity ranges from 1.9 to 28.4 %, averaging 18.72 %. Vertical permeability ranges from 0.01 to 500 mD (average 53.20 mD). A plot of helium porosity against permeability for the 167 core samples (Figure 4.4B) indicates a positive correlation, and that, in general, the amalgamated sandstone facies have the highest porosity and permeability.

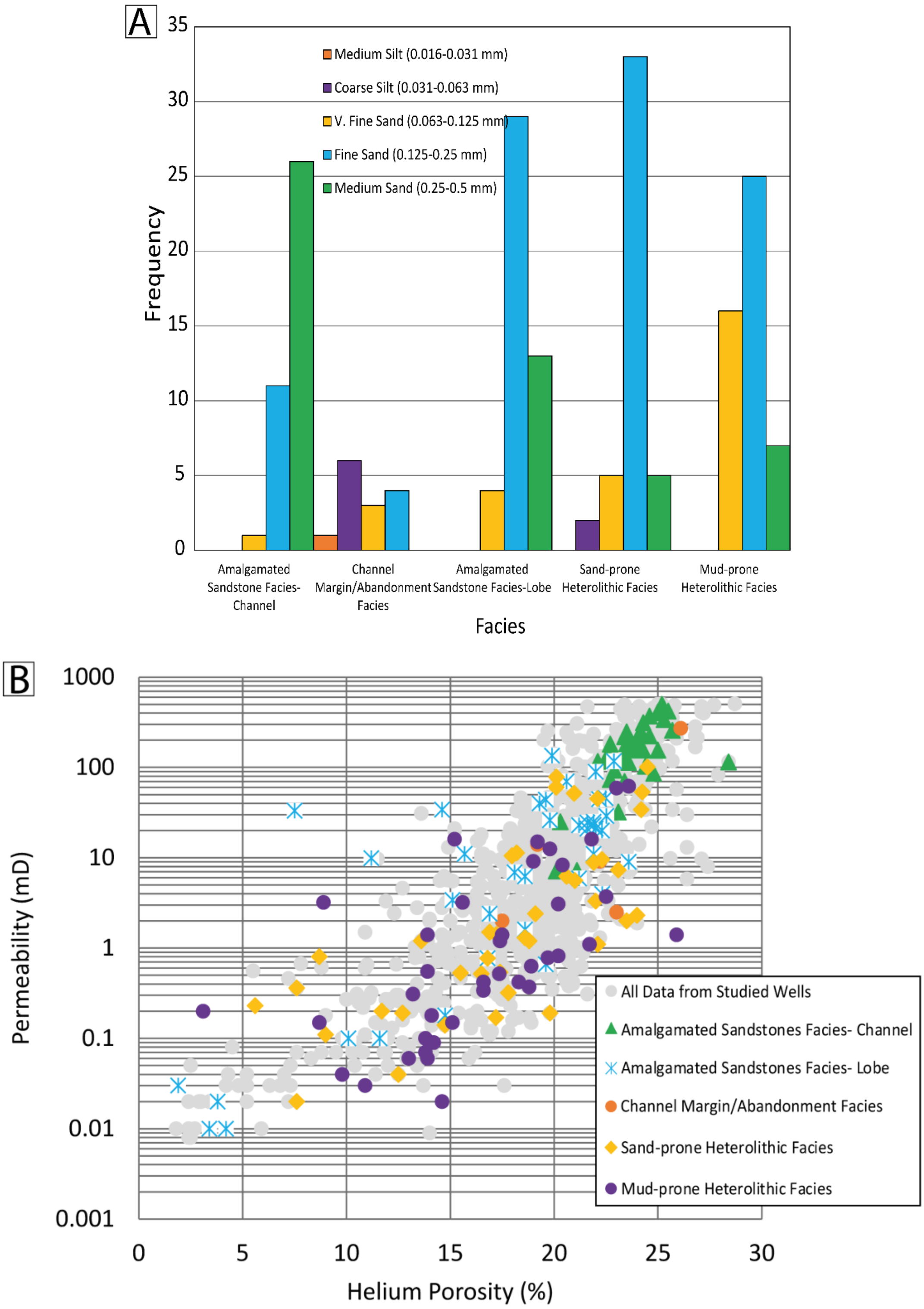

Figure 4.4. (A) Relative proportion of grain size of the Forties Sandstone Member for 191 samples used in this study; (B) Plot of core permeability against core porosity for the studied Forties Sandstone reservoirs. The higher permeabilities in the 10 to > 100 mD range and porosities > 20 % are predominantly for the proximal amalgamated sandstones facies (see Figure 4.3A). This compares markedly to the sand-prone and mud-prone heterolithic facies where permeabilities can be > 0.1 mD and porosities frequently > 10 %.

4.5.3 Detrital mineralogy and sorting

The studied samples of the Forties Sandstone Member are essentially arkose, subarkose and, seldom, lithic arkose (Figure 4.5). The sandstones have an average, present-day framework composition of $Q_{69.2}F_{27.2}R_{3.6}$. The sorting ranges from poorly- to well-sorted, and the framework grains are mostly sub-rounded to rounded.

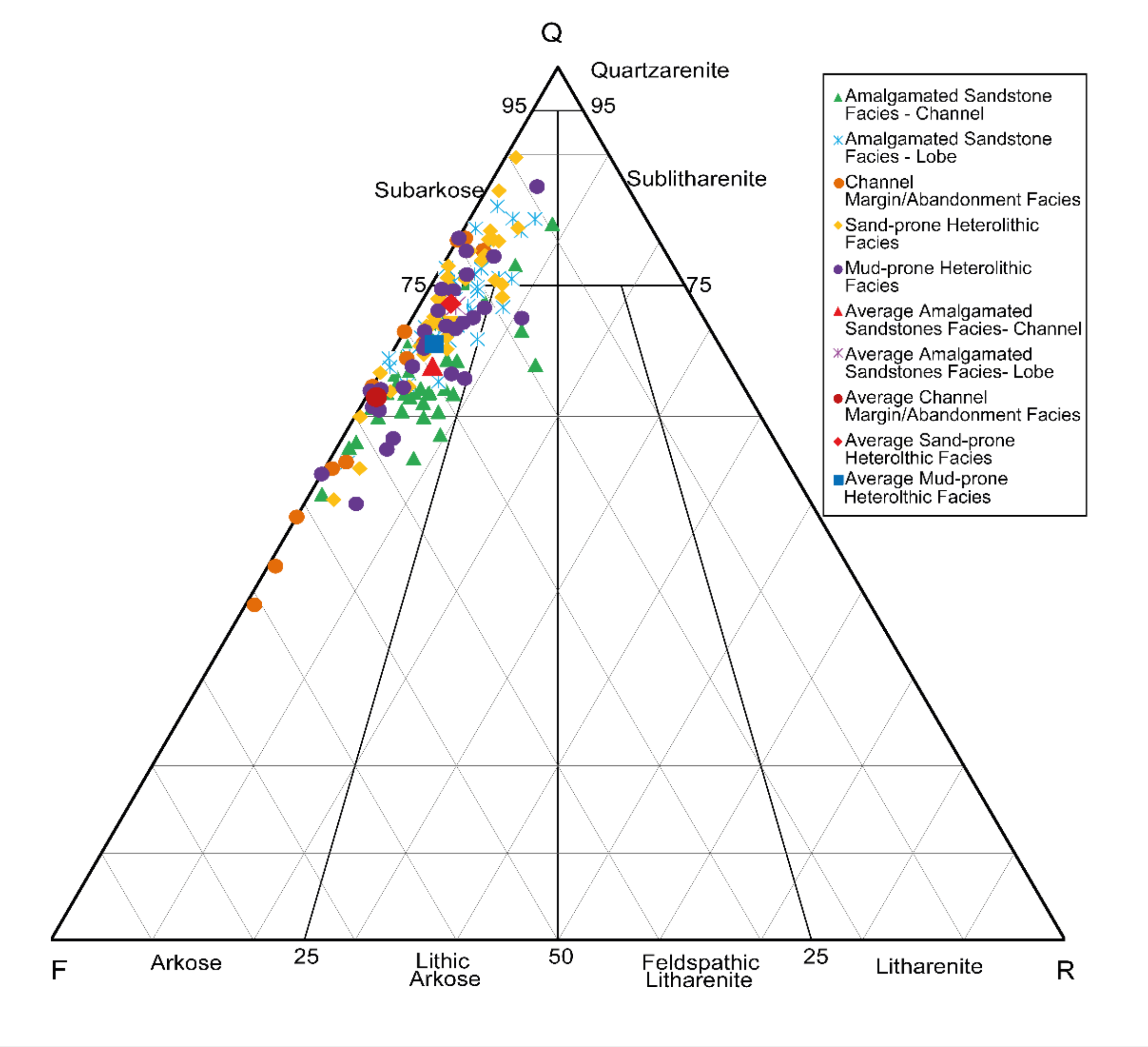

Figure 4.5. QFR plot after Folk, 1980 showing the compositional mineralogy of the Forties Sandstone Member for all the wells used in this study. Most of the sandstones are arkosic to subarkosic, with a smaller proportion represented by lithic arkoses.

Detrital framework grains mainly consists of monocrystalline quartz (5.30- 60.30 %; average 37.49 %), polycrystalline quartz, which also doubles up as a metamorphic rock fragment, (0-6 %; average 1.71 %), microcline (0-2.7 %; average 0.25 %), orthoclase (1.3-21.7 %; average 9.58 %), and plagioclase (0-10.3 %; average 4.69 %). Thus, potassium feldspars are predominant over plagioclase. Detrital mica occurs in variable amounts (0-35 %; average 5.96

%); however, biotite (0-33.5 %; average 3.94 %) predominates over muscovite (0-12 %; average 2.02 %). Lithic fragments consist of metamorphic (trace), polycrystalline quartz, mudclasts (0-3.7 %; average 0.24 %), and volcanic rock fragments (< 1%). Accessory minerals are largely glauconite and heavy minerals (e.g., rutile). Detrital matrix mainly consists of brownish to green (and often yellow) smectitic clays, ranging from 0.3 to 44 % (average 10.26 %) (e.g., Figure 4.6A & B). The clays are characterized by high birefringence (Figure 4.6A & B).

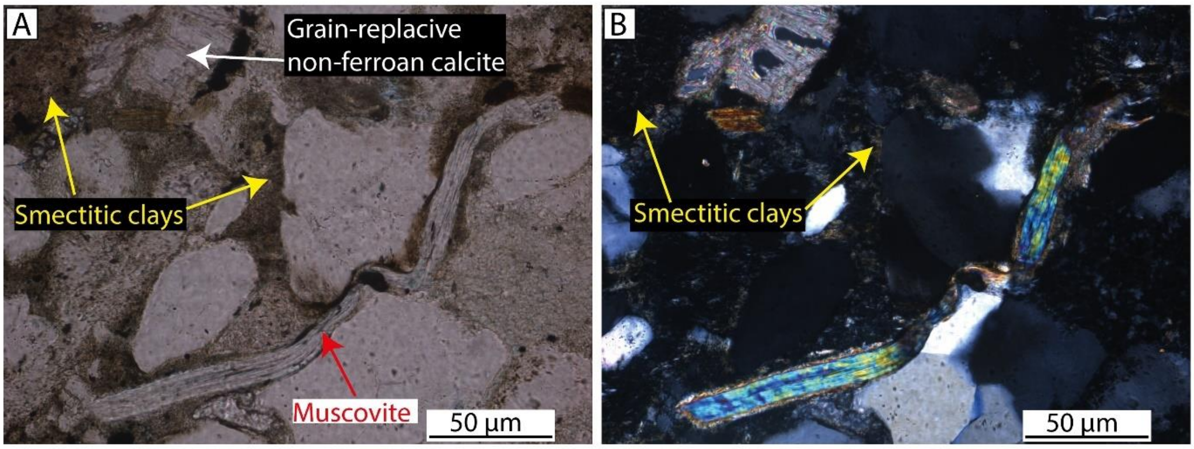

Figure 4.6. (A) PPL photomicrograph showing greenish to brown, high birefringence smectitic detrital matrix. Note the bending of detrital muscovite due to ductile deformation. (B) XPL photomicrograph of (A). [PPL= plane polarized light; XPL=cross polarized light].

4.5.4 EDS phase maps results

EDS phase maps can highlight the distribution of mineral phases within sandstones samples. A 2 mm by 2 mm (at 300x magnification) EDS phase maps for 3 sandstones samples each, which represent proximal, medial and distal fan, were acquired, analysed and interpreted. Figure 4.7A-I shows the montaged BSE images, maps of clay minerals distributions within intergranular porosity, and EDS mineralogical maps for the 3 sandstones samples (i.e., 3 images for each sample). However, due to the limitations of the EDS mapping technique in differentiating between grain-coating and pore-filling clays, the exact amounts of grain-coating and pore-filling clays for each sample were determined from point counting alone. In addition, although no model standard was developed to test the automated quant mineralogy, conscientious efforts were made to acquire the EDS maps and process them, with the help of X-ray maps, EDS spectra, and phase maps. The results of the comparison between EDS phase maps and petrographic point count data for the sandstones samples are summarized in Table

4.2. The results show that the EDS phase maps analysis matches largely well with the point count datasets (Table 4.2).

In the proximal-fan sample from Nelson field, well 22/11-6, kaolinite and non-ferroan calcite (Figure 4.7A, B & C) are the most dominant pore-filling cements, and the detrital grains are largely characterized by incomplete clay coatings of illite/illite-smectite (Figure 4.7B). In the medial-fan sample from Pierce field, well 23/27-5, however, chlorite is the most dominant grain-coating and pore-filling clay (4.7D, E & F), with very thick coatings that often develop into pore-filling clays (Figure 4.7E). In the distal-fan sample from Blane field, well 30/03a-1, authigenic kaolinite is the most abundant pore-filling clay (Figure 4.7H, G & I). Furthermore, coatings of illite/illite-smectite are better developed in terms of coverage on detrital grains (Figure 4.7G) than in the proximal-fan sample from the Nelson field, well 22/11-6.

Table 4.2. Comparison between EDS phase maps results and point count data.

Well/sample depth (m)	**Nelson-22/11-6/2206**		**Pierce-23/27-5/2734**		**Blane-30/03a-1/3097**	
Mineral	EDS phase map abundance (%)	Point count abundance (%)	EDS phase map abundance (%)	Point count abundance (%)	EDS phase map abundance (%)	Point count abundance (%)
Quartz	50.26	37.7	57.53	39	57.26	43.5
K-feldspar	5.8	6.02	7.8	10	4.81	3
Plagioclase	6.75	4	6.32	5.6	6.9	8.5
Rock fragment	0	1.7	0	3	0	5
Chlorite	0	3.7	21.71	6.7	0.21	0.5
Illite/illite-smectite	6.02	6.3	0.84	6.7	15.78	18
Kaolinite	3.32	4	0.32	2	9.3	1
Total grain-coating clays (chlorite and illite/illite-smectite)	-	5.3	-	3	-	10
Calcite	4.15	8.6	0.11	0	0.73	1
Siderite	0	0	0	0	0.1	0.5
Pyrite	0	0	0	0	0	0

Rutile	0.1	0.1	0.21	0	0.1	0
Intergranular porosity	17.5	7.6	2.63	2.7	4.39	7
Intragranular porosity	0	1.7	0	2.3	0	2.5

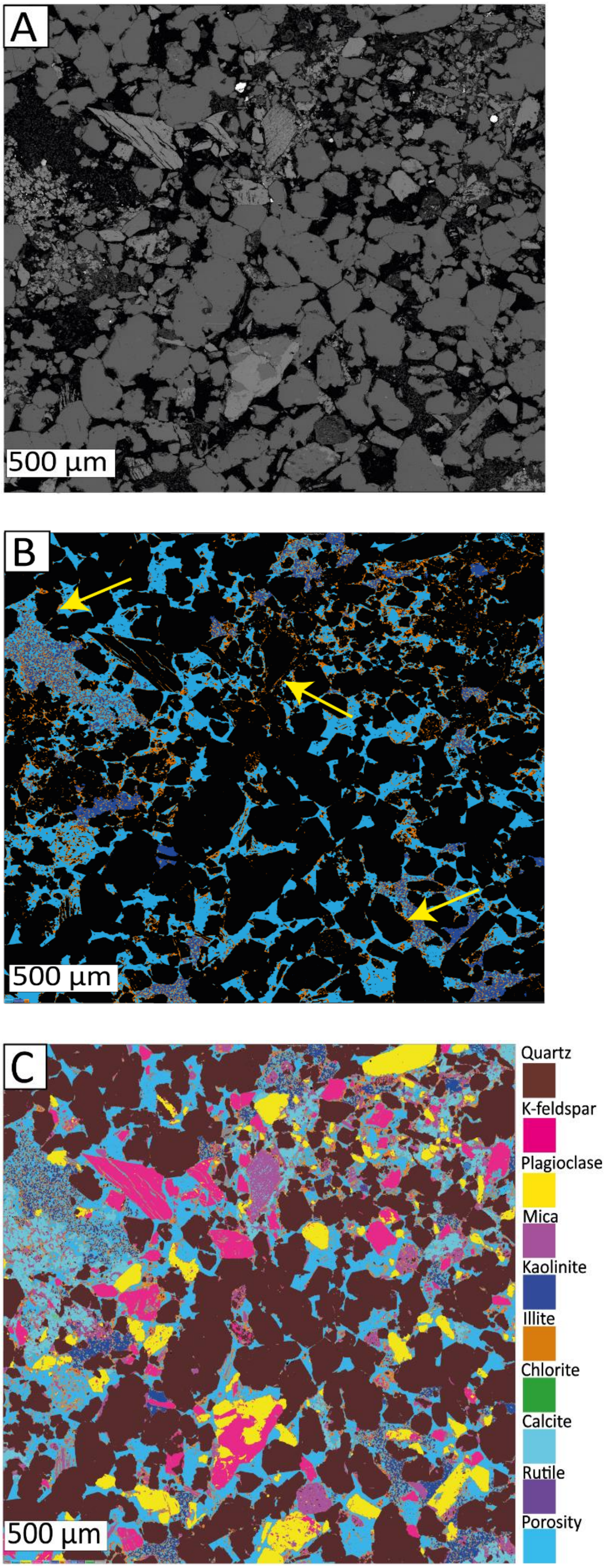
A
500 µm
B
500 µm
C
500 µm
Quartz
K-feldspar
Plagioclase
Mica
Kaolinite
Illite
Chlorite
Calcite
Rutile
Porosity

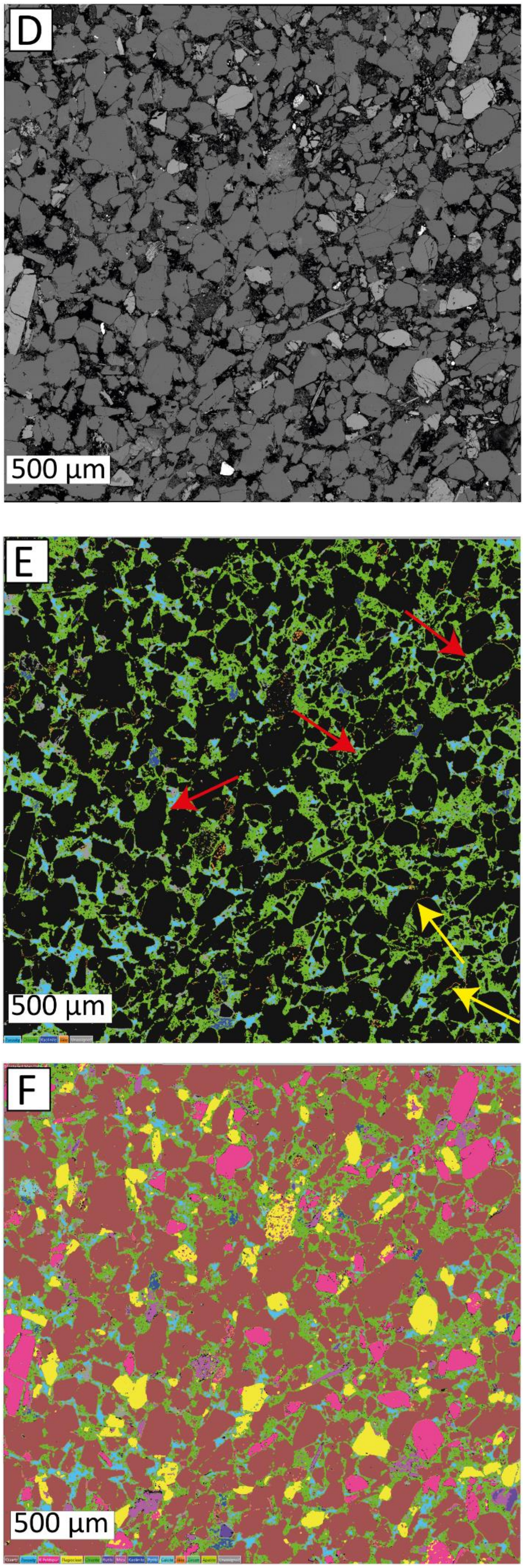
D
500 µm
E
500 µm
F
500 µm

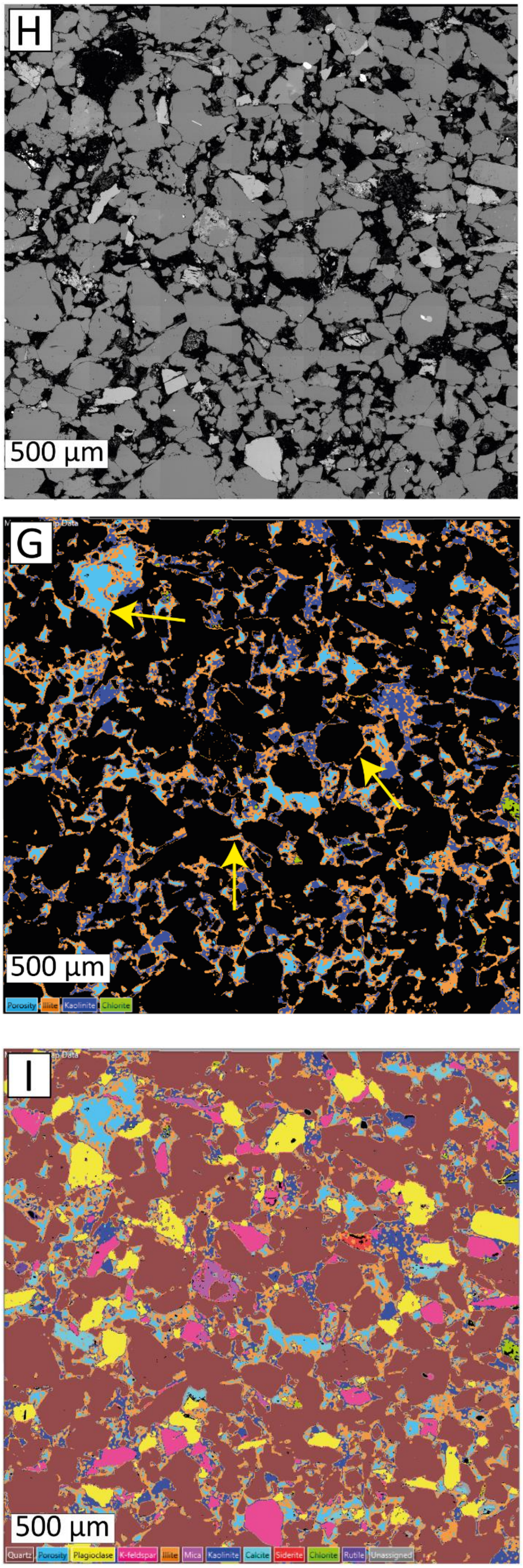
H
500 µm
G
500 µm
Porosity
Illite
Kaolinite
Chlorite
I
500 µm
Quartz
Porosity
Plagioclase
K-feldspar
Illite
Mica
Kaolinite
Calcite
Siderite
Chlorite
Rutile
Unassigned

Figure 4.7. Results of EDS phase maps for 3 selected sandstones samples of the proximal, medial, and distal Forties Sandstone Member showing the mode of occurrence and distribution of clay minerals in the sandstones. (A), (B), and (C): BSE image, clay minerals distribution map, and EDS phase map for the proximal fan amalgamated sandstones facies, respectively. **Nelson field**, well 22/11-6, 2206.45 m TVDSS. In this sample, kaolinite and non-ferroan calcite are the dominant pore-filling cements, and grain-coating illite/illite-smectite form largely incomplete coats around detrital grains (yellow arrows); (D), (E), and (F): BSE image, clay minerals distribution map, and EDS phase map for the medial fan sand-prone heterolithic facies, respectively. **Pierce field**, well 23/27-5, 2733.75 m TVDSS. In this sample, chlorite is the main clay mineral (red arrows), with some illite (yellow arrows). It occurs as thick grain-coating (red arrows) and pore-filling clay. (G) (H) (I): BSE image, clay minerals distribution map, and EDS phase map from distal fan amalgamated sandstones facies, respectively. **Blane field**, well (30/03a-1), 2733.75 m TVDSS. Based on the clay mineral distribution map (G) kaolinite is the dominant pore-filling clay, and grain-coating illite/illite-smectite are more well-developed in terms of coverage (yellow arrows) compared to those in the proximal fan sample in (B).

4.5.5 Diagenetic processes and products

The main diagenetic processes and products that affect the reservoir quality of the Forties Sandstone Member include mechanical compaction, precipitation of cements, mineral dissolution, and replacement of chemically unstable detrital grains by clay minerals, and carbonate cements. The authigenesis of cements consists of clay minerals, quartz overgrowths, and carbonates.

4.5.5.1 Porosity loss by mechanical compaction and by cementation

The Forties Sandstone Member has been affected by mechanical compaction. The degree of compaction in the sandstones was assessed based on the nature of grain contacts, amount of ductile grains, and the extent of porosity loss by compaction (COPL) and by cementation (CEPL) using the method described by Lundegard, 1992 (Figure 4.8). Grain contacts are point type (Figure 4.9A), concavo-convex (Figure 4.9B), and floating (Figure 4.9C). The impact of mechanical compaction in sandstones with point and floating grain contacts is low, as the grains barely touch one another. In contrast, sandstones with concavo-convex grain contacts have relatively higher impact of mechanical compaction (Figure 4.9B). Furthermore, sandstones with high amounts of ductile grains (mica and mudclasts), which occur in the medial to distal Forties Fan, have suffered more impact of mechanical compaction, as the ductile grains form pseudomatrix upon compaction, thereby blocking pore throats (e.g., Figure 4.9 D). On the contrary, due to the presence of floating grains, sandstones with well-developed, early carbonate cements (e.g., Figure 4.9 C) exhibit less impact of mechanical compaction on porosity loss than those with little or no early carbonate cements. However, porosity loss, in this case, is by cementation than by compaction (Figure 4.8).

To determine the extent of porosity loss by compaction and by cementation, the initial or depositional porosity for the Forties Sandstone Member was obtained from published literature. The initial, depositional porosity has been estimated as 36 % (Whyatt et al., 1992) and up to 40 % (Allsop, 1994). As a result, an average of 40 % initial porosity has been used to calculate porosity loss by compaction and cementation using the method of Lundegard (1992). In general, based on the plot of porosity loss by compaction against porosity loss by cementation, it has been established that more porosity is lost by compaction than by cementation in the Forties Sandstone Member (Figure 4.8).

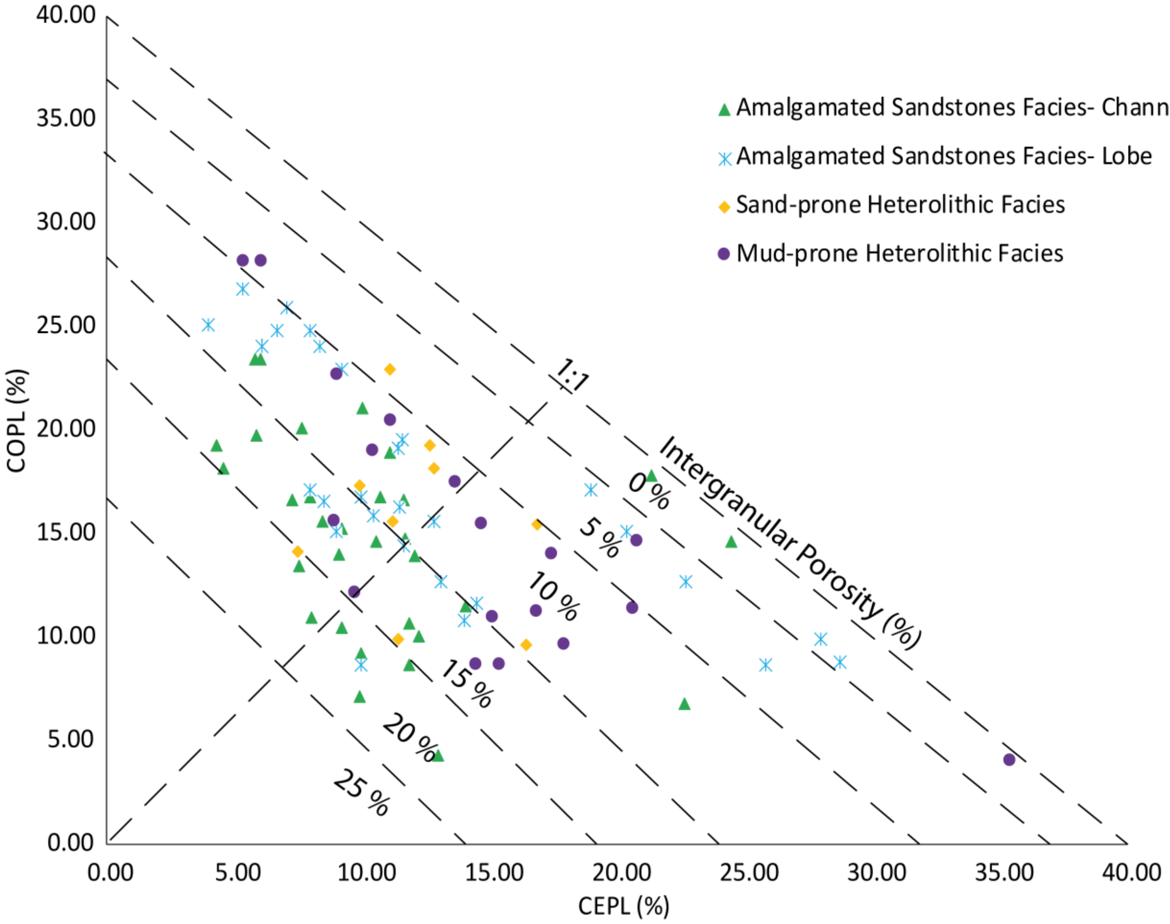

Figure 4.8. Plot of compactional porosity loss against cementational porosity loss for the Forties Sandstone Member (modified after Lundegard, 1992). From this plot, more intergranular porosity is lost due to compaction than due to cementation.

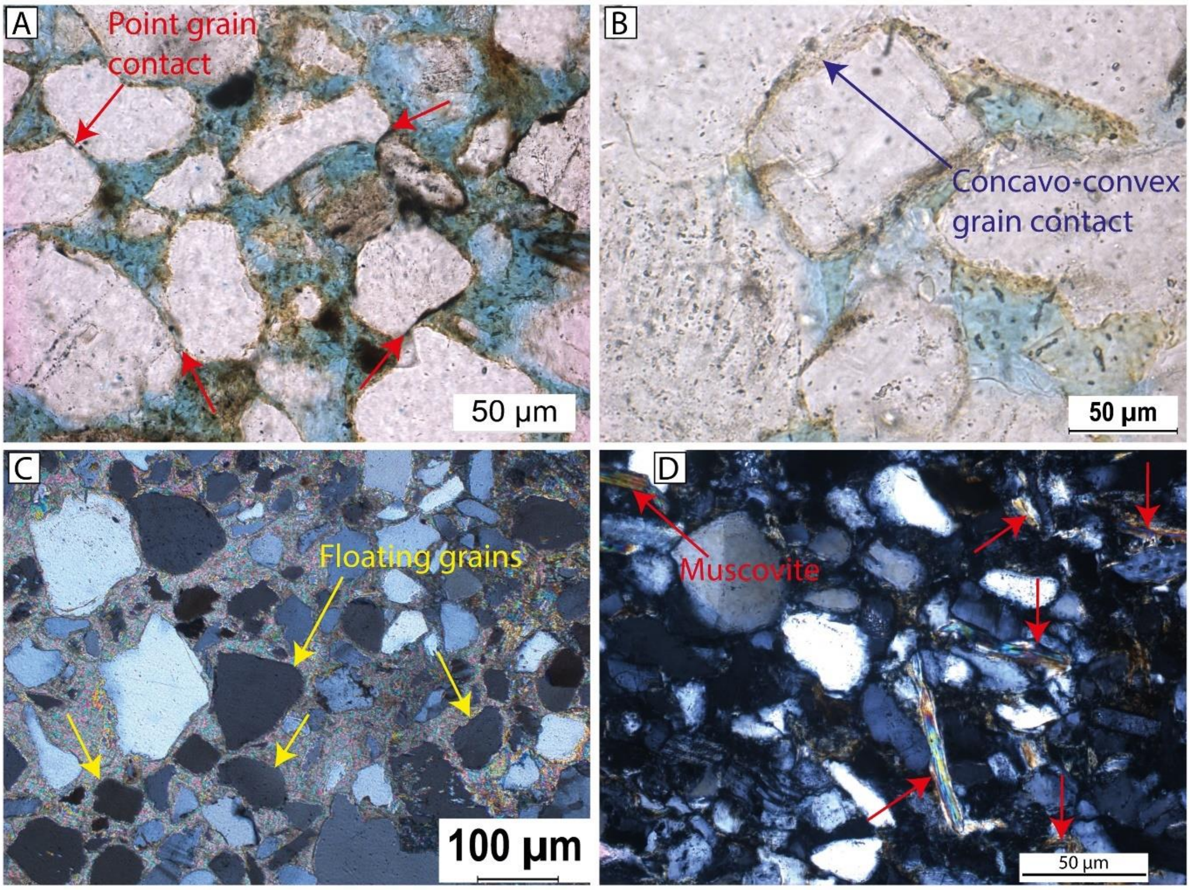

Figure 4.9. Thin-section photomicrographs showing the types of grain contacts and, thus, the extent of mechanical compaction in the Forties Sandstone Member. (A) PPL photomicrograph of point-type grain contacts showing less impact of mechanical compaction; (B) PPL photomicrograph of concavo-convex grain contact, suggesting moderate impact of mechanical compaction; (C) XPL photomicrograph of floating grains due to early, shallow burial carbonate cementation, which has arrested mechanical compaction; (D) XPL photomicrograph of moderate to high impact of mechanical compaction due to ductile deformation by mica (muscovite) grains. [PPL= plane polarized light; XPL= cross polarized light].

4.5.5.2 Clay cements

Clay minerals are the main diagenetic constituents in the Forties reservoirs. Based on petrographic observations, SEM morphological features, and EDS analysis, authigenic clay minerals in the Forties Sandstone Member are of five types: chlorite, illite, mixed-layer illite/smectite, illite, and kaolinite. Each of these clays exhibits varying morphological features, textures, and concentrations.

Authigenic chlorite is the most dominant clay mineral in the sandstones, and occurs in four main habits: (1) grain-coating (0-9.7 %; average 1.84 %; Figure 4.10A). The coatings are made up of platelets oriented parallel to the grain surfaces, and are commonly thin and relatively continuous. (2) Pore-lining chlorites (Figure 4.10B). These are commonly thin and continuous, and are made up of platelets arranged perpendicular to grain surfaces and surround open and moldic pores. (3) Grain-replacive (0-17 %; average 1.09 %). Chlorite plates replace partially to pervasively dissolved lithic fragments (metamorphic and volcanic) (e.g., Figure 4.10 C & D), and mica grains (Figure 4.10E). (4) Pore-filling (0-16 %; average 3.39 %). These are chlorites that fill intergranular pores, and are probably products of replacement of detrital pore-filling smectitic clays, or they were formed from direct precipitation from porewater (neoformation) (Figure 4.10F).

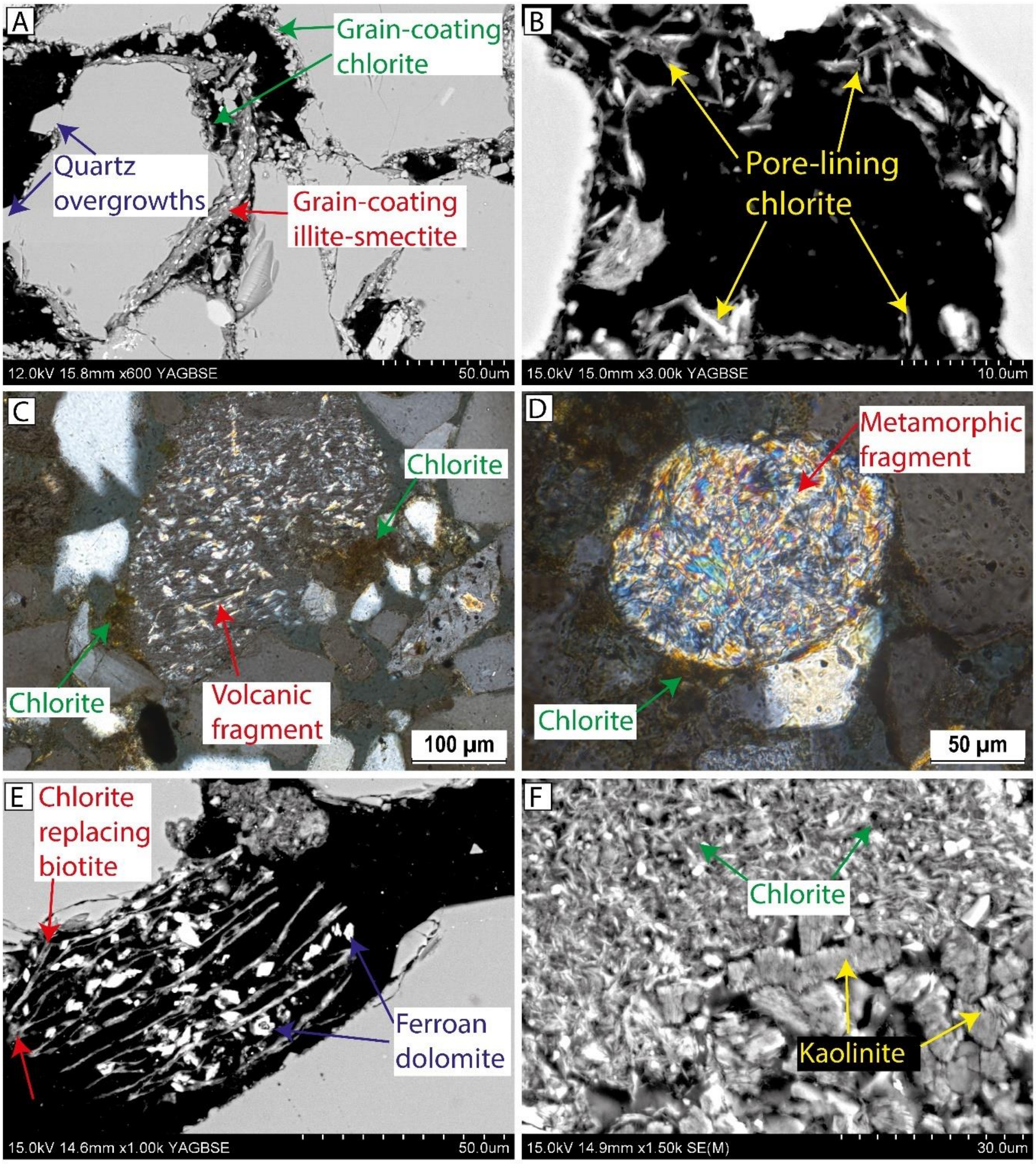

Figure 4.10. BSEM and thin-section photomicrographs illustrating the mode of occurrence and origins of chlorite in the Forties Sandstone Member. (A) BSEM image of grain-coating chlorite and illite-smectite. Note how quartz overgrowths have developed where the grain-coating clays are absent; (B) BSEM image showing pore-lining chlorite preserving intergranular porosity by preventing quartz cementation; (C) XPL photomicrograph showing the formation of chlorite from dissolution/alteration of volcanic rock fragment (VRF), where the latter is being replaced by chlorite; (D) XPL photomicrograph of metamorphic rock fragment (MRF) being replaced by chlorite (green arrow); (E) BSEM image showing the formation of chlorite and ferroan dolomite by the replacement of detrital biotite. Thus, this indicates that the biotite is a precursor for chlorite; (F) BSEM image showing pore-filling chlorite and kaolinite, destroying intergranular porosity. [XPL= cross polarized light].

Formed generally from smectite and mostly under mesogenetic conditions, authigenic illite occurs as fibrous, hair-like crystal aggregates. The illite in the sandstones commonly occurs as: (1) grain-coating (0-10 %; average 1.68 %; Figure 4.11A). Grain-coating illite occasionally occurs on the same detrital grains with chlorite, indicating the same (or similar) timing of precipitation and diagenetic conditions. (2) Pore-filling (0-9 %; average 2.13 %; Figure 4.11B). The illite fills and bridges intergranular pores, reducing reservoir porosity and permeability. (3) Grain- and/or cement-replacive illite (0-17 %; average 1.89 %; e.g., Figure 4.11C). Replacive illite occurs as replacement of kaolinite (e.g., Figure 4.11C), smectite (e.g., Figure 4.11D), and dissolved feldspar and mica grains.

Mixed layer illite/smectite (I/S) mainly occur as: (1). Grain-coating. The mixed-layer illite/smectite coats detrital grains (e.g., Figure 4.11E) and also prevent the formation of quartz overgrowth when they coat detrital quartz . (2) Detrital pore-filling cement (0.3-44 %; average 10.26 %) (Figure 4.6A & B). Illite/smectite fills intergranular pores, lowering reservoir quality. It transforms into illite with increasing depth and temperature (e.g., Figure 4.11D). (2) Grain-replacive (0.3-4.7 %; average 0.05 %). Partially or completely dissolved, detrital feldspar and mica grains are replaced by mixed layer illite /smectite, which are then converted to illite at depth.

Kaolinite, which is characterized by vermicular or booklet forms, occurs as: (1) grain-replacive (0-11 %; average 0.36 %). Replacive kaolinites occupy leached feldspar and mica grains, reducing secondary porosity (e.g., Figure 4.11B). (2) Pore-filling kaolinite (0-14.7 %; average 1.81 %) (Figures 4.10F & 4.11F). The intergranular, pore-filling kaolinites form adjacent to etched feldspar and mica grains, that is, in open, intergranular pores. Although the intergranular kaolinites contain abundant microporosity, they cause significant reduction of reservoir quality by occluding porosity.

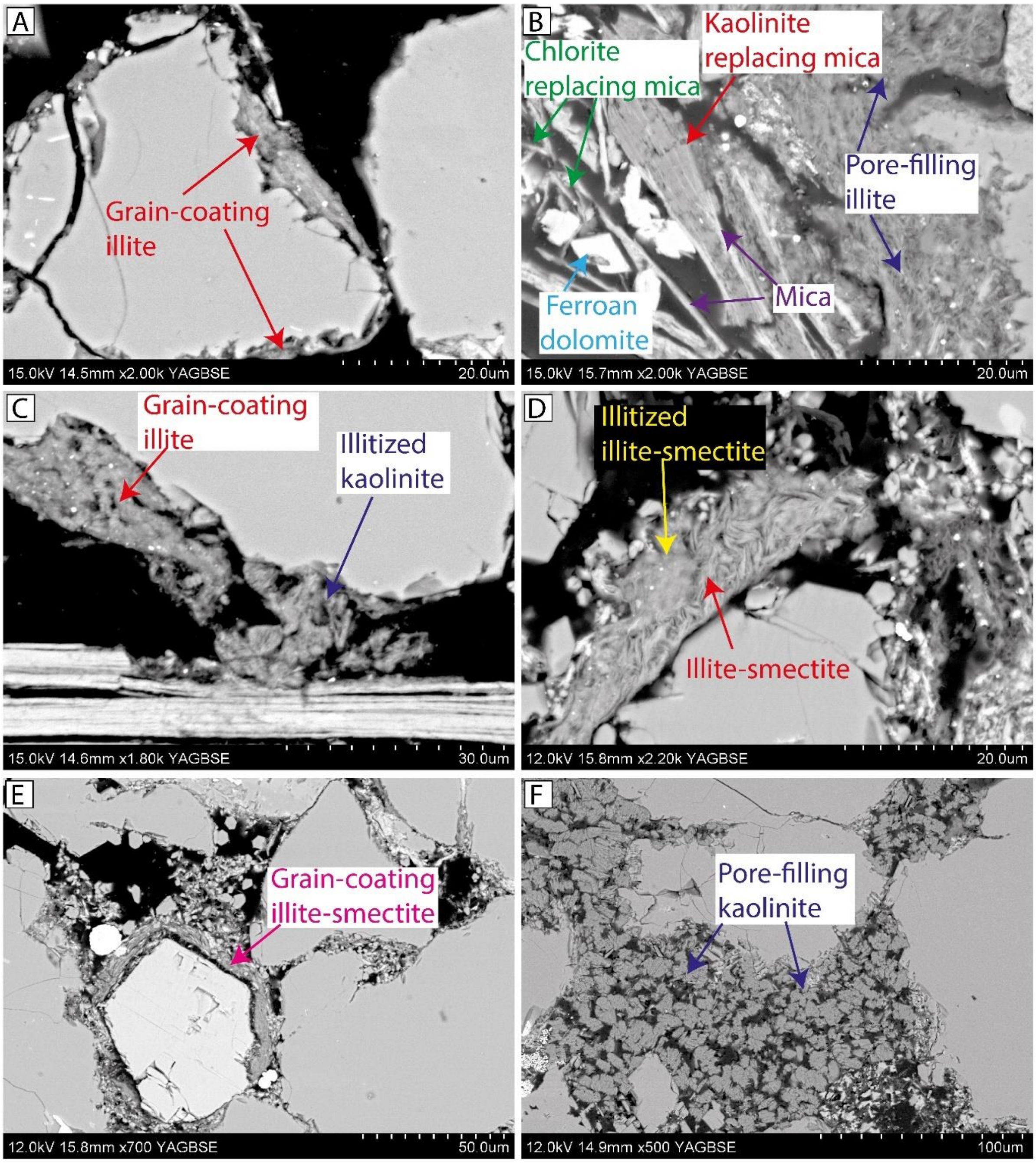

Figure 4.11. BSEM images showing the type and mode of occurrence of illite, illite-smectite, and kaolinite in the studied Forties Sandstone Member. (A) BSEM image showing grain-coating illite inhibiting the development of quartz cement; (B) BSEM image of pore-filling illite and grain-replacive chlorite, kaolinite and ferroan dolomite. The detrital biotite being altered serves as a precursor for chlorite, ferroan dolomite, and kaolinite; (C) BSE image of illitized kaolinite. The detrital mica grain (bottom) seems to have served as a precursor for kaolinite, which was then illitized to form grain-coating and pore-filling kaolinite; (D) BSEM image of illite-smectite being replaced by illite, filling intergranular porosity and destroying reservoir quality; (E) BSEM image of grain-coating, mixed-layer illite smectite forming a complete coat around a heavy mineral grain; (F) BSEM image showing pore-filling, largely-vermiform kaolinite destroying intergranular porosity.

To effectively evaluate the role authigenic, pore-filling clays (chlorite, illite, and kaolinite) on reservoir quality of the Forties Sandstone Member, samples with ductile grains and carbonate cements contents higher than 5 % each were excluded because such samples might have been subjected to intense mechanical compaction and pervasive carbonate cementation, respectively. The results of the analysis are shown in Figure 4.12A-F, suggesting that the clay minerals have variable impacts on reservoir quality. Chlorite content of between 3 and 10 % can lower intergranular (thin section) porosity and permeability to < 5 % and < 1 mD, respectively (Figure 4.12A & B). On the other hand, plots of illite against porosity and permeability (Figure 4.12B & C) show no discernible trend, probably due to fibrous morphology and smaller crystal size; however, little illite content as low as 2 % can have detrimental impact on reservoir permeability (< 1 mD) (Figure 4.12D), due to its pore-bridging effect. Furthermore, kaolinite content as low as 2 % can significantly occlude intergranular porosity and block pore throats, probably due to their larger crystal size and blocky morphology, lowering porosity and permeability to < 5 % and < 1 mD, respectively (Figure 4.12E & F).

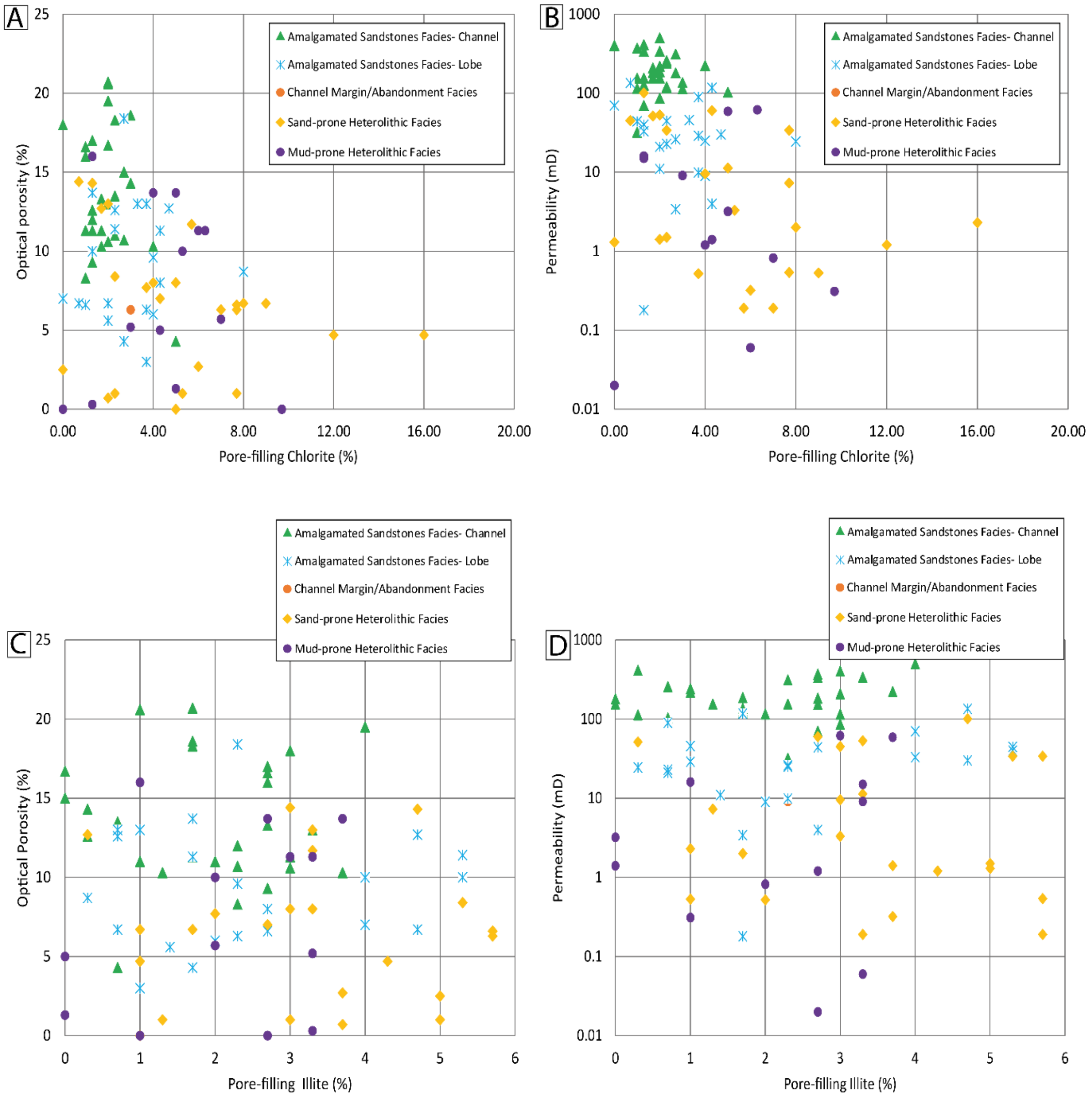
A
Optical porosity (%)
25
20
15
10
5
0
0.00
4.00
8.00
12.00
16.00
20.00
Pore-filling Chlorite (%)
▲ Amalgamated Sandstones Facies- Channel
✳ Amalgamated Sandstones Facies- Lobe
● Channel Margin/Abandonment Facies
◆ Sand-prone Heterolithic Facies
● Mud-prone Heterolithic Facies
B
Permeability (mD)
1000
100
10
1
0.1
0.01
0.00
4.00
8.00
12.00
16.00
20.00
Pore-filling Chlorite (%)
▲ Amalgamated Sandstones Facies- Channel
✳ Amalgamated Sandstones Facies- Lobe
● Channel Margin/Abandonment Facies
◆ Sand-prone Heterolithic Facies
● Mud-prone Heterolithic Facies
▲ Amalgamated Sandstones Facies- Channel
✳ Amalgamated Sandstones Facies- Lobe
● Channel Margin/Abandonment Facies
◆ Sand-prone Heterolithic Facies
● Mud-prone Heterolithic Facies
C
Optical Porosity (%)
25
20
15
10
5
0
0
1
2
3
4
5
6
Pore-filling Illite (%)
▲ Amalgamated Sandstones Facies- Channel
✳ Amalgamated Sandstones Facies- Lobe
● Channel Margin/Abandonment Facies
◆ Sand-prone Heterolithic Facies
● Mud-prone Heterolithic Facies
D
Permeability (mD)
1000
100
10
1
0.1
0.01
0
1
2
3
4
5
6
Pore-filling Illite (%)

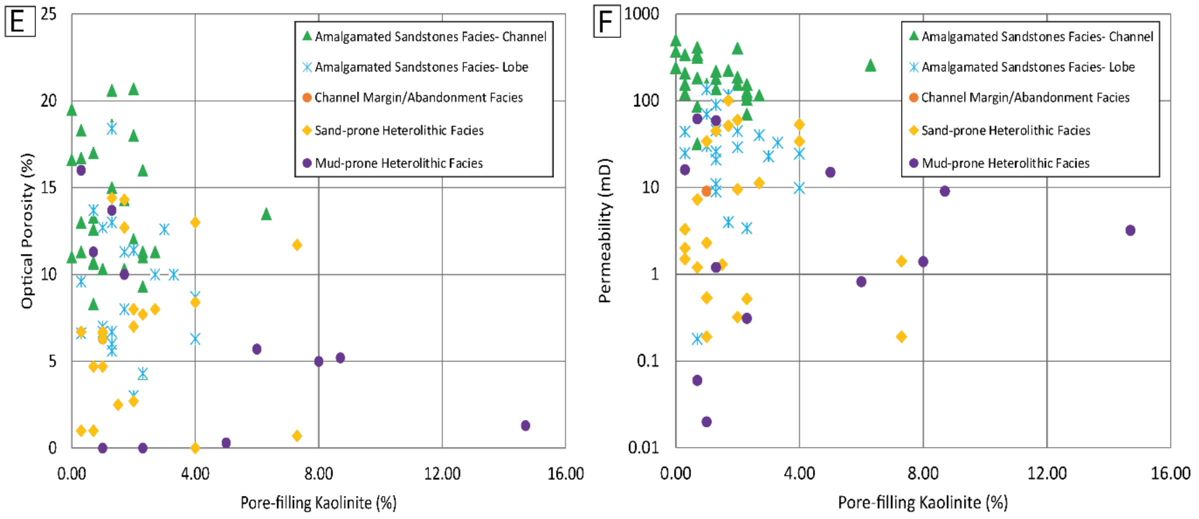

Figure 4.12. Impact of pore-filling, diagenetic clays on reservoir quality. (A) Plot of optical porosity against pore-filling chlorite. Porosity decreases with an increase in pore-filling chlorite. (B) Plot of permeability against pore-filling chlorite. Chlorite significantly lowers permeability by bridging and blocking pore throats. (C) Plot of optical porosity against pore-filling illite. The illite has variable impact on porosity. (D) Plot of permeability against pore-filling illite. Based on the plot, illite appears to have more impact on reservoir permeability by bridging pore throats than it has on porosity in (C). (E) Plot of optical porosity against pore-filling kaolinite. Kaolinite as low as 2 % can significantly occlude intergranular porosity. (F) Plot of permeability against intergranular kaolinite. The higher the kaolinite content, the lower the permeability.

4.5.5.3 Quartz overgrowths and microquartz

In the studied sandstones, quartz cement (0-9.3 %; average 2.73 %) occurs as euhedral and syntaxial overgrowths around quartz grains and grows into the intergranular pores (Figure 4.13A & B). The cement occurs as partial to complete cover around detrital quartz grains, reducing primary intergranular porosity (Figure 4.13C & D). Petrographically, the boundary between an overgrowth and a detrital quartz grain is usually identified by dust rim or thin clay coatings (< 2 µm). Due to lack of well-developed and thick clay coats, quartz overgrowths are more abundant in sandstones with clean quartz grain surfaces (Figure 4.13C & D) compared to those characterised by the presence of grain-coating clays. Ferroan calcites engulf, and hence postdates, quartz overgrowths. Where well-developed, grain-coating chlorite and illite/illite-smectite appeared to have inhibited quartz cementation (Figures 4.10A & 4.11A). In some samples, however, grain-coating chlorite and illite precipitated after quartz cementation, suggesting that they postdate quartz overgrowths. Nonetheless, the clay coatings will arrest further quartz cementation. Moreover, results of CL analysis have revealed that, in some samples, quartz cement are early in sandstones that have undergone less mechanical compaction (Figure 4.13 E & F).

Microquartz coatings occur in trace amount (< 0.3 %).

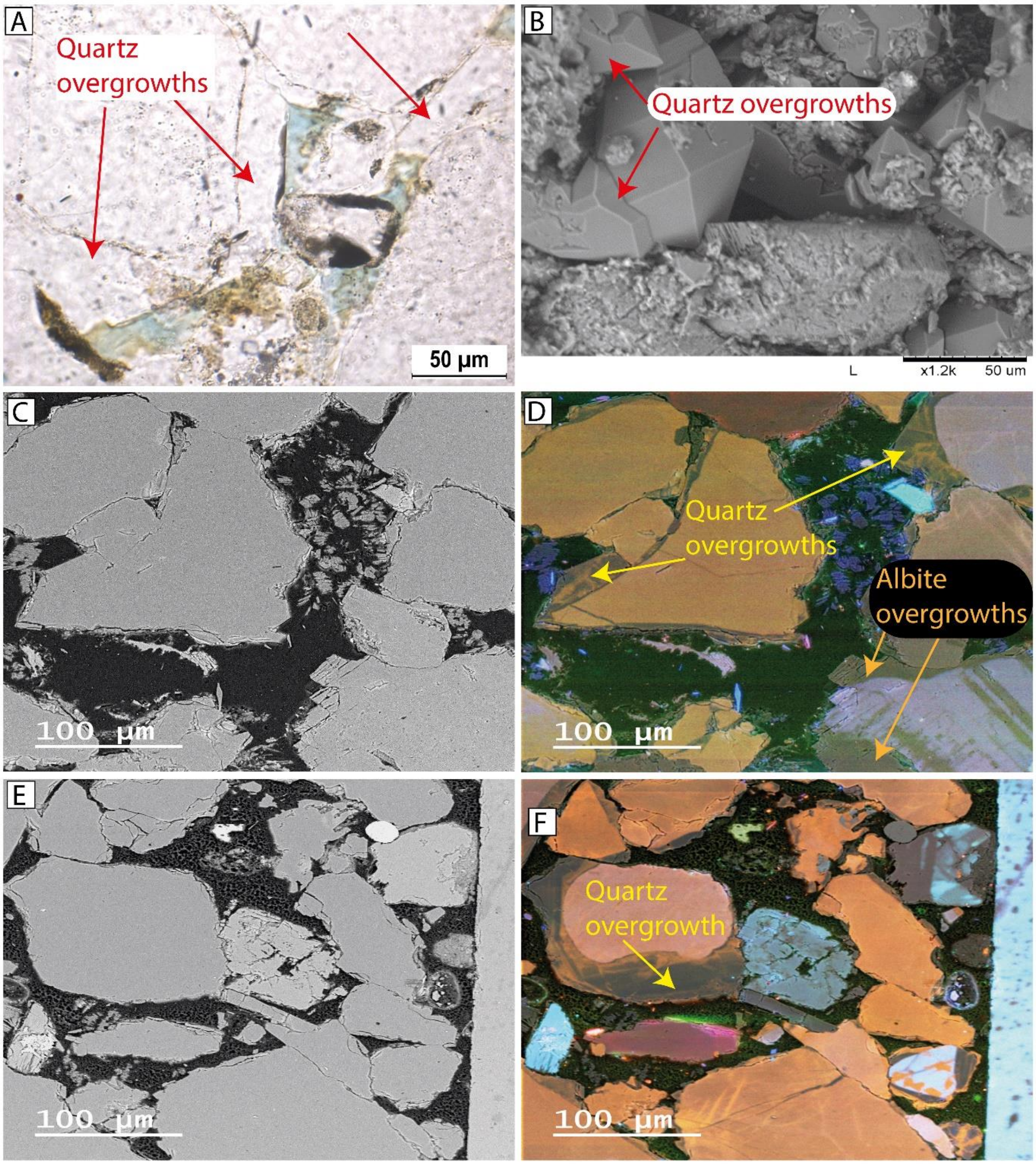

Figure 4.13. Thin-section photomicrographs, SEM, SEM-CL images showing the nature of quartz cements in the studied Forties Sandstone Member. (A) PPL photomicrograph of blocky, syntaxial quartz overgrowth destroying intergranular porosity. The quartz cement was developed due to absence of grain-coating clays; (B) SEM image showing the development of quartz cement in 3-dimensional view. The quartz cements grow into the pore space, occluding intergranular porosity; (C) SEM image of detrital grains. Note the absence of quartz overgrowth; (D) SEM-CL colour image showing quartz and albite overgrowths on detrital quartz and K-feldspar grains, respectively, from the same field view as (C); (E) SEM showing detrital grains in a less compacted sandstone. Note the absence of quartz overgrowth on the middle left grain; (F) SEM-CL colour image showing quartz overgrowth from the same image as (E). The overgrowth can be regarded as early and almost form a complete cover around the quartz grains.

4.5.5.4 Carbonates cements

Petrographic and SEM-EDS analyses have shown that carbonate cements in the Forties Sandstone Member are the second most abundant cements (0-43.6 %; average 3.49 %). The cements occur mainly as pore-filling, and consists of non-ferroan calcite, ferroan calcite, siderite, and dolomite.

Early, pre-compactional non-ferroan calcite occurs as patchy (Figure 4.14A) and blocky, poikilotopic (Figures 4.9C & 4.14B) cement. Occurring near mudstone-sandstone contacts, the blocky, poikilotopic calcite are characterized by floating grains and commonly show evidence of pervasive dissolution, probably due to influx of acidic or meteoric fluids, resulting in porosities that are either well-preserved and fairly connected or completely filled by late ferroan calcite (Figure 4.14C). The cement also forms from dissolution of bioclastic grains, probably transported from shelf to deepwater settings.

Ferroan calcite occurs as deep blue, patchy and pore-filling cement. The cement also occurs as replacement of pervasively dissolved non-ferroan calcite and feldspar grains (e.g., Figure 4.14C). Ferroan calcite engulfs, and hence postdates, the quartz overgrowths. The ferroan calcite cement also commonly precipitates where non-ferroan calcite had dissolved.

Siderite commonly occurs as pore-filling cement in loosely packed sandstones (Figure 4.14D). The cements are often associated with dolomite, pyrite, and dissolved mica grains, which are likely to have served as principal sources of Fe required for the precipitation of the siderite crystals rhombs (Mansurbeg et al., 2008). Frequently, the cements undergo dissolution (Figure 4.14D), probably because of the influx of meteoric fluids during sea level lowstand or due to influx of acidic fluids from organic source rocks.

Dolomite occurs as both pore-filling and grain-replacive cement, which frequently form in the vicinity of leached mica grains (Figures 4.10E and 4.11B). Dolomites are closely associated with siderite and pyrite.

Plots of pore-filling carbonate cements against intergranular porosity (Figure 4.15A) and permeability (Figure 4.15B) show that carbonate cements have had less impact on reservoir quality, except where the cements exceed 20 % by volume, decreasing intergranular porosity and permeability to < 5 % and < 1 mD, respectively (Figure 4.15A & B)

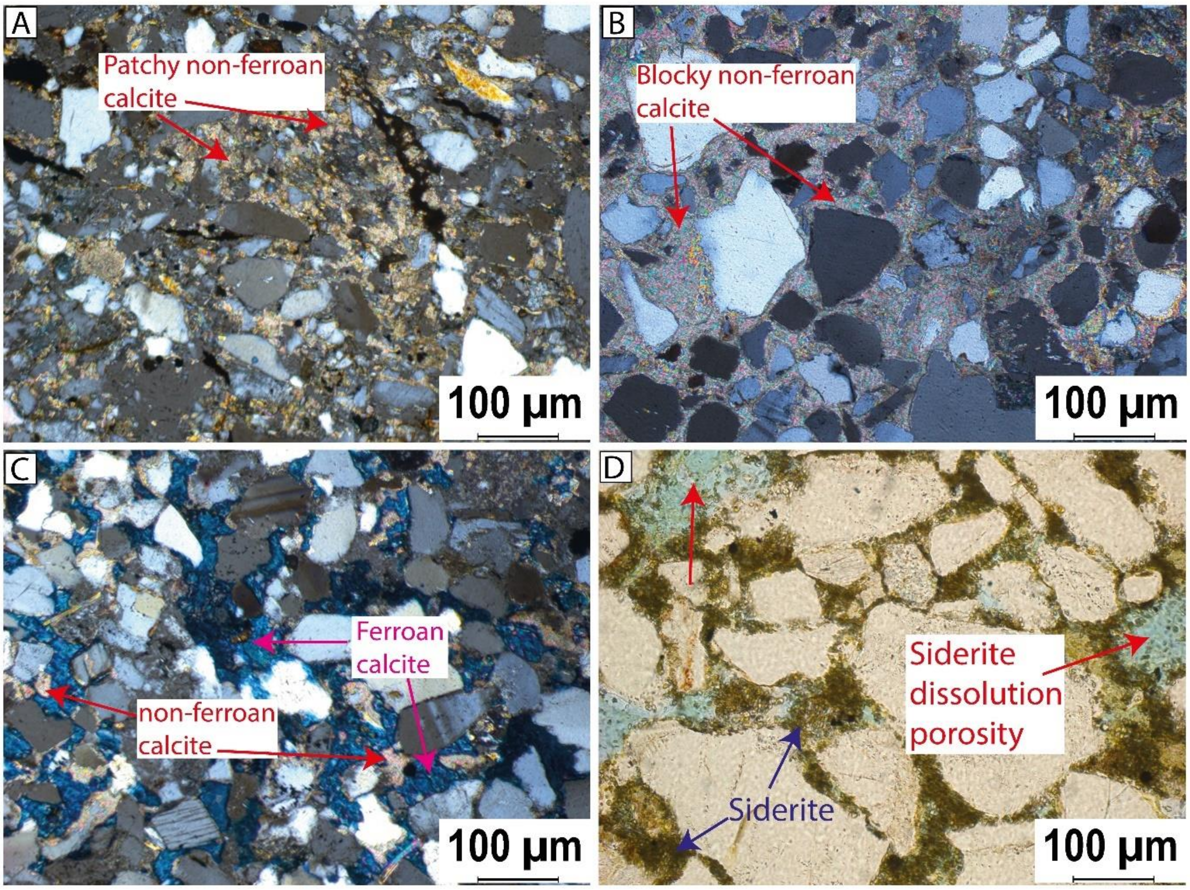

Figure 4.14. Thin-section photomicrographs showing the types and mode of occurrence of carbonate cements and their dissolution. (A) XPL photomicrograph of patchy, non-ferroan calcite destroying intergranular porosity; (B) XPL photomicrograph of early, blocky, poikilotopic non-ferroan calcite destroying reservoir quality; (C) XPL photomicrograph showing the formation of ferroan calcite from replacement of non-ferroan calcite. Notice the remnant non-ferroan calcite (red arrows); (D) PPL thin-section photomicrograph showing siderite cement being dissolved, creating secondary, intergranular porosity. [PPL= plane polarized light; XPL= cross polarized light].

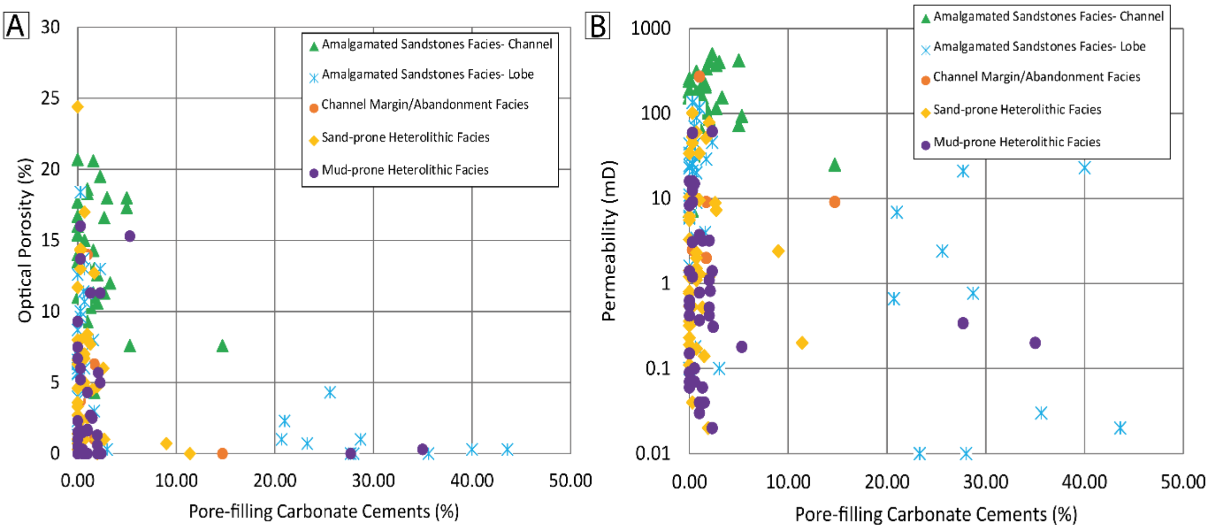

Figure 4.15. Role of pore-filling carbonate cements on reservoir quality. (A) Plot of optical porosity against pore-filling carbonate cements. The plot shows that carbonate cements have less impact on porosity, unless where well-developed (> 20% by volume). (B) Plot of permeability against pore-filling carbonates. The impact of carbonate cements on permeability is similar to the one on porosity, where well-developed carbonate cements (of > 20 % by volume) have deleterious impact on both porosity and permeability and, hence, on reservoir quality.

4.5.6 Precipitation temperatures of carbonate cements

Table 4.3 shows the results of the carbon and oxygen isotopes analysis for carbonate cements and their calculated temperatures of precipitations. The carbon and oxygen isotopes values range from -21.12 to +9.48 PDB (average -7.04) and -13.55 to -4.99 PDB (average -9.43), respectively (Table 4.3). The precipitation temperatures for the carbonate cements were calculated using fractionation equations of Friedman and O'Neil (1977) for calcite, Matthews and Katz (1977) for dolomite, and Carothers et al. (1988) for siderite. The oxygen isotope ($\delta^{18}O$) values for the Central North Sea's Early Tertiary meteoric and sea waters, which precipitated the carbonate cements, were -10 ‰ and -0.9 ‰ respectively (Shackleton and Kennett, 1974; Stewart, 1995). Results of the temperature calculations indicate that the precipitation temperatures for non-ferroan calcites range from -4 ˚C to 33 ˚C (average 17 ˚C) under meteoric pore waters, and 35 ˚C to 94 ˚C (average 68 ˚C) under marine pore waters (Table 4.3). Precipitated under marine pore water, the non-ferroan calcites were formed at temperatures close to that of the maximum burial (120-130 ˚C; Figure 3.3A & B), which is highly unlikely based on petrographic evidence of floating grains in the cement (e.g., Figure 4.14B). The non-ferroan calcite, therefore, is assumed to have precipitated in meteoric pore fluid. Similarly, ferroan calcite is believed to have precipitated under marine pore fluid based on the very light carbon isotope values and the fact that they replace non-ferroan calcite, with precipitation temperatures ranging from 57 °C to 90 °C (average 67 °C) under seawater (Table 4.3). Dolomite precipitation temperatures range between 54 °C and 56 °C (average 55 °C) under marine porewater. The precipitation temperatures for siderite range from 32 °C to 47 °C (average 40 °C) (Table 4.3) under marine condition.

Table 4.3. Stable isotope data and precipitation temperatures for carbonate cements of the Forties Sandstone Member.

Field/Well	**Depth (m)**	**Carbonate cement type**	**$\delta^{13}C$ VPDB**	**$\delta^{18}O$ VPDB**	**$\delta^{18}O$ SMOW (Calculated, ‰)**	**Temperature (°C) $\delta^{18}O$ SMOW = -10 ‰**	**Temperature (°C) $\delta^{18}O$ SMOW = -0.9 ‰**
Nelson/22/11-6	2206.45	Non-Ferroan Calcite	-8.66	-12.18	18.35	26	83
Nelson/22/11-6	2210.41	Non-Ferroan Calcite	-2.32	-6.54	24.16	2	44
Nelson/22/11-6	2211.02	Non-Ferroan Calcite	-3.98	-8.82	21.82	11	58
Nelson/22/11-6	2211.02	Non-Ferroan Calcite	-4.30	-8.96	21.68	11	59
Montrose/22/17-A12	2496.31	Non-Ferroan Calcite	-7.38	-11.94	18.60	25	81
Arran/23/16b-9	2710.28	Non-Ferroan Calcite	-4.12	-10.23	20.36	17	68
Everest/22/10a-4	2538.07	Non-Ferroan Calcite	-7.22	-13.27	17.23	31	92
Everest/22/10a-T6	2499.97	Non-Ferroan Calcite	-5.63	-13.55	16.94	33	94
Pierce/23/27-5	2726.74	Non-Ferroan Calcite	-2.47	-4.99	25.77	-4	35
Pierce/23/27-5	2727.05	Non-Ferroan Calcite	-5.70	-9.07	21.56	12	60
Pierce/23/27-5	2727.05	Non-Ferroan Calcite	-5.66	-9.06	21.57	12	60
Pierce/23/27-8	2477.11	Non-Ferroan Calcite	-7.78	-12.09	18.45	25	82

Montrose/22/17-1	2510.33	Feroan Calcite	-19.04	-10.67	19.91	11	71
Montrose/22/17-1	2510.03	Feroan Calcite	-21.12	-8.62	22.02	11	57
Montrose/22/17-1	2508.05	Feroan Calcite	-20.45	-8.82	21.82	10	58
Arran/23/16b-9	2710.89	Feroan Calcite	-8.53	-13.10	17.41	19	90
Montrose/22/17-1	2508.5	Feroan Calcite	-20.40	-8.79	21.84	30	58
Pierce/23/27-8	2479.55	Siderite	9.48	-9.30	21.33	-	47
Everest/22/10a-4	2537.46	Siderite	0.26	-5.88	24.85	-	32
Everest/22/10a-4	2556.97	Dolomite	0.59	-6.25	24.46	-	56
Everest/22/14a-2	2620	Dolomite	-3.40	-5.99	24.73	12	54

4.5.7 Paragenesis

Diagenetic cements in the Forties Sandstone Member were formed during both early (eodiagenesis) and late (mesodiagenesis) diagenesis (Figure 4.16). The diagenetic processes in the sandstones have been described *sensu* Morad et al. (2010).The early, eodiagenesis occurs at shallow depth and at temperatures < 70 °C, whereas the late, mesodiagenesis occurs at deeper burial (> 2km) and at temperatures > 70 °C (Morad et al., 2010) (Figure 4.16). The early diagenetic products in the Paleocene turbidite sandstones have been controlled by several interrelated parameters that include depositional facies, detrital composition, relative sea level, and pore-water chemistry (Mansurbeg et al., 2008). Early diagenetic alterations have exerted a strong control on the pattern of late diagenetic alterations and reservoir quality evolution of the sandstones.

Mechanical compaction started during eodiagenesis and has continued into mesodiagenesis (Figure 4.16). With the exception of ferroan calcite, which was formed during late diagenesis, all other carbonate cements were formed during early, eodiagenesis (Figure 4.16). Feldspar and mica grains dissolution and the resulting kaolinitization started during eodiagenesis and continued into mesodiagenesis. Illitization of kaolinite and albitization of feldspars started during mesodiagenesis. Grain coating smectite was formed during eodiagenesis, which was largely converted to chlorite, illite-smectite, and illite during mesodiagenesis. Pyrite is a minor cement that was formed during eodiagenesis, probably due to sulphate reduction. Hydrocarbon emplacement started during eodiagenesis and continued into mesodiagenesis.

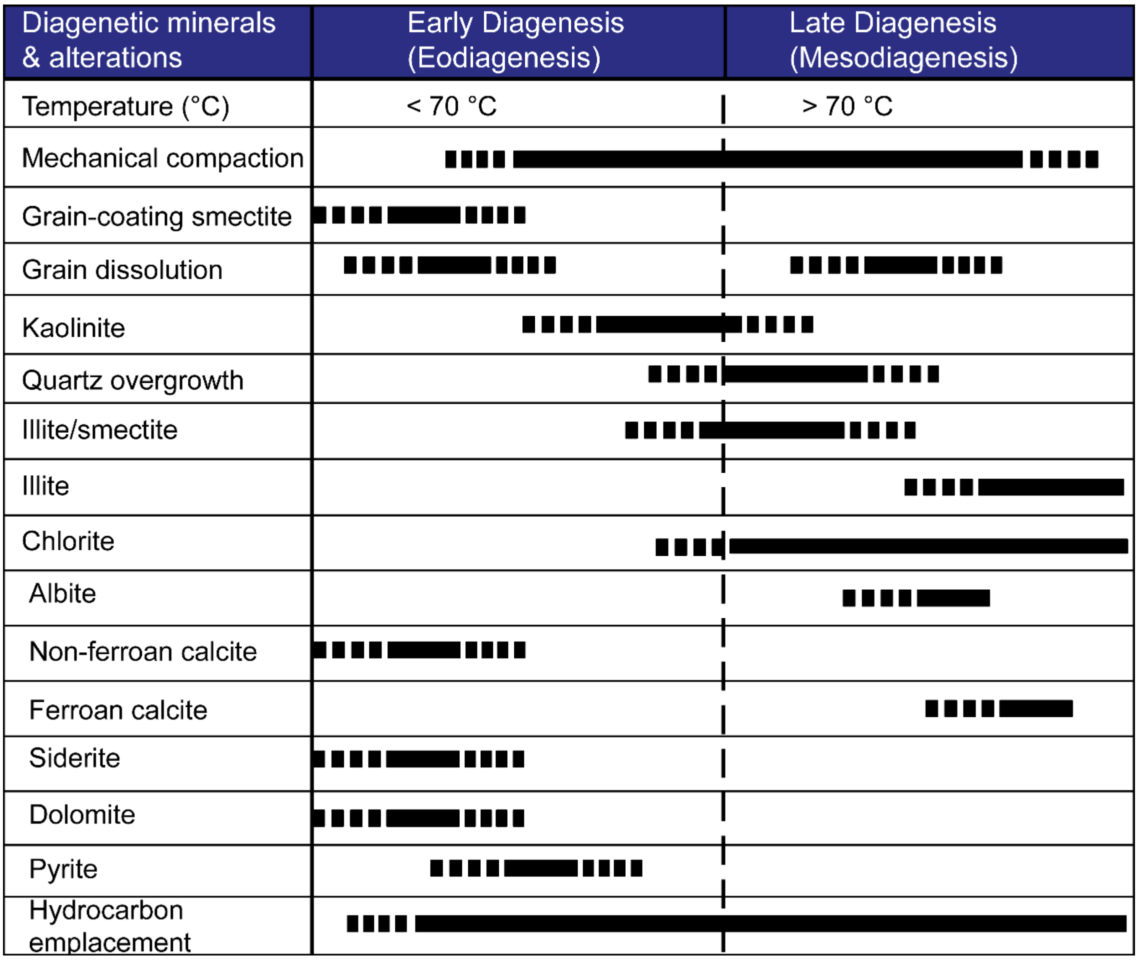

Figure 4.16. Paragenetic sequence of diagenetic processes and products in the Forties Sandstone Member. The transition from eodiagenesis to mesodiagenesis occurs at a temperature > 70 °C (as suggested by Morad et al 2010), where, for instance, kaolinite begins to transform to illite, and smectite to chlorite.

4.6 Discussions

4.6.1 Origin of grain-coating clays

Detrital clay coats serve as important precursors for authigenic clay coats in siliciclastic reservoirs (Bloch et al., 2002; Matlack et al., 1989; Pittman et al., 1992; Stricker, 2016; Worden and Morad, 2003). The origin of depositional, detrital clay coats in deep-water turbidites can be attributed to three sources: (1) clay coats inherited from shelf, which, depending on grain shape, might be partially or completely abraded during transport to deepwater environments (Sullivan et al., 1999; Yezerski and Shumaker, 2018). (2) detrital, grain-coating clays emplaced during sediments redistribution and dewatering of high-density flows (Houseknecht and Ross, 1992; Porten et al., 2019). (3) clay coats emplaced due to alteration of rock fragments (Bahlis and de Ros, 2013) and detrital biotite (e.g., Figure 4.10 C, D & E).

In the studied sandstones, the occurrence of clay coatings with brownish to yellow birefringence has been observed, which indicates detrital origin probably from smectite (Bahlis and de Ros, 2013; Ulmer-Scholle et al., 2015) (e.g., Figure 4.6A & B). These clay coatings are especially preserved in detrital grains that have concave grain shape, known as 'embayment' (Figure 4.17 A, B & C). The curve-shaped grains help in preserving inherited clay coats because they are resistant to abrasion. This, therefore, suggests that the detrital clay coats have been inherited from continental, deltaic, or shallow marine/shelf environments. Similarly, diagenetic clay coatings could grow from remnant clay coats on sub-angular to sub-rounded grains during burial, often forming complete coats.

The occurrence of water-escape structures has also been observed in the studied cores of the Forties Sandstone Member (e.g., Figure 4.17D), indicating that detrital clay coatings have been emplaced by sediment dewatering. The detrital clay coatings have undergone transformations during diagenesis and serve as precursors to and/or nucleation sites for the formation of authigenic grain-coating clays.

Alteration of volcanic and metamorphic rock fragments (Figure 4.10C & D), transformation of authigenic clays (e.g., kaolinite to illite) (Figure 4.11C), and dissolution/alteration of ferromagnesian grains (e.g., mica) (Figure 4.10E) have contributed to the formation of grain-coating clays in the sandstones.

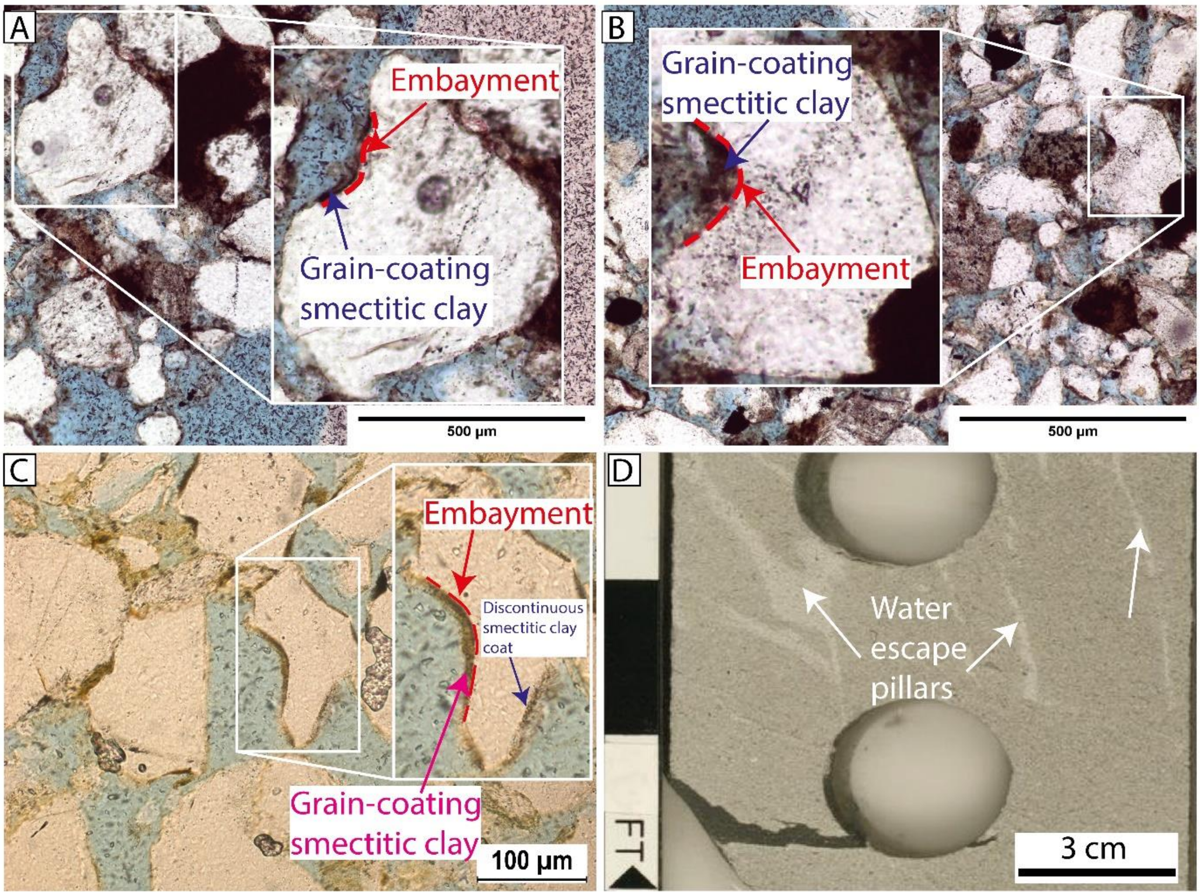

Figure 4.17. Preservation of detrital, smectitic clay coatings on detrital grains characterized by embayments (curve shape) and emplacement of detrital clay coatings due to sediment dewatering. (A-C) PPL thin-section photomicrographs showing how detrital grain-coating clays are preserved on grains characterized by embayments, which are resistant to abrasion during transport. Notice the absence or discontinuity of clay coatings on the convex parts of the grains, on which the clay coats are susceptible to abrasion; (D) Core image of water escape pillars in the Forties Sandstone, formed due to sediment dewatering. This process results in the distribution and emplacement of clay coatings in massive deep-water turbidite sandstones (*see* Porten et al., 2019). [PPL= plane polarized light].

4.6.1.1 Chlorite

To explain the formation of chlorite in the Forties reservoirs, possible precursors have been reviewed. (1) transformation of smectite (Berger et al., 2009; Shaw and Conybeare, 2003; Worden et al., 2020). The intrinsic association between chlorite and mixed-layer chlorite/smectite suggests that the authigenic chlorites are a product of smectite transformation during late shallow and deep burial diagenesis. The formation of chlorite from smectite requires high alkaline P^H and high Fe and Mg ion concentrations (Chen et al., 2011), and the transformation commonly occurs through a mixed layer chlorite-smectite stage (Chang et al., 1986; Tian et al., 2008).

Grain-coating and pore-filling chlorites in the Forties Sandstone Member have been analysed using SEM-EDS using Fe/Mg ratio (Hillier and Velde, 1992):

Based on the Fe/Mg ratio and EDS elemental maps (Figure 4.18 A-D), both pore-filling (e.g., Figure 4.18A & B) and grain-coating (e.g., Figure 4.18C & D) chlorites in the studied Forties Sandstone Member can be classified as Fe-rich (Grigsby, 2001), with average Fe/Mg ratio ranging from 0.71-0.83. The Fe content increases towards open pores, indicating interaction with pore fluids rich in Fe. The Fe might have been supplied from alteration of biotite (e.g., Figure 4.10E) and/or alteration of volcanic and metamorphic fragments (e.g., Figure 4.11C & D).

(3) Alteration of Fe- and Mg-rich grains such as mica (biotite), mudclasts, amphibole, metamorphic, and volcanic rock fragments serve as adequate sources of Fe and Mg ions required for the formation of chlorite (e.g., Anjos et al., 2003; Pittman et al., 1992; Worden and Morad, 2003). Dissolution of Fe- and Mg-rich minerals releases Fe and Mg ions, which remain in the pore fluids and later precipitate as neoformed chlorite. Figure 4.10C shows the dissolution of a volcanic fragment and the process has resulted in the precipitation of chlorite in the Forties Sandstones. Furthermore, the alteration of detrital biotite has led to the formation of both grain-coating (e.g., Figures 4.10E and 4.18C & D) and grain-replacive chlorite (e.g., Figure 4.10 E).

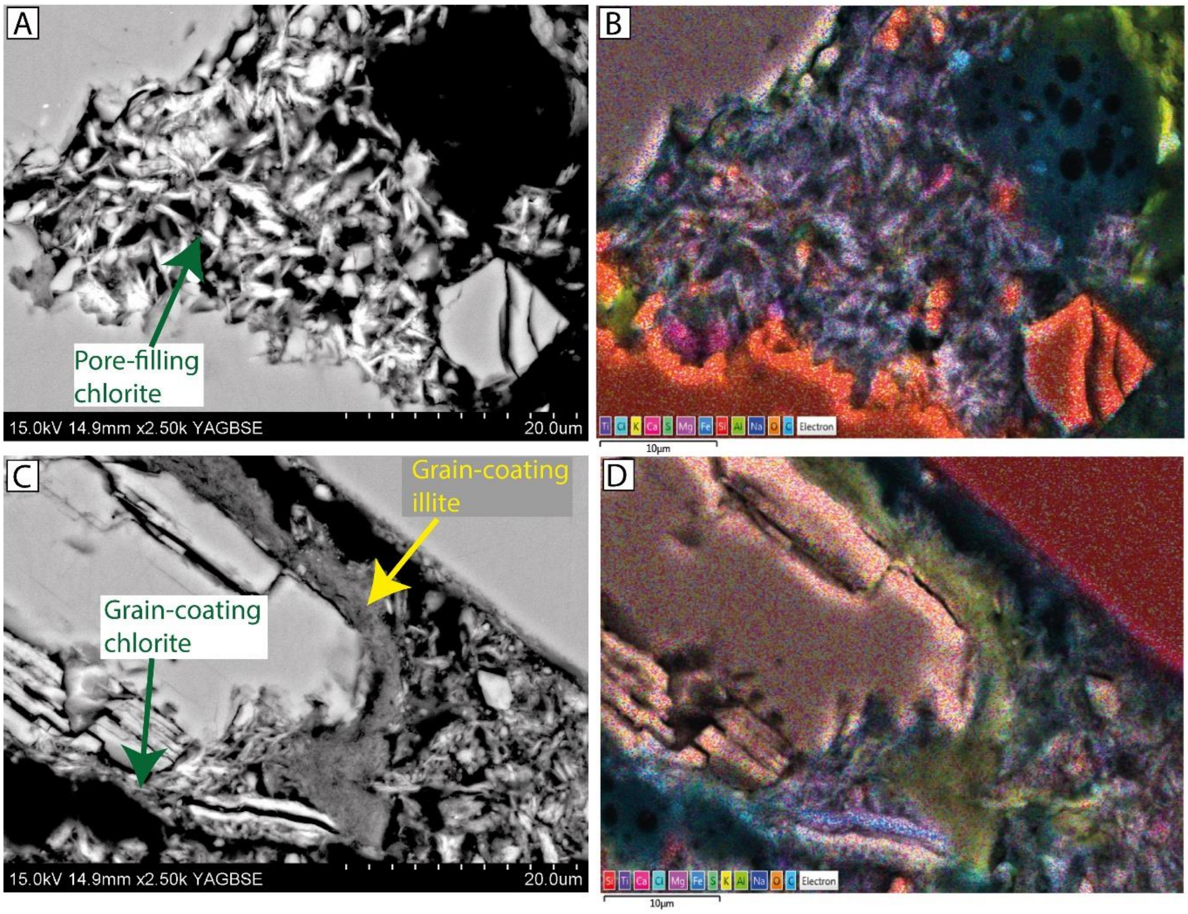

Figure 4.18. Pore-filling and grain-coating chlorite and elemental maps showing the distribution of Fe element in the chlorites. Based on the colour maps (B and D), the chlorites are Fe-rich. (A) BSEM image showing pore-filling chlorite; (B) Elemental map showing the distribution of Fe element in the chlorite from the same field view as (A); (C) BSEM image showing grain-coating chlorite and illite. Pierce field, well 23/27-5, 2729.48 m TVDSS; (D) Elemental map showing the distribution of Fe element in the chlorite from the same field view as (C).

4.6.1.2 Illite

Illite occurs as a pore-filling cement (Figure 4.11B) and as grain coat (Figure 4.11A) on detrital grains. Thin-section petrography and SEM analysis indicate that grain-coating illite are often absent at grain contacts, suggesting a largely late diagenetic origin. Two mechanisms explain the origin of the illite observed in the sandstones: (1) transformation of smectite through a mixed layer illite/smectite (e.g., Figure 4.11D). The alteration of smectite into illite occurs at a temperature below 90 °C (Worden and Morad, 2003) and may also occur at a very low temperature between 20 °C and 30 °C (Bautier et al., 1992) and at shallow depth (< 500 m). Illite formed from smectite has flaky morphology. (2) transformation of kaolinite into illite (e.g., Figure 4.11 C), which occurs at a temperature above 120 °C (Bjørlykke et al., 1995). Illitization of kaolinite requires a source K^+ to complete (Lai et al., 2018), and the observed dissolution of K-feldspar in the sandstones might have provided the K^+ required for the illitization process. Additionally, microscopic observations reveal that the quantity of illite generally increases with depth, particularly in the deeper medial and distal wells, whereas that of kaolinite decreases with depth, thereby corroborating the concept of illitization of kaolinite. Illites formed from kaolinite have sheet-like morphology. (3) Alteration of feldspar and muscovite. Illite replaces feldspar and mica grains and fills their grain-dissolved pores. In some sandstone samples of the Forties Sandstone Member, illite co-exists with chlorite (Figure 4.18 C & D), indicating similar conditions and timing of formation.

4.6.1.3 Kaolinite

Kaolinite is an early diagenetic cement in the Forties Sandstone Member, and the kaolinite in the Paleocene sandstones of Central North Sea have been interpreted to have formed from feldspar dissolution during “meteoric-water flushing” (Stewart, 1995). Meteoric flushing in turbidite sandstones occurs at shallow burial depth as a result of a major fall in the relative sea level, precipitating vermiform kaolinite (Mansurbeg, 2007; Mansurbeg et al., 2008). During the Early Tertiary, within the Central North Sea and at shallow burial (< 500 m), a combination of delta progradation and sea level fall occurred after the deposition of the sandstones of the Montrose Group (Reynolds, 1994), which is likely to have provided sufficient head required for meteoric flushing (Stewart, 1995). Furthermore, blocky kaolinite has been observed in the sandstones, which are probably products of late diagenesis. The blocky kaolinite forms at higher temperature (≤ 100 °C) than the lower-temperature, vermiform kaolinite (Stewart, 1995). The blocky kaolinite is likely to have formed as the product of dissolution and alteration of detrital feldspar by organic acids generated from hydrocarbon source rocks (Wang et al., 2019), or due to transformation of kaolinite into dickite in the absence of K^+. Kaolinite transforms into illite in the presence of K^+ at temperature above 120 °C (Bjørlykke et al., 1995).

4.6.2 Impact of grain-coating and pore-filling clays for reservoir quality of the Forties Sandstone Member

Grain-coating clays enhance porosity preservation in deeply buried sandstones by inhibiting the development of ubiquitous, pore-occluding quartz overgrowths (Ajdukiewicz and Larese, 2012; Anjos et al., 2003; Berger et al., 2009; Ehrenberg, 1993; Pittman et al., 1992). Clay coatings can, however, significantly decrease reservoir quality when they occur as very thick coats, filling intergranular porosity (Morad et al., 2010; Taylor et al., 2010. Regardless of coating mineralogy, origin and morphology, highest porosities can be preserved where grain-coating clays are well-developed (Pittman et al., 1992; Stricker, 2016).

The impact of grain-coating clays on reservoir quality preservation and quartz cement prevention is commonly evaluated by determining the extent or percentage of clay-coating coverage on sand grains (e.g., Busch et al., 2020; Dutton et al., 2018; Kordi, 2013). In the studied Forties Sandstone Member, measurements of grain-coating clays (chlorite and illite/illite-smectite) coverage have indicated that porosity and permeability are preserved with increasing clay-coating coverage (Figure 4.19 A & B). High porosity and permeability occur where grain-coating clays coverage exceeds 50 % (Figure 4.19 A & B). Similarly, generally low-quartz cement values were recorded where grain-coating clays coverage is above 50 % (Figure 4.20).

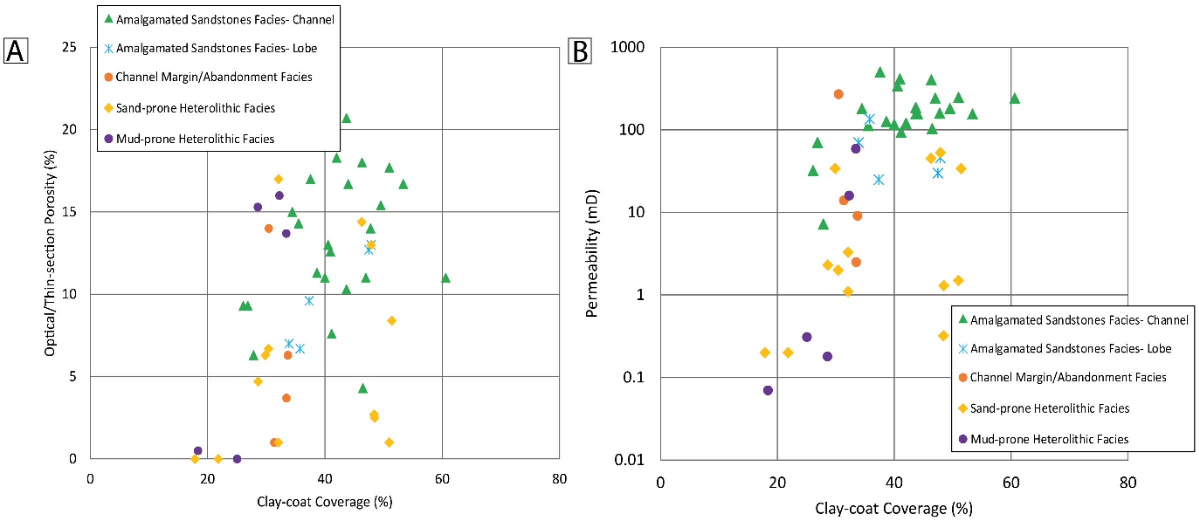

Figure 4.19. Relationship between clay-coating coverage and optical porosity and permeability in the Forties Sandstone Member. (A) Plot of optical porosity against clay-coating coverage. The plot shows a positive correlation. Porosity is preserved with increasing clay-coating coverage; (B) Plot of permeability against clay-coating coverage. The plot shows positive correlation. Reservoir permeability is preserved with increasing clay-coating coverage.

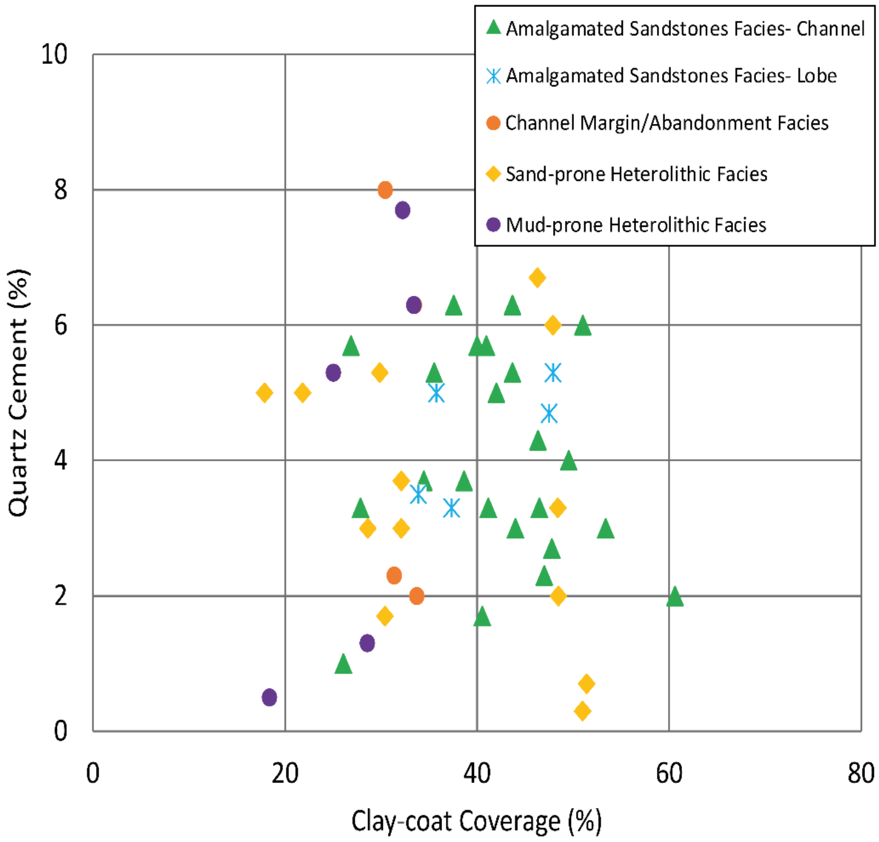

Figure 4.20. Relationship between quartz cement against clay-coating coverage. The plot shows negative correlation between quartz cement and clay-coating coverage. Quartz cement is inhibited when the clay-coating coverage exceeds 40 %.

Furthermore, plots of clay-coating coverage against depth and quartz cement against depth (Figure 4.21A & B) have indicated that, generally, coatings coverage increase with depth, resulting in a decrease in the volume of quartz cements. This suggests that as temperature increases, due to increasing burial depths, clay-coating coverage increases, which results in low quartz cementation (Figure 4.21 A & B). This interpretation also holds true for most of the sand-prone heterolithic facies (Figure 4.21A & B). Although some mud-prone heterolithic facies exhibit low clay-coating coverage, they still have low quartz cement volume (Figure 4.20A). This is probably because, apart from having grain-coating clays, the facies are characterized by high pore-filling clays, which are also effective in preventing quartz cementation as they cover surface area of grains (Porten et al., 2019; Shaw and Conybeare, 2003).

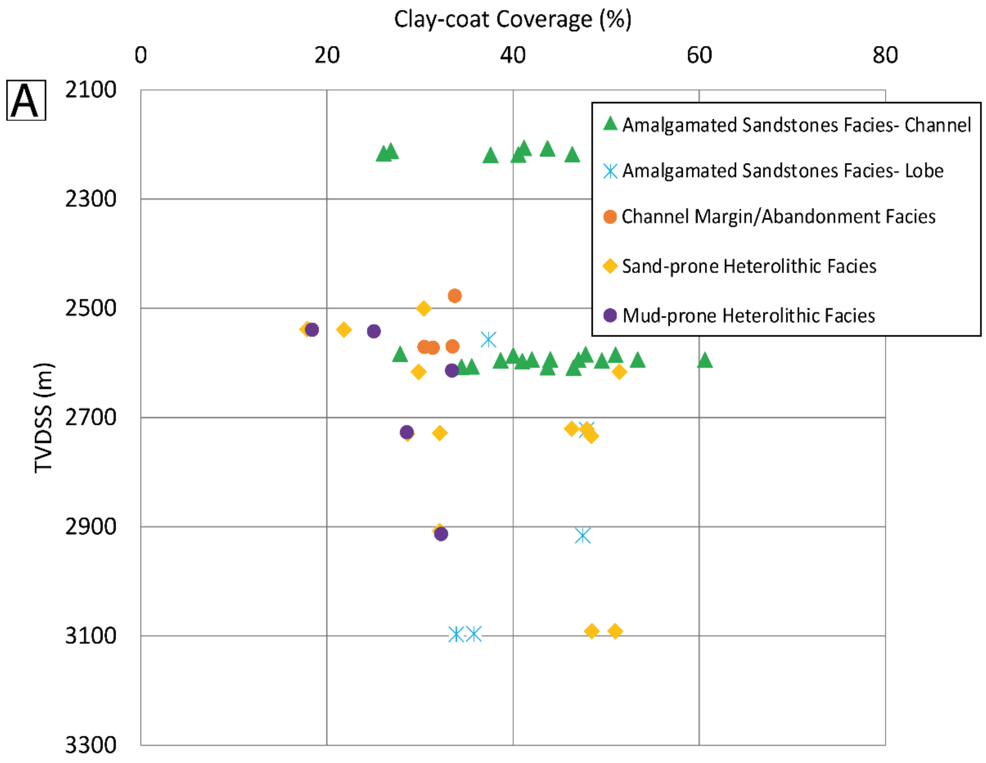

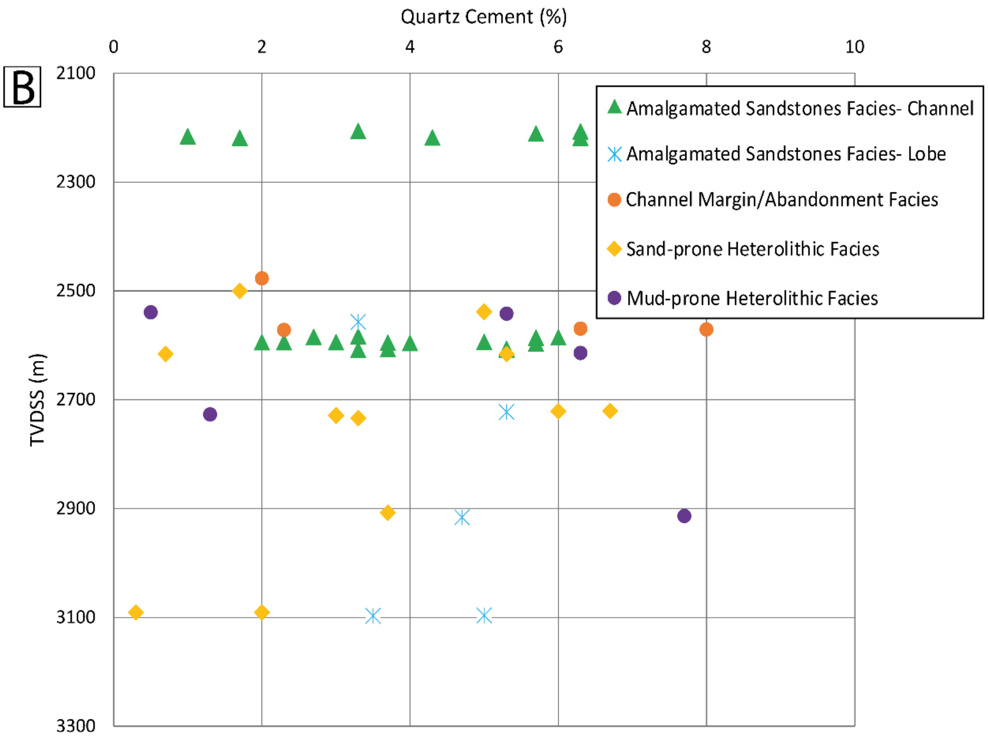

Figure 4.21. Variation of clay-coating coverage and quartz cement with depth. (A) Plot of clay-coating coverage against depth. The plot shows that, generally, as depth increases, clay-coating coverage also increases, notably in the amalgamated sandstones and sand-prone heterolithic facies, which leads to decrease in volumes of quartz cement in (B). (B) Plot of quartz cement against depth. Generally, quartz cement decreases with an increase in depth due to increasing clay-coating coverage.

While grain-coating clays have a positive impact on reservoir quality, pore-filling authigenic clays (chlorite, illite, and kaolinite) on the other hand, have negative impacts on reservoir quality (Figure 4.12A-F), by occluding porosity and bridging pore throats. The pore-filling clays, depending on their crystal size and morphology, have variable threshold values, beyond which they significantly impact reservoir quality. Pore-filling chlorite content of > 3-10 % has deleterious impact on intergranular thin-section porosity and permeability, decreasing them to < 5 % and 1 mD, respectively (Figure 4.12A & B). Because of it is fibrous appearance, authigenic illite has less impact on porosity than on permeability (Figure 4.12C & D), with a threshold value as low as 2 % for permeability and up to 6 % for porosity. Being coarser than illite and relatively chlorite, kaolinite as low as 2 % has negative impact on porosity and permeability (Figure 4.12E & F). With increasing salinity and pH, flocculation processes result in the distribution of clay minerals and other flocculated materials (Gibbs, 1985). This might result in the increase in pore-filling clays, thereby decreasing reservoir quality in turbidite sandstones.

4.6.3 Linking grain-coating clays coverage with grain size

Measurements of clay-coating coverage on at least 50 randomly selected detrital quartz grains alongside their long axis were carried out on 50 selected samples of the Forties Sandstone Member using the JMicrovision software package (v.1.3.3) based on the method described by Dutton et al. (2018). Average clay-coating coverage as well as mean grain size for each sample were then established. A plot of mean grain size against average clay-coating coverage (Figure 4.22) shows no discernible trend (with the coefficient of correlation, R^2, value of 0.004), suggesting that grain size has no impact on clay-coating coverage. Nevertheless, in terms of the average clay-coating coverage, the plot seems to suggest that, the finer the grains, the higher the average clay-coating coverage (Figure 4.22). This is probably due, in part, to size fractionation effect during transport by sediment gravity flows.

However, it is well-established in the literature that, because of their smaller surface area per volume, coarser-grained sands and sandstones require less amount grain-coating clays to form complete clay coats on detrital sand grains compared with their finer-grained counterparts (e.g., Bloch et al., 2002; Kordi, 2013; Shammari et al., 2020; Wilson, 1992; Wooldridge et al., 2017). In the Forties Sandstone Member, in contrast, grain size does not seem to typically impact clay-coating coverage (Figure 4.22).

Furthermore, during their long-distance transport from continental, deltaic or shallow marine/shelf environments to deep-water settings, sand grains with inherited clay coatings might be partly or pervasively abraded, removing the precursor clay coats especially from the convex parts of the sand grains (Bahlis and de Ros, 2013; Yezerski and Shumaker, 2018). Thus, sand grains that are characterized by indentations (or embayments) might have some remnant clay coatings (Figure 4.17 A, B & C). However, coarser-grained sands have been reported to be more susceptible to abrasion of clay coatings during transport than finer-grained sands (Ajdukiewicz et al., 2010). This probably explains the lack of significant impact of grain size on clay-coating coverage in the Forties Sandstone Member, and also suggests that the finer-grained, medial to distal fan heterolithic facies could potentially have well-preserved clay coats, resulting in good clay-coating coverage. Additionally, the findings of the present study support this interpretation. Clay coatings have been found to be discontinuous, probably due to abrasion, on convex parts of sand grains, whereas coatings are preserved on grains that have indentations or embayments (e.g., Figure 4.17 A, B & C).

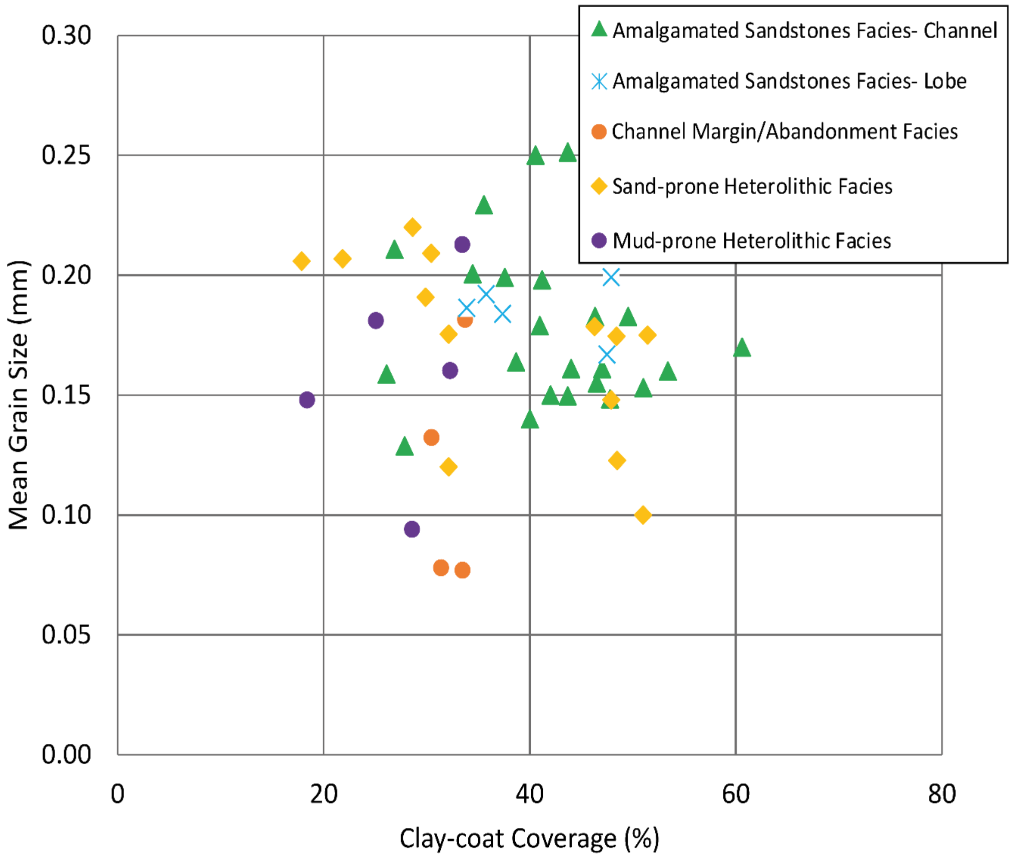

Figure 4.22. Relationship between grain size and clay-coating coverage. The trend shows no definite correlation, implying that grain size has no impact on clay-coating coverage. The plot, therefore, suggests that the heterolithic sandstones, which are commonly thought to make poor reservoirs, could potentially have good clay-coating coverage that could preserve reservoir quality.

4.6.4 Relationship between grain-coating clays and compaction

The role of compaction in sandstones is largely evaluated using the intergranular volume (IGV), which is the sum of primary intergranular porosity, cements, and detrital matrix (Paxton et al., 2002). It is established from petrographic point count data and reported as a percentage of the total rock volume. The IGV has been widely used as a key parameter for determining the role of compaction on porosity loss during sandstones burial, by estimating the initial, depositional porosity (e.g., Ehrenberg, 1995; Lander and Walderhaug, 1999; Paxton et al., 2002). In the Forties Sandstone Member, the point count analysis has shown that the IGV was reduced to an average value of 31.57 % (for all the analysed 191 samples).

A plot of grain-coating clays (sum of chlorite and illite/illite-smectite) against intergranular volume (IGV) (Figure 4.23A) has shown that sandstones with high amount of grain-coating clays (of up to 10 %) have undergone less mechanical compaction and, hence, exhibit overall, higher intergranular volume (IGV). Sandstones with lower amount of grain coating clays, in contrast, have been subjected to a significant mechanical compaction and reduction of intergranular pore space, resulting in lower IGV (Figure 4.23A). Where clay coats are thick and continuous, they would potentially arrest chemical compaction at deeper burial by inhibiting pressure dissolution at grain-grain contacts. This suggests that the grain-coating clays have acted as inhibitors of compaction in the sandstones.

Furthermore, a plot of optical, thin-section porosity against IGV (Figure 4.23B) supports the interpretation that samples with higher amounts of grain-coating clays and, thus, relatively higher porosity have undergone less mechanical compaction than samples with lower grain-coating clays and lower porosity.

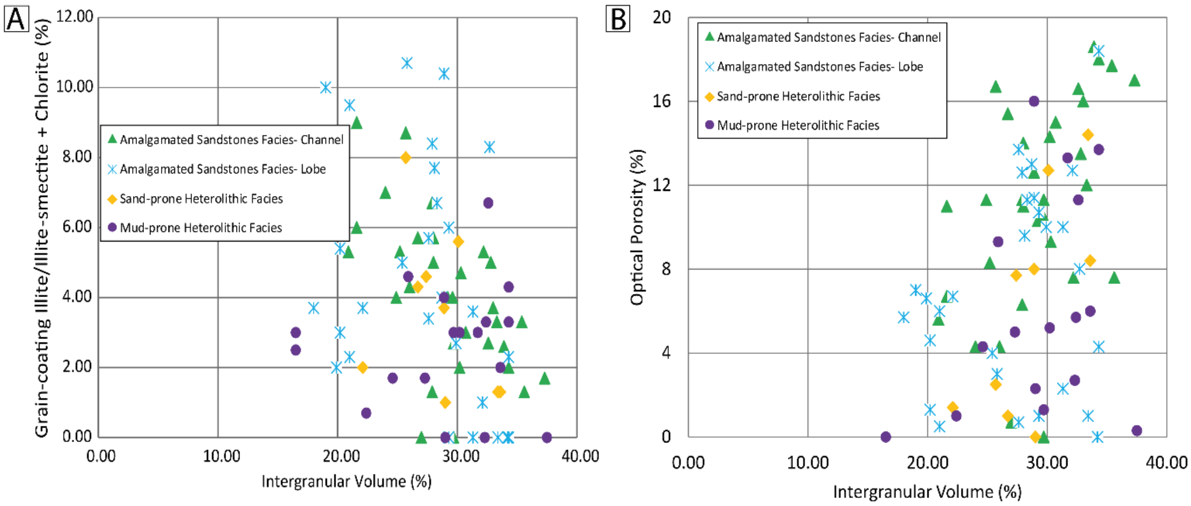

Figure 4.23. (A) Plot of grain-coating clays against IGV. The plot shows that the Forties sandstones with high grain-coating clays have been subjected to less mechanical compaction than the sandstones with lower grain-coating clays. (B) Plot of optical porosity against IGV corroborating the plot in (A), suggesting that sandstones with high porosity is preserved due to high grain-coating clays in the sandstones. Sandstones with low grain-coating clays have low porosity and, thus, low IGV. Note the datasets used in Figure 4.23 are the same as those used in constructing the plot of compaction porosity loss against cementational porosity loss in Figure 4.8.

4.6.5 Reservoir quality evolution of the Forties Sandstone Member

Figure 4.24 shows a simplified schematic model reflecting the various diagenetic processes, alterations, and products in the Forties Sandstone Member, indicating that diagenesis has had a significant impact on reservoir quality evolution of the sandstones. The diagenetic processes and products include: (1) mechanical compaction, which started during shallow burial and has continued into deep burial. Mechanical compaction involves grain rearrangement, grain fracturing and formation of pseudomatrix due to ductile deformation of micas and mudclasts. Overall, porosity loss by compaction was by grain rearrangement and ductile deformation. (2) formation of smectite coatings. Smectite coatings are one of the early clay minerals in the deep-water Forties Sandstone Member (Figure 4.24), and were inherited from continental, deltaic, and/or shallow marine/shelf environments, and/or were emplaced through early sediment dewatering in the sandstones. The inherited smectites coatings are commonly discontinuous, but are transformed into either chlorite or illite via mixed-layer smectites during burial diagenesis, often forming a complete coatings on grains during burial diagenesis (Figure 4.24). The chlorite, illite and mixed-layer illite-smectite coatings, where well-developed, have inhibited the formation of authigenic quartz overgrowths in the sandstones, and quartz cement volume decreases from proximal (3.62 %) to distal fan (1.78) due to the impact of clay coatings and pore-filling clays. However, pore-filling chlorite illite, kaolinite, and detrital mixed-layer illite-smectite have had a negative impact on reservoir quality (e.g., Figure 4.12) by occluding porosity and bridging pore throats. (3) Precipitation of kaolinite. Kaolinite is an early clay cement (Figure 4.16) and was formed due alteration of detrital feldspars (Figure 4.24) (4) Formation of illite. Illite was formed during late early eodiagenesis and continued into deep-burial mesodiagenesis (Figure 4.16), commonly from replacement of smectite and kaolinite (Figures 4.11C & D and 4.24). (5) Precipitation of early and late carbonate cements (Figures 4.16 & 4.24). Early pore-filling carbonate cements, consisting of non-ferroan calcite, siderite, and dolomite, are the second most abundant cements and have reduced reservoir porosity and permeability, where well-developed, (Figure 4.14A-C).Their dissolution generates significant intergranular porosity (e.g., Figure 4.14D) (6) formation of quartz cement. Based on petrographic evidence, the formation of quartz overgrowths in the Forties Sandstone started during early diagenesis and has continued into deep-burial mesodiagenesis (Figures 4.16 & 4.24). The cement developed where clay coatings are thin, discontinuous, poorly-developed, or absent, and decreases in volume from proximal to distal fan (Figure 4.24). (7) creation of secondary intra- and inter-granular porosity. In many sandstones, dissolution of feldspar, mica, rock fragments, and carbonate cement has considerably enhanced the formation of localized secondary intragranular intergranular porosity (e.g., Figure 4.14D).

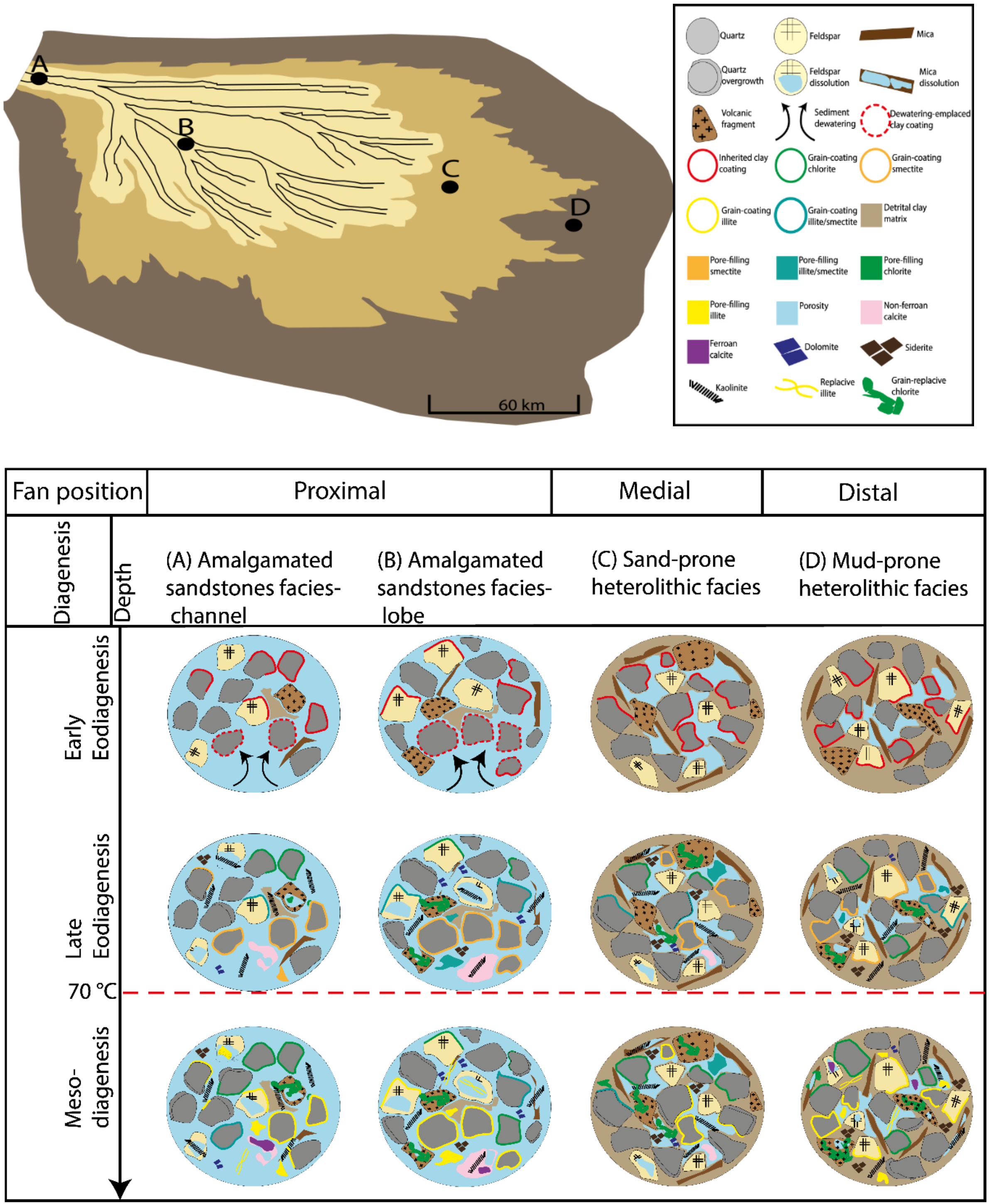

Helium Porosity (%):	20.3 - 24.8	3.4 - 25.08	5.6 - 24.5	3.1 - 25.9
Permeability (mD):	25-500	0.01 - 139	0.02 - 101	0.01 - 61.8
Average clay-coating coverage (%):	26-61	34 - 48	18 - 51	18 - 33
Average quartz cement volume (%):	3.62	3.03	2.62	1.78

Figure 4.24. Schematic conceptual model for the facies control and diagenesis of the Forties Sandstone Member reservoir quality evolution. The model shows the role played by inherited clay coats, clay coats emplaced during sediment dewatering, carbonate cements, quartz overgrowths, and mineral dissolutions in reservoir quality evolution of the Forties Sandstone Member.

4.7 Conclusions

- Diagenesis has played a vital role in reservoir quality evolution of the Forties Sandstone Member, and has been largely influenced by depositional facies and detrital composition. Mechanical compaction is the main driver for porosity loss than cementation.

- Grain-coating chlorite, illite-smectite, and illite were mainly sourced from detrital smectite, which was inherited from continental, transitional or marine/shelf environments and/or those emplaced during sediment dewatering. Alteration of detrital biotite and volcanic fragments has contributed to the formation of grain-coating chlorite.

- Grain-coating clays have preserved reservoir quality by preventing quartz cementation, and 40-50 % clay-coating coverage is required to significantly inhibit quartz cementation in the sandstones. Quartz cement decreases in volume from proximal to distal fan, with the average volume ranging from 3.62 to 1.78 %, respectively.

- Pore-filling, diagenetic illite and kaolinite as low as 2 % each, due to their fibrous and blocky morphology, respectively, have had a detrimental effect on reservoir quality of the sandstones, whereas pore-filling chlorite has a threshold value ranging from 3 to 10 %.
- Sandstones characterized by higher grain-coating clays ranging from 6-11 % have suffered less impact of mechanical compaction than those with lower grain-coating clays, resulting in more porosity preservation in the former than in the latter.

- Grain size had no impact on clay coat coverage, suggesting that the smaller grain-sized medial to distal fan heterolithic sandstones facies have the potentials to form good clay-coating coverage to preserve reservoir quality.

- Generally, carbonate cements had less impact on reservoir quality of the sandstones, except where the cements volume reached 20-40 %, and their dissolution could potentially create significant secondary, intergranular porosity in the sandstones.

Chapter 5: Experimental diagenesis using a present-day submarine turbidite sands

This chapter has been written in a manuscript format, and will be submitted to Journal of Chemical Geology.

Chapter 5: Experimental diagenesis using a present-day submarine turbidite sands

5.1 Summary

Hydrothermal-reactor experiments were carried out to investigate the occurrence and formation of grain-coating chlorite and microquartz on detrital quartz and feldspar grains, and to understand how these coatings inhibit the formation of quartz and feldspar (albite) overgrowths in order to improve the understanding of reservoir quality in ancient turbidite sandstones. The starting material was the modern-day proximal and distal Bute Inlet sediments, British Columbia, Canada, and the samples were heated to 250 °C at water vapour pressure in a hydrothermal reactor for 72 hours (3 days). The experiments were run with and without silica in the reactor. Both pre- and post-experiment samples were studied using scanning electron microscope (SEM) equipped with energy dispersive X-ray spectrometer (EDS). SEM/SEM-EDS and bulk XRD analyses suggest that the main precursor for chlorite coatings was Mg-rich clay (clinochlore), which is crucial for the formation of chlorite coatings in the reacted sediments. The results of the experiments showed that, where the precursor clay material was insufficient (< 1 %), notably in the proximal Bute samples, chlorite coatings were poorly developed, with maximum average coatings coverage of 47 %. In contrast, the distal Bute sample, with an initial precursor chlorite content of up to 6 %, has generated chlorite volume ranging from 19 to 27 % after the experiments. Additionally, results of the measurements of average chlorite-coating coverage on the distal, post-experiment Bute samples have shown that detrital quartz and plagioclase (albite) have an average chlorite-coat coverage ranging from 46 to 66 % and 64 to 77 %, respectively, compared to the pre-experiment, distal Bute sample, which had an initial, average chlorite-coat coverage of 9 and 17 % for quartz and albite, respectively. Coatings of chlorite and microcrystalline quartz (with an average microquartz-coating coverage of 38 %) have inhibited the formation of quartz and albite overgrowths, where well developed. The chlorite and microquartz produced in the study are similar in morphology and composition to those in naturally-occurring sandstones reservoirs, and the results generated can provide quantitative data that can be used as inputs for modelling. Additionally, the results indicate that authigenic clay coats have developed from detrital clay coats and that mud content is crucial for the temperature-induced growth of authigenic clay coats. Furthermore, the findings of this study would help identify depositional processes and environments in ancient deep-water fans systems that are favourable for the formation of detrital clay coats, which recrystallize at deeper burial to form excellent coating coverage to inhibit quartz cementation and, thus, preserve reservoir quality.

5.2 Introduction

Authigenic quartz cement is one of the main porosity destroyers in deeply buried siliciclastic reservoirs (Bukar, 2013; Houseknecht, 1987; Worden et al., 2000). Grain-coating clays (e.g., chlorite and mixed layer clays) and coatings of microcrystalline quartz have been identified as porosity-preserving cements in deeply-buried sandstones reservoirs (Aase et al., 1996; Bloch et al., 2002; Ehrenberg, 1993; French et al., 2012; Pittman et al., 1992; Stricker, 2016; Stricker and Jones, 2018). They inhibit the nucleation of quartz overgrowths by developing a diffusion barrier between the detrital quartz surface and the primary pore system, restricting silica supply to the detrital grain surface (Ajdukiewicz and Larese, 2012). The effectiveness of clay coatings in porosity preservation largely depends on their mineralogy, thickness, and extent (coverage) (Ajdukiewicz and Larese, 2012; Pittman et al., 1992). Many studies on the role of clay coatings on reservoir quality preservation have largely focused on the coatings ability to prevent the development of quartz cement on detrital quartz alone (e.g., Ajdukiewicz and Larese, 2012; Chen et al., 2011; Dutton et al., 2018; Kordi, 2013). Depending on sandstones compositions, however, albite overgrowths can develop on feldspar grains (Chowdhury and Noble, 1993; González-Acebrón et al., 2010), growing into the pore space and destroying intergranular porosity, notably in arkosic sandstones. Consequently, understanding the formation of clay coatings on both quartz and feldspar grains is crucial for comprehensive reservoir quality evaluation in deeply-buried sandstones.

Porosity-preserving clays in sandstones occur as detrital and/or authigenic coatings (Aagaard et al., 2000; Ajdukiewicz and Larese, 2012; Bahlis and de Ros, 2013; Haile et al., 2015; Kordi, 2013; Matlack et al., 1989). Detrital clay coats develop in primary depositional environment, formed during or shortly after sediment deposition through, for instance, mechanical infiltration (Matlack et al., 1989), or sediment dewatering in deep-water settings (Houseknecht and Ross, 1992; Porten et al., 2019). Detrital clays in deep-water sandstones could also be inherited from continental, transitional, or shallow marine/shelf environments (Bahlis and de Ros, 2013; Yezerski and Shumaker, 2018). Authigenic clay coats, on the other hand, develop through direct precipitation (neoformation) (Dutton et al., 2018; Kordi, 2013), thermally-driven recrystallization of precursor, detrital coats (Ehrenberg, 1993), and through in situ development from alteration of detrital precursors (Aagaard et al., 2000; Ajdukiewicz and Larese, 2012; Haile et al., 2015). Smectite and berthierine, for instance, are widely reported as precursors for chlorite (e.g., Aagaard et al., 2000; Chen et al., 2011; Haile et al., 2015; Worden et al., 2020; Worden and Morad, 2003). Nonetheless, little is known about the transformation of precursor clays to diagenetic clay coatings, the volume change resulting from the transformation, and whether the diagenetic coatings formed are sufficient to coat detrital quartz and feldspars in order to prevent the formation of quartz and feldspar overgrowths, respectively.

Additionally, since porosity-preserving, authigenic clay coats are reported to form largely from recrystallization and alteration of detrital clay coats (e.g., Bahlis and de Ros, 2013; Ehrenberg, 1993), it is important to establish the amount and extent of coverage of detrital clay coats required to form complete authigenic clay coatings in ancient sandstones in order to inhibit the development of quartz and feldspar cements as well as improve reservoir quality prediction. However, the role played by detrital clay coatings in the formation of authigenic clay coatings cannot be accurately established in ancient sandstones owing to partial or complete transformation of the detrital clay coatings during burial diagenesis. In the deep-water turbidite sandstones of the Palaeocene Forties Sandstone Member, Central North Sea, for example, where thermally-driven alteration of precursor, detrital smectite clay coats to form chlorite, illite, and mixed layer-illite smectite has occurred, it is difficult (if not impossible) to determine the extent of transformation as well as the amount or volume of precursor detrital clay coats required to form complete authigenic coats in the sandstones. Nevertheless, by conducting experimental studies on diagenesis using modern, deep-water sediment samples with initial, known volume and coverage of precursor detrital clays, reservoir quality prediction and better understanding of the ancient deep-water turbidite sandstones could be enhanced. The modern-day, deep-water Bute Inlet, British Columbia, Canada, was chosen for its accessibility and submarine channel and lobe deposits (Hage, 2019; Heijnen et al., 2020; Zeng et al., 1991). Therefore, the focus of the present study is to understand, through laboratory synthesis, the role played by precursor, detrital chlorite coatings (clinochlore) in the formation of authigenic chlorite coatings; to investigate the formation of authigenic chlorite coatings from direct precipitation (neoformation); and to establish chlorite coatings coverage on detrital quartz and feldspar grains using the modern-day, Bute Inlet sediments, with established volume and coverage of precursor clays. The main objectives of the study are to:

(1) Use samples from the Bute Inlet to simulate diagenesis in turbidite sandstones by using hydrothermal reactor experiments in order to provide quantitative data that can be used as inputs for modelling

(2) Establish the role played by detrital clay coats in the formation of authigenic clay coats, and understand the formation of microquartz coatings and their role in arresting the formation of macro-quartz cement.

(3) Measure and determine the percentage of the average chlorite- and microquartz-coating coverage in the post-experiment samples from the Bute system.

5.3 Background Geology of the Bute Inlet

Bute Inlet, located along the southwestern coast of the British Columbia, Canada (Figure 5.1 A & B), is about 80km long and 4 km wide, ranging in water depths from 200 to 650 m. The Bute system has been recognized as a classic fjord, characterized by seafloor sedimentation that resembles those developed on some large submarine fans (Gales et al., 2018; Hage, 2019; Zeng et al., 1991). The fjord is fed by Homathko and Southgate Rivers, contributing 75 % and 19 % of the annual freshwater discharge into the fjord, respectively (Zeng et al., 1991). Turbidity currents in the Bute Inlet are initiated at the head of the fjord, on the fronts of the prograding and submerged delta of Homathko and Southgate Rivers (Hage, 2019). The turbidity flows, which have been linked to the periods of high river discharge, may originate as slumps, moving downslope and transforming into turbidity currents, or as highly concentrated river flows (Hage, 2019; Prior et al., 1987). The downslope movement of flows occurs through the single, sinuous, and long submarine channel (about 30 km long and 100-400 m wide) incised into the seafloors (Prior et al., 1986; Prior and Bornhold, 1984; Zeng et al., 1991).

Coarse- to fine-grained sands are largely remobilized from the delta fronts of the Homathko and Southgate Rivers and transported by turbidity currents up to 70 km from the head of the fjord (Prior and Bornhold, 1989; Zeng et al., 1991). Although it is relatively small and roughly linear, the modern Bute Inlet depositional system has been identified as an ideal site to study the link between rivers and deep-water sediment transport, with morphological features resembling those of many large, deep-sea fans (Hage, 2019; Zeng et al., 1991). The fjord is relatively easy to access and, hence, allows for findings of experimental studies simulating deep-water flows, processes, and deposits to be tested and expanded in natural environments (e.g., Hughes Clarke, 2016).

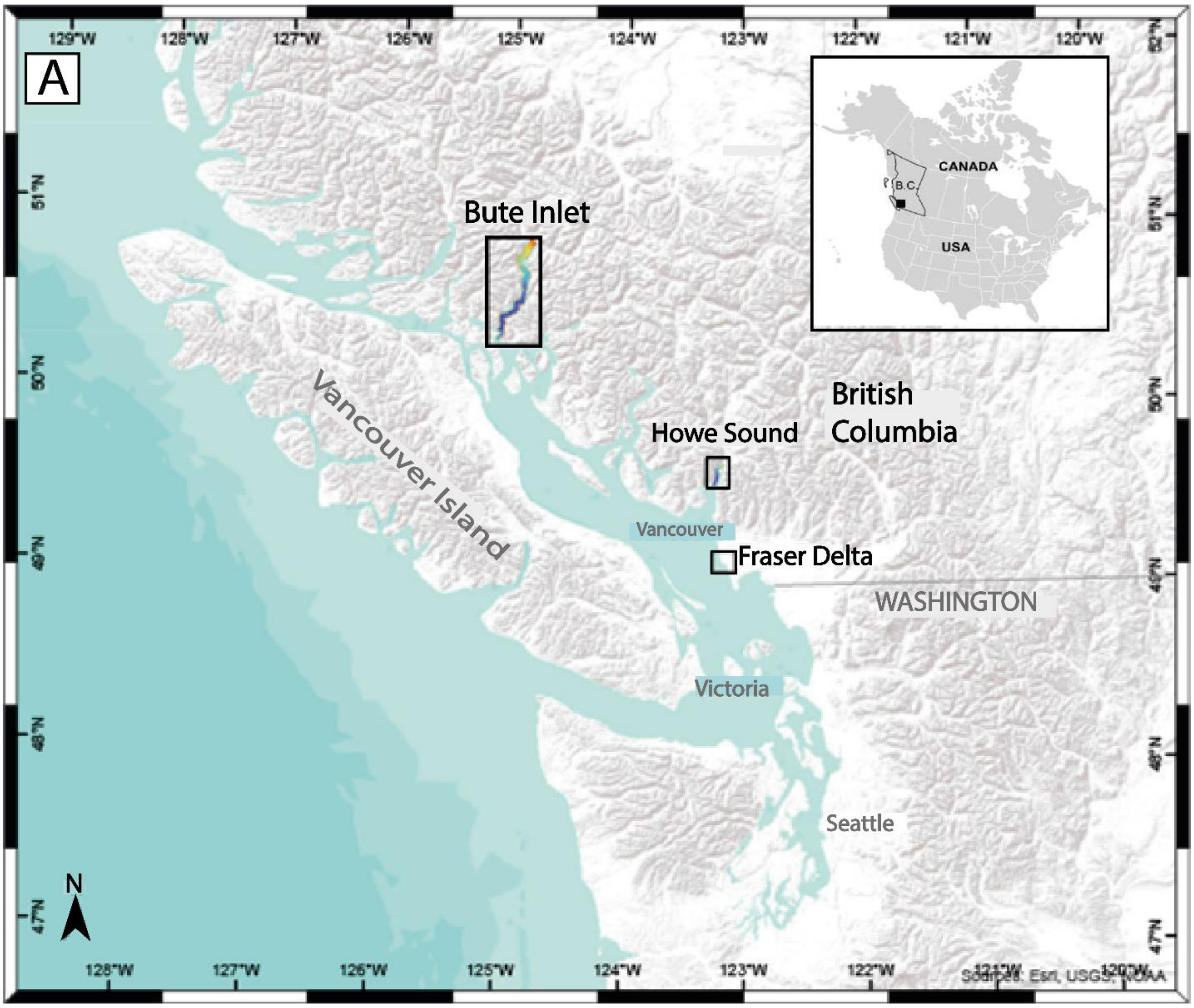
A
Bute Inlet
Howe Sound
British Columbia
Vancouver Island
Vancouver
Fraser Delta
WASHINGTON
Victoria
Seattle
CANADA
B.C.
USA
N
129°W
128°W
127°W
126°W
125°W
124°W
123°W
122°W
121°W
120°W
51°N
50°N
49°N
48°N
47°N
Sources: Esri, USGS, NOAA

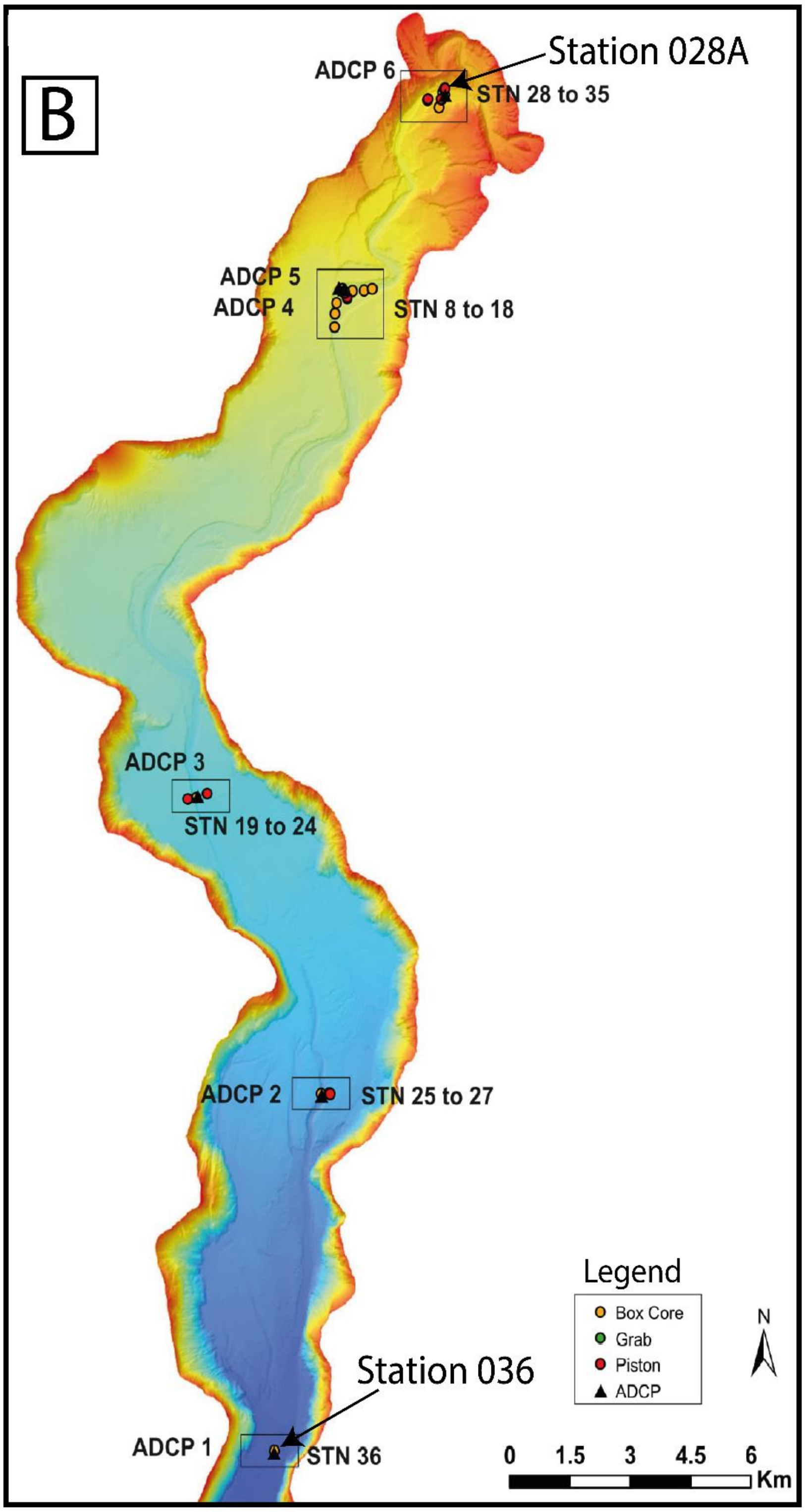

Figure 5.1. (A) Location of map of the Bute Inlet, British Columbia, Canada (modified after Esri USGS, NOAA). (B) Location of sampling points in the Bute Inlet. The samples used in this study were from Stations 028A and 036.

5.4 Sedimentary deposits

Sedimentary deposits of the Bute Inlet have indicated four principal facies associations: spillover lobes, channel-lobe complex, distal splay, and basin floor, with facies typical of the T_{a-e} divisions of the Bouma sequence (Bouma, 1962) (Zeng et al., 1991). Furthermore, recent core studies of the Bute sediments by Hage (2019) corroborates the four principal facies associations identified by Zeng et al. (1991). However, the samples used in the present study cover channel-lobe complex facies associations only, which were from Stations 028A and 036 (Figure 5.1B) and represent proximal channel and distal lobe depositional environments, respectively. Figure 5.2 shows syringe core image, thin section photomicrographs and backscattered electron (BSE) images for pre-experiment and post-experiment (with and without silica) and their associated extents of clay-coating coverage for samples from Station 028A (proximal Bute channel). The sample from Station 028A (incised channel) consists of dark to light grey , massive, fine- to medium-grained sand (average grain size 0.13 mm) (Figure 5.2). The thin-section photomicrographs and backscattered electron (BSE) images and clay-coating coverage in Figure 5.2 are discussed in later sections of this chapter. On the other hand, core sediment from Station 036 (distal lobe) consists of grey, fine silt to very fine sand (Figure 5.3), with the mean grain size of 0.041 mm. The deposits of the channel-lobe complex in the Bute Inlet have been interpreted to have formed from successive turbidity flows of similar magnitude and composition of suspended load (Zeng et al., 1991).

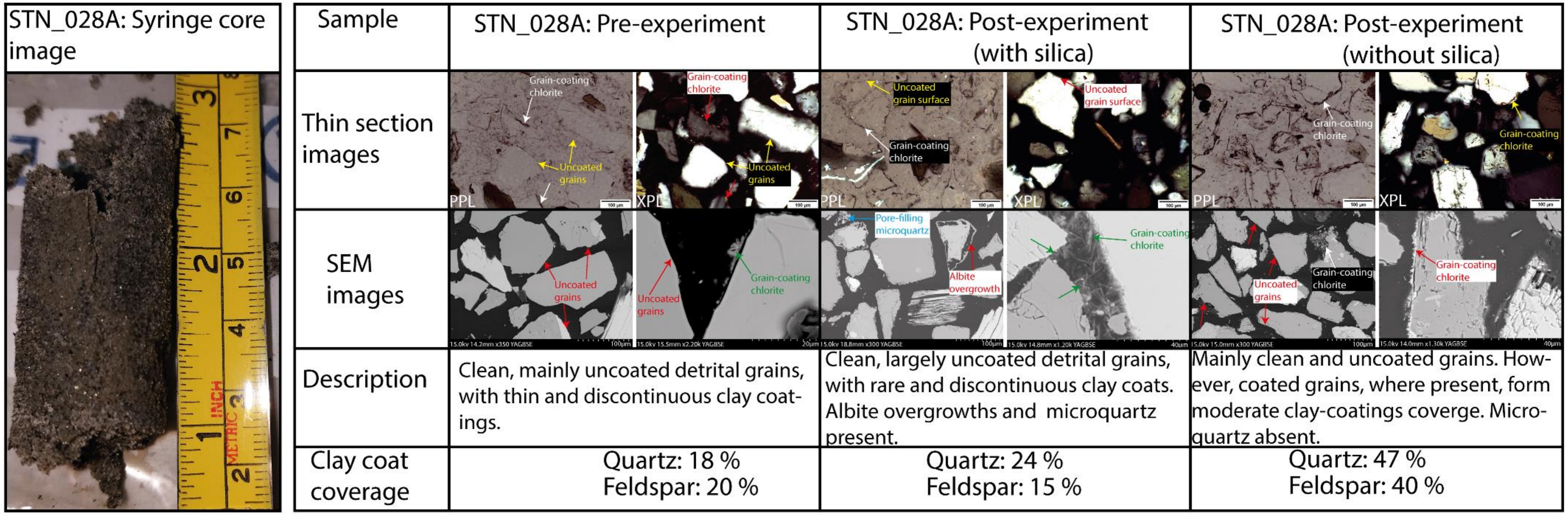

Sample	STN_028A: Pre-experiment	STN_028A: Post-experiment (with silica)	STN_028A: Post-experiment (without silica)
Description	Clean, mainly uncoated detrital grains, with thin and discontinuous clay coatings.	Clean, largely uncoated detrital grains, with rare and discontinuous clay coats. Albite overgrowths and microquartz present.	Mainly clean and uncoated grains. However, coated grains, where present, form moderate clay-coatings coverge. Microquartz absent.
Clay coat coverage	Quartz: 18 % Feldspar: 20 %	Quartz: 24 % Feldspar: 15 %	Quartz: 47 % Feldspar: 40 %

Figure 5.2. Syringe core image, thin-section photomicrographs, BSE images, sediment description, and associated clay-coating coverage for pre- and post-experiment samples from Station 028A (proximal Bute submarine channel). The thin-section photomicrographs and BSE images show coated and uncoated sediments, with their description and extent of clay coats coverage on detrital feldspar and quartz grains shown in the Figure.

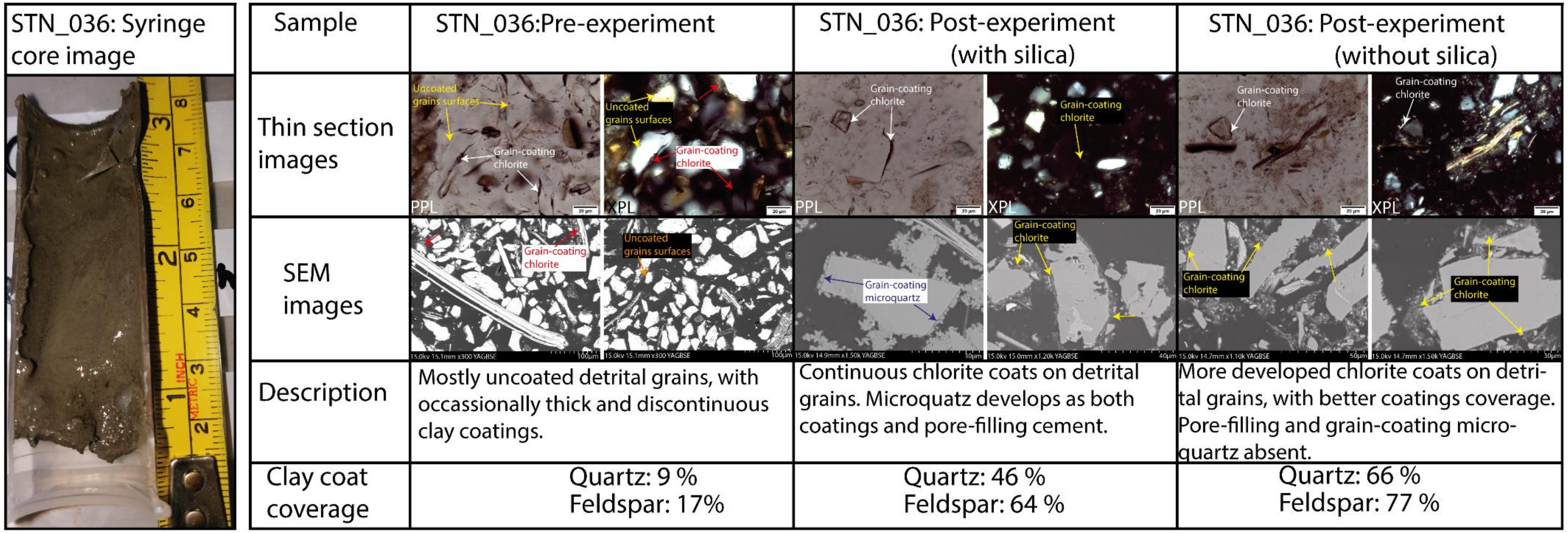

Sample	STN_036:Pre-experiment	STN_036: Post-experiment (with silica)	STN_036: Post-experiment (without silica)
Description	Mostly uncoated detrital grains, with occassionally thick and discontinuous clay coatings.	Continuous chlorite coats on detrital grains. Microquatz develops as both coatings and pore-filling cement.	More developed chlorite coats on detrital grains, with better coatings coverage. Pore-filling and grain-coating microquartz absent.
Clay coat coverage	Quartz: 9 % Feldspar: 17%	Quartz: 46 % Feldspar: 64 %	Quartz: 66 % Feldspar: 77 %

Figure 5.3. Syringe core image, thin section photomicrographs, BSE images, sediment description, and associated clay-coating coverage for pre- and post-experiment samples from Station 036 (distal Bute submarine lobe). The thin section photomicrographs and BSE images show coated and uncoated sediments, with their description and extent of clay-coating coverage on detrital feldspar and quartz grains shown in the Figure. Clay and microquartz coatings are more developed in these samples (Station 036) than in those from Station 028A.

5.5 Methods

5.5.1 Sampling

Two syringe sub-samples (Figures 5.2 and 5.3) were taken from piston core samples originally collected from Station 028A and Station 036 (Figure 5.1B), which represent proximal and distal Bute fan, respectively. The sub-samples were carefully divided into three portions (5g) for each sub-sample. Two polished thin sections were made from the first portions (1 each for Stations 028A and 036), which were utilized for pre-hydrothermal reactor experiments investigations under scanning electron microscope (SEM) in order to ascertain the sediments framework compositions and possible cements; the other four portions (2 for each sub-sample) were prepared for hydrothermal reactor experiments with and without silica, and then polished thin sections were prepared after the experiments for SEM/SEM-EDS analysis.

5.5.2 Analytical procedures

Petrographic analyses of the 6 polished thin sections were carried out using Hitachi SU70 scanning electron microscope (SEM), equipped with an energy dispersive spectrometer (EDS) for analysis of microstructure and composition. The samples were also studied using a petrographic light microscope. Six 2 mm by 2 mm EDS phase maps were acquired and analysed for both pre- and post-experiment samples, in order to establish their framework mineralogy, clay and microquartz coatings, and other cements. This enabled quantitative and qualitative determination of the extent of mineralogical transformations and precipitations, which occurred during the course of the experiments. Typical voltage used range from 12-15 kV. Clay- and microquartz-coatings coverage were measured using the Petrog (v. 4.5.9.2) and JMicrovision (v. 1.3.3) software packages based on the method described by Wooldridge et al. (2019) for modern-day sediments. Thicknesses of clay and microquartz coatings were measured using the ImageJ software. Grain size was determined by measuring the long axis of at least 100 randomly selected quartz and feldspar grains using the ImageJ software. To have the actual representation of the sediments grain size, SEM images for pre-experiment samples were used. Results of the EDS phase maps, and coatings coverage are shown in Table 5.1. Bulk XRD analysis was conducted on the two pre-reacted samples in order to establish the composition of the starting materials, and to compare with the results of the EDS phase maps.

5.5.3 Hydrothermal experiments

In this study, hydrothermal reactor experiments were conducted to synthesize grain-coating chlorite and microquartz, and to test the assumption that clay and microquartz coatings inhibit the development of authigenic quartz and feldspar cements. The applied experimental configuration and methodology has been taken from Charlaftis et al. (2021). The experiments were performed in a Parr Series 4560 Mini Reactor at the High-pressure High-temperature laboratory within the Integrated Chemical Reaction Facility (ICRF) at Durham University. The modern-day Bute Inlet sediments, with originally little detrital clay coats, were heated to 250 °C in a 0.1 M Na_2CO_3 solution for 3 days (72 hours) at water vapour pressure in order to simulate burial diagenetic processes, including precipitation of grain-coating clay minerals, mineral alteration and dissolution. Four syringe cores samples from the Bute Inlet (two from Stations 028A and 036 each) (Figures 5.2 and 5.3) were used. Although the two samples from each station are identical, they do not necessarily have the same composition percent. Four sets of hydrothermal reactor experiments were conducted on the samples, two of which were reacted with amorphous silica, and the other two without the silica. For each of the locations, therefore, two experiments were conducted, one with silica and the other without silica. The experiments were performed under strictly closed conditions in the reactor, with subsequent cooling to room temperature after each next run.

5.5.3.1 Experimental conditions

The experimental conditions were adopted from Charlaftis et al. (2021), and are described below. Additionally, these conditions were chosen to match other experiments (e.g. Aagaard et al., 2000; Charlaftis et al., 2021; Haile et al., 2015), which were designed to create the conditions required for the formation of quartz and clay minerals.

1. The experiments were conducted under strictly closed, zero-flow conditions, imitating a closed-system natural sandstone diagenesis. This is mainly because grain-coating chlorites are likely to develop from closed-system sandstone diagenesis at the bed scale (Worden et al., 2020).
2. The artificial solution of 0.1 M Na_2CO_3, which was Fe-free, was mainly chosen to be non-reactive Fe-rich minerals. Furthermore, Fe-rich clay minerals (e.g. chlorite) are preferentially stable under alkaline conditions (White et al., 1942).
3. Quartz dissolution has been reported to increase with an increase in pH into the alkaline region (Crundwell, 2017; Knauss and Wolery, 1989). Thus, the use of 0.1 M Na_2CO_3

solution coupled with a silica source can provide a silica-saturated solution, creating strong quartz-cementing conditions as indicated by previous hydrothermal-reactor experiments (Ajdukiewicz and Larese, 2012).

4. Previous experimental studies have shown that the duration and temperature for the experiments used in our study are adequate to generate clay coatings and quartz cement. The selected temperature exceeds the accepted thresholds of 80 °C and 60 °C for the formation quartz and chlorite cements, respectively (Aagaard et al., 2000; Charlaftis et al., 2021; Ehrenberg, 1993; Lander et al., 2008; Walderhaug et al., 2000; Worden and Morad, 2003).

5.6 Results and interpretations

5.6.1 Mineralogical transformations

In order to attempt to quantify the changes in mineralogy due to dissolution and precipitation of minerals, EDS phase maps for both pre- and post-experiment samples were acquired and analysed, and the results are summarized in Table 5.1 and Figures 5.4 (A, B & C) and 5.5 (A, B & C). The minerals identified through the EDS mapping of pre-experiment samples are the same as those identified through the bulk XRD analysis (Tables 5.1 & 5.2), albeit with different volume percentages. The volume of detrital quartz have largely remained unchanged in both pre- and post-reacted samples (Table 5.1), despite having subjected the sediments to very high temperature. Whereas the volumes of detrital plagioclase (albite) in the reacted and unreacted samples of Station 028A have largely remained the same, they have significantly decreased to as low as 9 % from originally up to 19 % in the post-experiment samples of Station 036 (Table 5.1), probably due to dissolution. For Station 028A sample, the EDS maps results indicate that there is a small decrease in K-feldspar content from 2.28 % in pre-reacted sediments to 1.48 and 1.02 % for post-experiment sample with and without silica, respectively (Table 5.1). The decrease might probably be due to slight dissolution and albitization of the K-feldspar. In Station 036 sample, however, the extent of dissolution/albitization of K-feldspar is higher, resulting in a decrease in the amount of K-feldspar from the initial 2 % to 0.2 and 0.1 % post-experiments (Table 5.1). While there is a decrease in the amounts of K-feldspar during the course of both experiments in Station 028A samples, there is, however, precipitation of grain-replacive albite (e.g., Figure 5.4C), from 0 % in pre-reaction sediments to 0.57 % and 4.19 % in post-reaction with and without silica, respectively (Table 5.1). Diagenetic albite are absent in Station 036 sample (Table 5.1), probably due to the impact of grain-coating clays (e.g.,

Figure 5.5B & C). Similarly, in Station 028A sample, authigenic albite overgrowth (e.g., Figure 5.1B), which are absent in the samples from Station 036, increases from 0 % in pre-reaction sediments to 1.59 % and 1.02 % in post-reaction samples with and without silica, respectively (Table 5.1).

Although chlorite occurs in trace amount (0.23 % each), based on EDS phase maps, in the reacted samples of Station 028A (Table 5.1; e.g., Figure 5.4B & C), it has significantly increased in volume percent in the reacted samples of Station 036 (19 and 27 %) (Table 5.1; e.g., Figure 5.5B & C) from originally 6 % (Table 5.1). As a result, chlorite-coating coverage are higher in post-experiment samples of Station 036 (Figures 5.3 and 5.5B & C; Table 5.1) than in their counterparts from Station 028A (Figures 5.2 and 5.4B & C; Table 5.1).

Authigenic quartz overgrowth is absent in both post-reacted samples of Station 036 (Figure 5.5B & C) probably due to high clay coatings; however, it occurs in trace amount in the silica-reacted sample of Station 028A (0.23 %; Table 5.1). Microquartz, occurring as both grain-coating and pore-filling, has precipitated in higher amount (up to 5 %) in the Station 036 sample reacted with silica (e.g., Figure 5.5B) compared to its counterpart sample from Station 028A (0.11 %; Table 5.1; Figure 5.4B).

Table 5.1. Results of EDS phase maps analyses showing sediments compositions before and after hydrothermal reactor experiments for samples of Stations 028A and 036. Note that the measurements of clay-coating coverage on both pre- and post-experiment samples of Station 028A were carried out using high-resolution thin sections photomicrographs due to paucity of clay coats in the processed EDS phase maps.

Mineral/parameter	**STN_028A (pre-experiment) weight %**	**STN_028A (post-experiment-with silica) weight %**	**STN_028A (post-experiment-without silica) weight %**	**STN_036 (pre-experiment) weight %**	**STN_036 (post-experiment-with silica) weight %**	**STN_036 (post-experiment-without silica) weight %**
Non-clays						
Quartz	14.46	15.26	14.27	8.00	7.00	5.00
K-feldspar	2.28	1.48	1.02	2.00	0.20	0.10
Plagioclase (Albite)	23.71	25.51	24.01	19.00	9.00	10.30
Mica	5.66	4.78	4.64	6.00	4.00	5.40
Pyrite	0.11	0.00	0.00	0.10	0.00	0.00
Rutile	0.22	0.11	0.57	0.00	0.00	0.00
Amphibole	0.00	0.00	0.00	0.20	0.10	0.10
Apatite	0.05	0.34	0.11	0.10	0.00	0.10
Authigenic Albite	0.00	0.57	4.19	0.00	0.00	0.00
Albite overgrowth	0.00	1.59	1.02	0.00	0.00	0.00
Quartz overgrowth	0.00	0.23	0.00	0.00	0.00	0.00
Microquartz		0.11	0.00	0.00	5.00	
Total non-clays	*46.49*	*49.98*	*49.83*	*35.40*	*25.30*	*21.00*
Clays (pore-filling + grain-coating)						
Chlorite	0.00	0.23	0.23	6.00	19.00	27.00
Illite	0.00	0.00	0.00	0.00	0.00	0.00
Kaolinite	0.00	0.00	0.00	0.00	0.00	0.00
Illite/smectite	0.00	0.00	0.00	0.00	0.00	0.00
Detrital clay volume	0.00	0.00	0.00	6.00	0.00	0.00
Total clays	0.00	*0.23*	*0.23*	*6.00*	19.00	27.00
Average chlorite-coating coverage (%)	Quartz = 18 Albite = 20	Quartz = 24 Albite = 15	Quartz = 47 Albite = 40	Quartz = 9 Albite = 17	Quartz = 46 Albite = 64	Quartz = 66 Albite = 77
Average microquartz-coating coverage (%)					38	
Chlorite average Fe/(Fe+Mg) ratio		0.70	0.50			
Porosity (%)						
Intergranular porosity	54	50	50	60	56	52

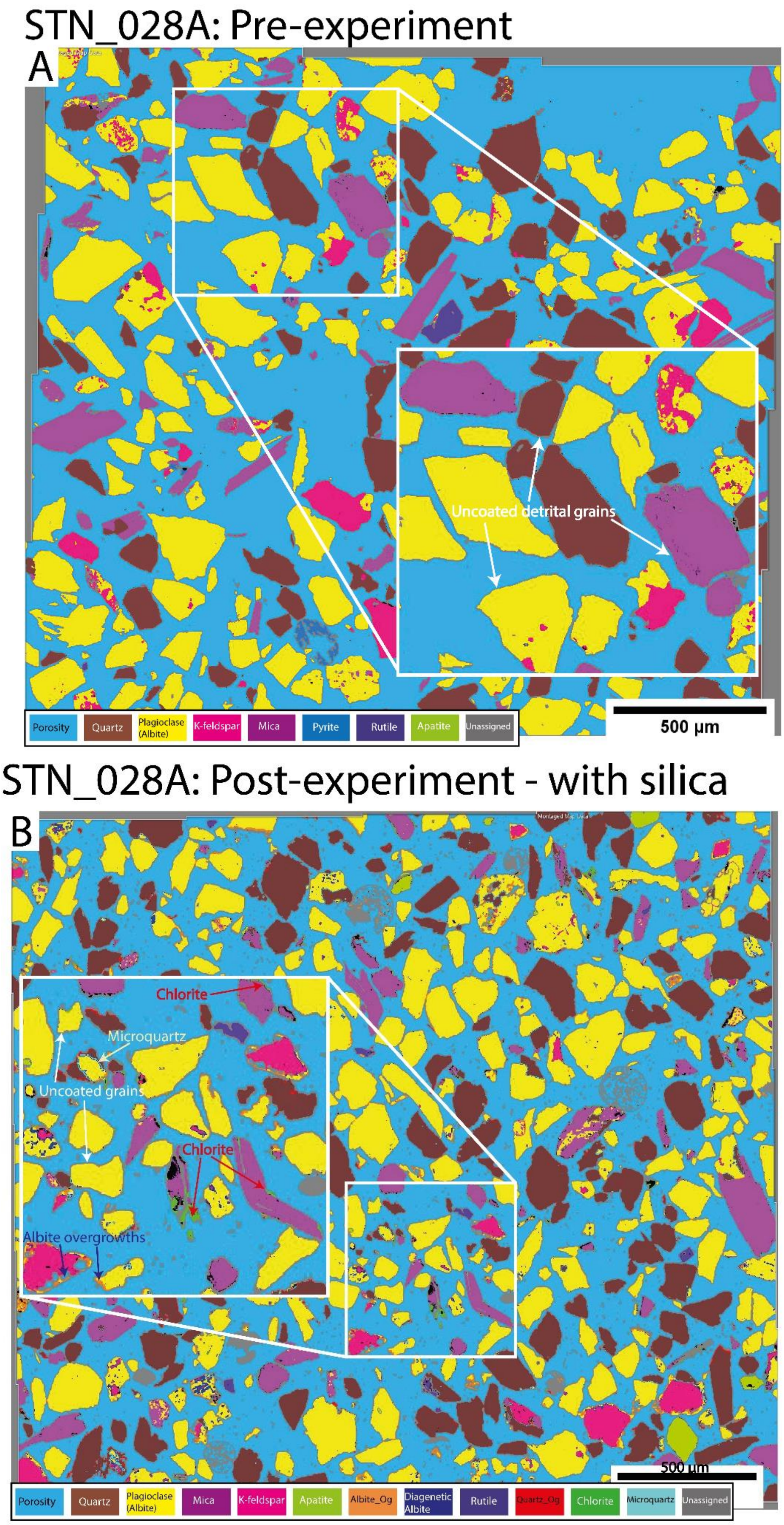
STN_028A: Pre-experiment
A
Uncoated detrital grains
500 µm
Porosity
Quartz
Plagioclase (Albite)
K-feldspar
Mica
Pyrite
Rutile
Apatite
Unassigned
STN_028A: Post-experiment - with silica
B
Chlorite
Microquartz
Uncoated grains
Chlorite
Albite overgrowths
500 µm
Porosity
Quartz
Plagioclase (Albite)
Mica
K-feldspar
Apatite
Albite_Og
Diagenetic Albite
Rutile
Quartz_Og
Chlorite
Microquartz
Unassigned

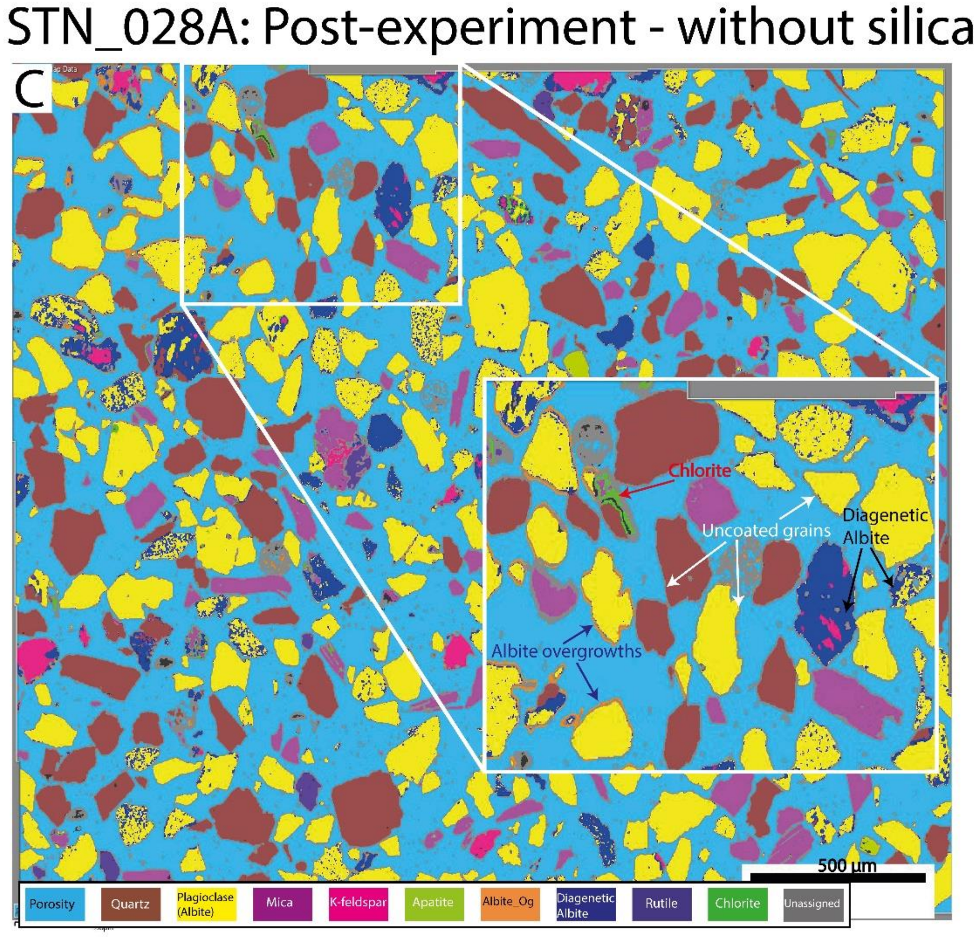

Figure 5.4. (A) Processed EDS phase map for pre-experiment sample of Station 028A showing the distribution of framework minerals. Note the absence of grain-coating and pore-filling clays. (B) Processed EDS phase map for post-experiment (with silica) sample for Station 028A. Notice the formation of albite overgrowths on K-feldspar grains, some coatings of microquartz on grains, and the paucity of chlorite coatings on detrital grains. (C) Analysed EDS phase map for post-experiment (without silica) sample for Station 028A. In this sample, chlorite coatings appear to be generally absent on the detrital grains, and diagenetic albite has developed on partially to pervasively dissolved detrital plagioclase (albite) and K-feldspar grains.

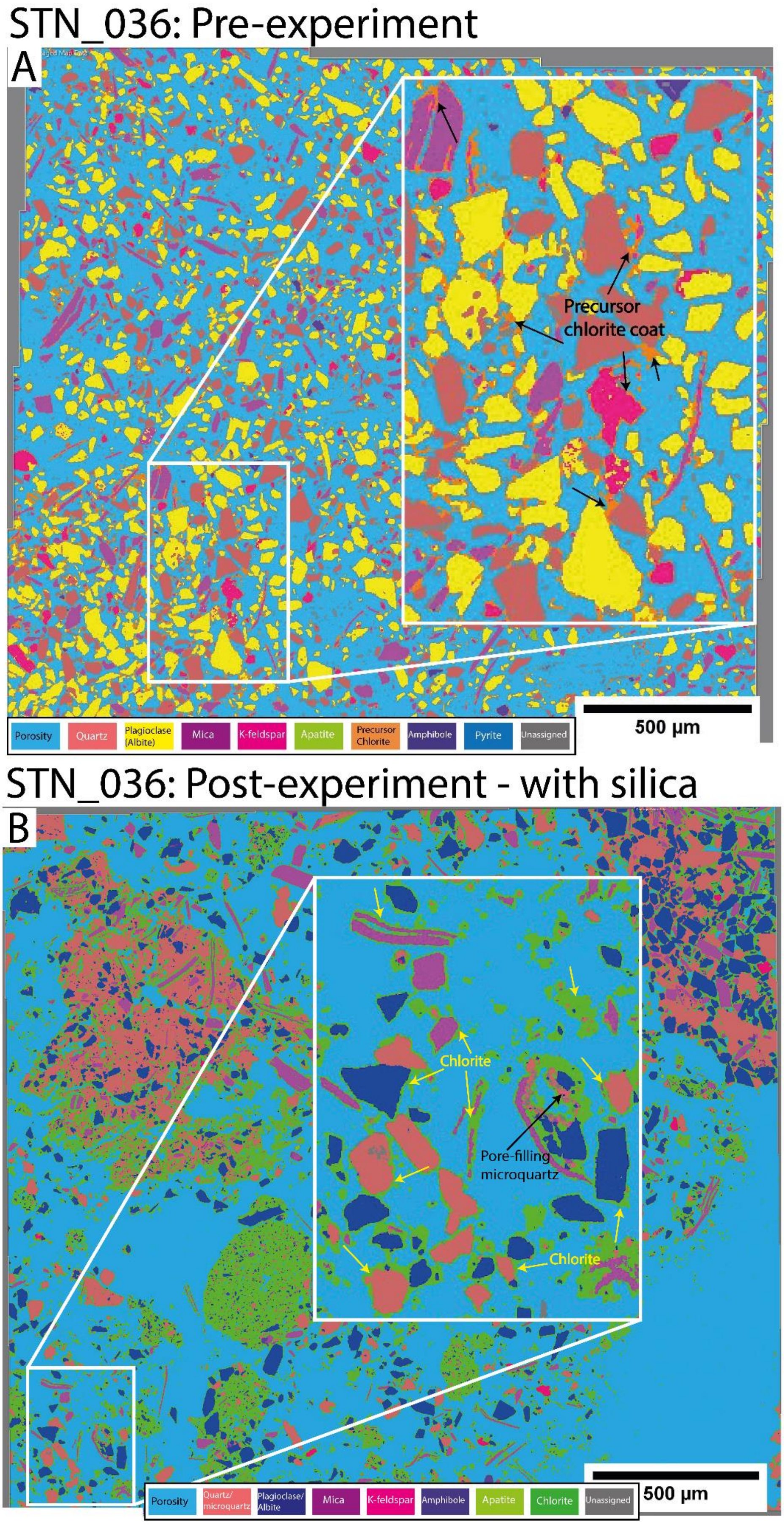
STN_036: Pre-experiment
A
Precursor chlorite coat
Porosity
Quartz
Plagioclase (Albite)
Mica
K-feldspar
Apatite
Precursor Chlorite
Amphibole
Pyrite
Unassigned
500 µm
STN_036: Post-experiment - with silica
B
Chlorite
Pore-filling microquartz
Chlorite
Porosity
Quartz/ microquartz
Plagioclase/ Albite
Mica
K-feldspar
Amphibole
Apatite
Chlorite
Unassigned
500 µm

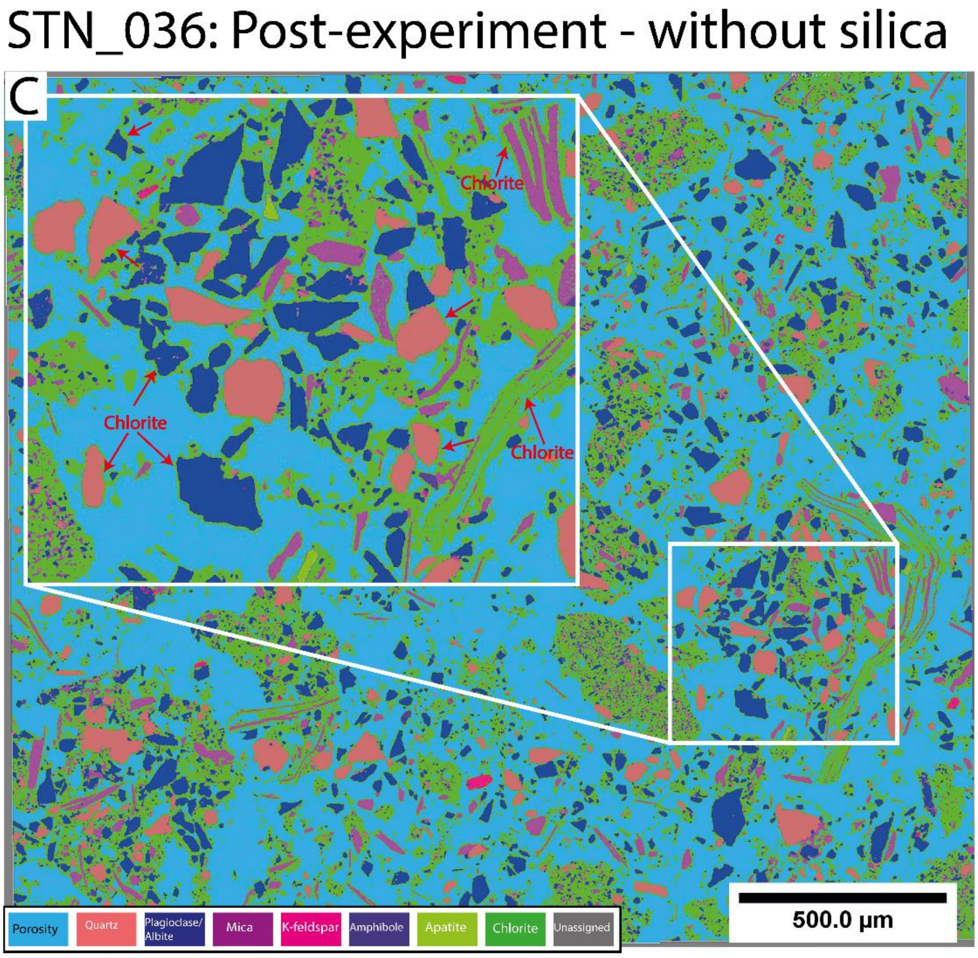

Figure 5.5. (A) Analysed EDS phase map for pre-experiment sample of Station 036, showing the distribution of framework minerals and precursor grain-coating chlorite. (B) Processed EDS phase map for post-experiment sample of Station 036 reacted with silica, showing the distribution of grain-rimming chlorite and pore-filling chlorite and microquartz cements. (C) Analysed EDS phase map for post-experiment sample of Station 036 reacted without silica. In this sample, chlorite coatings appear to be more developed on detrital grains compared to the preceded sample, resulting in high chlorite-coat coverage. Notice how chlorite replaces detrital mica (biotite) grains. For percentages of chlorite-coat coverage in these samples, see Table 5.1.

5.6.2 Bulk XRD results

Bulk XRD data for pre-reacted samples of Stations 028A and 036 (Table 5.2) reveals that the detrital framework grains consist of quartz (15 % each), K-feldspar (microcline) (5-7 %), and biotite (6-9 %). Clinochlore (Mg-rich chlorite) ranges from 3-5 % and occurs as both grain-coating precursor clay and pore-filling detrital matrix. Two types of amphiboles have been identified: edenite (15 %) and ferro-tschermakite (16 %).

Table 5.2. Bulk XRD results for Station s 028A and 036 used in the study.

Mineral (%)	**Station 028A**	**Station 036**
Quartz	15.0	15.0
Albite	49.0	55.0
Microcline	7.0	5.0
Biotite	9.0	6.0
Clinochlore	5.0	3.0
Edenite(Amphibole)	15.0	0.0
Ferro-tschermakite (Amphibole)	0.0	16.0
Total	100.0	100.0

5.6.3 Chlorite- and microquartz-coat coverage measurements

Using high-resolution thin-section photomicrographs and processed EDS phase maps, measurement of chlorite-coating coverage was carried out on at least 50 randomly selected detrital quartz and feldspar (albite) grains each for both pre- and post-experiment samples from Stations 028A and 036. However, due to paucity of microquartz in the silica-reacted sample of Station 028A, measurement of microquartz-coating coverage was carried out on 50 quartz grains in the post-experiment sample (with silica) of Station 036 alone, and the results show that average microquartz-coating coverage is 38 % (Table 5.1). The measurements of clay- and microquartz-coatings coverage were carried using the JMicrovision (v. 1.3.3) and the Petrog (v. 4.5.9.2) pieces of software. Results of chlorite-coating coverage measurements for all samples are shown in Figures 5.2 & 5.3 and Table 5.1. The results indicate that detrital quartz and albite grains in pre- and post-experiment with and without silica samples for Station 028A have average clay-coat of coverage of 18 and 20 %, 24 and 15 %, and 47 and 40 %, respectively (Figure 5.2; Table 5.1), suggesting that the post-reacted sediment without silica develop the highest clay-coating coverage. Similarly, in Station 036, detrital quartz and albite grains in pre- and post-experiment with and without silica samples have average clay-coat of 9 and 17 %, 46 and 64 %, and 66 and 77 % (respectively), indicating that the post-experiment without silica sample has the highest clay-coating coverage (Figure 5.3; Table 5.1).

Furthermore, the results indicate that the reacted samples from Station 036 have the highest clay-coating coverage than their counterparts from Station 028A. This is probably due to variation in the volume of precursor clays in the pre-experiment samples (Table 5.1). Results of the EDS phase maps have indicated that, while the pre-experiment sample of Station 028A has total volume of precursor clays of < 1 %, its counterpart from station 036 has total volume of precursor clays of up to 6 % (Table 5.1). In addition, the results indicated that the silica-reacted sediments in both samples have less clay-coating coverage than those reacted without silica (Figures 5.2 & 5.3; Table 5.1), implying that the presence of silica in the system reduces the surface area available for the precipitation of clay coatings.

5.6.4 Detrital and authigenic clays

Based on SEM morphological characteristics (e.g., Figures 5.2 & 5.3), bulk XRD analysis (Table 5.2), and EDS phase maps analysis, chlorite is the detrital and authigenic clay mineral (Figure 5.6). However, while precursor detrital clay coatings, authigenic chlorite coats, and pore-filling chlorite in both pre- and post-experiment samples of Station 036 are more abundant and well-developed, their counterparts from Station 028A occur in trace amounts (< 1 %) (Table 5.1). The chlorite occurs as grain-coating (Figure 5.6A & B), pore-filling (Figure 5.6C), and as replacement of detrital feldspar (Figure 5.6D), mica (biotite; Figure 5.6E), and clay matrix (Figure 5.6F). Authigenic, grain-coating chlorite grows in two forms: (1) parallel to grain surface (e.g., Figure 5.6A). These are formed from recrystallization of precursor detrital clinochlore (Mg-rich chlorite). Although it is extremely difficult to differentiate them from the detrital chlorite coats, their presence has been confirmed in the post-reacted sediments due to a significant increase in clay-coating coverage (Figure 5.3; Table 5.1), notably in the reacted samples without silica. (2) perpendicular to grain surface. Authigenic grain-coating chlorite was formed by direct precipitation (neoformation) on detrital quartz and feldspars (e.g., Figures 5.2 & 5.6B), which grows perpendicular to grain surface. Additionally, chlorite has been observed to replace or grow from pore-filling clay matrix (Figure 5.6F). Some grain-replacive chlorite, which replace feldspar and/or mica grains, exhibit fan-like morphology (e.g., Figure 5.6D & E).

In order to further study the growth habits of grain-coating chlorite in post-reacted sediments of the Bute Inlet, thin sections photomicrographs have been examined (Figure 5.7A-D). Grain-coating chlorite appear as dark brown coats around detrital grains in both plane and cross-polarized lights (Figure 5.7A & B), and grows either parallel (Figure 5.7A & B) or perpendicular (Figure 5.7C) to grains surfaces. The perpendicular chlorite often exhibits fan-like morphology (Figure 5.7C). The coats might be continuous (Figure 5.7A, B, & C) or discontinuous (Figure 5.7D), with some grains completely uncoated (Figure 5.7D).

The thickness of chlorite coats ranges from 2 to 13 µm (average 6 µm) and 0.7 to 27 µm (average 7 µm) for Station 028A sample reacted with and without silica respectively, indicating that chlorite coats thickness increases with decreasing silica content. Similarly, in Station 036 sample, chlorite thickness ranges from 2 to 7 µm (average 5 µm) and 1 to 7 µm (average 3 µm) for the reacted samples with and without silica, respectively.

Grain-coating chlorite was classified in terms of Fe/(Fe+Mg) ratio (Hillier and Velde, 1992) based on SEM/SEM-EDS analysis, and the results show that the chlorite coats are of two types: Mg-rich and Fe-rich (Grigsby, 2001), with an average Fe/(Fe+Mg) ratio of 0.5 and 0.7, respectively, indicating that apart from the precursor Mg-rich chlorite, an Fe-rich chlorite, probably from biotite, was formed during the course of the experiments.

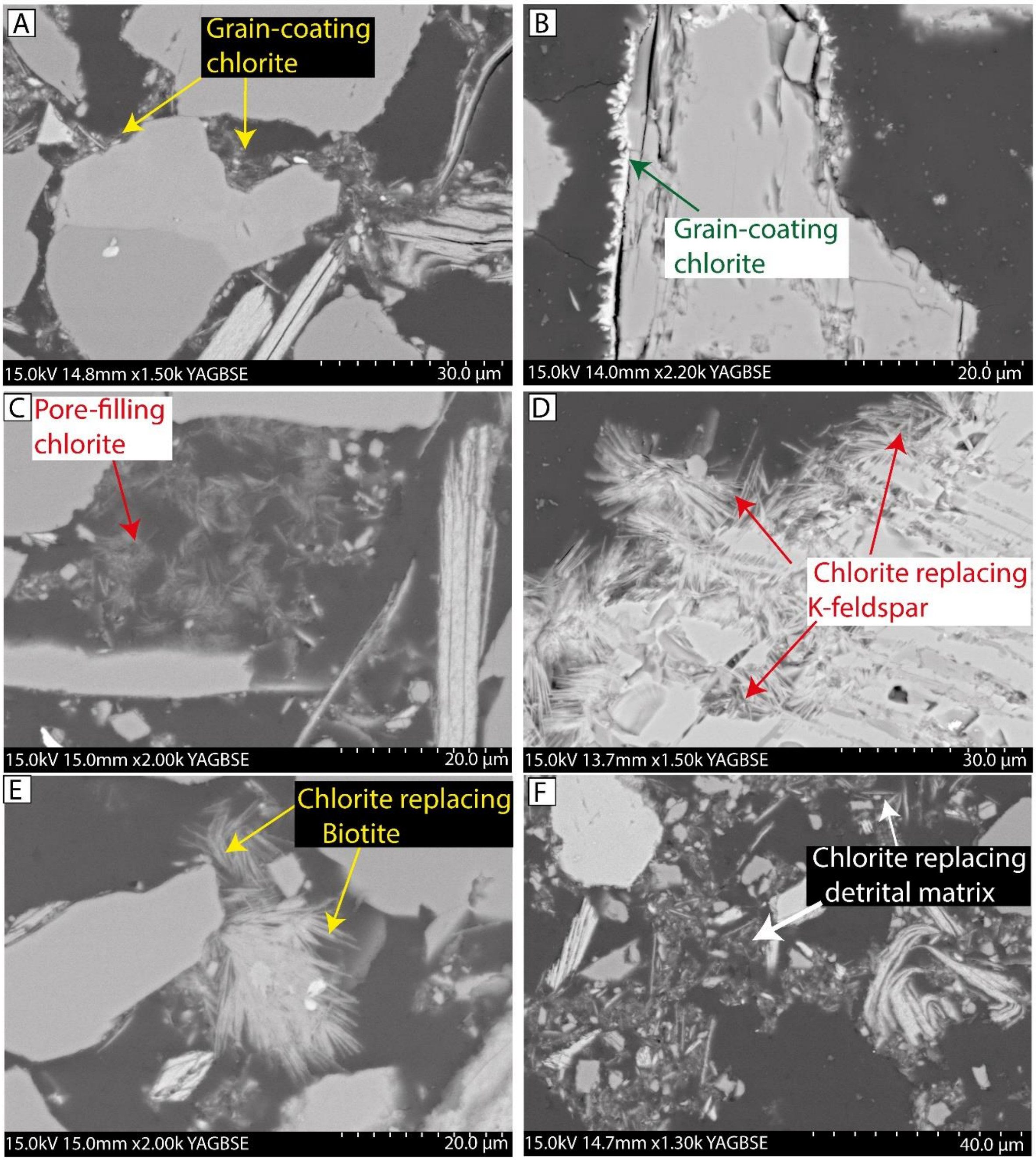

Figure 5.6. BSEM images showing examples of grain-coating, pore-filling, and grain-replacing chlorite in the reacted samples of the Bute Inlet. (A) BSEM image of grain-coating chlorite, growing parallel to quartz grain surface and from a precursor chlorite coat, probably clinochlore. Station 036 sample reacted without silica; (B) BSEM image of neoformed grain-coating chlorite growing perpendicular to detrital albite grain surface. Station 028A sample reacted without silica; (C) BSEM image showing pore-filling chlorite destroying intergranular porosity. Station 036 sample reacted with silica.; (D) BSEM image of grain-replacive chlorite, replacing partly dissolved K-feldspar. Station 028A sample reacted without silica; (E) BSEM image showing fan-like, grain-replacive chlorite, replacing detrital biotite. Station 036 sample reacted with silica; (F) BSEM image showing pore-filling chlorite growing from or replacing precursor pore-filling chlorite, probably Mg-rich chlorite. Station 036 sample reacted without silica.

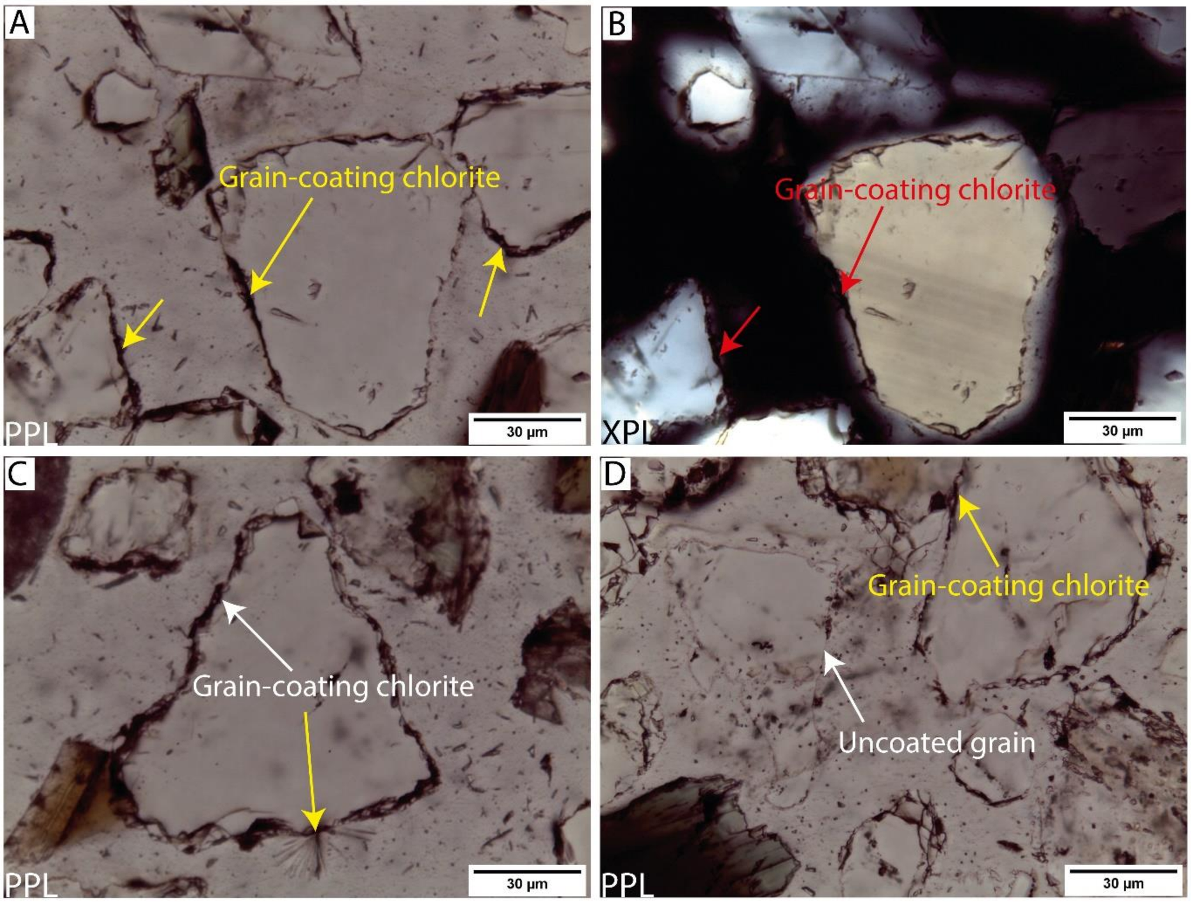

Figure 5.7. High-resolution, thin-section photomicrographs of grain-coating chlorite. (A) Plane polarized light (PPL) image of grain-coating chlorite on detrital grains showing largely continuous coats. (B) Cross-polarized light (XPL) image of (A). (C) Well-developed grain-coating chlorite on detrital quartz, growing both parallel (white arrow) and perpendicular to grain surface (yellow arrow). (D) Plane polarized light (PPL) image showing coated and uncoated detrital grains. Note that the images were from the reacted sample (without silica) of Station 028A, proximal Bute Inlet.

5.6.5 Albite cement

Authigenic albite occurs as replacement of partly or pervasively dissolved detrital plagioclase and K-feldspar (e.g., Figure 5.8A & B), and as overgrowths on feldspars (Figure 5.8C & D). Albite precipitates as thin (Figure 5.8C) or thick (Figure 5.8D) overgrowths on detrital plagioclase or K-feldspars, with the overgrowths' thicknesses ranging from 0.4 to 32 µm (average 7.8 µm). The overgrowths, which may or may not be compositionally identical to their host detrital grains, often grow into partly or pervasively dissolved, host feldspar grains, suggesting that they postdate the dissolution. (e.g., Figure 5.8C). Occasionally, the overgrowths surround moldic pores, which are developed from the post-overgrowth dissolution of detrital K-feldspar or plagioclase host grains (Figure 5.8E & F). Grain-replacive albite, on the other hand, replaces both dissolved plagioclase and K-feldspar grains, and the replacement has been thought to occur in a dissolution-precipitation manner (Milliken et al., 1989). The replacement occurs as blocky, irregular albite on plagioclase or K-feldspar grains (e.g., Figure 5.8A), as pervasive replacement of dissolved K-feldspar (e.g., Figure 5.8B), or as thin, vein-like albite on K-feldspar grains. The blocky, irregular albitization textures are similar to those described by Chowdhury and Noble (1993) from Early Carboniferous sandstones of the Abert Formation, Moncton sub-basin, South-eastern New Brunswick; and those described by Milliken et al. (1989) from the Texas Gulf Coast sandstones. The amount of K-feldspar decreases in all post-experiment samples (Table 5.1), presumably due to dissolution and albitization.

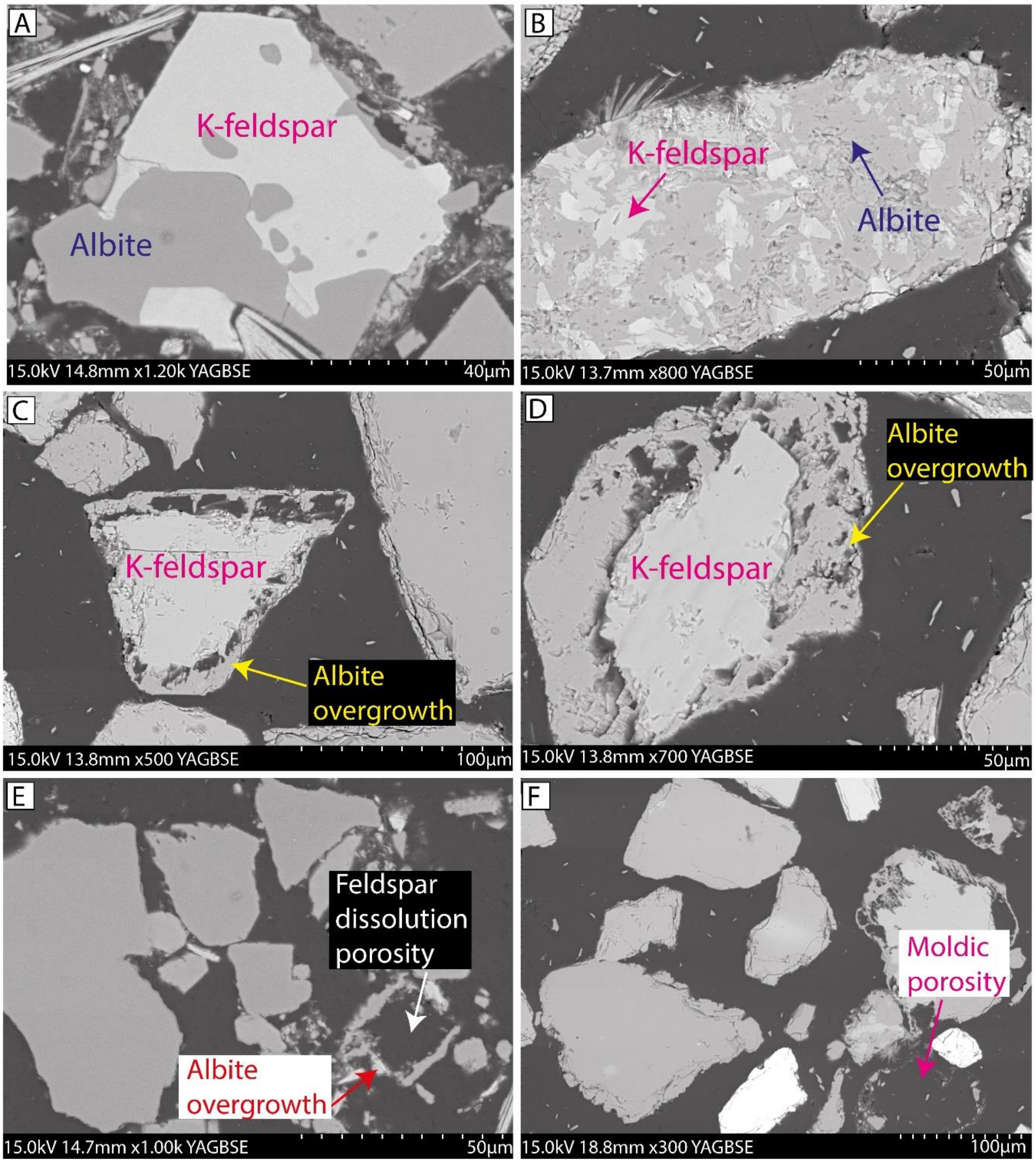

Figure 5.8. BSEM images showing examples of albitization of feldspar, development of albite overgrowths, and dissolution of feldspars in the reacted samples of the Bute Inlet. (A) BSEM image showing blocky albitization of K-feldspar. Station 028A sample reacted without silica; (B) BSEM image showing pervasive albitization of K-feldspar. Station 028A sample reacted without silica; (C) BSEM image showing development of thin albite overgrowth. Note how the overgrowth grows into the dissolved K-feldspar, suggesting that dissolution predated the development of the overgrowth. Station 028A sample reacted without silica; (D) BSEM image showing development of thick albite overgrowth on detrital K-feldspar. Station 028A sample reacted without silica; (E) BSEM image showing dissolved feldspar grain being rimmed by albite overgrowth. Station 036 sample reacted without silica; (F) BSEM image showing a moldic pore, formed from a complete dissolution of a feldspar grain. Station 028A sample reacted with silica.

5.6.6 Quartz overgrowths

Angular, blocky authigenic quartz overgrowths have been observed in the proximal-channel, Station 028A sample reacted with silica, based on SEM/SEM-EDS analysis (Figure 5.9A & B), with thicknesses ranging from 2-17 µm (average 9 µm). However, the overgrowths occur in trace amount in the sample, and have not been observed in samples that were not reacted with silica during the experiments. The authigenic quartz overgrowths were developed where coatings of clays and/or microcrystalline quartz are absent on detrital quartz grains (Figure 5.9A & B).

5.6.7 Microcrystalline quartz cement

The authigenesis of silica in the silica-reacted sediments of the Bute Inlet developed two main habits: (1) microquartz coatings (Figure 5.9C); and (2) intergranular pore-filling microquartz (Figure 5.9D). The lengths of microquartz crystals range from 1- 6 µm (average 3 µm) and 1-7 µm (average 3 µm) for Station 028A and Station 036 samples, respectively. The microquartz coatings cover detrital grains, such as biotite (Figure 5.8C), albite (Figure 5.9E), and quartz (Figure 5.9F), but are in optical continuity with detrital quartz grains alone. EDS phase map data for post-experiment sample with silica from Station 028A shows the total microquartz content is 0.11 % (Table 5.1), even though some unreacted silica was recovered after the experiment. In the post-experiment sample of Station 036, however, the amount of microquartz is higher (5 %) and no unreacted silica was recovered. The intergranular pore-filling microquartz consists of randomly oriented crystal aggregates that are similar in size and habit to the grain-coating microquartz (Figure 5.9D).

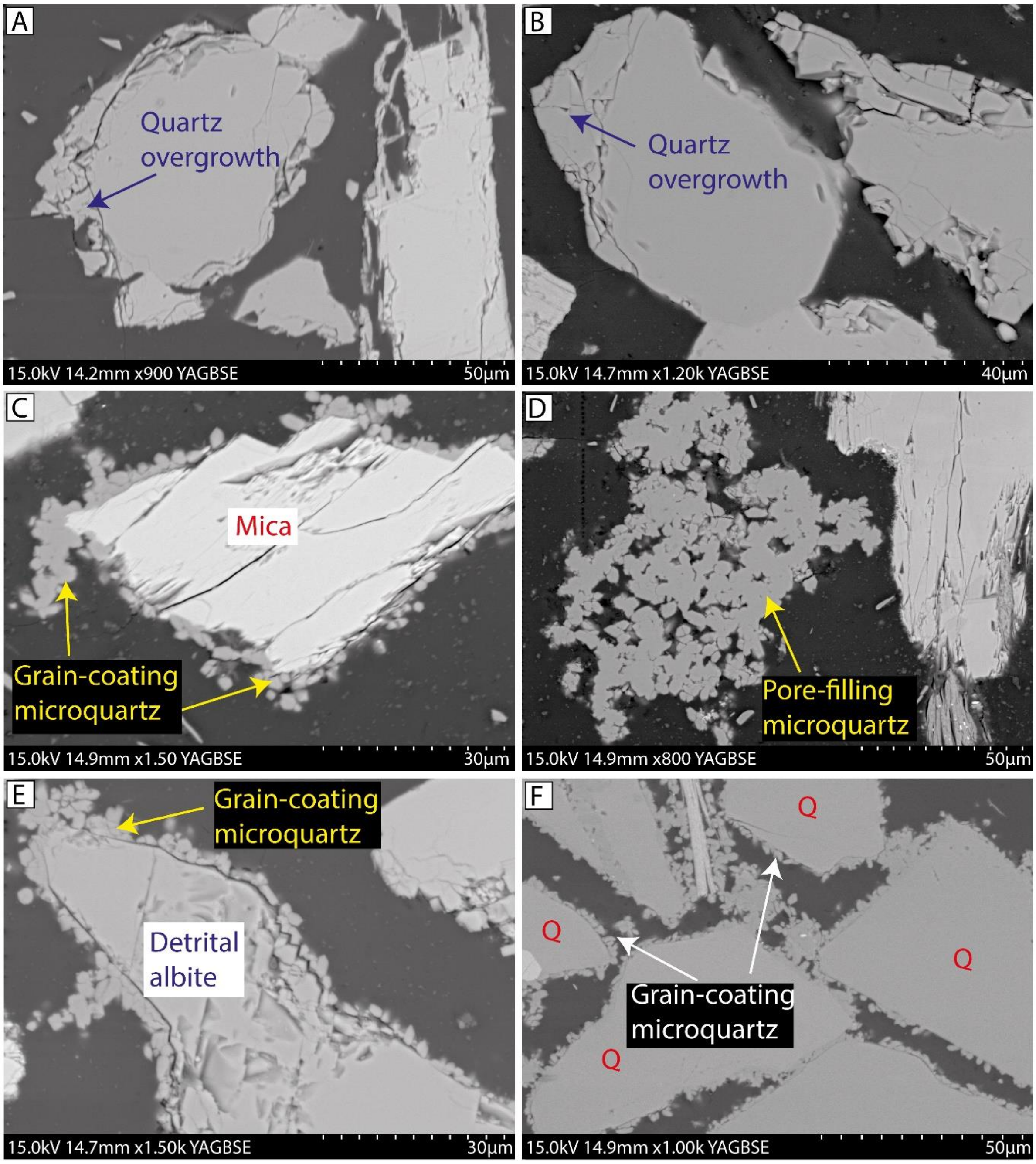

Figure 5.9. BSEM images showing examples of quartz overgrowths, grain-coating, and pore-filling microcrystalline quartz in the reacted samples of the Bute Inlet. (A) BSEM image showing blocky quartz overgrowth. The pointed/sharp edges of the overgrowth suggests authigenic origin. Station 028A sample reacted with silica; (B) BSEM image showing the formation of blocky quartz overgrowth on detrital quartz. Station 028A sample reacted with silica; (C) BSEM image showing microcrystalline quartz coating detrital mica. Station 028A sample reacted with silica; (D) BSEM image showing development of pore-filling microcrystalline quartz destroying intergranular porosity. Station 028A sample reacted with silica; (E) BSEM image showing the formation of microcrystalline quartz coating detrital albite. Station 028A sample reacted with silica; (F) BSEM image showing the precipitation of microcrystalline quartz coating detrital quartz, preventing the formation of macro quartz overgrowth. Station 036 sample reacted with silica.

5.6.8 Detrital grain dissolution

Because of their unstable chemical composition, detrital feldspars undergo dissolution, which results in the formation of secondary, intragranular porosity (Figure 5.8E & F). Partly and pervasively dissolved feldspars have been observed in the four post-experiment Bute samples (e.g., Figure 5.8F). In addition, pervasively dissolved feldspars form moldic, open pores, which are often surrounded by albite overgrowth (Figure 5.8E & F). The alteration and dissolution of mica grains were also noticed, and have created secondary dissolution pores within the grains.

5.7 Discussion

5.7.1 Impact of albitization of feldspars on reservoir quality

Albitization of detrital K-feldspar and plagioclase is common in subsurface sandstones, and is one of the most significant changes that affect sandstones reservoir quality evolution (Chowdhury and Noble, 1993; González-Acebrón et al., 2010; Morad et al., 2000, 1990; Saigal et al., 1988). Dissolution of K-feldspar and plagioclase could enhance the development of secondary porosity in sandstones. The albitization of feldspars, in contrast, can replace and/or occlude the secondary intragranular porosity created due to dissolution, thereby destroying reservoir quality (Chowdhury and Noble, 1993). Furthermore, feldspar dissolution can significantly affect sandstones original framework composition, which results in the formation of several diagenetic products such as kaolinite, illite, dickite, and calcite (Boles, 1982; Morad et al., 2000, 1990; Saigal et al., 1988). Therefore, while dissolution improves secondary intragranular porosity in feldspars, albitization reduces the secondary porosity developed, by filling the dissolution pores and, hence, destroying reservoir quality. Understanding the process of albitization in sandstones is, thus, useful in reservoir quality evaluation as well as the mass transport of Na^+ in the subsurface (Chowdhury and Noble, 1993).

5.7.2 Sources of K^+ and Na^+ for feldspar authigenesis

Authigenic albite overgrowths have been reported to precipitate concomitantly with authigenic quartz overgrowths in the North Sea reservoirs at temperatures of about 110 ˚C and 2.5 km depth of burial (Nedkvitne et al., 1993). In addition, thick, well-developed albite overgrowths grow into intergranular porosity (e.g., Figure 5.8D), thus destroying reservoir quality. Based on fluid inclusion data, a temperature of 90 ˚C has been reported for the onset of authigenic albite cementation for the Triassic Sherwood Sandstone of the West Ireland Basin, with the maximum albite authigenesis temperature ranging from 105 to 110 °C (Schmid et al., 2004). Although the formation of albite in sandstones has been attributed to high-temperature, deep-burial diagenetic environments, albite in lacustrine sediments might form at a relatively lower temperature (60 °C) from Na^+ enriched brine due to dissolution of evaporites (Chowdhury and Noble, 1993). This could equally serve as a source of Na^+ for albitization in high-temperature mesodiagenetic environments. Additionally, a study of salt-dome-related diagenesis in Tertiary turbidite reservoirs from Espirito Santo Basin, Brazil by Oliveira and De Ros (2018) has revealed that mesogenetic compactional fluids were progressively modified due to close proximity to salt domes, leading to development of ubiquitous feldspar albitization. Based on the distribution of feldspar albitization, the study has found that the fracture systems along the margins of the salt domes acted as preferential pathways for such hot brines.

Authigenic K-feldspar overgrowths are absent in the studied samples. This is probably due to the low amount of starting K-feldspar content in the sediments compared with the plagioclase feldspars (Table 5.1).

There are several potential sources of K^+ and Na^+ for feldspar authigenesis, with the most common sources being the dissolution of detrital feldspars (Ulmer-Scholle et al., 2015), volcanic fragments (Worden et al., 2020), and clay transformations (e.g., conversion of smectite to illite) (Worden and Morad, 2003). External sources largely consist of products of diagenetic alterations, such as pressure solution of silt-size feldspars in associated mudrocks, and brines derived from dewatering of evaporites (Ulmer-Scholle et al., 2015). In the reacted sediments of the Bute Inlet, the dissolution of both detrital K-feldspar and plagioclase has been observed. Nevertheless, bulk XRD results of the pre-reacted sediments from Stations 028A and 036 have indicated that albite is the plagioclase feldspar. Consequently, it is difficult to differentiate between detrital and authigenic albite in the reacted sediments, especially where detrital plagioclase had completely dissolved and authigenic albite has replaced it, or where complete albitization of K-feldspar has occurred. Furthermore, authigenic albite also occurs as an overgrowth on detrital albite and on K-feldspar. The K^+ derived from the dissolution of K-feldspar can be used to form illite.

Overall, the detrital albite appears to be the main source of Na^+ for the formation of the albite overgrowth and the grain-replacive albite cement. Despite the albitization of feldspars observed in the reacted samples, fresh feldspars are still retained. This is probably because albitization reactions occur very fast and quickly reach completion once started (Boles, 1982; Chowdhury and Noble, 1993), thus retaining fresh, unaltered feldspars.

5.7.3 Experimental development of clay and microquartz coatings

The effect of grain coating clays, notably chlorite, on precipitation of quartz and albite overgrowths on detrital quartz and feldspars, respectively, was determined in the laboratory using the hydrothermal reactor experiments. Quartz, feldspars (albite and K-feldspar), and mica grains were used as the main starting materials for the experiment in a 0.1 M Na_2CO_3 at 250 °C for 72 hours (3 days). After the experiment, authigenic chlorite coatings had developed on detrital quartz and feldspar grains (e.g., Figure 5.5B & C), and where coatings are absent, quartz and albite overgrowths were formed, respectively (e.g., Figures 5.8C & D and 5.9A &B). The experiments have shown that the physical obstruction of nucleation sites by the clay coats is an effective mechanism by which the development of ubiquitous quartz and albite overgrowths can be inhibited.

Two possible precursors for chlorite have been identified: (1) grain-coating and pore-filling clinochlore (Mg-rich chlorite), based on bulk XRD results of pre-reacted samples. (2) dissolved and/or altered detrital micas (biotite) are another precursor for chlorite observed in the reacted sediments (e.g., Figures 5.5C and 5.6E). Results of the SEM/SEM-EDS analysis of Fe/(Fe+Mg) ratio (Table 5.1) for chlorites have shown that the chlorites are both Mg- and Fe-rich, indicating that they were sourced from clinochlore (Mg-rich chlorite) and other Fe-rich grains (e.g., biotite and/or amphibole), respectively. Furthermore, the results of the hydrothermal reactor experiments using samples from Station 036 suggest that precursor chlorite from clinochlore, for instance, was crucial for the formation of well-developed, diagenetic chlorite. However, because such precursor chlorite was insufficient in the sample from Station 028A, minor chlorite was formed (Table 5.1; Figure 5.4B & C), resulting in low chlorite-coat coverage in the samples (Figure 5.2; Table 5.1). This further suggests that the precursor clinochlore was more crucial in the formation of chlorite than the biotite, despite the sufficient amount of biotite in the pre- and post-reacted samples of Station 028A (Table 5.1).

Chlorite coatings that were better developed on detrital quartz and feldspars occur near altered mica grains (e.g., Figures 5.5C and 5.6C & E). While grain-coating chlorite appears to have prevented quartz and albite cementation, pore-filling chlorite, resulting from alteration of mica and detrital clay matrix, seem to have significantly occluded intergranular porosity, where well-developed (e.g., Figure 5.5C and 5.6C & F).

In another experiment in which the Bute sediments were reacted with silica, microquartz coatings precipitated and appear to have prevented the development of quartz overgrowths

(Figure 5.9F). Additionally, the microquartz coatings have precipitated on detrital feldspar grains, inhibiting the development of authigenic feldspar (albite) overgrowth (Figure 5.9E). Pore-filling microquartz, nonetheless, have occluded intergranular porosity (Figure 5.9D).

In ancient sandstones, microquartz coatings were interpreted to have formed in sands rich in biogenic silica (e.g., sponge spicules) (Aase and Walderhaug, 2005; Hendry and Trewin, 1995) during shallow burial eodiagenesis at a temperature of 50 °C (Vagle et al., 1995). In the present study, microquartz coatings have been observed to be engulfed by chlorite coats, indicating that they predate chlorite coats. Furthermore, grain-coating microcrystalline quartz have been identified as an effective mechanism for porosity preservation in deeply buried sandstone reservoirs (e.g., Aase et al., 1996; French et al., 2012; French and Worden, 2013; Weibel et al., 2010; Worden et al., 2012); they help in stabilizing grain-grain contacts, thereby increasing sandstones resistance to pressure dissolution and preserving intergranular porosity(Lima and De Ros, 2002). High porosity and permeability have been recorded in the Devonian Uere sandstones of the Solimoes Basin, Brazilian Amazonia, due to grain-coating microquartz, with the optimum coatings thickness ranging between 5 and 10 µm and the optimum volume of 4-6 % (Lima and De Ros, 2002).

In general, grain-coating chlorite can significantly inhibit the formation of authigenic quartz and albite overgrowths in deeply buried reservoirs by preserving porosity, and mica grains can serve as important precursors for chlorite coats, especially in closed system diagenesis where Fe is readily available. In submarine fans, owing to hydrodynamic processes, high amounts of mica grains tend to be deposited in the distal fan (Mansurbeg et al., 2008; Marchand et al., 2015), implying the likelihood of forming high amount of authigenic chlorite should mica alteration occur. This is corroborated by the findings of this study, where chlorite was observed to have replaced detrital mica (biotite) grains in the Paleocene Forties Sandstone Member (Chapter 3). However, porosity will be significantly lost due to compaction if the mica content is high due to their high susceptibility to ductile deformation. Coatings of microquartz have been observed to prevent quartz and albite cementation in the reacted modern sediments of the Bute Inlet; therefore, sands rich in microquartz coatings would preserve porosity as well as reservoir quality should deep burial occur.

5.7.4 Relation between hydrothermal reactor experiments and natural diagenesis

SEM-EDS observations have shown that chlorite coatings, which appeared to be recrystallized or neoformed, are similar in morphology and, for the most part, chemistry to naturally-occurring chlorites. This suggests strongly that the chlorite coatings formed during the experiments are the same as those developed during natural diagenesis in sandstones, in that both require precursors and a threshold temperature between 90 and 120 °C . Berthierine, for instance, is one of the common precursor for chlorite in sandstones (Aagaard et al., 2000; Chen et al., 2011; Worden and Morad, 2003), whereas mica and inherited clinochlore clays were the main precursors for chlorite in this study. Furthermore, the sediment used in the hydrothermal reactor experiments for this study were heated to a temperature (250 °C) beyond the threshold temperature required for the formation of chlorite in natural diagenesis.

Although the hydrothermal reactor experiments, which simulate diagenesis in the laboratory, were carried out at conditions closely related to natural reservoirs, there are significant differences between the two: (i) the reactor experiments are characterized by short experimental time compared with natural diagenesis, which takes millions of years to complete or occur; and (ii) the simplified mineralogy of the starting material and the formation water chemistry (Haile et al., 2015). In this study, for example, one of the main consequences of the simplification is the formation of chlorite from predominantly a single, clinochlore precursor, which could be less common in natural diagenesis where smectite, berthierine, and kaolinite (and siderite) can serve as precursors for chlorite (Iijima and Matsumoto, 1982; McKinley et al., 2003; Worden et al., 2020; Worden and Morad, 2003). Furthermore, unlike the experimental formation water, which has rather constant composition, the formation water in natural sandstones might be either meteoric or marine during diagenesis, with complex variation in the amount of dissolved cations.

Silica and aluminium, among others, have been identified as essential ingredients for the formation of clay minerals (e.g., chlorite) in sandstone reservoirs (Haile et al., 2015; Worden et al., 2020; Worden and Morad, 2003). The Si and Al are sourced by reactive clays, redistribution of quartz, and alteration of plagioclase feldspar. In the reacted sediments of this study, the Si and Al incorporated into the authigenic chlorite formed might have been sourced from reacted silica, and from dissolved plagioclase feldspar. The study, therefore, demonstrates that, although Si and Al sourced by transformation of clay minerals are lacking, feldspar may serve as a potential source of Si and Al to form chlorite, especially with the possible supply of

Fe and Mg from the observed, altered mica grains. This is similar to what is obtainable in natural sandstones as noticed by Morad and Aldahan (1987), even though the Fe and Mg were sourced from rock fragments in their study. Additionally, the decrease in albite content in the reacted Station 036 samples and the corresponding high chlorite content support this interpretation.

Nevertheless, despite the similarities and the differences between the hydrothermal reactor experiments and natural diagenesis, the study shows that the formation of chlorite on clean quartz and feldspar grains is possible, and occur quite fast at the studied temperature of 250 °C.

5.7.5 Limitations of the hydrothermal-reactor experiments

Although the hydrothermal-reactor experiments are different from real-world systems, the following limitations and ways of improving the experiments have been identified.

1. The hydrothermal reactor experiments conducted with silica gel in the reactor started with excess supply of silica in the system to initiate micro and macro quartz cementation. In natural diagenetic settings, however, such conditions develop over prolonged periods of geologic time, with silica and other reactants being derived from multiple sources.
2. The experiments were conducted at high temperature (250 °C) for 72 h. Nevertheless, there is the need to conduct the experiments at both current and lower temperature for longer periods of time in order to effectively understand the mechanisms of transformation of both detrital grains as well as clay minerals at various stages of the experiments.
3. Further experiments need to be conducted to study the role of fluid chemistry using a volumetrically low fluid-to-sediment ratio in a reactor setup that would allow fluid sampling at various experimental conditions. This would enable the effective understanding of the microenvironment for clay minerals precipitation and would help develop a broader understanding of the chemical and reaction parameters for the formation of authigenic clay minerals.

5.7.6 Implications for reservoir quality prediction in ancient turbidite reservoirs

Clean, clay-free sandstones are often thought to have the best reservoir quality; however, such sandstones are susceptible to ubiquitous quartz cementation during burial. Sandstones with clay coatings, on the other hand, could prevent quartz cementation at deeper burial, thereby preserving reservoir quality. Our study has shown that the synthesized chlorite coatings are similar in morphology and composition to those found in natural sandstones reservoirs. In addition, the study has revealed that precursor detrital clay is key to forming well-developed chlorite coats, with high chlorite-coatings coverage. The results of the experiments have shown that the Bute sediments from Station 036, with precursor chlorite content of 6 % and an initial average chlorite-coat coverage of 9 and 17 % for quartz and albite grains (respectively), have, upon heating to 250 °C, generated chlorite volume ranging from 19 to 27 %, with average chlorite-coat coverage ranging from 46 to 66 % for quartz and 64 to 77 % for albite grains (Figure 5.3; Table 5.1). These chlorite coatings have prevented the formation of quartz and albite overgrowths and, thus, preserve reservoir quality. The reacted sediments from Station 028A, in contrast, have poorly-developed chlorite coats, probably due to insufficient volume of precursor detrital clay (< 1 %), with average chlorite-coat coverage ranging from 24 to 47 % for quartz and 15 to 40 % for albite grains (Figure 5.2) that have managed to develop coats.

Consequently, since the results of the experiments have shown that precursor detrital clays are essential for the continuous growth of diagenetic clays, with increasing temperature, it is important to identify depositional environments and processes in deep-water sandstones that could potentially lead to the formation and occurrence of detrital clay coats in ancient turbidite reservoirs. For instance, detrital clay coats in deep-water turbidites are reported to have been inherited from continental, transitional, and shallow marine/shelf environments before being transported to deep-water settings (Bahlis and de Ros, 2013; Yezerski and Shumaker, 2018). Thus, although such inherited coats might be susceptible to abrasion during transport, submarine channels, which are close to shelf, could potentially have remnant detrital clay coats that might recrystallize to form continuous, diagenetic coats during burial diagenesis, thereby preserving reservoir quality. In addition, detrital clay coats have been interpreted to form during sediment dewatering in submarine channels and lobe axis areas (e.g., Collins et al., 2015; Houseknecht and Ross, 1992; Porten et al., 2019), which could form diagenetic coatings at deeper burial. Furthermore, the occurrence of high mica content in low-energy, distal submarine fan owing to fractionation of turbidity currents based on grain shape and density (Mansurbeg et al., 2008; Marchand et al., 2015; Stammer, 2014), and their subsequent alteration, could lead to the formation of grain-coating chlorite to prevent quartz and albite cementation.

5.8 Conclusions

- A multi-batch hydrothermal reactor formation of chlorite and microquartz coatings has been shown to occur at the temperature of 250 °C within 3 days (72 hours) under simulated reservoir conditions.
- Although studies of natural sandstones have largely focused on the formation of grain-coating clays on detrital quartz for the prevention of quartz cementation, this study has demonstrated that grain-coating chlorite could develop on both clean quartz and feldspar grains, and their formation has prevented the development of quartz and feldspar overgrowths, thereby preserving reservoir quality.
- Hydrothermally dissolved albite and probably K-feldspar could have supplied the required Al and Si for the precipitation of the chlorite coatings.
- The formation of extensive chlorite coatings seem to require a clinochlore (Mg-rich chlorite) precursor, and the hydrothermally formed chlorite coatings are similar to those in natural sandstones. The initial chlorite volume of 6 % has increased to 19-27 % after the reactor experiments, generating up to 77 % average chlorite-coating coverage on detrital grains.
- Chlorite coatings were poorly developed in post-experiment samples with less than 1 % initial detrital clays, generating coatings coverage of 47 % maximum.
- Alteration of detrital biotite has contributed to the formation of chlorite coatings.
- The formation of microquartz coatings has prevented the formation of authigenic, macroquartz cement.

Chapter 6: Summary and future work

As global attention progressively shifts towards increased carbon capture and storage (CCS) and transition to low carbon economy, the importance of deep-water turbidite reservoirs is still as valuable for CO_2 sequestration. Understanding the role of clay minerals and different diagenetic components that could potentially react with CO_2 is vital for any successful CO_2 sequestration projects (Xia and Wilkinson, 2017; Yanzhong et al., 2020). Many turbidite sandstones, for instance, have a lot of carbonate cements in them (e.g., Mansurbeg et al., 2009, 2008; Stewart, 1995), and injection of CO_2 into the sandstones could dissolve the carbonate cements, create secondary porosity, open up new flow pathways, precipitate other minerals, and cause CO_2 to be released overtime. Consequently, the understanding of diagenesis and reservoir quality evolution of sandstones might help identify excellent reservoirs with good porosity and permeability, which are suitable for carbon capture and storage projects. This requires a comprehensive assessment of the sandstones reservoir properties, facies distribution, and migration pathways prior to any CO_2 injection.

6.1 Reservoir quality of the Forties Sandstone Member

Reservoir quality in the Forties Sandstone Member is controlled by depositional processes (resulting from variation of grain size and clay content) and by burial diagenesis. These two factors have been discussed in detail in Chapters 3 and 4, respectively. In order to help understand and predict better reservoir quality in deep-water sandstones, the depositional characteristics and diagenetic alterations as the main controls of reservoir quality variation and heterogeneity of the Forties Sandstone Member will be integrated in this chapter.

6.1.1 Depositional processes control

An experimental study of turbidity currents by Stammer (2014) has shown that sediments are spatially fractionated based on grain density and grain shape, resulting in large-scale spatial variations in texture and composition. Denser, coarser-grained sediments transported in a turbidity current tend to settle first at the base of a high-density turbidity flow in the channel and lobe axis areas, whereas the finer-grained, less-dense fractions remain in the flow and are progressively deposited in the lobe off-axis depositional settings (Huang et al., 2020; Marchand et al., 2015).

Depositional processes exerted a strong control on reservoir quality of the Forties Sandstone Member from proximal to distal fan, and from lobe axis to lobe margin settings, resulting in spatial variation in textural parameters (such as grain size, sorting and clay content) and, hence, reservoir quality of submarine fan deposits. Distribution of textural parameters are largely linked to the energy of the medium of transportation and depositional system. The proximal fan, amalgamated sandstones, which are predominantly products of high-density turbidity currents, have the best reservoir quality because they are mainly well-sorted, medium-grained sandstones, with the highest porosity and permeability (1.9-28.4 % and 0.01-500 mD, respectively). The coarser grain size, better sorting, less pore-filling clays (Figures 3.10A and 3.19A & B), and low amount of ductile grains content (Figure 3.10B) characterized by these sandstones facies have resulted in larger pore throats and better reservoir connectivity for effective fluid flow compared with finer-grained sandstones. The distal fan, mud-prone heterolithic sandstones facies, which are largely products of low-density turbidity currents and debris flows, have the poorest reservoir quality due to finer grain size (Figures 3.10A and 3.19A & B), high detrital pore-filling clays (Figures 3.10A and 3.19C & D), and abundant ductile grains (Figure 3.10B). These have contributed to smaller pore throats and poorer reservoir connectivity for fluid flow compared with the amalgamated sandstones facies. The amount of pore-filling detrital and authigenic clays, which have a deleterious effect on reservoir quality of the Forties sandstones, ranges from 10 to 30 % (Figure 3.19C & D), lowering the core porosity (helium) and permeability to generally < 10 % and < 1 mD, respectively.

6.1.2 Diagenetic control

Diagenetic processes and alterations have had a significant impact on the modification of primary, depositional porosity and permeability, and, thus, on reservoir quality of the Forties Sandstone Member. Results of petrographic studies of the sandstones have revealed that mechanical compaction was a key driver for reducing primary intergranular porosity (Figure 4.8) and porosity was lost mainly due to compaction than due to cementation (Figure 4.8). Additionally, the amount of ductile grains content has been linked to intergranular, optical porosity (Figure 6.1). Heterolithic sandstones with abundant ductile grains (consisting of mica and mudclasts) ranging from 5-10 % have suffered higher ductile deformation, thereby reducing the intergranular, optical porosity to generally < 5 % (Figure 6.1). In contrast, the amalgamated sandstones facies, which have < 5 % ductile grains content, have higher intergranular, optical porosity (of > 5 %) (Figure 6.1).

Although the Forties Sandstone Member is within quartz cementation domain (> 1.5 Km), based on burial history plots (Figure 3.3), there was no observed pressure dissolution of quartz grains due to impact of chemical compaction, which are commonly characterized by stylolite grain contacts that leads to quartz dissolution and cementation in deeply buried sandstones. This is presumably because of the relatively shallow burial depths of the sandstones (2200 to 3100 m TVDSS). Point count data has shown that sandstones with high amount of grain-coating clays (of up to 10 % of whole rock volume), consisting of chlorite, illite, and mixed-layer illite-smectite, have undergone less mechanical compaction and, consequently, exhibit overall, higher intergranular volume (IGV) (Figure 4.23A). Sandstones with lower amount of grain coating clays, in contrast, have been subjected to a significant mechanical compaction and reduction of intergranular pore space, resulting in lower IGV (Figure 4.23A). Where clay coats are thick and continuous, they would potentially arrest chemical compaction at deeper burial by inhibiting pressure dissolution at grain-grain contacts.

The formation of thick, continuous, and well-developed clay coats, which were originally from smectitic clays, has preserved reservoir quality in the Forties Sandstone Member (Figure 3.16C) by inhibiting quartz cementation. Additionally, sandstones with high clay-coating coverage (> 40 %) have generally low quartz cement volume (Figure 3.16C). Nevertheless, sandstones with thin, discontinuous, and poorly-developed clay coats have higher amount of quartz cement. Such sandstones commonly have low clay-coating coverage, which could not significantly inhibit quartz cementation. Thus, clay-coating coverage of > 40 %, which corresponds to volume of grain-coating clays of 8-10 % (Figure 3.16D), might be required to prevent quartz cementation in the Forties Sandstones based on their relatively shallow, present-day burial depths (2200-3100 m TVDSS).

Carbonate cements, consisting of ferroan and non-ferroan calcite, dolomite, and siderite, where well-developed, have lowered the reservoir quality of the Forties Sandstone Member. Petrographic evidence have shown that the cements are early, due to floating grains. Ferroan calcite commonly occurs as replacement of non-ferroan calcite, where the latter had undergone dissolution. The dissolution of carbonate cements (e.g., siderite; Figure 4.14D) has created secondary intergranular porosity that are often well-preserved.

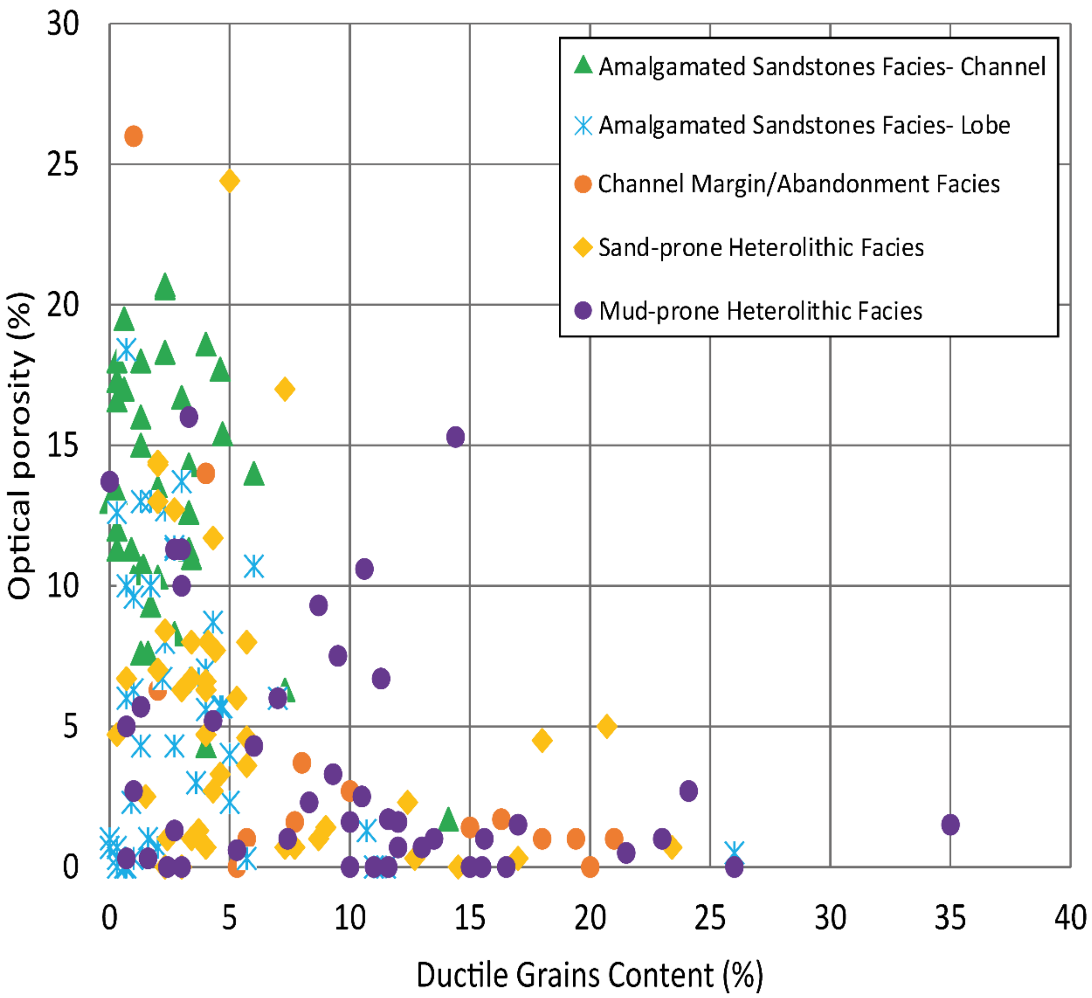

Figure 6.1. Plot of optical, thin-section porosity against ductile grains content showing negative correlation. Intergranular, optical porosity is lost when ductile grains content reaches 5-10 %.

6.2 Principal findings

Figure 6.2 shows the summary of the main findings of this research, indicating the role of depositional and diagenetic controls on reservoir quality evolution of the Forties Sandstone Member and the experimental studies of the Bute Inlet sediments. These have been discussed in detail in chapters 3, 4, and 5, and in sections 6.1.1 and 6.1.2 of this chapter. In both systems, there is a downfan decrease in grain size and an increase in clay content (Figure 6.2). Detrital clay coatings are the most important precursors for authigenic coats in order to arrest quartz cementation.

6.2.1 Impact of clays on quartz cementation

Quartz cement is one of the most important cements that occlude intergranular porosity in sandstone reservoirs (Bjorlykke and Egeberg, 1993; McBride, 1989; Worden and Morad, 2000). Finer-grained sandstones, unlike their coarser-grained counterparts, are reported to require a significant volumes of clay coatings (1-13 %) to form excellent clay-coating coverage due to their large surface area per volume (Bloch et al., 2002; Pittman et al., 1992). In addition, distal-fan, fine-grained turbidite sandstones of the Palaeocene Shetland Faroes Basin, British continental shelf have been reported to have the most abundant quartz cement compared to the proximal-fan, coarser-grained turbidite sandstones (Mansurbeg et al., 2008). In contrast, our study of the Forties Sandstone Member has found that the distal-fan, finer-grained heterolithic turbidite sandstones have the least, average quartz cement volume (1.78 %) compared with those of the proximal-fan, coarser-grained amalgamated turbidite sandstones, which have an average quartz cement volume of 3.62 % (Figure 4.24; also, see Appendix I: point count data summary). This is due to relatively well-developed grain-coating clays and abundant pore-filling clays, which both cover detrital grains surface area and inhibit quartz cementation in the distal-fan, finer-grained heterolithic facies (Figure 6.2). Furthermore, characterized by excellent porosity and permeability that facilitate fluid flow, due to coarser grains and less pore-filling clays, the proximal fan, amalgamated sandstones are prone to developing more quartz cement if they are uncoated with clays (Figure 6.2).

Consequently, the amalgamated sandstones, which have the best original porosity and permeability, would be more susceptible to quartz cementation (especially if less clay-coated) when deeply buried, in contrast to the distal fan heterolithic facies, which might seem to have lower original porosity and permeability but are maintained due to the impact of clays.

6.2.2 Significance of precursor detrital clays

Detrital clays play a key role in the formation of authigenic clays, as they undergo recrystallization and transformation (Figure 6.2). As a result, information on precursor, detrital clays (such as clay type and volume) produce crucial input data required for construction of diagenetic models. However, the role of detrital clays cannot be adequately quantified in ancient sandstones such as the Forties, where such clays have undergone partial to pervasive recrystallization and transformation. To address this problem, our experimental study simulating diagenesis using the modern-day sediments from the Bute Inlet, has demonstrated the role played by detrital clays in the formation of authigenic clay coats. Results of the experiments have revealed that detrital clay coats, with initial percentage coverage of 18-20 % on detrital grains and a clay volume of < 1 % per whole rock volume, were poorly recrystallized and transformed in the post-experiment samples from Station 028A (proximal Bute Inlet), generating coatings coverage of 15 to 47 % on some coated detrital grains and a clay volume of < 1 %. Additionally, the distal, post-experiment samples from Station 036, Bute Inlet, with an initial percentage coverage of 9-17 % on detrital grains and a clay volume of 6 %, have generated coatings coverage percent ranging from 46 to 77 % and clay volume ranging from 19 to 27 %, respectively. The well-developed coatings have arrested the formation of authigenic quartz and feldspar overgrowths. These quantitative data would give an insight into volume change resulting from the recrystallization and transformation of precursor, detrital clays during diagenesis. The results also suggest that contrary to a widely believed notion that clean sands form the best reservoir quality, sands with some clays are required to form coatings that would inhibit quartz cementation, and that the clean sands have exposed surfaces available for quartz cementation, as demonstrated by the Bute sediments (Figure 6.2).

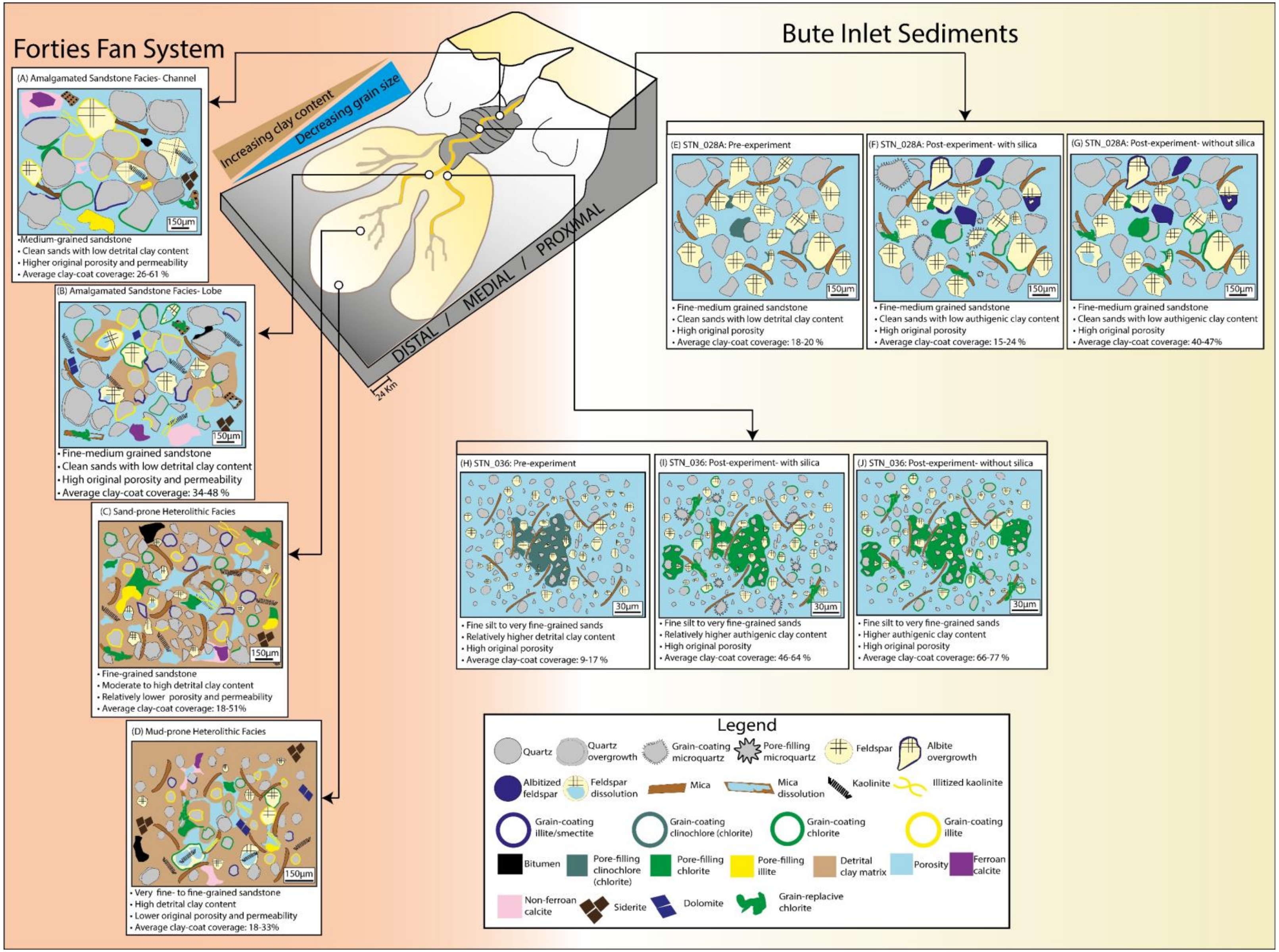
Forties Fan System
Bute Inlet Sediments
Increasing clay content
Decreasing grain size
DISTAL / MEDIAL / PROXIMAL
24 Km
(A) Amalgamated Sandstone Facies- Channel
150µm
•Medium-grained sandstone
• Clean sands with low detrital clay content
• Higher original porosity and permeability
• Average clay-coat coverage: 26-61 %
(B) Amalgamated Sandstone Facies- Lobe
150µm
• Fine-medium grained sandstone
• Clean sands with low detrital clay content
• High original porosity and permeability
• Average clay-coat coverage: 34-48 %
(C) Sand-prone Heterolithic Facies
150µm
• Fine-grained sandstone
• Moderate to high detrital clay content
• Relatively lower porosity and permeability
• Average clay-coat coverage: 18-51%
(D) Mud-prone Heterolithic Facies
150µm
• Very fine- to fine-grained sandstone
• High detrital clay content
• Lower original porosity and permeability
• Average clay-coat coverage: 18-33%
(E) STN_028A: Pre-experiment
150µm
• Fine-medium grained sandstone
• Clean sands with low detrital clay content
• High original porosity
• Average clay-coat coverage: 18-20 %
(F) STN_028A: Post-experiment- with silica
150µm
• Fine-medium grained sandstone
• Clean sands with low authigenic clay content
• High original porosity
• Average clay-coat coverage: 15-24 %
(G) STN_028A: Post-experiment- without silica
150µm
• Fine-medium grained sandstone
• Clean sands with low authigenic clay content
• High original porosity
• Average clay-coat coverage: 40-47%
(H) STN_036: Pre-experiment
30µm
• Fine silt to very fine-grained sands
• Relatively higher detrital clay content
• High original porosity
• Average clay-coat coverage: 9-17 %
(I) STN_036: Post-experiment- with silica
30µm
• Fine silt to very fine-grained sands
• Relatively higher authigenic clay content
• High original porosity
• Average clay-coat coverage: 46-64 %
(J) STN_036: Post-experiment- without silica
30µm
• Fine silt to very fine-grained sands
• Higher authigenic clay content
• High original porosity
• Average clay-coat coverage: 66-77 %
Legend
Quartz
Quartz overgrowth
Grain-coating microquartz
Pore-filling microquartz
Feldspar
Albite overgrowth
Albitized feldspar
Feldspar dissolution
Mica
Mica dissolution
Kaolinite
Illitized kaolinite
Grain-coating illite/smectite
Grain-coating clinochlore (chlorite)
Grain-coating chlorite
Grain-coating illite
Bitumen
Pore-filling clinochlore (chlorite)
Pore-filling chlorite
Pore-filling illite
Detrital clay matrix
Porosity
Ferroan calcite
Non-ferroan calcite
Siderite
Dolomite
Grain-replacive chlorite

Figure 6.2. Schematic summary diagram demonstrating the role of depositional characteristics (such as grain size and clay content) and diagenetic alterations in the studied Forties Fan system and the modern-day Bute Inlet sediments. There is downfan decrease in grain size and increase in clay content in both systems. The diagram highlights the significance of precursor, detrital clays in the systems, notably in the Bute, in the formation of authigenic clays, and microquartz precipitated in silica-reacted sediments. Additionally, clay coats were formed on both quartz and feldspar grains, preventing the formation of quartz and albite overgrowths, respectively, where well-developed.

6.3 Implications for carbon capture and storage (CCS)

As hydrocarbon production attains mature stage in almost all major oil and gas fields of the axial Forties Fan system (Hempton et al., 2005), the Forties Sandstone Member can be a potential site for geologic carbon capture and storage (CCS). Reservoir porosity and permeability have been identified as key controls on the efficiency and effectiveness of CO_2 injection into the subsurface geological formations for both CO_2 storage and enhanced hydrocarbon recovery, because low-porosity and/or low-permeability are often influenced by high volume of clay mineral and ductile grains, poor sorting, quartz cementation, and illite growth (Xia and Wilkinson, 2017), which the present study has investigated. Geologic CO_2 storage, which mainly involves injecting CO_2 into deep, depleted hydrocarbon reservoirs, is considered to be the most effective method for long-term storage of large quantities of CO_2 (Celia and Nordbotten, 2009; Myer, 2011). Physical trapping and solubility trapping, which involve trapping of CO_2 in structural and stratigraphic traps and dissolution of CO_2 into the pore water (respectively), are the most common geologic CO_2 storage mechanisms (e.g., Li and Pang, 2016; Shukla et al., 2010). More recently, however, mineral trapping, involving carbonation of CO_2 to form calcite and dolomite, with Ca^{2+} and Mg^{2+} as key elements required for the process, are considered as the safest and most stable storage mechanism (Yang et al., 2017). In addition, an experimental study by Yanzhong et al. (2020) simulating mineral trapping in anorthite-free arkosic sandstones using $CaCl_2$-rich formation water, has precipitated calcite and kaolinite, suggesting that saline pore waters rich in $CaCl_2$, NaCl, KCl, and $MgCl_2$ are crucial for mineral trapping of CO_2. The experimental study of the mineral trapping of CO_2 by Yanzhong et al. (2020) involves: (1) Preparing sandstones rich in K-feldspar and albite, and placing them in a reactor containing 200 ml solution of $CaCl_2$, NaCl, KCl, and $MgCl_2$, with purity of more than 96%, 99.5%, 99.5%, 98% respectively. (2) Injecting CO_2 (with a purity of more than 99.995%) into the reactor by pumping in order to maintain P_{CO2} of 4.0 ± 0.1 Mpa and to attain CO_2 saturation during the whole experiments. (3) Heating the reactor to temperatures of 100 °C and 150 °C, with a heating rate of 4 °C/min, for 48 h and 96 h, respectively. During the experiments, calcite and kaolinite precipitated, whereas albite and K-feldspar partly dissolved. The results of the experiments, therefore, suggest that the carbonation of CO_2 to form calcite has taken place during the experiments by mineral trapping of CO_2.

Consequently, characterized by good reservoir porosity and permeability, effective seal (Sele claystones) and an anticlinal closure (e.g., the Forties-Montrose High), the Forties Sandstone Member could be an ideal candidate for physical trapping. Additionally, the sandstones highly-saline pore waters (Crawford et al., 1991) and their arkosic composition (Figure 3.6A) make them the excellent potential sites for mineral trapping.

6.4 Summary

- Depositional facies (involving grain size, sorting and clay content) and diagenesis have played a vital role in reservoir quality evolution of the Forties Sandstone Member of the Sele Formation.
- Mechanical compaction is the main driver for porosity loss than cementation.
- The optimum pore-filling clays volume and ductile grains content, which have a deleterious effect on reservoir quality, range from 10-30 % and 5-10 % (respectively), lowering intergranular porosity and permeability to generally < 10 % and 1 mD, respectively.
- Grain-coating chlorite, illite-smectite, and illite have inhibited the development of quartz cementation in the sandstones, with the optimum clay-coating coverage ranging from 40 to 50 % (based on the present-day burial depths of 2200-3200 m).
- Quartz cement volume does not increase with decreasing grain size, and generally decreases from proximal to distal fan (from average 3.62 to 1.78 %, respectively) due to the impact of grain-coating clays and increasing pore-filling clays, which both cover the surface area of detrital grains.
- Grain size has no impact on clay-coating coverage, but the coatings coverage is controlled by provenance, sediment dewatering, and diagenesis.
- Carbonate cements are early cements that have prevented early compaction and have had less impact on reservoir quality, but where well-developed and have undergone dissolution, they could significantly improve reservoir quality.
- Experimental simulation of diagenesis using the modern-day, deep-water sediments from Bute Inlet (British Columbia, Canada) has shown that precursor clays are crucial for the formation of authigenic clays, and that clean sands with less precursor, detrital clay (< 1 %) form poor clay-coating coverage (max 47 %) post-experiment, whereas dirty sands with precursor, detrital clay content of up to 6 % form better clay-coating coverage (max 77 %) post-experiment.

6.5 Suggestions for future work

6.5.1 Hydrothermal reactor experiments

Our hydrothermal reactor experiments to model the effect of high temperature on chemical diagenesis of the modern Bute Inlet sediments have shown that clay minerals, quartz overgrowths, albite, and coatings of chlorite and microquartz have formed during the experiments, which were conducted on 4 samples at 250 °C for 72 hours. However, in order to acquire more robust input data for reservoir quality simulation software such as Touchstone or PetroMod, the experiments should be conducted on more representative samples that span the various depositional environments of submarine fan systems using longer durations of the experiments. In addition, the experiments should also be carried out using real reservoir pore fluids on disaggregated, ancient samples of the Forties Sandstone Member, for instance, for improved understanding of the diagenesis of other deeper turbidite sandstone reservoirs elsewhere. Furthermore, pressure might be introduced to represent high-pressure high-temperature (HPHT) systems, coupled with real-time recording of changes of porosity and permeability. This would significantly improve the understanding of diagenesis in deeply-buried sandstone reservoirs.

6.5.2 Fluid inclusion micro-thermometry, quartz cementation models and SIMS analysis

Although cathodoluminescence analysis has been used to study the extent and phases (where available) of quartz overgrowths, fluid inclusion data is required to establish the precipitation temperature for quartz cement, and the use of high-accuracy, high-resolution secondary ion mass spectrometry (SIMS) analysis is further suggested to complement the fluid inclusion thermometry. This would help effectively constrain precipitation temperatures more accurately, thereby aiding better assessment of quartz cementation histories in the sandstones. Moreover, to fully understand the kinetics of quartz cement precipitation and to accurately predict the amount of quartz cementation as well as the percentage of pore space occluded due to quartz cement, models for quartz cementation for the Forties Sandstone Member need to be constructed. This would enable direct comparison with the point count data and potentially give further insights into the observed relatively low quartz cements in the sandstones, despite having attained the sufficient temperature for precipitation of the cement.

6.5.3 Micro-CT work for fluid flow simulation

X-ray computed tomography (micro-CT) has been widely employed in petroleum geology as a technique which allows the 3D imaging and analysis of internal features of sandstones reservoirs (e.g., Appoloni et al., 2007; Markussen et al., 2019; Munawar et al., 2018; Zhang et al., 2019). Reservoir quality controls hydrocarbon storage capacity, distribution and flow within sandstones reservoirs. Although our study has shown that reservoir quality is controlled by sedimentary texture, depositional facies and diagenesis, it does not indicate the nature, location, and distribution of connected porosity. Additionally, there is lack of information on the role played by pore-lining clays on porosity preservation and connectivity. The study has shown that, while there is lack of notable change in helium porosity from proximal to distal fan, significant variation in sandstones permeability exists, which decreases by up to two orders of magnitude in the distal fan. The microscopic methodologies and techniques employed in the research to understand rock texture and fabric of the sandstones only examined the two-dimensional surfaces of rocks. In addition, while air drying of cores might affect the distribution of pore-filling/pore-lining clays as well as reservoir porosity and permeability, especially in friable, loosely-cemented cores, the cores of the Forties Sandstone Member studied were dried in a dry oven at 80 °C for 3 hours. Furthermore, although clay minerals are sensitive to temperature, the process of oven drying is unlikely to have caused the redistribution of pore-filling/pore-lining clays due to the short duration of the drying process. Consequently, the application of micro-CT technique would provide useful insights into the quantification of 3D internal pore architecture and construct fluid flow models to establish the effective transport capacity. Understanding the variability in permeability is crucially important for fluid flow models in the Forties Sandstone Member, and determining the main controls on permeability is key to further improve the producibility of the low-permeability, distal fan facies.

In addition, in order to understand the reactants for CCS and investigate the real-time change in porosity and permeability in turbidite reservoirs, cores could be injected with CO_2 under some sort of high-pressure, high-temperature (HPHT) experiments.

6.5.4 Implications for other deep-water systems

This study has highlighted the possible role of provenance and sediment dewatering in the formation of grain-coating clays in deep-water sandstones. Precursor clay coatings on framework grains develop on continental, transitional, and shallow marine/shelves environments, and, depending on grain shape and distance of transport, are partly or completely abraded (Bahlis and de Ros, 2013; Yezerski and Shumaker, 2018). Thus, sediments with concave, abrasion-resistant grain shape (embayment) and sourced from a proximal setting, are more likely to have preserved, inherited clay coats than those characterized by convex, abrasion-susceptible grain shape and sourced from a distal setting. Additionally, clay coats are emplaced during dewatering of sediments, in which trapped fluids escape shortly after sediment deposition. The Forties Fan system has been classified as a restricted, sand-rich basin floor fan system (Den Hartog Jager et al., 1993), characterized by a proximal source, with clay coats being both inherited and emplaced during dewatering. It is, therefore, suggested that the role of role of inherited clay coats and those formed during dewatering be thoroughly evaluated in a range of similar, deeper sedimentary basins in the North Sea and around the South Atlantic continental margins.

References

Aagaard, P., Jahren, J.S., Harstad, A.O., Nilsen, O., Ramm, M., 2000. Formation of grain-coating chlorite in sandstones. Laboratory synthesized vs . natural occurrences . Clay Miner. 35, 261–269. https://doi.org/10.1180/000985500546639.

Aase, N.E., Bjørkum, P.A., Nadeau, P.H., 1996. The effect of grain-coating microquartz on preservation of reservoir porosity. Am. Assoc. Pet. Geol. Bull. 80, 1654–1673. https://doi.org/10.1306/64eda0f0-1724-11d7-8645000102c1865d.

Aase, N.E., Walderhaug, O., 2005. The effect of hydrocarbons on quartz cementation: Diagenesis in the Upper Jurassic sandstones of the Miller Field, North Sea, revisited. Pet. Geosci. 11, 215–223. https://doi.org/10.1144/1354-079304-648.

Ajdukiewicz, J.M., Lander, R.H., 2010. Sandstone reservoir quality prediction: The state of the art. Am. Assoc. Pet. Geol. Bull. 94, 1083–1091. https://doi.org/10.1306/intro060110.

Ajdukiewicz, J.M., Larese, R.E., 2012. How clay grain coats inhibit quartz cement and preserve porosity in deeply buried sandstones: Observations and experiments. Am. Assoc. Pet. Geol. Bull. 96, 2091–2119. https://doi.org/10.1306/02211211075.

Ajdukiewicz, J.M., Nicholson, P.H., Esch, W.L., 2010. Prediction of deep reservoir quality using early diagenetic process models in the jurassic norphlet formation, Gulf of Mexico. Am. Assoc. Pet. Geol. Bull. 94, 1189–1227. https://doi.org/10.1306/04211009152.

Allsop, T., 1994. Early compaction history of marine siliciclastic sediments. Durham University. pp. 267-345.

Altaner, S.P., 1978. Smectite group. Encyclopaedia of Earth Science. Springer, Berlin, Heidelberg, p. 216. https://doi.org/10.1007/978-1-4020-3609-5.

Anjos, S.M.C., De Ros, L.F., Silva, C.M.A., 2003. Chlorite Authigenesis and Porosity Preservation in the Upper Cretaceous Marine Sandstones of the Santos Basin, Offshore Eastern Brazil, in: Worden, R. H. and Morad, S. (Ed.), Clay Mineral Cements in Sandstones. International Association of Sedimentologists Special Publications, pp. 289–316. https://doi.org/10.1002/9781444304336.ch13.

Aoudjit, H., Robert, M., Elsass, F., Curmi, P., 1995. Detailed study of smectite genesis in granitic saprolites by analytical electron microsopy. Clay Miner. 30, 135–147. https://doi.org/10.1180/claymin.1995.030.2.05.

Appoloni, C.R., Fernandes, C.P., Rodrigues, C.R.O., 2007. X-ray microtomography study of a sandstone reservoir rock. Nucl. Instruments Methods Phys. Res. Sect. A Accel. Spectrometers, Detect. Assoc. Equip. 580, 629–632. https://doi.org/10.1016/j.nima.2007.05.027.

Bahlis, A.B., de Ros, L.F., 2013. Origin and impact of authigenic chlorite in the Upper Cretaceous sandstone reservoirs of the Santos Basin, eastern Brazil. Pet. Geosci. 19, 185–199. https://doi.org/10.1144/petgeo2011-007.

Bailey, S.W., 1980. Structures of layer silicates, in: Brindley, G.W.; Brown, G. (Ed.), Crystal Structures of Clay Minerals and Their X-Ray Identification. Mineralogical Society, London, pp. 1–123.

Baker, M.L., Baas, J.H., 2020. Mixed sand–mud bedforms produced by transient turbulent flows in the fringe of submarine fans: Indicators of flow transformation. Sedimentology 67, 2645–2671. https://doi.org/10.1111/sed.12714.

Bautier, M.D., Peacor, D.R., O'Neil, J.R., 1992. Smectite-illite transition in Barbados accretionary wedge sediments: TEM and AEM evidence for dissolution/crystallization at low temperature. Clays Clay Miner. 40, 65–80. https://doi.org/10.1346/CCMN.1992.0400108.

Beaufort, D.; Cassagnabere, A.; Petit, S.; Lanson, B.; Berger, B.; Lacharpagne, J.C. and Johansen, H., 1998. Kaolinite-to-dickite reaction in sandstones reservoirs. Clay Miner. 33, 297–316.

Bell, D., Kane, I.A., Pontén, A.S.M., Flint, S.S., Hodgson, D.M., Barrett, B.J., 2018. Spatial variability in depositional reservoir quality of deep-water channel-fill and lobe deposits. Mar. Pet. Geol. 98, 97–115. https://doi.org/10.1016/j.marpetgeo.2018.07.023.

Berger, A., Gier, S., Krois, P., 2009. Porosity-preserving chlorite cements in shallow-marine volcaniclastic sandstones: Evidence from cretaceous sandstones of the sawan gas field, Pakistan. Am. Assoc. Pet. Geol. Bull. 93, 595–615. https://doi.org/10.1306/01300908096.

Biju-Duval, B., 2002. Sedimentary Geology. Editions Technip, Paris. pp. 320-333.

Bjørlykke, K., 2014. Relationships between depositional environments, burial history and rock properties. Some principal aspects of diagenetic process in sedimentary basins. Sediment. Geol. 301, 1–14. https://doi.org/10.1016/j.sedgeo.2013.12.002.

Bjorlykke, K., Aagaard, P., 1992. Clay Minerals in North Sea Sandstones, in: Houseknecht, D.W. and Pittman, E.D. (Ed.), Origin, Diagenesis, and Petrophysics of Clay Minerals in Sandstones. Spec. Pub. Soc. Econ. PaleontoL Mineral, pp. 65–80. https://doi.org/10.2110/pec.92.47.0065.

Bjorlykke, K., Aagaard, P., Dypvik, H., Hastings, D.S., Harper, A.S., 1986. Diagenesis and reservoir properties of Jurassic sandstones from the Haltenbanken area, offshore mid Norway., in: Habitat of Hydrocarbons on the Norwegian Continental Shelf. Proc. Conference, Stavanger, 1985. pp. 275–286.

Bjørlykke, K., Aagaard, P., Egeberg, P.K., Simmons, S.P., 1995. Geochemical constraints from formation water analyses from the North Sea and the Gulf Coast Basins on quartz, feldspar and illite precipitation in reservoir rocks, in: Cubit, J.M. and England, W.A. (Ed.), Geological Society Special Publication. Spec. Publ. Geol. Soc. London, pp. 33–50. https://doi.org/10.1144/GSL.SP.1995.086.01.03.

Bjorlykke, K., Egeberg, P.K., 1993. Quartz cementation in sedimentary basins. Am. Assoc. Pet. Geol. Bull. 77, 1538–1548. https://doi.org/10.1306/bdff8ee8-1718-11d7-8645000102c1865d.

Bloch, S., 1991. Empirical prediction of porosity and permeability in sandstones. Am. Assoc. Pet. Geol. Bull. 75, 1145–1160. https://doi.org/10.1306/20b23c73-170d-11d7-8645000102c1865d.

Bloch, S., Lander, R.H., Bonnell, L., 2002. Anomalously high porosity and permeability in deeply buried sandstone reservoirs: Origin and predictability. Am. Assoc. Pet. Geol. Bull. 86, 301–328. https://doi.org/10.1306/61eedabc-173e-11d7-8645000102c1865d.

Block Vagle, G., Hurst, A., Dypvik, H., 1995. Origin of Quartz Cements in Some Sandstones from the Jurassic of the Inner Moray Firth (UK). Sedimentology 41, 363–377.

https://doi.org/10.1002/9781444304459.ch22.

Boggs, S., 2006. Principles of Sedimentology and Stratigraphy. Pearson Education Limited. pp. 368-380.

Boles, J.R., 1982. Active albitization of plagioclase, Gulf Coast Tertiary. Am. J. Sci. 282, 165–180. https://doi.org/10.2475/ajs.282.2.165.

Boles, J. R., Franks, S.G. 1979. Clay diagenesis in Wilcox sandstones of southwest Texas: implications of smectite diagenesis on sandstone cementation. J. Sediment. Petrol. 49, 55–70. https://doi.org/10.1306/c1ea490f-16c9-11d7-8645000102c1865d.

Booth, J.S., 1979. Recent history of mass-wasting of the upper continental slopes, northern Gulf of Mexico, as interpreted from the consolidation states of the sediments, in: Doyle, L. J.; Pilkey, O.H. (Ed.), Geology of Continental Slopes. Soc. Econ. Paleontologists and Mineralogists Spec. Pub., pp. 153–164.

Bouma, A.H., 1962. Sedimentology of Some Flysch Deposits. Elsevier, Amsterdam. p. 168.

Bowman, M.B.., 1998. Cenozoic, in: Glennie, K.W. (Ed.), Petroleum Geology of the North Sea. pp. 350–375.

Boyle, E.A., Edmond, J.M., Sholkovitz, E.R., 1977. The mechanism of iron removal in estuaries. Geochim. Cosmochim. Acta 41, 1313–1324. https://doi.org/10.1016/0016-7037(77)90075-8.

Brennand, T.P., Van Hoorn, B., James, K.H., Glennie, K.W., 2009. Historical review of north sea exploration, Petroleum Geology of the North Sea: Basic Concepts and Recent Advances: Fourth Edition. pp. 1-41. https://doi.org/10.1002/9781444313413.ch1.

Brigatti, M.F., Galán, E., Theng, B.K.G., 2013. Structure and Mineralogy of Clay Minerals, in: Bergaya, F.; Theng, B.K.G. and Lagaly, G. (Ed.), Developments in Clay Science. pp. 21–81. https://doi.org/10.1016/B978-0-08-098258-8.00002-X.

Bukar, M., 2013. Does oil emplacement stop diagenesis and quartz cementation in deeply buried sandstone reservoirs. University of Liverpool. pp. 42-110.

Burke, K., 1972. Longshore drift, submarine canyons, and submarine fans in development of Niger Delta. AAPG Bulletin 56 (10), pp. 1975-1983.

Burley, S.D., MacQuaker, J.H.S., 1992. Authigenic Clays, Diagenetic Sequences and Conceptual Diagenetic Models in Contrasting Basin-Margin and Basin-Center North Sea Jurassic Sandstones and Mudstones, in: D.W. Houseknecht and E.D. Pittman) (Ed.), Origin, Diagenesis, and Petrophysics of Clay Minerals in Sandstones. Society of Economic Paleontologists and Mineralogists Special Publication, Tulsa, OK, pp. 81–110. https://doi.org/10.2110/pec.92.47.0081.

Busch, B., 2016. Impact of grain coats on quartz overgrowth and reservoir properties. Karlsruhe Institute of Technology. pp. 30-76.

Busch, B., Hilgers, C., Adelmann, D., 2020. Reservoir quality controls on Rotliegend fluvio-aeolian wells in Germany and the Netherlands, Southern Permian Basin – Impact of grain coatings and cements. Mar. Pet. Geol. 112, 2-15. https://doi.org/10.1016/j.marpetgeo.2019.104075.

Carothers, W.W., Adami, L.H., Rosenbauer, R.J., 1988. Experimental oxygen isotope fractionation between siderite-water and phosphoric acid liberated CO2-siderite. Geochim. Cosmochim. Acta 52, 2445–2450. https://doi.org/10.1016/0016-7037(88)90302-X.

Cartigny, M.J.B., Ventra, D., Postma, G., van Den Berg, J.H., 2014. Morphodynamics and sedimentary structures of bedforms under supercritical-flow conditions: New insights from flume experiments. Sedimentology 61, 712–748. https://doi.org/10.1111/sed.12076.

Cazzola, C., Mutti, E., Vigna, B., 1985. Cengio Turbidite System, Italy, in: A. H. Bouma, W. R. Normark, and N.E.B. (Ed.), Submarine Fans and Related Turbidite Systems. Springer-Verlag, New York, pp. 179–183. https://doi.org/10.1007/978-1-4612-5114-9_26.

Celia, M.A., Nordbotten, J.M., 2009. Practical modeling approaches for geological storage of carbon dioxide. Ground Water 47, 627–638. https://doi.org/10.1111/j.1745-6584.2009.00590.x.

Chang, H.K., Mackenzie, F.T., Schoonmaker, J., 1986. Comparisons between the diagenesis of dioctahedral and trioctahedral smectite, Brazilian offshore basins. Clay Miner. 34, 407–423. https://doi.org/10.1346/CCMN.1986.0340408.

Charlaftis, D., Jones, S.J., Dobson, K.J., Crouch, J., Acikalin, S., 2021. Experimental study of chlorite authigenesis and influence on porosity maintenance in sandstones. J. Sediment. Res. 91, 197–212. https://doi.org/10.2110/JSR.2020.122.

Charles, R., Ryzhikov, K., 2015. Merganser Field: managing subsurface uncertainty during the development of a salt diapir field in the UK Central North Sea. Geol. Soc. London, Spec. Publ. 403, 261–298. https://doi.org/10.1144/SP403.15.

Chen, B., Wang, F., Shi, J., Chen, F., Shi, H., 2019. Origin and Sources of Minerals and Their Impact on the Hydrocarbon Reservoir Quality of the PaleogeneLulehe Formation in the Eboliang Area, Northern Qaidam Basin, China. Minerals 9, 436. https://doi.org/10.3390/min9070436.

Chen, G., Du, G., Zhang, G., Wang, Q., Lv, C., Chen, J., 2011. Chlorite cement and its effect on the reservoir quality of sandstones from the Panyu low-uplift, Pearl River Mouth Basin. Pet. Sci. 8, 143–150. https://doi.org/10.1007/s12182-011-0127-z.

Chowdhury, A.H., Noble, J.P.A., 1993. Feldspar albitization and feldspar cementation in the Albert Formation reservoir sandstones, New Brunswick, Canada. Mar. Pet. Geol. 10, 394–402. https://doi.org/10.1016/0264-8172(93)90083-5.

Chudi, O.K., Lewis, H., Stow, D.A.V., Buckman, J.O., 2016. Reservoir quality prediction of deep-water Oligocene sandstones from the west Niger Delta by integrated petrological, petrophysical and basin modelling. Geol. Soc. Spec. Publ. 435, 245–264. https://doi.org/10.1144/SP435.8.

Collins, J., Kenyon-Roberts, S., Cullen, B., White, J., Bordas-Le Floch, N., Downey, J., 2015. Arran Field: A complex heterolithic reservoir on the margins of the Forties Fan System. Geol. Soc. Spec. Publ. 403, 185–217. https://doi.org/10.1144/SP403.10.

Coplen, T.B., Kendall, C., Hopple, J., 1983. Comparison of stable isotope reference samples. Nature 302, 236–238. https://doi.org/10.1038/302236a0.

Covault, J.A., 2011. Submarine fans and canyon-channel systems: A review of processes, products, and models. Nat. Educ. Knowl. 3, 1–19.

Crawford, R., Littlefair, R.W., Affleck, L.G., 1991. The Arbroath and Montrose Fields, Blocks 22/17, 18, UK North Sea. Geol. Soc. Mem. 14, 211–217. https://doi.org/10.1144/GSL.MEM.1991.014.01.26.

Curtis, C.D., 1983. Geochemistry of porosity enhancement and reduction in clastic sediments, in: Brooks, J. (Ed.), Petroleum Geochemistry and Exploration of Europe. Blackwells, Oxford, pp. 113–125. https://doi.org/10.1144/GSL.SP.1983.012.01.12.

Curtis, C.D., Hughes, C.R., Whiteman, J.A., Whittle, C.K., 1985. Compositional variation within some sedimentary chlorites and some comments on their origin. Mineral. Mag. 49, 375–386. https://doi.org/10.1180/minmag.1985.049.352.08.

Daneshvar, E., Worden, Richard H., 2017. Feldspar alteration and Fe minerals: Origin, distribution and implications for sandstone reservoir quality in estuarine sediments, in: Armitage, P. J., Butcher, A. R., Churchill, J. M., Csoma, A. E., Hollis, C., Lander, R. H., Omma, J.E.&, Worden, R. H. (Eds.), Geological Society Special Publication. Geological Society, London, Special Publications, pp. 123–139. https://doi.org/10.1144/SP435.17.

Darby D., Haszeldine, R.S. & Couples, G., 1996. Pressure Cells and Pressure Seals in the Central North Sea. Mar. Pet. Geol. 13, 865-878.

Davis, C., Haughton, P., McCaffrey, W., Scott, E., Hogg, N., Kitching, D., 2009. Character and distribution of hybrid sediment gravity flow deposits from the outer Forties Fan, Palaeocene Central North Sea, UKCS. Mar. Pet. Geol. 26, 1919–1939. https://doi.org/10.1016/j.marpetgeo.2009.02.015.

Davison, I., Alsop, I., Birch, P., Elders, C., Evans, N., Nicholson, H., Rorison, P., Wade, D., Woodward, J., Young, M., 2000. Geometry and late-stage structural evolution of Central Graben salt diapirs, North Sea. Mar. Pet. Geol. 17, 499–522. https://doi.org/10.1016/S0264-8172(99)00068-9.

De'Ath, N.G., Schuyleman, S.F., 1981. The geology of the Magnus Oilfield, in: Illing, L. V. and Hobson, G.D. (Ed.), Petroleum Geology of the Continental Shelf of North-West Europe. Heyden, London, pp. 342–351.

Deegan, C.E., Scull, B.J., 1977. A proposed standard lithostratigraphic nomenclature for the Mesozoic of the central and northern North Sea, Mesozoic of the Northern North Sea Symposium, 77, p. 25.

Deer, W. A.; Howie, R. A. and Zussman, J., 1992. An Introduction to the rock-forming minerals. 3rd Edition. Pearson Education Limited. pp. 208-227.

Den Hartog Jager, D., Giles, M.R., Griffiths, G.R., 1993. Evolution of Paleogene submarine fans of the North Sea in space and time. Pet. Geol. Conf. Proc. 4, 59–71. https://doi.org/10.1144/0040059.

Dickinson, W.R., Seely, D.R., 1979. Structure and Stratigraphy of Forearc Regions. AAPG Bulletin, 63, 2–31.

Dickinson, W.R., Suczek, C., 1979. Plate tectonics and sandstone composition. Am. Assoc. Pet. Geol. Bull. 63, 2164–2182. https://doi.org/10.1306/2f9188fb-16ce-11d7-8645000102c1865d.

Dos Anjos, S.M.C., De Ros, L.F., De Souza, R.S., De Assis Silva, C.M., Sombra, C.L., 2000. Depositional and diagenetic controls on the reservoir quality of Lower Cretaceous Pendencia sandstones, Potiguar rift basin, Brazil. Am. Assoc. Pet. Geol. Bull. 84, 1719–1742. https://doi.org/10.1306/8626c375-173b-11d7-8645000102c1865d.

Dowey, P.J., Worden, R.H., Utley, J., Hodgson, D.M., 2017. Sedimentary controls on modern sand grain coat formation. Sediment. Geol. 353, 46–63. https://doi.org/10.1016/j.sedgeo.2017.03.001.

Dutton, S.P.; Hutton, M.E.; Ambrose, W.A.; Childers, A.T.; Loucks, R.G., 2018. Preservation of reservoir quality by chlorite coats in deep Tuscaloosa Sandstones, Central Louisiana, USA. Gulf Coast Assoc. Geol. Soc. 7, 46–58.

Dutton, S.P., 2008. Calcite cement in Permian deep-water sandstones, Delaware Basin, west Texas: Origin, distribution, and effect on reservoir properties. Am. Assoc. Pet. Geol. Bull. 92, 765–787. https://doi.org/10.1306/01280807107.

Ehrenberg, S.N., 1997. Influence of Depositional Sand Quality and Diagenesis on Porosity and Permeability: Examples from Brent Group Reservoirs, Northern North Sea. SEPM J. Sediment. Res. Vol. 67, 197–211. https://doi.org/10.1306/d4268531-2b26-11d7-8648000102c1865d.

Ehrenberg, S.N., 1995. Measuring sandstone compaction from modal analyses of thin sections: how to do it and what the results mean. J. Sediment. Res. A Sediment. Petrol. Process, v. 65A, no. 2, pp. 369–379. https://doi.org/10.1306/d42680c7-2b26-11d7-8648000102c1865d.

Ehrenberg, S.N., 1993. Preservation of anomalously high porosity in deeply buried sandstones by grain-coating chlorite: examples from the Norwegian Continental Shelf. AAPG Bulletin, 77, 1260–1286.

Ehrenberg, S.N., Aagaard, P., Wilson, M.J., Fraser, A.R., Duthie, D.M.L., 1993. Depth-Dependent Transformation of Kaolinite to Dickite In Sandstones of the Norwegian Continental Shelf. Clay Miner. 28, 325–352. https://doi.org/10.1180/claymin.1993.028.3.01.

Eldrett, J., Tripsanas, E., Davis, C., Mckie, T., Vieira, M., Osterloff, P., Sandison, T., 2015. Sedimentological evolution of Sele Formation deep-marine depositional systems of the Central North Sea. Tert. Deep. Reserv. North Sea Reserv. Geological Society, London, Special Publications, 403, pp 1-36. https://doi.org/10.1144/SP403.9.

Emery, D., Myers, K.J., Young, R., 1990. Ancient subaerial exposure and freshwater leaching in sandstones. Geology 18, 1178–1181.

Fesharaki, O., García-Romero, E., Cuevas-González, J., López-Martínez, N., 2007. Clay mineral genesis and chemical evolution in the Miocene sediments of Somosaguas, Madrid Basin, Spain. Clay Miner. 42, 187–201. https://doi.org/10.1180/claymin.2007.042.2.05.

Fildani, A., Clark, J., Covault, J.A., Power, B., Romans, B.W., Aiello, I.W., 2018. Muddy sand and sandy mud on the distal Mississippi fan: Implications for lobe depositional processes. Geosphere 14, 1051–1066. https://doi.org/10.1130/GES01580.1.

Fisher, Q.J., Knipe, R.J., Worden, R.H., 2000. Microstructures of Deformed and Non-Deformed Sandstones from the North Sea: Implications for the Origins of Quartz Cement in Sandstones, in: Worden, R.H.; Morad, S. (Ed.), Quartz Cementation in Sandstones. Blackwells, Oxford, UK, pp. 129–146. https://doi.org/10.1002/9781444304237.ch10.

Fisher, R.V., 1983. Flow transformations in sediment gravity flows. Geology 11, 273–274.

Folk, R.L., 1980. Petrology of sedimentary rocks. Hemphill Publishing Company, Austin, Texas, p. 182.

Fraser, H.J., 1935. Experimental Study of the Porosity and Permeability of Clastic Sediments. J. Geol. 43, 910–1010. https://doi.org/10.1086/624388.

French, M.W., Worden, R.H., 2013. Orientation of microcrystalline quartz in the Fontainebleau Formation, Paris Basin and why it preserves porosity. Sediment. Geol. 284–285, 149–158.

https://doi.org/10.1016/j.sedgeo.2012.12.004.

French, M.W., Worden, R.H., Mariani, E., Larese, R.E., Mueller, R.R., Kliewer, C.E., 2012. Microcrystalline Quartz Generation and the Preservation of Porosity In Sandstones: Evidence from the Upper Cretaceous of the Subhercynian Basin, Germany. J. Sediment. Res. 82, 422–434. https://doi.org/10.2110/jsr.2012.39.

Friedman, I. and O'Neil, J.R., 1977. Compilation of stable isotope fractionation factors of geochemical interest, 6th ed, Data of geochemistry. United Sates Geological Survey Professional Paper, pp440KK.

Friis, H., Molenaar, N., Varming, T., 2014. Chlorite meniscus cement - implications for diagenetic mineral growth after oil emplacement. Terra Nov. 26, 14–21. https://doi.org/10.1111/ter.12061.

Gales, J.A., Talling, P.J., Cartigny, M.J.B., Hughes Clarke, J., Lintern, G., Stacey, C., Clare, M.A., 2018. What controls submarine channel development and the morphology of deltas entering deep-water fjords? Earth Surf. Process. Landforms 44, 535–551. https://doi.org/10.1002/esp.4515.

Garland, C.R., 1993. Miller field: reservoir stratigraphy and its impact on development, in: Parker, J.R. (Ed.), Petroleum Geology of Northwest Europe: Proceedings of the 4th Congress. The Geological Society of London, pp. 401–414.

González-Acebrón, L., Arribas, J., Mas, R., 2010. Role of sandstone provenance in the diagenetic albitization of feldspars. A case study of the Jurassic Tera Group sandstones (Cameros Basin, NE Spain). Sediment. Geol. 229, 53–63. https://doi.org/10.1016/j.sedgeo.2010.06.005.

Górska, M.E., 2019. Verification of gravity-flow models: Case study from the lower eocene sediments (tylmanowa site, SE Poland). Baltica 32, 30–50. https://doi.org/10.5200/baltica.2019.1.4.

Gould, K., Pe-Piper, G., Piper, D.J.W., 2010. Relationship of diagenetic chlorite rims to depositional facies in Lower Cretaceous reservoir sandstones of the Scotian Basin. Sedimentology 57, 587–610. https://doi.org/10.1111/j.1365-3091.2009.01106.x

Grier, S.P., Marschall, D.M., 1992. Reservoir Quality: Part 6. Geological Methods. ME 10 Dev. Geol. Ref. Man. (AAPG Methods Explor. Ser. No. 10), pp. 275–277.

Griffiths, J., Worden, R.H., Wooldridge, L.J., Utley, J.E.P., Duller, R.A., 2019a. Compositional variation in modern estuarine sands: Predicting major controls on sandstone reservoir quality. Am. Assoc. Pet. Geol. Bull. 103, 797–833. https://doi.org/10.1306/09181818025.

Griffiths, J., Worden, R.H., Wooldridge, L.J., Utley, J.E.P., Duller, R.A., 2018. Detrital Clay Coats, Clay Minerals, and Pyrite: A Modern Shallow-Core Analogue For Ancient and Deeply Buried Estuarine Sandstones. J. Sediment. Res. 88, 1205–1237. https://doi.org/10.2110/jsr.2018.56.

Griffiths, J., Worden, R.H., Wooldridge, L.J., Utley, J.E.P., Duller, R.A., Edge, R.L., 2019b. Estuarine clay mineral distribution: Modern analogue for ancient sandstone reservoir quality prediction. Sedimentology 66, 2011–2047. https://doi.org/10.1111/sed.12571.

Grigsby, J.D., 2001. Origin and growth mechanism of authigenic chlorite in sandstones of the lower vicksburg formation, south texas. J. Sediment. Res. 71, 27–36. https://doi.org/10.1306/060100710027.

Hage, S., 2019. Turbidity current processes and products in the fjords of British Columbia (Canada). University of Southampton. pp. 8-48.

Haile, B.G., Czarniecka, U., Xi, K., Smyrak-Sikora, A., Jahren, J., Braathen, A., Hellevang, H., 2019. Hydrothermally induced diagenesis: Evidence from shallow marine-deltaic sediments, Wilhelmøya, Svalbard. Geosci. Front. 10, 629–649. https://doi.org/10.1016/j.gsf.2018.02.015.

Haile, B.G., Hellevang, H., Aagaard, P., Jahren, J., 2015. Experimental nucleation and growth of smectite and chlorite coatings on clean feldspar and quartz grain surfaces. Mar. Pet. Geol. 68, 664–674. https://doi.org/10.1016/j.marpetgeo.2015.02.006.

Haughton, P.D.W., Barker, S.P., McCaffrey, W.D., 2003. "Linked" debrites in sand-rich turbidite systems - Origin and significance. Sedimentology 50, 459–482. https://doi.org/10.1046/j.1365-3091.2003.00560.x.

Heald, M.T., and Larese, R.E., 1974. Influence of Coatings on Quartz Cementation. SEPM J. Sediment. Res. Vol. 44, 1269–1274. https://doi.org/10.1306/212f6c94-2b24-11d7-8648000102c1865d.

Heijnen, M.S.; Clare, M.A.; Cartigny, M.J.B.; Talling, P.J.; Hage, S.; Lintern, D.G.; Stacey, C.; Parsons, D.R.; Simmons, S.M.; Chen, Y.; Sumner, E.J.; Dix, J.K.; John E.; Clarke, H., 2020. Rapidly-migrating and internally-generated knickpoints can control submarine channel evolution. Nat. Commun. 11, 1-15.

Hempton, M., Marshall, J., Sadler, S., Hogg, N., Charles, R., Harvey, C., 2005. Turbidite reservoirs of the Sele formation, Central North Sea: Geological challenges for improving production. Pet. Geol. Conf. Proc. 6, 449–459. https://doi.org/10.1144/0060449.

Hendry, J.P, Wilkinson, M.; Fallick, A.E., 2000. Ankerite Cementation in Deeply Buried Jurassic Sandstone Reservoirs of the Central North Sea. SEPM J. Sediment. Res. Vol. 70 (2. https://doi.org/10.1306/d4268bd5-2b26-11d7-8648000102c1865d.

Hendry, J.P., Trewin, N.H., 1995. Authigenic quartz microfabrics in Cretaceous turbidites: evidence for silica transformation processes in sandstones. J. Sediment. Res. A Sediment. Petrol. Process. 65, 380–392. https://doi.org/10.1306/d42680cc-2b26-11d7-8648000102c1865d.

Heritier, F.E., Lossel, P., Wathne, E., 1979. Frigg field - large submarine- fan trap in Lower Eocene rocks of North Sea Viking Graben. Am. Assoc. Pet. Geol. Bull. 63, 1999–2020. https://doi.org/10.1306/2F918856-16CE-11D7-8645000102C1865D.

Hillier, S., 1994. Pore-Lining chlorites in siliciclastic reservoir sandstones: Electron microprobe, SEM and XRD data, and implications for their Origin. Clay Miner. 29, 665–679.

Hillier, S., Velde, B., 1992. Chlorite interstratified with a 7 Å mineral: an example from offshore Norway and possible implications for the interpretation of the composition of diagenetic chlorites. Clay Miner. 27, 475–486. https://doi.org/10.1180/claymin.1992.027.4.07.

Hiscott, R.N., 1979. Clastic Sills and Dikes Associated with Deep-Water Sandstones, Tourelle Formation, Ordovician, Quebec. SEPM J. Sediment. Res. Vol. 49, 1–10. https://doi.org/10.1306/212f76a3-2b24-11d7-8648000102c1865d.

Houseknecht, D., 1987. Assessing the Relative Importance of Compaction Processes and Cementation to Reduction of Porosity in Sandstones. AAPG Bulletin, 71 (6), pp. 633–

642.

Houseknecht, D.W., Ross, L.M., 1992. Clay Minerals in Atokan Deep-Water Sandstone Facies, Arkoma Basin: Origins and Influence on Diagenesis and Reservoir Quality. Orig. Diagenesis, Petrophysics Clay Miner. Sandstones 227–240. https://doi.org/10.2110/pec.92.47.0227.

Huang, Y., Kane, I.A., Zhao, Y., 2020. Effects of sedimentary processes and diagenesis on reservoir quality of submarine lobes of the Huangliu Formation in the Yinggehai Basin, China. Mar. Pet. Geol., 120, pp. 1-23. https://doi.org/10.1016/j.marpetgeo.2020.104526.

Huggett, J.M., 2015. Clay Minerals, in: Reference Module in Earth Systems and Environmental Sciences. Science Direct, pp. 1–8.

Huggett, J.M., 1996. Aluminosilicate diagenesis in a Tertiary sandstone-mudrock sequence from the central North Sea, UK. Clay Miner. 31, 523–536. https://doi.org/10.1180/claymin.1996.031.4.10.

Hughes Clarke, J.E., 2016. First wide-angle view of channelized turbidity currents links migrating cyclic steps to flow characteristics. Nat. Commun. 7. https://doi.org/10.1038/ncomms11896.

Iijima, A., Matsumoto, R., 1982. Berthierine and chamosite in coal measures of Japan. Clays Clay Miner. 30, 264–274. https://doi.org/10.1346/CCMN.1982.0300403.

Ito, M., 2008. Downfan transformation from turbidity currents to debris flows at a channel-to-lobe transitional zone: The lower Pleistocene Otadai Formation, Boso Peninsula, Japan. J. Sediment. Res. 78, 668–682. https://doi.org/10.2110/jsr.2008.076.

Jacka, A.D., Beck, R.H., St. Germain, L.C., Harrison, S.C., 1968. Permian deep-sea fans of the Delaware Mountain Group (Guadalupian), Delaware basin. Guadalupian Facies, Apache Mt. Area, West Texas 68, 49–90.

Jeans, C. V., 1989. Clay Diagenesis in Sandstones and Shales: An Introduction. Clay Miner. 24, 127–136. https://doi.org/10.1180/claymin.1989.024.2.02.

Jennette, D.C., Garfield, T.R., Mohrig, D.C., Cayley, G.T., 2000. The Interaction of Shelf Accommodation, Sediment Supply and Sea Level in Controlling the Facies, Architecture and Sequence Stacking Patterns of the Tay and Forties/Sele Basin-Floor Fans, Central North Sea, in: Weimer, P., Bouma, A.H. and Perkins, B.F. (Ed.), Deep-Water Reservoirs of the World: 20th Annual. 3–6 December, Houston, USA, pp. 402–421. https://doi.org/10.5724/gcs.00.15.0402.

Jiang, S., 2012. Clay Minerals from the Perspective of Oil and Gas Exploration, in: Valaskova, M. (Ed.), Clay Minerals in Nature - Their Characterization, Modification and Application. IntechOpen, pp. 21–35.

Johns, D.R., Mutti, E., 1981. Facies and geometry of turbidite sandstone bodies and their relationship to deep sea fan systems, in: International Association of Sedimentologists Abstracts; 2nd European Regional Meeting. Bologna, p. 89.

Jones, D.W., Large, S., McQueen, A., Helmi, A., 2015. Reservoir geology of the Paleocene Forties Sandstone Member in the Fram discovery, UK Central North Sea. Geol. Soc. Spec. Publ. 403, 219–246. https://doi.org/10.1144/SP403.13.

Kane, I.A., Pontén, A.S.M., Vangdal, B., Eggenhuisen, J.T., Hodgson, D.M., Spychala, Y.T., 2017. The stratigraphic record and processes of turbidity current transformation across deep-marine lobes. Sedimentology 64, 1236–1273. https://doi.org/10.1111/sed.12346.

Keller, G.H., Lambert, D.N., Bennett, R.H., 1979. Geotechnical properties of continental slope deposits - Cape Hatteras to Hydrographer Canyon, in: Doyle, L. E.; Pilkey, O.H. (Ed.), Geology of Continental Slopes. Soc. Econ. Paleon. and Min. Spec. Publ., pp. 131–153.

Kessler, L.G., Zang, R.D., Englehorn, J.A., Eger, J.D., 1980. Stratigraphy and sedimentology of a Palaeocene submarine fan complex, Cod Field, Norwegian North Sea. Sediment. North Sea Reserv. Rocks. NPF Artic. 8, p. 1.

Kilhams, B., Morton, A., Borella, R., Wilkins, A., Hurst, A., 2014. Understanding the provenance and reservoir quality of the Sele Formation sandstones of the UK Central Graben utilizing detrital garnet suites. Geol. Soc. Spec. Publ. 386, 129–142. https://doi.org/10.1144/SP386.16.

Kilhams, B., Morton, A., Borella, R., Wilkins, A., Hurst, A., 2013. Understanding the provenance and reservoir quality of the Sele Formation sandstones of the UK Central Graben utilizing detrital garnet suites. Geol. Soc. Spec. Publ. 386, 129–142. https://doi.org/10.1144/SP386.16.

Klein, G.V., 1982. Sandstone Depositional Models for Exploration for Fossil Fuels. International Human Resources Development Corporation, pp. 120-130.

Kneller, B., McCaffrey, W., 1999. Depositional effects of flow nonuniformity and stratification within turbidity currents approaching a bounding slope; deflection, reflection, and facies variation. J. Sediment. Res. 69, 980–991. https://doi.org/10.2110/jsr.69.980.

Knox, R.W.O., Holloway, S., 1992. Paleogene of the central and northern North Sea, in: Knox, R.W.O'B. and Cowdey, W.G. (Ed.), Lithostratigraphic Nomenclature of the UK North Sea. British Geological Survey, Nottingham, p. 206.

Kordi, M., 2013. Characterization and prediction of reservoir quality in chlorite-coated sandstones: evidence from the Late Cretaceous Lower Tuscaloosa Formation at Cranfield Field, Mississippi, U.S.A. The University of Texas at Austin, pp. 27-172.

Kroeger, K.F., Thrasher, G.P., Sarma, M., 2019. The evolution of a Middle Miocene deep-water sedimentary system in northwestern New Zealand (Taranaki Basin): Depositional controls and mechanisms. Mar. Pet. Geol. 101, 355–372. https://doi.org/10.1016/j.marpetgeo.2018.11.052.

Kuenen, P.H., Sengupta, S., 1970. Experimental marine suspension currents, competency and capacity. Geol. en Mijnbouw. 49, 89–118.

Kunka, J.M., Williams, G., Cullen, B., Boyd-Gorst, J., Dyer, G.R., Garnham, J.A., Warnock, A., Wardell, J., Davis, A., Lynes, P., 2003. The Nelson Field, Blocks 22/11, 22/61, 22/7, 22/12a, UK North Sea, in: Gluyas, J.G. and Hichens, H.M. (Ed.), Geological Society Memoir. Geological Society, London, London, pp. 617–646. https://doi.org/10.1144/GSL.MEM.2003.020.01.50.

Kupecz, J.A., Gluyas, J., Bloch, S., 1997. Reservoir quality prediction in sandstones and carbonates: An overview. AAPG Memoir, v. 69, pp. VII-XXIV.

Lai, J., Wang, G., Cai, C., Fan, Z., Wang, S., Chen, J., Luo, G., 2018. Diagenesis and reservoir quality in tight gas sandstones: The fourth member of the Upper Triassic Xujiahe Formation, Central Sichuan Basin, Southwest China. Geol. J. 53, 629–646. https://doi.org/10.1002/gj.2917.

Lander, R.H., Larese, R.E., Bonnell, L.M., 2008. Toward more accurate quartz cement models: The importance of euhedral versus noneuhedral growth rates. Am. Assoc. Pet. Geol. Bull.

92, 1537–1563. https://doi.org/10.1306/07160808037.

Lander, R.H., Walderhaug, O., 1999. Predicting porosity through simulating sandstone compaction and quartz cementation. AAPG Bull. (American Assoc. Pet. Geol. 83, 433–449. https://doi.org/10.1306/00aa9bc4-1730-11d7-8645000102c1865d.

Lanson, B.; Beaufort, D.; Berger, G.; Baradat, J. and L., J.C., 1996. Illitization of Diagenetic Kaolinite-to-dickite Conversion Series: Late-stage Diagenesis of the Lower Permian Rotliegend Sandstone Reservoir, Offshore of the Netherlands. SEPM J. Sediment. Res. Vol. 66, 501–518. https://doi.org/10.1306/d4268392-2b26-11d7-8648000102c1865d.

Lanson, B., Beaufort, D., Berger, G., Bauer, A., Cassagnabère, A., Meunier, A., 2002. Authigenic kaolin and illitic minerals during burial diagenesis of sandstones: a review. Clay Miner. 37, 1–22. https://doi.org/10.1180/0009855023710014.

Leclair, S.F., Arnott, R.W.C., 2005. Parallel Lamination Formed by High-Density Turbidity Currents. J. Sediment. Res. 75, 1–5. https://doi.org/10.2110/jsr.2005.001.

Leithold, E.L., Blair, N.E., Wegmann, K.W., 2016. Source-to-sink sedimentary systems and global carbon burial: A river runs through it. Earth-Science Rev. 153, 30–42. https://doi.org/10.1016/j.earscirev.2015.10.011.

Li, Y., Pang, Z., 2016. Capacity and suitability assessment of deep saline aquifers for CO2 sequestration in the Bohai Bay Basin, East China. Environ. Earth Sci. 75, 1–15. https://doi.org/10.1007/s12665-016-5269-2.

Lien, T., Midtbø, R.E., Martinsen, O.J., 2006. Depositional facies and reservoir quality of deep-marine sandstones in the Norwegian Sea. Nor. Geol. Tidsskr. 86, 71–92.

Lima, R.D., De Ros, L.F., 2002. The role of depositional setting and diagenesis on the reservoir quality of Devonian sandstones from the Solimões Basin, Brazilian Amazonia. Mar. Pet. Geol. 19, 1047–1071. https://doi.org/10.1016/S0264-8172(03)00002-3.

Lowe, D.R., 1982. Sediment gravity flows: II. Depositional models with special reference to the deposits of high-density turbidity currents. J. Sediment. Petrol. 52, 279–297. https://doi.org/10.1306/212f7f31-2b24-11d7-8648000102c1865d.

Lowe, D.R., 1979. Sediment gravity flows: their classification and some problems of application to natural flows and deposits., in: Doyle, L.J., Pilkey, O.H. (Ed.), Geology of Continental Slopes. Spec. Publ. - Soc. Econ. Paleontol. Mineral., pp. 75–82.

Lowe, D.R., 1976. Subaqueous liquefied and fluidized sediment flows and their deposits. Sedimentology 23, 285–308. https://doi.org/10.1111/j.1365-3091.1976.tb00051.x.

Lundegard, P. D., 1992. Sandstone porosity loss - a “big picture’’ view of the importance of compaction.” J. Sediment. Petrol. 62, 250–260. https://doi.org/10.1306/d42678d4-2b26-11d7-8648000102c1865d.

Lynch, F.L., 1997. Frio shale mineralogy and the stoichiometry of the smectite-to-illite reaction: The most important reaction in clastic sedimentary diagenesis. Clays Clay Miner. 45, 618–631.

Lynch, F.L., 1996. Mineral/water interaction, fluid flow, and frio sandstone diagenesis: Evidence from the rocks. Am. Assoc. Pet. Geol. Bull. 80, 486–504.

Ma, B., Cao, Y., Eriksson, K.A., Jia, Y., Gill, B.C., 2017. Depositional and diagenetic controls on deeply-buried Eocene sublacustrine fan reservoirs in the Dongying Depression, Bohai Bay Basin, China. Mar. Pet. Geol. 82, 297–317. https://doi.org/10.1016/j.marpetgeo.2017.02.014.

Ma, B., Cao, Y., Wang, Y., Jia, Y., 2016. Origin of carbonate cements with implications for petroleum reservoir in Eocene sandstones, northern Dongying depression, Bohai Bay Basin, China. Energy Explor. Exploit. 34, 199–216. https://doi.org/10.1177/0144598716629871.

Mansurbeg, H., 2007. Diagenesis and Reservoir-Quality Evolution of Deep-Water Turbidites: Links to Basin Setting, Depositional Facies, and Sequence Stratigraphy. University of Uppasala, pp. 9-32.

Mansurbeg, H., Caja, M.A., Marfil, R., Morad, S., Remacha, E., Garcia, D., Martin-Crespo, T., El-Ghali, M.A.K., Nystuen, J.P., 2009. Diagenetic Evolution and Porosity Destruction of Turbiditic Hybrid Arenites and Siliciclastic Sandstones of Foreland Basins: Evidence from the Eocene Hecho Group, Pyrenees, Spain. J. Sediment. Res. 79, 711–735. https://doi.org/10.2110/jsr.2009.060.

Mansurbeg, H., De Ros, L.F., Morad, S., Ketzer, J.M., El-Ghali, M.A.K., Caja, M.A., Othman, R., 2012. Meteoric-water diagenesis in late Cretaceous canyon-fill turbidite reservoirs from the Espírito Santo Basin, eastern Brazil. Mar. Pet. Geol. 37, 7–26. https://doi.org/10.1016/j.marpetgeo.2012.03.009.

Mansurbeg, H., Morad, S., Salem, A., Marfil, R., El-ghali, M.A.K., Nystuen, J.P., Caja, M.A., Amorosi, A., Garcia, D., La Iglesia, A., 2008. Diagenesis and reservoir quality evolution of palaeocene deep-water, marine sandstones, the Shetland-Faroes Basin, British continental shelf. Mar. Pet. Geol. 25, 514–543. https://doi.org/10.1016/j.marpetgeo.2007.07.012.

Mao, S.W., Bao, Z.D., Wang, X.X., Gao, Y.S., Song, J., Wang, Z.C., Liu, W., Zhang, L., Wei, M.Y., Bao, Y.F., 2019. Origin of carbonate cements and reservoir evolution of tight sandstone in the Upper Triassic Yanchang Formation, Ordos Basin, China. Aust. J. Earth Sci. 66, 1175–1194. https://doi.org/10.1080/08120099.2019.1596981.

Marchand, A.M.E., Apps, G., Li, W., Rotzien, J.R., 2015. Depositional processes and impact on reservoir quality in deepwater Paleogene reservoirs, US Gulf of Mexico. Am. Assoc. Pet. Geol. Bull. 99, 1635–1648. https://doi.org/10.1306/04091514189.

Marfil, R., Delgado, A., Rossi, C., Iglesia, A. La, Ramseyer, K., 2003. Origin and Diagenetic Evolution of Kaolin in Reservoir Sandstones and Associated Shales of the Jurassic and Cretaceous, Salam Field, Western Desert (Egypt). Clay Miner. Cem. Sandstones 34, 317–342. https://doi.org/10.1002/9781444304336.ch14.

Markussen, Ø., Dypvik, H., Hammer, E., Long, H., Hammer, Ø., 2019. 3D characterization of porosity and authigenic cementation in Triassic conglomerates/arenites in the Edvard Grieg field using 3D micro-CT imaging. Mar. Pet. Geol. 99, 265–281. https://doi.org/10.1016/j.marpetgeo.2018.10.015.

Matlack, K.S., Houseknecht, D.W., Applin, K.R., 1989. Emplacement of clay into sand by infiltration. J. Sediment. Petrol. 59, 77–87. https://doi.org/10.1306/212F8F21-2B24-11D7-8648000102C1865D.

Matthews, A., Katz, A., 1977. Oxygen isotope fractionation during the dolomitization of calcium carbonate. Geochim. Cosmochim. Acta 41, 1431–1438. https://doi.org/10.1016/0016-7037(77)90249-6.

McBride, Earle F., 1989. Quartz cement in sandstones: a review. Earth Sci. Rev. 26, 69–112. https://doi.org/10.1016/0012-8252(89)90019-6.

McKinley, J.M., Worden, R.H., Ruffell, A.H., 2003. Smectite in Sandstones: A Review of the Controls on Occurrence and Behaviour During Diagenesis, in: Worden, R.H. and Morad, S. (Ed.), Clay Mineral Cements in Sandstones. Int. Assoc. Sedimentol. Spec. Publ., pp. 109–128. https://doi.org/10.1002/9781444304336.ch5.

Middleton, G. V, Hampton, M.A., 1973. Part I. Sidement gravity flows: mechanics of flow and deposition, in: Middleton, G.V.; Bouma, A.H. (Ed.), Turbidites and Deep Water Sedimentation. Soc. Econ. Paleontol. Mineral., Pac. Sect., Short Course, p. 38.

Milliken, K.L., 2003. Late Diagenesis and Mass Transfer in Sandstone-Shale Sequences. Treatise on Geochemistry 7–9, 159–190. https://doi.org/10.1016/B0-08-043751-6/07091-2.

Milliken, K.L., McBride, E.F., Land, L.S., 1989. Numerical assessment of dissolution versus replacement in the subsurface destruction of detrital feldspars, Oligocene Frio Formation, South Texas. J. Sediment. Petrol. 59, 740–757. https://doi.org/10.1306/212F9061-2B24-11D7-8648000102C1865D.

Moore, D.M. and Reynolds Jr., R.C., 1997. X-ray diffraction and the identification and analysis of clay minerals, Clays and Clay Minerals. Oxford University Press, Oxford, pp. 819-842. https://doi.org/10.1346/ccmn.1990.0380416.

Moore, D.G., 1977. Submarine slides, in: Rockslides and Avalanches v. I: Developments in Geotechnical Engineering 14a. Elsevier, Amsterdam, pp. 563–604.

Morad, S., Al-Ramadan, K., Ketzer, J.M., De Ros, L.F., 2010. The impact of diagenesis on the heterogeneity of sandstone reservoirs: A review of the role of depositional fades and sequence stratigraphy. Am. Assoc. Pet. Geol. Bull. 94, 1267–1309. https://doi.org/10.1306/04211009178.

Morad, S., Aldahan, A.A., 1987. Diagenetic chloritization of feldspars in sandstones. Sediment. Geol. 51, 155–164. https://doi.org/10.1016/0037-0738(87)90046-7.

Morad, S., Bergan, M., Knarud, R., Nystuen, J.P., 1990. Albitization of detrital plagioclase in Triassic reservoir sandstones from the Snorre Field, Norwegian North Sea. J. Sediment. Petrol. 60, 411–425. https://doi.org/10.1306/212F91AB-2B24-11D7-8648000102C1865D.

Morad, S., Ismail, H.N.B., De Ros, L.F., Al-Aasm, I.S., Serrhini, N. -E, 1994. Diagenesis and formation water chemistry of Triassic reservoir sandstones from southern Tunisia. Sedimentology 41, 1253–1272. https://doi.org/10.1111/j.1365-3091.1994.tb01452.x.

Morad, S., Ketzer, J.M., De Ros, L.R., 2000. Spatial and temporal distribution of diagenetic alterations in siliciclastic rocks: Implications for mass transfer in sedimentary basins. Sedimentology 47, 95–120. https://doi.org/10.1046/j.1365-3091.2000.00007.x.

Moraes, M.A.S., De Ros, L.F., 1992. Depositional, Infiltrated and Authigenic Clays in Fluvial Sandstones of the Jurassic Sergi Formation, Recôncavo Basin, Northeastern Brazil, in: Origin, Diagenesis, and Petrophysics of Clay Minerals in Sandstones. Society of Economic Paleontologists and Mineralogists Special Publication, pp. 197–208. https://doi.org/10.2110/pec.92.47.0197.

Morton, A.C., Hallsworth, C.R., Wilkinson, G.C., 1993. Stratigraphic evolution of sand provenance during Paleocene deposition in the Northern North Sea area, in: Parker, J.R. (Ed.), Petroleum Geology Conference Proceedings. Published by The Geological Society, London, pp. 73–84. https://doi.org/10.1144/0040073.

Mudge, D.C. and Copestake, P., 1993. A revised Lower Palaeogene lithostratigraphy for the Outer Moray Firth. Mar. Pet. Geol. 9, 53–69.

Mudge, D.C., 2015. Regional controls on Lower Tertiary sandstone distribution in the North Sea and NE Atlantic margin basins. Geol. Soc. Spec. Publ. 403, 17–42. https://doi.org/10.1144/SP403.5.

Munawar, M.J., Chengyan, L., Dong, C., Xianguo, Z., Haiyan, Z., Xiao, S., Azeem, T., Muhammad Aleem, Z., Cunfei, M., 2018. Architecture and reservoir quality of low-permeability Eocene lacustrine turbidite sandstone from the Dongying Depression, East China. Open Geosci. accepted, 87–112.

Mutti, E.., Ricci Lucchi, F., 1975. Turbidite facies and facies associations, in: Turbidites and Deep Water Sedimentation. Int. Sediment. Congr., IX, Nice, pp. 21–36.

Mutti, E.., Ricci Lucchi, F., 1972. Turbidites of the Northern Apennines: Introduction to facies analysis. Int. Geol. Rev. 20, 125–166. https://doi.org/10.1080/00206817809471524.

Mutti, E., 1979. Turbidites et cones sous-margins profonds, in: Homewood, P. (Ed.), Srdimentation Detrique (Fluviatile, Littorale et Marine). pp. 353-419.

Myer, L., 2011. Global Status of Geologic CO2 Storage Technology Development. United States carbon sequestration Counc. Rep., pp. 3-17.

Neal, J.., 1996. A summary of Paleogene sequence stratigraphy in northwest Europe and the North Sea, in: Knox, R.W.O'B., Corfield, R.M. and Dunay, R.E. (Ed.), Correlation of the Early Paleogene in Northwest Europe. Geological Society, London, Special Publications, pp. 15–42.

Nedkvitne, T., Karlsen, D.A., Bjørlykke, K., Larter, S.R., 1993. Relationship between reservoir diagenetic evolution and petroleum emplacement in the Ula Field, North Sea. Mar. Pet. Geol. 10, 255–270. https://doi.org/10.1016/0264-8172(93)90108-5.

Nichols, G., 2009. Sedimentology and Stratigraphy, Second. ed. Wiley-Blackwell, pp. 250-257.

Niu, B., Ishida, H., 2000. Different rates of smectite illitization in mudstones and sandstones from the Niigata Basin, Japan. Clay Miner. 35, 163–173. https://doi.org/10.1180/000985500546558.

Normark, W.R., 1970. Growth patterns of deep- sea fans. Am. Assoc. Pet. Geol. Bull. 54, 2170–2195.

Oliveira, D.M., De Ros, L.F., 2018. Meteoric water and salt-dome-related diagenesis in tertiary turbidite reservoirs from the Espírito Santo Basin, Brazil. J. Sediment. Res. 88, 1362–1380. https://doi.org/10.2110/jsr.2018.68.

Oluwadebi, A.G., Taylor, K.G., Dowey, P.J., 2018. Diagenetic controls on the reservoir quality of the tight gas Collyhurst Sandstone Formation, Lower Permian, East Irish Sea Basin, United Kingdom. Sediment. Geol. 371, 55–74. https://doi.org/10.1016/j.sedgeo.2018.04.006.

Osborne, M., Haszeldine, R.S., Fallick, A.E., 1994. Variation in kaolinite morphology with growth temperature in isotopically mixed pore-fluids, Brent Group, UK North Sea. Clay Miner. 29, 591–608. https://doi.org/10.1180/claymin.1994.029.4.15.

Paxton, S.T., Szabo, J.O., Ajdukiewicz, J.M., Klimentidis, R.E., 2002. Construction of an intergranular volume compaction curve for evaluating and predicting compaction and porosity loss in rigid-grain sandstone reservoirs. Am. Assoc. Pet. Geol. Bull. 86, 2047–

2067. https://doi.org/10.1306/61eeddfa-173e-11d7-8645000102c1865d.

Piper, D.J.W., Normark, W.R., 1983. Turbidite depositional patterns and flow characteristics, Navy submarine fan, California borderland. Sedimentology 30, 681–694. https://doi.org/10.1002/9781444304473.ch33.

Pittman, E.D., Larese, R.E., Heald, M.T., 1992. Clay Coats: Occurrence and Relevance To Preservation of Porosity in Sandstones, in: Housenknecht, D W. and Pittman, E. (Ed.), Origin, Diagenesis, and Petrophysics of Clay Minerals in Sandstones. SEPM, Special Publication, pp. 241–255. https://doi.org/10.2110/pec.92.47.0241.

Platt, J.D., 1993. Controls on Clay Mineral Distribution and Chemistry in the Early Permian Rotliegend of Germany. Clay Miner. 28, 393–416. https://doi.org/10.1180/claymin.1993.028.3.05.

Porten, K.W., Kane, I.A., Warchoł, M.J., Southern, S.J., 2016. A Sedimentological Process-Based Approach To Depositional Reservoir Quality of Deep-Marine Sandstones: An Example From the Springar Formation, Northwestern Vøring Basin, Norwegian Sea. J. Sediment. Res. 86, 1269–1286. https://doi.org/10.2110/jsr.2016.74.

Porten, K.W., Warchoł, M.J., Kane, I.A., 2019. Formation of detrital clay grain coats by dewatering of deep-water sands and significance for reservoir quality. J. Sediment. Res. 89, 1231–1249. https://doi.org/10.2110/jsr.2019.65.

Posamentier, H.W., Erskine, R.D., Mitchum, R.M., 1991. Models for Submarine-Fan Deposition within a Sequence-Stratigraphic Framework, in: Weimer, P.; Link, M.. (Ed.), Seismic Facies and Sedimentary Processes of Submarine Fans and Turbidite Systems. Springer Science+Business Media, New York, pp. 127–136. https://doi.org/10.1007/978-1-4684-8276-8_6.

Primmer, T.J., Cade, C.A., Evans, J., Gluyas, J.G., Hopkins, M.S., Oxtoby, N.H., Craig Smalley, P., Warren, E.A., Worden, R.H., 1997. Global patterns in sandstone diagenesis: Their application to reservoir quality prediction for petroleum exploration. AAPG Mem. 69, 61–77.

Prior, D.B., Bornhold, B.D., 1989. Submarine sedimentation on a developing Holocene fan delta. Sedimentology 36, 1053–1076. https://doi.org/10.1002/9781444304473.ch34.

Prior, D.B., Bornhold, B.D., 1984. Geomorphology of slope instability features; Squamish Harbour, Howe Sound, British Columbia. Geol. Surv. Canada, Open File Rep.

Prior, D.B., Bornhold, B.D., Johns, M.W., 1986. Active sand transport along a fjord-bottom channel, Bute Inlet, British Columbia. Geology 14, 581–584. https://doi.org/10.1130/0091-7613(1986)14<581:ASTAAF 2.0.CO;2.

Prior, D.B., Bornhold, B.D., Wiseman, W.J., Lowe, D.R., 1987. Turbidity current activity in a British Columbia Fjord. Science (80-.), 237, 1330–1333.

Reading, H.G., 1996. Sedimentary Environements: Processes, Facies, and Stratigraphy, Third Edit. ed. Blackwell Publishing Ltd, pp. 395-399.

Reading, H.G., Richards, M., 1994. Turbidite systems in deep-water basin margins classified by grain size and feeder system. Am. Assoc. Pet. Geol. Bull. 78, 792–822. https://doi.org/10.1306/A25FE3BF-171B-11D7-8645000102C1865D.

Reynolds, T., 1994. Quantitative analysis of submarine fans in the Tertiary of the North Sea Basin. Mar. Pet. Geol. 11, 202–207. https://doi.org/10.1016/0264-8172(94)90096-5.

Ricci Lucchi, F., 1981. The Marnoso-arenacea: a migrating turbidite basin (over-supplied) by a highly efficient dispersal system, in: Excursion Guidebook. 2nd IAS European Reg. Meeting, Bologna, pp. 232–275.

Ruffell, A., McKinley, J.M., Worden, R.H., 2002. Comparison of clay mineral stratigraphy to other proxy palaeoclimate indicators in the Mesozoic of NW Europe. Philos. Trans. R. Soc. A Math. Phys. Eng. Sci. 360, 675–693. https://doi.org/10.1098/rsta.2001.0961.

Ryu, I.-C., Niem, A.R., 1999. Sandstone diagenesis, reservoir potential, and sequence stratigraphy of the Eocene Tyee Basin, Oregon. J. Sediment. Res. 69, 384–393. https://doi.org/10.2110/jsr.69.384.

Saigal, G.C., Morad, S., Bjorlykke, K., Egeberg, P.K., Aagaard, P., 1988. Diagenetic albitization of detrital K-feldspar in Jurassic, Lower Cretaceous, and Tertiary clastic reservoir rocks from offshore Norway, I. Textures and origin. J. Sediment. Petrol. 58, 1003–1013. https://doi.org/10.1306/212F8EE5-2B24-11D7-8648000102C1865D.

Salles, T., Lopez, S., Eschard, R., Lerat, O., Mulder, T., Cacas, M.C., 2008. Turbidity current modelling on geological time scales. Mar. Geol. 248, 127–150. https://doi.org/10.1016/j.margeo.2007.10.004.

Sayers, C.M., den Boer, L.D., 2016. The elastic anisotropy of clay minerals. Geophysics 81, pp. 193–203. https://doi.org/10.1190/GEO2016-0005.1.

Schmid, S., Worden, R.H., Fisher, Q.J., 2004. Diagenesis and reservoir quality of the Sherwood Sandstone (Triassic), Corrib Field, Slyne Basin, west of Ireland. Mar. Pet. Geol. 21, 299–315. https://doi.org/10.1016/j.marpetgeo.2003.11.015.

Scott, E.D., Gelin, F., Jolley, S.J., Leenaarts, E., Sadler, S.P., Elsinger, R.J., 2010. Sedimentological control of fluid flow in deep marine turbidite reservoirs: Pierce Field, Uk Central North Sea. Geol. Soc. Spec. Publ. 347, 113–132. https://doi.org/10.1144/SP347.9.

Shackleton, N.J. and, Kennett, J.P., 1974. Paleotemperature History of the Cenozoic and the Initiation of Antarctic Glaciation: Oxygen and Carbon Isotope Analyses in DSDP Sites 277, 279 and 281, 29th ed, Initial Reports of the Deep Sea Drilling Project, 29. US Government printing office, Washington. https://doi.org/10.2973/dsdp.proc.29.117.1975.

Shammari, S., Franks, S., M. Soliman, O., 2011. Depositional and Facies Controls from Infiltrated/Inherited Clay Coatings: Unayzah Sandstones, Saudi Arabia. AAPG Annu. Conv. Exhib. Houston, Texas, USA, pp.1-26. https://doi.org/10.3997/2214-4609-pdb.248.366

Shanmugam, G., 2000. 50 years of the turbidite paradigm (1950s-1990s): Deep-water processes and facies models-a critical perspective. Mar. Pet. Geol. 17, 285–342. https://doi.org/10.1016/S0264-8172(99)00011-2.

Shanmugam, G., 1997a. Deepwater exploration: Conceptual models and their uncertainties. NAPE (Nigerian Assoc. Pet. Explor. Bull. 22.

Shanmugam, G., 1997b. The Bouma Sequence and the turbidite mind set. Earth-Science Rev. 42, 201–229.

Shanmugam, G., Moiola, R.J., 1991. Types of submarine fan lobes: models and implications. Am. Assoc. Pet. Geol. Bull. 75, 156–179. https://doi.org/10.1306/0C9B276D-1710-11D7-8645000102C1865D.

Shanmugam, G., Moiola, R.J., 1988. Submarine Fans : Characteristics , Models , Classification

, and Reservoir Potential. Earth Science Reviews, 24, 383–428.

Shanmugam, G., Spalding, T.D., Rofheart, D.H., 1993. Process sedimentology and reservoir quality of deep-marine bottom- current reworked sands (sandy contourites): an example from the Gulf of Mexico. Am. Assoc. Pet. Geol. Bull. 77, 1241–1259. https://doi.org/10.1306/bdff8e52-1718-11d7-8645000102c1865d.

Shaw, H.F., Conybeare, D.M., 2003. Patterns of Clay Mineral Diagenesis in Interbedded Mudrocks and Sandstones: An Example from the Palaeocene of the North Sea, in: R.H Worden and S. Morad (Ed.), Clay Mineral Cements in Sandstones. International Association of Sedimentologists, pp. 129–145. https://doi.org/10.1002/9781444304336.ch6.

Shukla, R., Ranjith, P., Haque, A., Choi, X., 2010. A review of studies on CO2 sequestration and caprock integrity. Fuel 89, 2651–2664. https://doi.org/10.1016/j.fuel.2010.05.012.

Smith, J.T., Ehrenberg, S.N., 1989. Correlation of carbon dioxide abundance with temperature in clastic hydrocarbon reservoirs: relationship to inorganic chemical equilibrium. Mar. Pet. Geol. 6, 129–135. https://doi.org/10.1016/0264-8172(89)90016-0.

Sneider, R.M., 1990. Introduction: reservoir description of sandstones, in: J.H. Barwis, J.G. McPherson, and J.R.J.S. (Ed.), Sandstone Petroleum Reservoirs: Springer-Verlag, New York, pp. 1-2.

Środoń, J., 1999. Nature of Mixed-Layer Clays and Mechanisms of Their Formation and Alteration. Annu. Rev. Earth Planet. Sci. 27, 19–53. https://doi.org/10.1146/annurev.earth.27.1.19.

Stammer, J.G., 2014. Hydrodynamic fractionation of minerals and textures in submarine fans: Quantitative analysis from outcrop, experimental, and subsurface studies. ProQuest Diss. Theses. Colorado School of Mines, pp. 1-62.

Stanley, D.J., 1982. Welded slump-graded sand couplets: evidence for slide generated turbidity currents. Geo-Marine Lett. 2, 149–155. https://doi.org/10.1007/BF02462756.

Stewart, R.N.., 1995. Regional diagenetic porosity change in palaeocene oilfield sandstones, U.K. North Sea. University of Glasgow, pp. 16-52.

Stewart, R.N.T., Haszeldine, R.S., Fallick, A.E., Wilkinson, M., Macaulay, C.I., 2000. Regional distribution of diagenetic carbonate cement in Palaeocene deepwater sandstones: North Sea. Clay Miner. 35, 119–133. https://doi.org/10.1180/000985500546521.

Storvoll, V., Bjørlykke, K., Karlsen, D., Saigal, G., 2002. Porosity preservation in reservoir sandstones due to grain-coating illite: A study of the Jurassic Garn Formation from the Kristin and Lavrans fields, offshore Mid-Norway. Mar. Pet. Geol. 19, 767–781. https://doi.org/10.1016/S0264-8172(02)00035-1.

Stricker, S., 2016. Influence of fluid pressure on the diagenesis of clastic sediments. Durham University, UK, pp. 61-109.

Stricker, S., Jones, S.J., 2018. Enhanced porosity preservation by pore fluid overpressure and chlorite grain coatings in the Triassic Skagerrak, Central Graben, North Sea, UK. Geol. Soc. Spec. Publ. 435, 321–341. https://doi.org/10.1144/SP435.4.

Stricker, S., Jones, S.J., Sathar, S., Bowen, L., Oxtoby, N., 2016. Exceptional reservoir quality in HPHT reservoir settings: Examples from the Skagerrak Formation of the Heron Cluster, North Sea, UK. Mar. Pet. Geol. 77, 198–215.

https://doi.org/10.1016/j.marpetgeo.2016.02.003.

Sullivan, M., Coombes, T., Imbert, P., Ahamdach-Demars, C., 1999. Reservoir quality and petrophysical evaluation of Paleocene sandstones in the West of Shetland area. Pet. Geol. Northwest Eur. Proc. 5th Conf. 1, 627–633. https://doi.org/10.1144/0050627.

Surdam, R.C., Crossey, L.J., Hagen, E.S., Heasler, H.P., 1989. Organic-inorganic interactions and sandstone diagenesis. Am. Assoc. Pet. Geol. Bull. 73, 1–23. https://doi.org/10.1306/703c9ad7-1707-11d7-8645000102c1865d.

Swarbrick, R.E., Osborne, M.J., Grunberger, D., Yardley, G.S., Macleod, G., Aplin, A.C., Larter, S.R., Knight, I., Auld, H.A., 2000. Integrated study of the Judy Field (Block 30/7a) - an overpressured Central North Sea oil/gas field. Mar. Pet. Geol. 17, 993–1010. https://doi.org/10.1016/S0264-8172(00)00050-7.

Talling, P.J., 2013. Hybrid submarine flows comprising turbidity current and cohesive debris flow: Deposits, theoretical and experimental analyses, and generalized models. Geosphere 9, 460–488. https://doi.org/10.1130/GES00793.1.

Talling, P.J., Amy, L.A., Wynn, R.B., Peakall, J., Robinson, M., 2004. Beds comprising debrite sandwiched within co-genetic turbidite: Origin and widespread occurrence in distal depositional environments. Sedimentology 51, 163–194. https://doi.org/10.1111/j.1365-3091.2004.00617.x.

Talling, P.J., Masson, D.G., Sumner, E.J., Malgesini, G., 2012. Subaqueous sediment density flows: Depositional processes and deposit types. Sedimentology 59, 1937–2003. https://doi.org/10.1111/j.1365-3091.2012.01353.x.

Tang, L., Gluyas, J., Jones, S., 2018. Porosity preservation due to grain coating illite/smectite: Evidence from Buchan Formation (Upper Devonian) of the Ardmore Field, UK North Sea. Proc. Geol. Assoc. 129, 202–214. https://doi.org/10.1016/j.pgeola.2018.03.001.

Taylor, A.M., Goldring, R., 1993. Description and analysis of bioturbation and ichnofabric. J. - Geol. Soc. 150, 141–148. https://doi.org/10.1144/gsjgs.150.1.0141.

Taylor, T.R., Giles, M.R., Hathon, L.A., Diggs, T.N., Braunsdorf, N.R., Birbiglia, G. V., Kittridge, M.G., MacAulay, C.I., Espejo, I.S., 2010. Sandstone diagenesis and reservoir quality prediction: Models, myths, and reality. Am. Assoc. Pet. Geol. Bull. 94, 1093–1132. https://doi.org/10.1306/04211009123.

Thiry, M. and, Jacquin, T., 1993. Clay mineral distribution related to rift activity, sea-level changes and paleoceanography in the Cretaceous of the Atlantic Ocean. Clay Miner. 28, 61–84. https://doi.org/10.1180/claymin.1993.028.1.07.

Thompson, P.J., Butcher, P.D., 1990. The geology and geophysics of the Everest Complex. Am. Assoc. Pet. Geol. Bull. 74, 778.

Thyne, G., Boudreau, B.P., Ramm, M., Midtbø, R.E., 2001. Simulation of potassium feldspar dissolution and illitization in the Statfjord Formation, North Sea. Am. Assoc. Pet. Geol. Bull. 85, pp. 621–635. https://doi.org/10.1306/8626c965-173b-11d7-8645000102c1865d.

Tian, J.F., Chen, Z.L., Fan, Y.F., Li, P.P., Song, L.J., 2008. The occurrence, growth mechanism and distribution of authigenic chlorite in sandstone. Bull. Mineral. Petrol. Geochemistry 27, 200–205.

Ulmer-Scholle, D.S., Scholle, P.A., Schieber, J., Raine, R.J., 2015. A Color Guide to the

Petrography of Sandstones, Siltstones, Shales and Associated Rocks, A Color Guide to the Petrography of Sandstones, Siltstones, Shales and Associated Rocks. AAPG, 109, pp. 275-293. https://doi.org/10.1306/m1091304

Underwood, M.B., Bachman, S.B., 1982. Sedimentary facies associations within subduction complexes, in: Leggett, J.K. (Ed.), Geological Society Special Publication. Geol. Soc. London Spec. Publ., pp. 537–550. https://doi.org/10.1144/GSL.SP.1982.010.01.35.

Vining, B.A., Ioannides, N.S., Pickering, K.T., 1993. Stratigraphic relationships of some Tertiary lowstand depositional systems in the Central North Sea, in: Parker, J.R. (Ed.), Petroleum Geology Conference Proceedings. Geological Society, London, pp. 17–29. https://doi.org/10.1144/0040017.

Virolle, M., Brigaud, B., Luby, S., Portier, E., Féniès, H., Bourillot, R., Patrier, P., Beaufort, D., 2019. Influence of sedimentation and detrital clay grain coats on chloritized sandstone reservoir qualities: Insights from comparisons between ancient tidal heterolithic sandstones and a modern estuarine system. Mar. Pet. Geol. 107, 163–184. https://doi.org/10.1016/j.marpetgeo.2019.05.010.

Walderhaug, O., 2000. Modeling quartz cementation and porosity in Middle Jurassic Brent Group sandstones of the Kvitebjørn Field, northern North Sea. Am. Assoc. Pet. Geol. Bull. 84, 1325–1339.

Walderhaug, O., 1996. Kinetic modeling of quartz cementation and porosity loss in deeply buried sandstone reservoirs. Am. Assoc. Pet. Geol. Bull. 80, 731–745.

Walderhaug, O., 1994. Temperatures of quartz cementation in Jurassic sandstones from the Norwegian continental shelf - evidence from fluid inclusions. J. Sediment. Res. A Sediment. Petrol. Process. 64 A, 311–323. https://doi.org/10.1306/d4267d89-2b26-11d7-8648000102c1865d.

Walderhaug, O., BjØrkum, P.A., 2003. The effect of stylolite spacing on quartz cementation in the Lower Jurassic StØ Formation, Southern Barents Sea. J. Sediment. Res. 73, 146–156. https://doi.org/10.1306/090502730146.

Walderhaug, O., Porten, K.W., 2007. Stability of Detrital Heavy Minerals on the Norwegian Continental Shelf as a Function of Depth and Temperature. J. Sediment. Res. 77, 992–1002. https://doi.org/10.2110/jsr.2007.091.

Walker, R.G.; Martinsen, O.J., 1999. Deep water facies and depositional environments, Cretaceous, mid-Norway: Conference Abstract, in: American Association of Petroleum Geologists/Society for Sedimentary Geology, Annual Meeting 1999, Denver, USA, p. 1.

Walker, R.G., 1978. Deep-water sandstone facies and ancient submarine fans: models for exploration for stratigraphic traps. AAPG Bulletin, 62, 932–966.

Wang, J., Cao, Y., Xiao, J., Liu, K., Song, M., 2019. Factors controlling reservoir properties and hydrocarbon accumulation of the Eocene lacustrine beach-bar sandstones in the Dongying Depression, Bohai Bay Basin, China. Mar. Pet. Geol. 99, 1–16. https://doi.org/10.1016/j.marpetgeo.2018.09.022.

Waples, D.W., Pacheco, J., Vera, A., 2004. A method for correcting log-derived temperatures in deep wells, calibrated in the Gulf of Mexico. Pet. Geosci. 10, 239–245. https://doi.org/10.1144/1354-079302-542.

Weibel, R., 1999. Effects of Burial on the Clay Assemblages in the Triassic Skagerrak Formation, Denmark. Clay Miner. 34, 619–635.

https://doi.org/10.1180/claymin.1999.034.4.08.

Weibel, R., Friis, H., Kazerouni, A.M., Svendsen, J.B., Stokkendal, J., Poulsen, M.L.K., 2010. Development of early diagenetic silica and quartz morphologies - Examples from the Siri Canyon, Danish North Sea. Sediment. Geol. 228, 151–170. https://doi.org/10.1016/j.sedgeo.2010.04.008.

Weibel, R., Nielsen, M.T., Therkelsen, J., Jakobsen, F.C., Bjerager, M., Mørk, F., Mathiesen, A., Hovikoski, J., Pedersen, S.S., Johannessen, P.N., Dybkjær, K., 2020. Illite distribution and morphology explaining basinal variations in reservoir properties of Upper Jurassic sandstones, Danish North Sea. Mar. Pet. Geol. 116, 1–23. https://doi.org/10.1016/j.marpetgeo.2020.104290.

Weibel, R., Olivarius, M., Kjøller, C., Kristensen, L., Hjuler, M.L., Friis, H., Pedersen, P.K., Boyce, A., Andersen, M.S., Kamla, E., Boldreel, L.O., Mathiesen, A., Nielsen, L.H., 2017. The influence of climate on early and burial diagenesis of Triassic and Jurassic sandstones from the Norwegian-Danish Basin. Depos. Rec. 3, 60–91. https://doi.org/10.1002/dep2.27.

Weimer, P., Pettingill, H.S., 2007. Global Overview of Deep-water Exploration and Production Executive Summary 4 Global Overview of Deep-water Exploration and Production. AAPG, 56, 7–11. https://doi.org/10.1306/1240888St56285.

Weimer, P., Slatt, R.M., 2004. The Petroleum Systems of Deepwater Settings. Society of Exploration Geophysicists Distinguished Instructor Short Course Notes, p. 488. https://doi.org/10.1190/1.9781560801955.

White, J.F., Taylor, M.C., Vincent, G.P., 1942. Chemistry of Chlorites. Ind. Eng. Chem. 34, pp. 782–792. https://doi.org/10.1021/ie50391a003.

Whyatt, M., Bowen, J.M., Rhodes, D.N., 1992. The Nelson Field: A successful application of a development geoseismic model in North Sea exploration. Geol. Soc. Spec. Publ. 67, 283–305. https://doi.org/10.1144/GSL.SP.1992.067.01.11.

Wills, J.M., Peattie, D.K., 1990. The Forties Field and the evolution of a reservoir management strategy. North Sea oil gas Reserv. – II. Springer, Dordrecht, pp.1–23. https://doi.org/10.1007/978-94-009-0791-1_1.

Wilson, M.D., 1992. Inherited Grain-Rimming Clays in Sandstones From Eolian and Shelf Environments: Their Origin and Control on Reservoir Properties. Orig. Diagenesis, Petrophysics Clay Miner. Sandstones 209–225. https://doi.org/10.2110/pec.92.47.0209.

Wise, J.W., Smellie, J., Aghib, F., Jarrard, R., Krissek, L., 2001. Authigenic smectite clay coats in CRP-3 drillcore, Victoria Land Basin, Antarctica, as a possible indicator of fluid flow: A progress report, Terra Antarctica, 8 (3), pp. 281-298.

Wooldridge, L. J., Worden, R.H., Griffiths, J., Thompson, A., Chung, P., 2017. Biofilm origin of clay-coated sand grains. Geology 45, 875–878. https://doi.org/10.1130/G39161.1.

Wooldridge, L.J., Worden, R.H., Griffiths, J., Utley, J.E.P., 2019a. How to quantify clay-coat grain coverage in modern and ancient sediments. J. Sediment. Res. 89, 135–146. https://doi.org/10.2110/jsr.2019.6.

Wooldridge, L.J., Worden, R.H., Griffiths, J., Utley, J.E.P., 2019b. Clay-coat diversity in marginal marine sediments. Sedimentology 66, 1118–1138. https://doi.org/10.1111/sed.12538.

Wooldridge, Luke J., Worden, R.H., Griffiths, J., Utley, J.E.P., 2017. Clay-Coated Sand Grains In Petroleum Reservoirs: Understanding Their Distribution Via A Modern Analogue. J. Sediment. Res. 87, 338–352. https://doi.org/10.2110/jsr.2017.20.

Wooldridge, L.J., Worden, R.H., Griffiths, J., Utley, J.E.P., Thompson, A., 2018. The origin of clay-coated sand grains and sediment heterogeneity in tidal flats. Sediment. Geol. 373, 191–209. https://doi.org/10.1016/j.sedgeo.2018.06.004.

Worden, R.H., Armitage, P.J., Butcher, A.R., Churchill, J.M., Csoma, A.E., Hollis, C., Lander, R.H., Omma, J.E., 2018. Petroleum reservoir quality prediction: Overview and contrasting approaches from sandstone and carbonate communities, in: P.J. Armitage, A. Butcher, J. Churchill, A. Csoma, C. Hollis, R.H. Lander, J.O. and R.H.W. (Ed.), Geological Society Special Publication. Geological Society, London, Special Publications, pp. 1–31. https://doi.org/10.1144/SP435.21.

Worden, R.H., French, M.W., Mariani, E., 2012. Amorphous silica nanofilms result in growth of misoriented microcrystalline quartz cement maintaining porosity in deeply buried sandstones. Geology 40, 179–182. https://doi.org/10.1130/G32661.1.

Worden, R.H., Griffiths, J., Wooldridge, L.J., Utley, J.E.P., Lawan, A.Y., Muhammed, D.D., Simon, N., Armitage, P.J., 2020. Chlorite in sandstones. Earth-Science Rev. 103105. https://doi.org/10.1016/j.earscirev.2020.103105.

Worden, R.H., Mayall, M., Evans, I.J., 2000. The effect of Ductile-Lithic sand grains and quartz cement on porosity and permeability in Oligocene and lower Miocene clastics, South China Sea: Prediction of reservoir quality. Am. Assoc. Pet. Geol. Bull. 84, 345–359. https://doi.org/10.1306/c9ebcde7-1735-11d7-8645000102c1865d.

Worden, R.H., Morad, S., 2003. Clay Minerals in Sandstones: Controls on Formation, Distribution and Evolution, in: Clay Mineral Cements in Sandstones. Blackwell Publishing Ltd., Oxford, UK, pp. 1–41. https://doi.org/10.1002/9781444304336.ch1.

Worden, R.H., Morad, S., 2000. Quartz Cementation in Oil Field Sandstones: A Review of the Key Controversies, in: Worden, R. H. and Morad, S. (Ed.), Quartz Cementation in Sandstones. Wiley-Blackwell, Oxford, pp. 1–20. https://doi.org/10.1002/9781444304237.ch1.

Xia, C., Wilkinson, M., 2017. The geological risks of exploring for a CO2 storage reservoir. Int. J. Greenh. Gas Control 63, 272–280. https://doi.org/10.1016/j.ijggc.2017.05.016.

Yang, L., Xu, T., Feng, G., Liu, K., Tian, H., Peng, B., Wang, C., 2017. CO2-induced geochemical reactions in heterogeneous sandstone and potential conditions causing the tight cementation. Appl. Geochemistry 80, 14–23. https://doi.org/10.1016/j.apgeochem.2017.03.003.

Yanzhong, W., Nianmin, Z., Xu, C., Yingchang, C., Guanghui, Y., Gluyas, J.G., Miruo, L., 2020. Geologic CO2 storage in arkosic sandstones with CaCl2-rich formation water. Chem. Geol. 558, pp. 1-13. https://doi.org/10.1016/j.chemgeo.2020.119867.

Yezerski, D.J., Shumaker, N., 2018. PS Improving Prediction of Porosity Preservation in Thermally-Stressed Deep Marine Sandstones: A Synthesis of Grain-Coating Chlorite Observations*, in: AAPG 2017 Annual Convention and Exhibition. Search and Discovery Article, Houston, Texas, pp. 1-6.

Zeng, J., Lowe, D.R., Prior, D.B., Wiseman, W.J., Bornhold, B.D., 1991. Flow properties of turbidity currents in Bute Inlet, British Columbia. Sedimentology 38, 975–996. https://doi.org/10.1111/j.1365-3091.1991.tb00367.x.

Zhang, P., Lee, Y. Il, Zhang, J., 2019. A review of high-resolution X-ray computed tomography applied to petroleum geology and a case study. Micron 124, pp. 2-8. https://doi.org/10.1016/j.micron.2019.102702.

Appendix I: Petrographic, COPL-CEPL, and Clay-coating Coverage Measurements Data

- Point count data summary
- COPL-CEPL data
- Clay-coating coverage measurements data

Point count data summary

Lithofacies; number of samples	Amalgamated Sandstone Facies- Channel; n=38			Amalgamated Sandstone Facies- Lobe; n=46			Channel Abandonment/Floodplain Facies- Lobe; n=14			Sand-prone Heterolithic Facies; n=45			Mud-prone Heterolithic Facies; n=48			Whole Unit; n=191		
Total	Min	Max	Average	Min	Max	Average	Min	Max	Average	Min	Max	Average	Min	Max	Average	Min	Max	Average
Detrital Grains																		
Monocrystalline quartz	29.70	48.70	39.31	24.00	60.30	40.33	5.30	38.00	21.39	17.00	52.30	37.12	9.00	51.30	32.27	5.30	60.30	35.96
Polycrystalline quartz (and rock fragment)	0.70	6.00	2.17	0.00	5.00	2.00	0.00	1.50	0.48	0.00	4.00	1.46	0.00	4.70	1.66	0.00	6.00	1.71
Mudclast	0.00	3.70	0.86	0.00	1.00	0.06	0.00	0.50	0.04	0.00	1.70	0.10	0.00	3.00	0.10	0.00	3.70	0.24
Total Detrital Feldspar	5.30	26.10	16.88	6.10	28.00	14.49	2.30	23.70	14.55	2.70	30.00	13.19	4.30	22.50	13.96	2.30	30.00	14.53
Orthoclase	1.30	21.70	11.67	2.30	20.30	9.05	2.00	19.30	10.69	1.70	19.70	8.66	2.50	17.70	8.97	1.30	21.70	9.58
Microcline	0.00	2.70	0.58	0.00	1.00	0.23	0.00	1.00	0.09	0.00	1.00	0.14	0.00	1.00	0.16	0.00	2.70	0.25
Detrital plagioclase	1.00	8.30	4.63	0.00	10.00	5.21	0.30	6.70	3.76	0.00	10.30	4.38	0.00	9.00	4.80	0.00	10.30	4.69
Total rock fragments	0.70	9.00	3.03	0.00	5.00	2.06	0.00	2.00	0.51	0.00	4.40	1.56	0.00	6.00	1.73	0.00	9.00	1.94
Total mica	0.00	10.40	1.61	0.00	26.00	3.91	1.00	21.00	10.92	0.30	23.40	5.91	0.00	35.00	9.96	0.00	35.00	5.96
Biotite	0.00	4.70	0.83	0.00	14.00	2.03	1.00	17.00	8.00	0.00	18.00	3.88	0.00	33.50	7.11	0.00	33.50	3.94
Muscovite	0.00	5.70	0.78	0.00	12.00	1.88	0.00	7.70	2.92	0.00	11.70	2.04	0.00	10.50	2.84	0.00	12.00	2.02
Total ductile grains	0.00	14.10	2.48	0.00	26.00	3.97	1.00	21.00	10.96	0.30	23.40	6.01	0.00	35.00	10.06	0.00	35.00	6.20
Glauconite	0.00	0.30	0.05	0.00	1.00	0.08	0.00	0.70	0.07	0.00	0.30	0.02	0.00	0.50	0.05	0.00	1.00	0.05
Heavy minerals	0.00	0.70	0.06	0.00	0.70	0.07	0.00	0.50	0.06	0.00	0.70	0.09	0.00	2.00	0.17	0.00	2.00	0.10
Detrital matrix	3.00	12.70	6.74	0.30	28.00	7.12	3.30	21.50	11.64	5.00	27.00	11.46	0.30	44.00	14.55	0.30	44.00	10.26
Diagenetics																		
Intergranular non-ferroan calcite	0.00	5.30	0.39	0.00	23.30	2.76	0.00	12.00	1.14	0.00	15.00	1.13	0.00	27.00	2.09	0.00	27.00	1.62
Grain-replacive non-ferroan calcite	0.00	3.00	0.14	0.00	8.00	0.65	0.00	0.30	0.06	0.00	5.00	0.27	0.00	7.30	0.28	0.00	8.00	0.33

Intergranular ferroan calcite	0.00	1.00	0.03	0.00	18.30	1.03	0.00	0.00	0.00	0.00	1.30	0.05	0.00	13.00	0.30	0.00	18.30	0.34
Grain-replacive ferroan calcite	0.00	2.30	0.18	0.00	15.30	1.05	0.00	5.70	0.57	0.00	5.00	0.61	0.00	13.00	0.59	0.00	15.30	0.62
Intergranular dolomite	0.00	7.70	0.33	0.00	17.00	1.98	0.00	2.70	0.19	0.00	3.00	0.20	0.00	0.70	0.10	0.00	17.00	0.63
Grain-replacive dolomite	0.00	0.30	0.01	0.00	2.00	0.08	0.00	0.00	0.00	0.00	1.70	0.07	0.00	0.00	0.00	0.00	2.00	0.04
Intergranular siderite	0.00	3.70	1.09	0.00	22.30	1.51	0.00	12.70	2.46	0.00	9.30	0.45	0.00	2.00	0.15	0.00	22.30	0.90
Grain-replacive siderite	0.00	1.30	0.03	0.00	1.30	0.06	0.00	10.50	1.78	0.00	7.70	0.19	0.00	0.00	0.00	0.00	10.50	0.20
Intergranular pyrite	0.00	2.00	0.48	0.00	1.70	0.64	0.30	3.30	1.62	0.00	6.00	1.43	0.00	8.00	1.71	0.00	8.00	1.13
Grain-replacive pyrite	0.00	1.00	0.17	0.00	2.50	0.40	0.00	4.30	1.76	0.00	2.70	0.37	0.00	3.00	0.30	0.00	4.30	0.42
Intergranular kaolinite	0.00	6.30	1.42	0.00	4.00	1.70	0.00	5.70	2.11	0.00	7.30	1.79	0.00	14.70	2.67	0.00	14.70	1.81
Grain-replacive kaolinite	0.00	1.30	0.15	0.00	6.00	0.35	0.00	1.00	0.26	0.00	1.50	0.23	0.00	11.00	0.69	0.00	11.00	0.36
Intergranular chlorite	0.00	5.00	2.01	0.00	8.00	2.29	0.70	9.00	3.74	0.00	16.00	4.83	0.00	9.70	4.10	0.00	16.00	3.39
Grain-replacive chlorite	0.00	1.30	0.59	0.00	2.30	0.62	0.30	11.00	2.04	0.00	17.00	1.62	0.00	8.00	1.15	0.00	17.00	1.09
Grain-coating chlorite	0.00	7.70	1.72	0.00	8.00	2.10	0.30	9.70	4.34	0.00	7.70	1.50	0.00	5.00	1.26	0.00	9.70	1.84
Intergranular illite/smectite	0.00	0.30	0.02	0.00	3.00	0.09	0.00	1.00	0.07	0.00	5.30	0.32	0.00	2.00	0.14	0.00	5.30	0.14
Grain-replacive illite/smectite	0.00	0.00	0.00	0.00	3.00	0.08	0.00	0.30	0.02	0.00	4.70	0.12	0.00	0.30	0.01	0.00	4.70	0.05
Grain-coating illite/illite-smectite	0.30	5.30	2.32	0.00	10.00	1.98	0.00	3.30	1.99	0.00	8.00	1.60	0.00	4.30	0.88	0.00	10.00	1.68
Intergranular illite	0.00	4.30	1.92	0.00	5.30	1.87	0.30	9.00	2.59	0.00	6.30	2.81	0.00	4.70	1.76	0.00	9.00	2.13
Grain-replacive illite	0.00	2.00	0.59	0.00	5.00	0.82	0.00	17.00	3.59	0.00	4.70	0.85	0.00	3.00	0.46	0.00	17.00	1.89
Total grain coating clays	1.30	9.00	4.04	0.00	10.70	4.08	0.70	10.70	6.33	0.00	9.70	3.11	0.00	6.70	2.14	0.00	10.70	3.52
Quartz overgrowth	1.00	6.30	3.62	0.00	9.30	3.03	0.00	8.00	2.96	0.30	8.00	2.62	0.00	7.70	1.78	0.00	9.30	2.73
Bitumen	0.00	1.70	0.54	0.00	3.30	0.53	0.00	6.70	2.31	0.00	7.00	0.95	0.00	22.00	2.08	0.00	22.00	1.15
Porosity																		
Intergranular optical porosity	0.70	18.80	11.43	0.00	15.70	3.81	0.00	17.00	2.45	0.00	23.70	4.22	0.00	15.70	3.05	0.00	23.70	5.13
Clay-lined intergranular optical porosity	0.00	5.70	1.75	0.00	7.30	1.69	0.00	9.00	1.94	0.00	7.00	1.14	0.00	5.00	0.73	0.00	9.00	1.35
Total optical porosity	1.70	20.70	13.18	0.00	18.40	5.50	0.00	26.00	4.39	0.00	24.40	5.36	0.00	16.00	3.78	0.00	26.00	6.48

Feldspar dissolution porosity	0.00	3.00	1.13	0.00	4.30	0.81	0.00	3.30	0.64	0.00	4.00	0.80	0.00	5.00	0.72	0.00	5.00	0.83
Clay-lined feldspar dissolution porosity	0.00	1.30	0.21	0.00	3.00	0.40	0.00	1.70	0.22	0.00	3.30	0.44	0.00	2.00	0.30	0.00	3.30	0.33
Total Feldspar dissolution porosity	0.00	4.00	1.34	0.00	5.30	1.20	0.00	4.40	0.86	0.00	5.00	1.24	0.00	5.00	1.01	0.00	5.30	1.16
Carbonate-cement dissolution porosity	0.00	0.00	0.00	0.00	5.00	0.17	0.00	0.00	0.00	0.00	0.00	0.00	0.00	0.50	0.01	0.00	5.00	0.04
Cements																		
Cements (pore-filling) total	6.00	25.30	13.94	8.00	45.60	19.80	11.60	37.00	23.96	11.60	44.20	23.03	5.20	50.00	25.85	5.20	50.00	21.22
Carbonate cements (pore-filling) total	0.00	14.70	1.84	0.00	43.60	7.27	0.00	14.70	3.80	0.00	25.00	1.82	0.00	35.00	2.63	0.00	43.60	3.49
Clays (authigenic and detrital) total	6.00	22.00	12.09	0.60	32.00	12.53	10.30	29.20	20.60	11.30	32.00	21.21	1.60	49.00	23.22	0.60	49.00	17.73
Authigenic, pore-filling clay minerals total	1.60	9.60	5.36	0.00	12.30	5.42	1.50	15.00	8.51	2.30	18.30	9.75	1.30	20.40	8.67	0.00	20.00	7.47
Compactional porosity loss (%) COPL	4.31	24.15	19.48	8.68	28.63	17.19				9.64	22.98	15.80	4.00	28.14	15.13	4.00	28.14	15.81
Cementational porosity loss (%) CEPL	4.28	24.50	10.51	3.97	28.72	12.70				7.47	16.90	12.69	5.39	35.42	14.64	3.97	35.42	12.30
Intergranular volume (IGV)	20.90	37.30	29.19	18.00	34.30	27.21				22.10	33.60	28.59	16.50	37.50	28.87	16.50	37.50	28.43
Helium porosity (%)	20.10	28.40	23.82	1.90	23.60	17.43	17.50	26.10	21.70	5.60	24.50	17.51	3.10	25.90	16.26	1.90	28.40	18.72
Vertical permeability (mD)	7.10	500.00	185.98	0.01	135.00	24.21	2.00	271.00	51.28	0.02	101.00	12.55	0.02	61.80	5.71	0.01	500.00	53.20
Mean grain size (mm)	0.12	0.36	0.27	0.07	0.44	0.22	0.03	0.22	0.10	0.05	0.32	0.19	0.07	0.30	0.17	0.03	0.44	0.2

COPL-CEPL data

Field/Well	TVDSS (m)	Facies	Total Pore-filling Cements	Intergranular Volume (IGV)	Compactional Porosity Loss (COPL)	Cementational Porosity Loss (CEPL)	Grain-coating Clays (GCC)
Nelson/22/11-6	2206.4	ASF-C	15.90	32.20	11.50	14.07	5.30
Nelson/22/11-6	2206.8	ASF-C	11.00	33.90	9.23	9.98	2.60
Nelson/22/11-6	2206.8	ASF-C	13.30	32.80	10.71	11.88	5.00
Nelson/22/11-6	2210.1	ASF-C	24.30	35.60	6.83	22.64	1.30
Nelson/22/11-6	2210.4	ASF-C	10.30	33.00	10.45	9.22	3.70
Nelson/22/11-6	2210.7	ASF-C	12.40	29.70	14.65	10.58	2.70
Nelson/22/11-6	2211.0	ASF-C	14.00	30.30	13.92	12.05	4.70
Nelson/22/11-6	2211.0	ASF-C	13.60	33.30	10.04	12.23	3.30
Nelson/22/11-6	2215.6	ASF-C	13.70	29.60	14.77	11.68	4.00
Nelson/22/11-6	2215.9	ASF-C	7.30	25.20	19.79	5.86	5.30
Nelson/22/11-6	2216.2	ASF-C	9.00	32.60	10.98	8.01	2.70

Nelson/22/11-6	2218.0	ASF-C	13.00	34.30	8.68	11.87	2.00
Nelson/22/11-6	2218.0	ASF-C	9.60	27.90	16.78	7.99	1.30
Nelson/22/11-6	2218.9	ASF-C	13.60	37.30	4.31	13.01	1.70
Nelson/22/11-8	2583.5	ASF-C	12.90	27.90	16.78	10.74	6.70
Nelson/22/11-8	2584.4	ASF-C	8.70	28.00	16.67	7.25	5.70
Nelson/22/11-8	2585.3	ASF-C	10.70	35.40	7.12	9.94	3.30
Nelson/22/11-8	2585.9	ASF-C	14.00	28.00	16.67	11.67	5.00
Nelson/22/11-8	2594.2	ASF-C	5.30	25.70	19.25	4.28	8.70
Nelson/22/11-8	2594.5	ASF-C	7.60	21.60	23.47	5.82	9.00
Nelson/22/11-8	2595.4	ASF-C	9.60	24.90	20.11	7.67	4.00
Nelson/22/11-8	2595.7	ASF-C	5.60	26.70	18.14	4.58	5.70
Nelson/22/11-8	2596.6	ASF-C	10.00	28.90	15.61	8.44	4.00
Nelson/22/11-8	2606.6	ASF-C	10.60	30.20	14.04	9.11	2.00
Nelson/22/11-8	2607.0	ASF-C	8.70	30.70	13.42	7.53	3.00

Nelson/22/11-8	2608.2	ASF-C	10.90	29.20	15.25	9.24	4.00
Nelson/22/11-8	2608.5	ASF-C	13.70	26.00	18.92	11.11	4.30
Pierce/23/27-8	2477.7	ASF-C	12.70	24.00	21.05	10.03	7.00
Pierce/23/27-8	2478.0	ASF-C	7.90	21.60	23.47	6.05	6.00
Pierce/23/27-8	2478.3	ASF-C	8.00	20.90	24.15	6.07	5.30
Pierce/23/27-8	2479.5	ASF-C	26.00	27.00	17.81	21.37	0.00
Pierce/23/27-8	2479.9	ASF-C	28.70	29.70	14.65	24.50	0.00
Montrose/22/17-1	2510.3	ASF-L	31.50	34.20	8.81	28.72	0.00
Montrose/22/17-1	2513.4	ASF-L	11.00	21.00	24.05	8.35	2.30
Everest/22/10a-4	2556.4	ASF-L	10.60	29.30	15.13	9.00	6.00
Everest/22/10a-4	2557.0	ASF-L	10.20	28.10	16.55	8.51	7.70
Everest/22_10a_T6	2475.6	ASF-L	15.20	28.90	15.61	12.83	10.40

Everest/22_10a_T6	2475.9	ASF-L	14.10	25.80	19.14	11.40	10.70
Everest/22_10a_T6	2476.5	ASF-L	9.60	27.60	17.13	7.96	5.70
Everest/22-10a-T6	2476.8	ASF-L	13.70	28.30	16.32	11.46	6.70
Everest/22_10a_T6	2477.1	ASF-L	8.00	21.00	24.05	6.08	9.50
Everest/22_10a_T6	2496.6	ASF-L	15.70	32.70	10.85	14.00	8.30
Everest/22_10a_T6	2496.9	ASF-L	22.90	27.60	17.13	18.98	3.40
Everest/22/14a-2	2619.0	ASF-L	10.60	20.20	24.81	7.97	5.40
Everest/22/14a-2	2620.0	ASF-L	31.10	33.40	9.91	28.02	0.00
Everest/22/14a-2	2620.0	ASF-L	10.90	34.30	8.68	9.95	2.30

Arran/23/16c-8	2580.7	ASF-L	12.40	28.70	15.85	10.43	4.00
Arran/23/16c-8	2581.0	ASF-L	12.00	27.90	16.78	9.99	8.40
Pierce/23/27-5	2735.6	ASF-L	13.60	29.90	14.41	11.64	2.70
Pierce/23/27-5	2739.2	ASF-L	26.00	31.30	12.66	22.71	0.00
Pierce/23/27-6	2899.3	ASF-L	14.40	25.40	19.57	11.58	5.00
Pierce/23/27-6	2899.6	ASF-L	8.90	20.20	24.81	6.69	3.00
Pierce/23/27-6	2900.5	ASF-L	28.30	34.30	8.68	25.84	0.00
Pierce/23/27-6	2902.0	ASF-L	7.30	18.00	26.83	5.34	3.70
Pierce/23/27-6	2903.2	ASF-L	24.00	29.30	15.13	20.37	0.00
Pierce/23/27-6	2904.1	ASF-L	15.00	31.30	12.66	13.10	3.60
Pierce/23/27-6	2905.4	ASF-L	5.30	19.90	25.09	3.97	2.00
Pierce/23/27-6	2916.0	ASF-L	16.40	32.10	11.63	14.49	1.00
Blane/30/03a-1	3096.0	ASF-L	12.00	22.10	22.98	9.24	3.70
Blane/30/03a-1	3097.0	ASF-L	9.50	19.00	25.93	7.04	10.00

Everest/22/10a-4	2536.5	SPHF	15.70	26.70	18.14	12.85	4.30
Everest/22/10a-4	2538.1	SPHF	20.00	29.00	15.49	16.90	1.00
Everest/22/10a-5	2538.1	SPHF	20.00	29.00	15.49	16.90	1.00
Everest/22_10a_T6	2437.2	SPHF	8.70	30.10	14.16	7.47	5.60
Everest/22/14a-2	2616.0	SPHF	18.20	33.60	9.64	16.45	1.30
Everest/22/14a-2	2619.0	SPHF	13.30	28.90	15.61	11.22	3.70
Arran/23/16c-8	2586.8	SPHF	12.00	27.40	17.36	9.92	4.60
Arran/23/16b-9	2720.3	SPHF	12.70	33.40	9.91	11.44	1.30
Pierce/23/27-6	2906.0	SPHF	14.40	22.10	22.98	11.09	2.00
Blane/30/03a-1	3091.0	SPHF	15.70	25.70	19.25	12.68	8.00
Montrose/22/17-A12	2494.8	MPHF	19.00	32.40	11.24	16.86	3.30
Montrose/22/17-A12	2495.4	MPHF	16.60	27.30	17.47	13.70	1.70

Montrose/22/17-A12	2496.0	MPHF	24.40	29.70	14.65	20.83	3.00
Montrose/22/17-A12	2496.3	MPHF	36.90	37.50	4.00	35.42	0.00
Everest/22_10a_T6	2435.7	MPHF	7.50	16.50	28.14	5.39	2.50
Everest/22_10a_T6	2435.7	MPHF	8.50	16.50	28.14	6.11	3.00
Everest/22/14a-2	2614.0	MPHF	16.90	34.30	8.68	15.43	3.30
Everest/22/14a-2	2614.0	MPHF	15.90	34.30	8.68	14.52	4.30
Arran/23/16c-8	2595.7	MPHF	11.10	31.70	12.15	9.75	3.00
Arran/23/16c-8	2591.7	MPHF	14.00	24.60	20.42	11.14	1.70
Arran/23/16c-8	2592.0	MPHF	19.90	33.60	9.64	17.98	2.00
Arran/23/16c-8	2593.8	MPHF	17.00	32.60	10.98	15.13	6.70
Arran/23/16c-8	2596.9	MPHF	12.90	25.90	19.03	10.45	4.60

Arran/23/16b-9	2710.9	MPHF	23.30	32.30	11.37	20.65	0.00
Pierce/23/27-6	2913.3	MPHF	10.60	28.90	15.61	8.95	4.00
Pierce/23/27-6	2914.5	MPHF	11.70	22.40	22.68	9.05	0.70
Pierce/23/27-6	2914.5	MPHF	17.40	29.00	15.49	14.70	0.00
Blane/30/03a-1	3089.0	MPHF	20.30	30.20	14.04	17.45	3.00

ASF-C: Amalagamated Sandstones Facies- Channel

ASF-L: Amalagamated Sandstones Facies- Lobe

SPHF: Sand-prone Heterolithic Facies

MPHF: Mud-prone Heterolithic Facies

Clay-coating coverage measurements data for the Forties Sandstone Member

Field/Well	TVDSS (m)	Facies	Coat Coverage (%)	Permeability (mD)	Core Porosity (%)	Quartz Cement (%)	Mean Grain Size (mm)	Grain-coating Clay volume (%)	Total Pore-filling Clays (%)	Total Pore-Filling Clays + Carbonates (%)	Optical Intergranular Porosity (%)
Nelson/22-11-6	2206.5	ASF-C	41	93	22.9	3.3	0.20	5.3	16	21.3	7.6
Nelson/22-11-6	2207.1	ASF-C	44	187	24	6.3	0.25	4	10.7	10.7	20.7
Nelson/22-11-6	2211	ASF-C	27	70	23.4	5.7	0.21	4.7	13.3	14.3	9.3
Nelson/22-11-6	2215.9	ASF-C	26	32	23.1	1	0.16	5.3	13.6	14.6	9.3
Nelson/22-11-6	2218	ASF-C	46	402	25	4.3	0.18	2	8.3	11.3	18
Nelson/22-11-6	2218.6	ASF-C	41	339	25.3	1.7	0.32	2.3	16.6	18.3	13
Nelson/22-11-6	2218.9	ASF-C	38	500	25	6.3	0.20	1.7	11.4	13.7	17
Nelson/22-11-8	2583.5	ASF-C	28	7.2	21.1	3.3	0.13	6.7	16	16.3	6.3
Nelson/22-11-8	2584.4	ASF-C	48	159	23.9	2.7	0.15	5.7	11	11	14
Nelson/22-11-8	2585.3	ASF-C	51	247	23.5	6	0.15	3.3	11.7	11.7	17.7
Nelson/22-11-8	2585.9	ASF-C	40	116	22.1	5.7	0.14	5	9.6	11.3	11
Nelson/22-11-8	2593.9	ASF-C	42	120	23.3	5	0.15	7	9.3	10.3	18.3
Nelson/22-11-8	2594.2	ASF-C	44	155	23.6	3	0.16	8.7	6	6	16.7
Nelson/22-11-8	2594.5	ASF-C	47	241	24.2	2.3	0.16	9	6.3	6.3	11
Nelson/22-11-8	2595.4	ASF-C	39	126	22.5	3.7	0.16	4	9.3	9.9	11.3
Nelson/22-11-8	2595.7	ASF-C	50	181	22.7	4	0.18	5.7	7.3	7.3	15.4
Nelson/22-11-8	2596.6	ASF-C	41	412	25	5.7	0.18	4	8.6	10.6	12.6
Nelson/22-11-8	2606.7	ASF-C	36	113	23.6	5.3	0.23	4	10.3	11.9	14.3
Nelson/22-11-8	2607	ASF-C	34	180	23.9	3.7	0.20	3	11	11.7	15
Nelson/22-11-8	2608.2	ASF-C	44	155	25	5.3	0.15	4	12	13.3	10.3
Nelson/22-11-8	2608.5	ASF-C	46	103	24.4	3.3	0.16	4.3	16	17.7	4.3
Nelson/22-11-8	2594.2	ASF-C	53	155	23.6	3	0.16	8.7	6	6	16.7

Nelson/22-11-8	2594.5	ASF-C	61	241	24.2	2	0.17	9	6.3	6.3	11
Nelson/22-11-8	2569.5	CMF	33	2.5	23	6.3	0.08	10.3	13.7	14	3.7
Nelson/22-11-8	2571	CMF	30	271	26.1	8	0.13	5.3	15.3	16.4	14
Nelson/22-11-8	2572	CMF	31	14	19.2	2.3	0.08	9.7	19.3	19.6	1
Pierce-23/27-8	2477.1	CMF	34	9.1	22.2	2	0.18	10.7	10.3	12	6.3
Arran-23/16b-9	2722.5	ASF-L	48	45.75	22.48	5.3	0.20	0.3	8.6	10.9	13
Pierce-23/27-6	2916	ASF-L	47	30	21.8	4.7	0.17	1	13.4	13.4	12.7
Blane-30-03a-1	3096	ASF-L	36	135	19.9	5	0.19	3.7	10.1	10.4	6.7
Blane-30-03a-1	3097	ASF-L	34	70	20.6	3.5	0.19	10	7.5	8	7
Everest-22-10a-4	2557	ASF-L	37	25	21.9	3.3	0.18	7.7	14.9	15.2	9.6
Montrose-22-17-A12	2500.3	SPHF	30	2	23.5	1.7	0.21	4.3	22.3	23	6.7
Everest-22-14a-2	2616	SPHF	51	34	24.2	0.7	0.18	1.7	18.6	19.6	8.4
Everest-22-14a-2	2616	SPHF	30	34	24.2	5.3	0.19	1.3	26.4	26.4	6.3
Everest-22-10a-4	2538.9	SPHF	22	0.2	11.7	5	0.21	1	16.6	23	0
Everest-22-10a-4	2538.1	SPHF	18	0.2	11.7	5	0.21	1	16.6	23	0
Arran-23/16b-9	2720.3	SPHF	46	45.05	22.09	6.7	0.18	1.3	11.3	11.6	14.4
Arran-23/16b-9	2721.3	SPHF	48	53.16	24.24	6	0.15	2.3	18.3	18.6	13
Pierce-23/27-5	2729.5	SPHF	29	2.3	24	3	0.22	5	31.6	32.3	4.7
Pierce-23/27-5	2733.85	SPHF	48	0.32	17.8	3.3	0.17	3	24.7	24.7	2.7
Pierce-23/27-5	2728.3	SPHF	32	1.1	22.1	3	0.18	0.7	29.7	30.4	17
Pierce-23/27-6	2907.8	SPHF	32	3.3	22	3.7	0.12	2.3	19.3	19.3	1
Blane-30-03a-1	3091	SPHF	51	1.5	16.9	0.3	0.10	8.7	20.3	21	1
Blane-30-03a-1	3091	SPHF	48	1.3	18.6	2	0.12	8	16.7	17.7	2.5
Pierce-23/27-5	2726.74	MPHF	29	0.18	14.1	1.3	0.09	4.3	25.9	31.2	15.3
Pierce-23/27-6	2913.28	MPHF	32	16	21.8	7.7	0.16	4	4.9	5.2	16
Everest-22-14a-2	2614	MPHF	33	59	23	6.3	0.21	3.3	13.7	14	13.7

Everest-22-10a-4	2542.03	MPHF	25	0.31	13.2	5.3	0.18	2	26.7	29.1	0
Everest-22-10a-4	2539.3	MPHF	18	0.07	13.8	0.5	0.15	1	41	41	0.5

ASF-C: Amalagamated Sandstones Facies- Channel

ASF-L: Amalagamated Sandstones Facies- Lobe

CMAF- Channel Margin/Abandonment Facies

SPHF: Sand-prone Heterolithic Facies

MPHF: Mud-prone Heterolithic Fa

Appendix II: SEM-EDS and CL Data

- SEM-EDS data
- CL data

SEM-EDS data

Electron Image 24

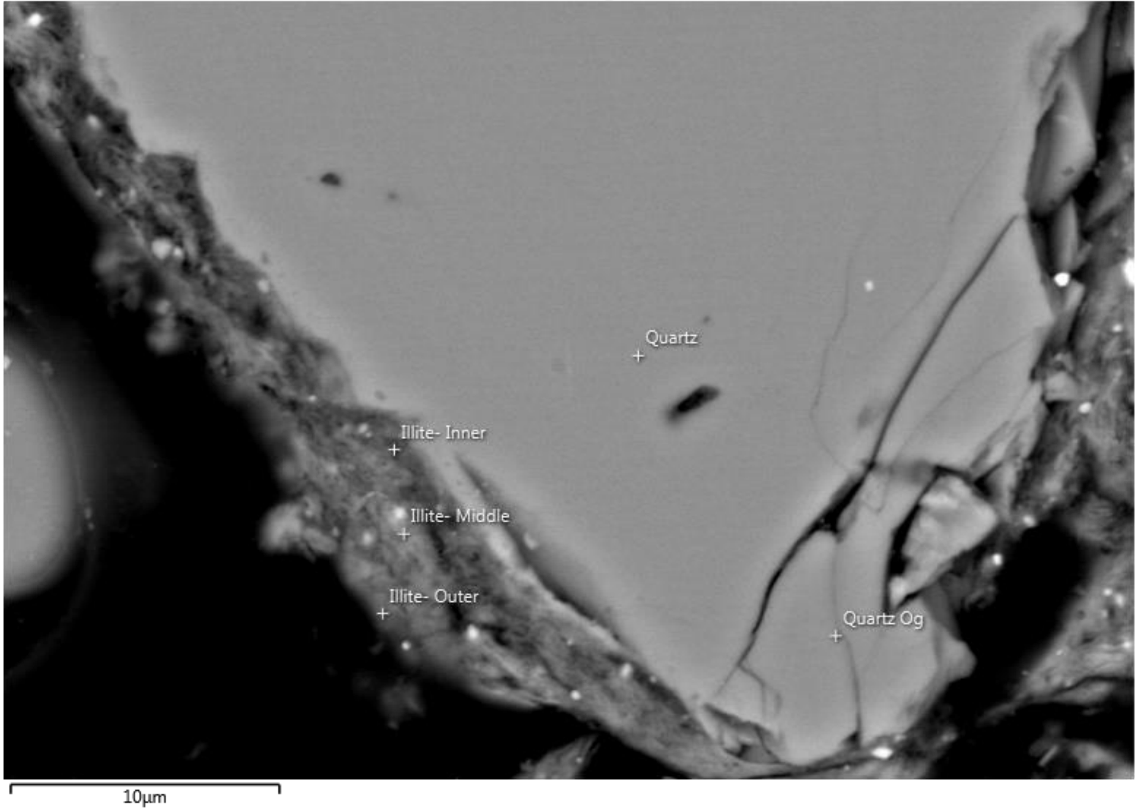

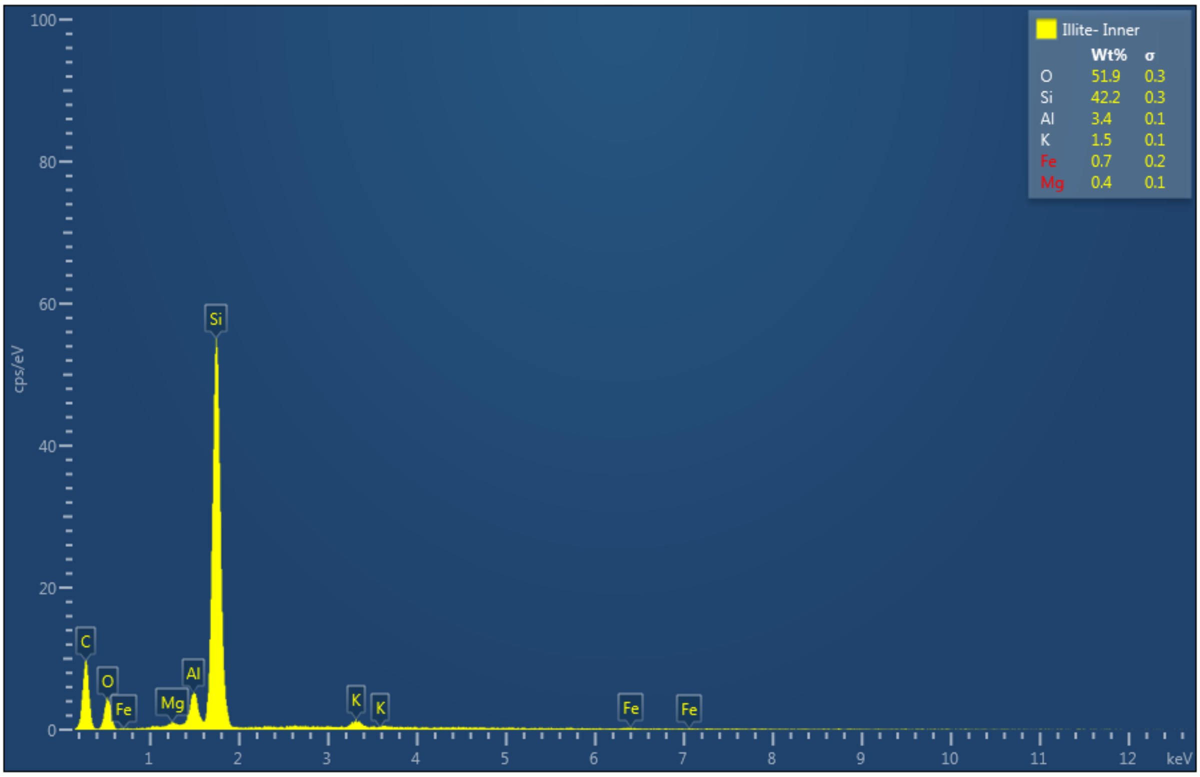

🟨 Illite- Inner

	Wt%	σ
O	51.9	0.3
Si	42.2	0.3
Al	3.4	0.1
K	1.5	0.1
Fe	0.7	0.2
Mg	0.4	0.1

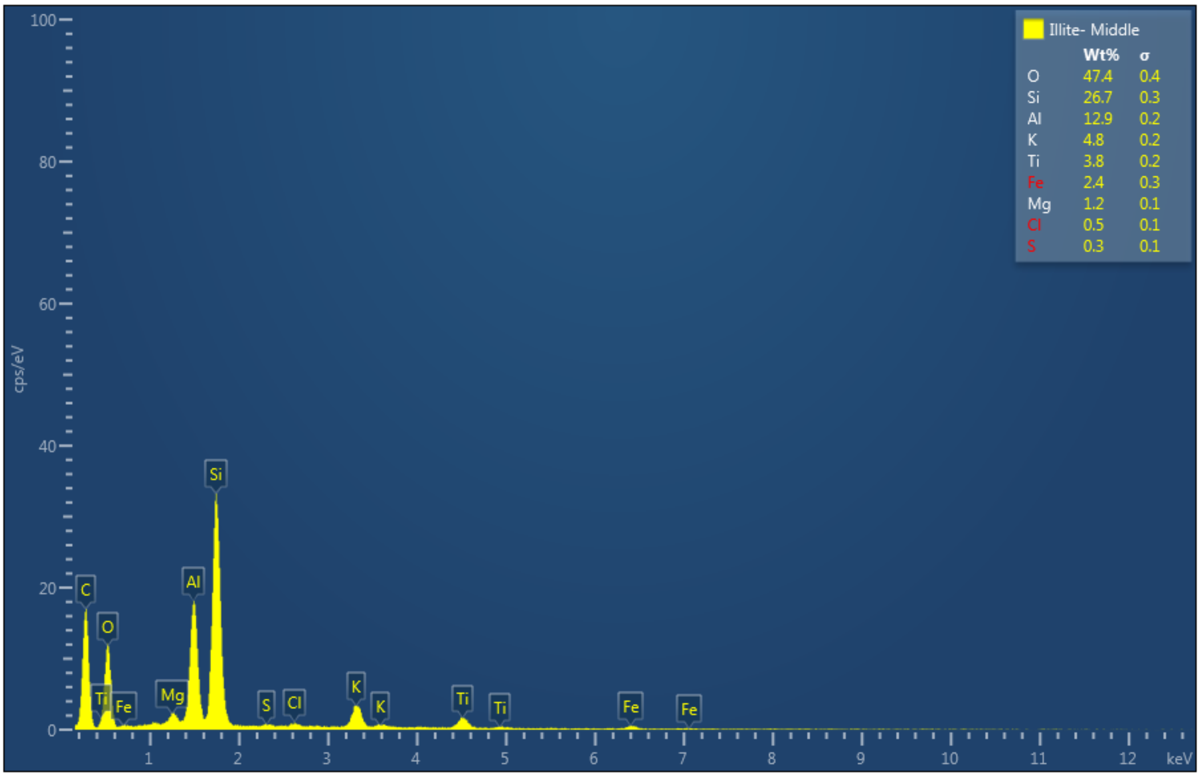

Illite- Middle

	Wt%	σ
O	47.4	0.4
Si	26.7	0.3
Al	12.9	0.2
K	4.8	0.2
Ti	3.8	0.2
Fe	2.4	0.3
Mg	1.2	0.1
Cl	0.5	0.1
S	0.3	0.1

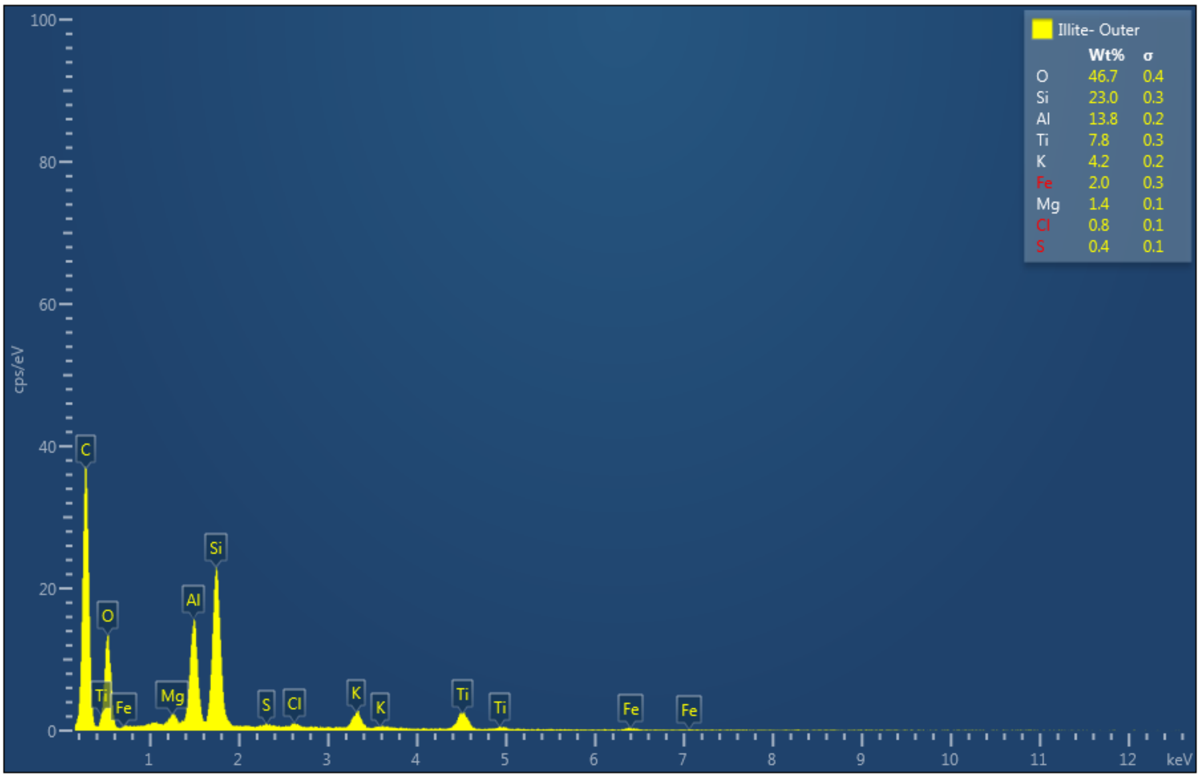

Illite- Outer

	Wt%	σ
O	46.7	0.4
Si	23.0	0.3
Al	13.8	0.2
Ti	7.8	0.3
K	4.2	0.2
Fe	2.0	0.3
Mg	1.4	0.1
Cl	0.8	0.1
S	0.4	0.1

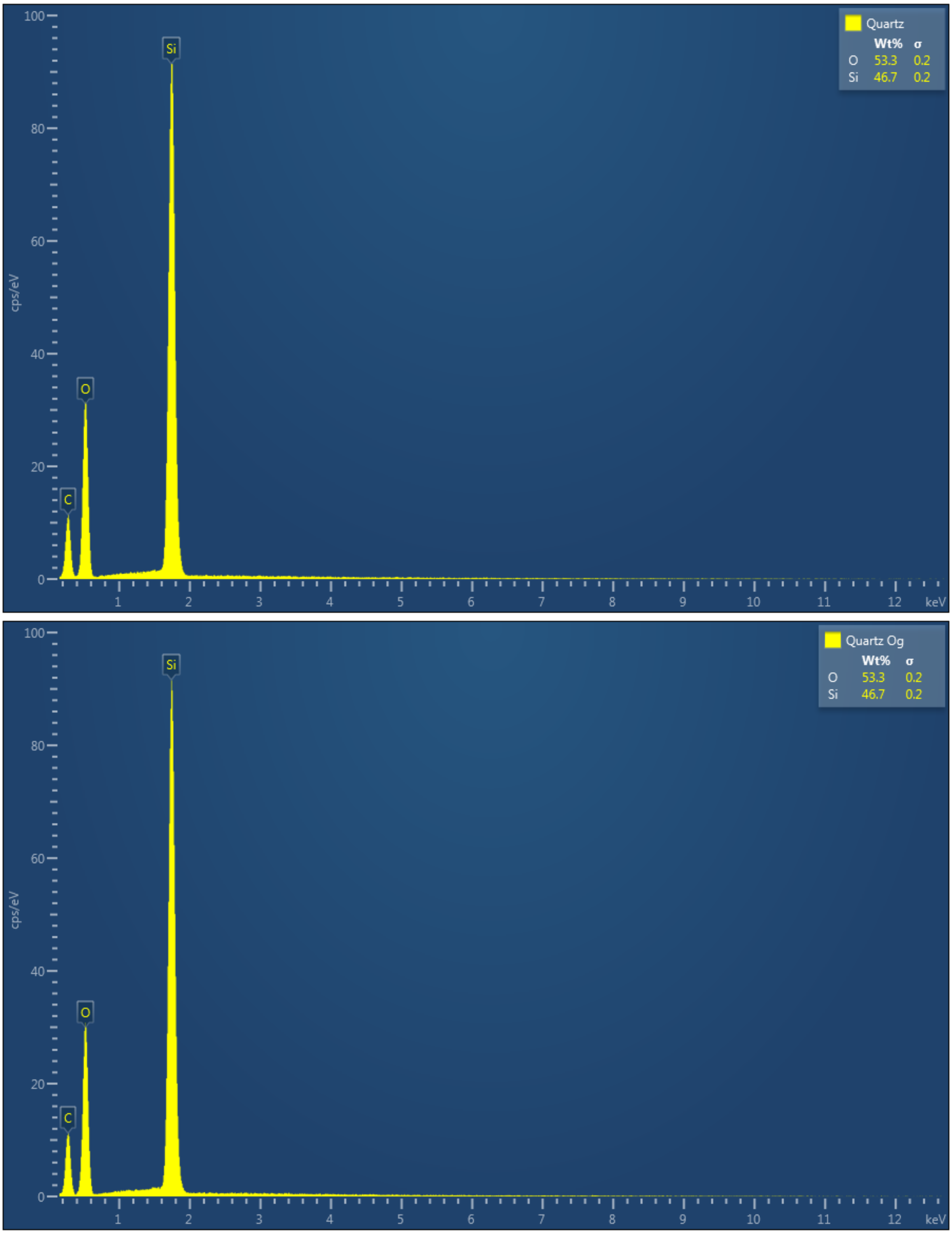

Figure II. SEM-EDS analysis of inner, middle, and outer parts of grain-coating illlite, detrital quartz, and quartz overgrowth, with their EDS spectra. Sample from Blane field, well 30/03a-1, 3096 m TVDSS.

Electron Image 16

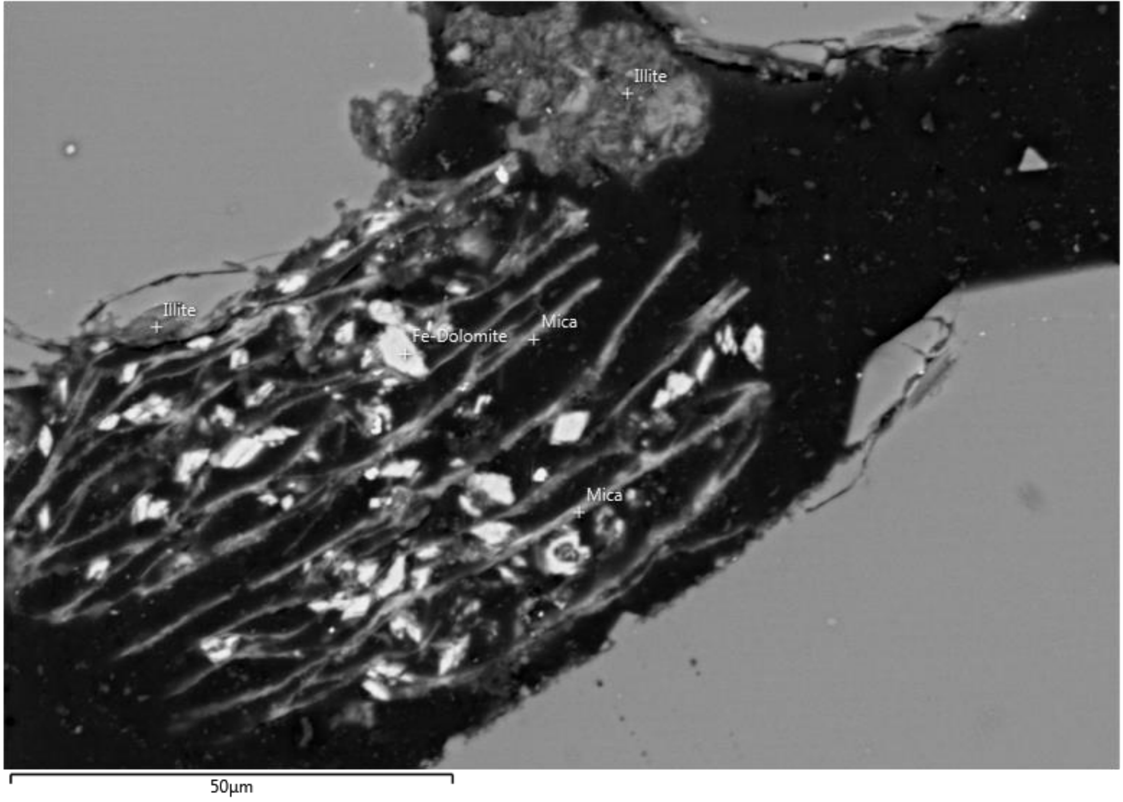

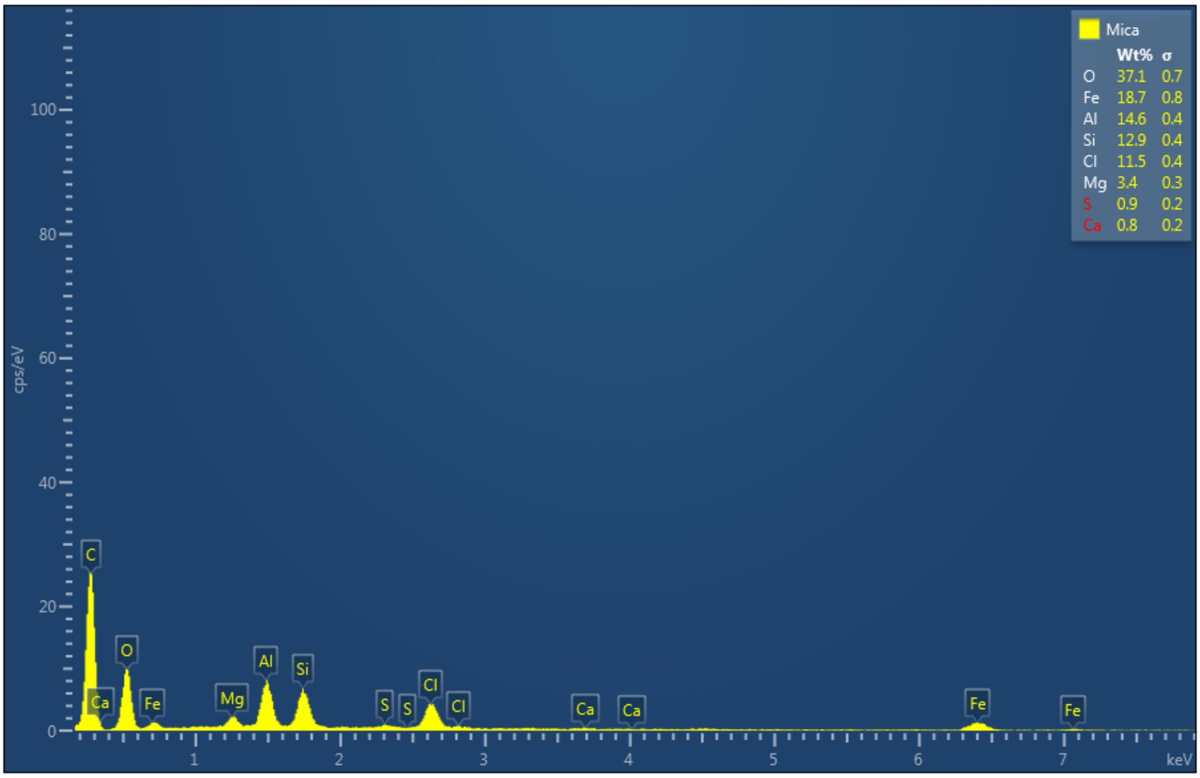

🟨 Mica

	Wt%	σ
O	37.1	0.7
Fe	18.7	0.8
Al	14.6	0.4
Si	12.9	0.4
Cl	11.5	0.4
Mg	3.4	0.3
S	0.9	0.2
Ca	0.8	0.2

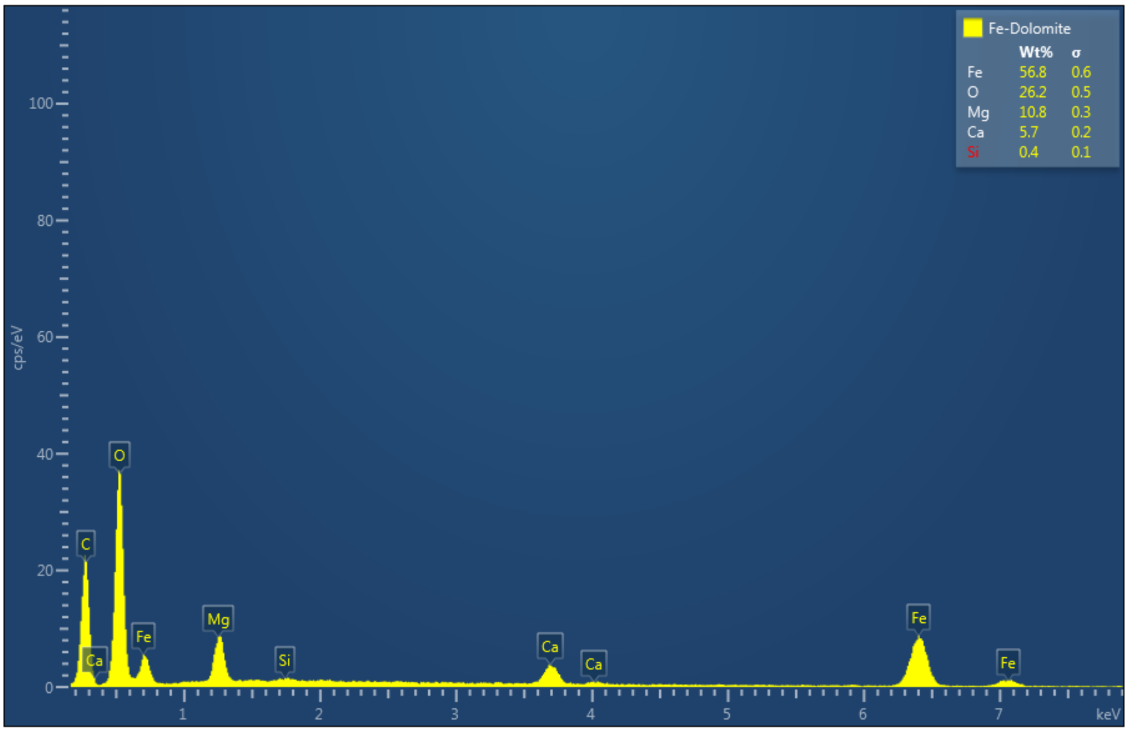
Fe-Dolomite
Wt% σ
Fe 56.8 0.6
O 26.2 0.5
Mg 10.8 0.3
Ca 5.7 0.2
Si 0.4 0.1
cps/eV
100
80
60
40
20
0
C
O
Ca
Fe
Mg
Si
Ca
Ca
Fe
Fe
1
2
3
4
5
6
7
keV

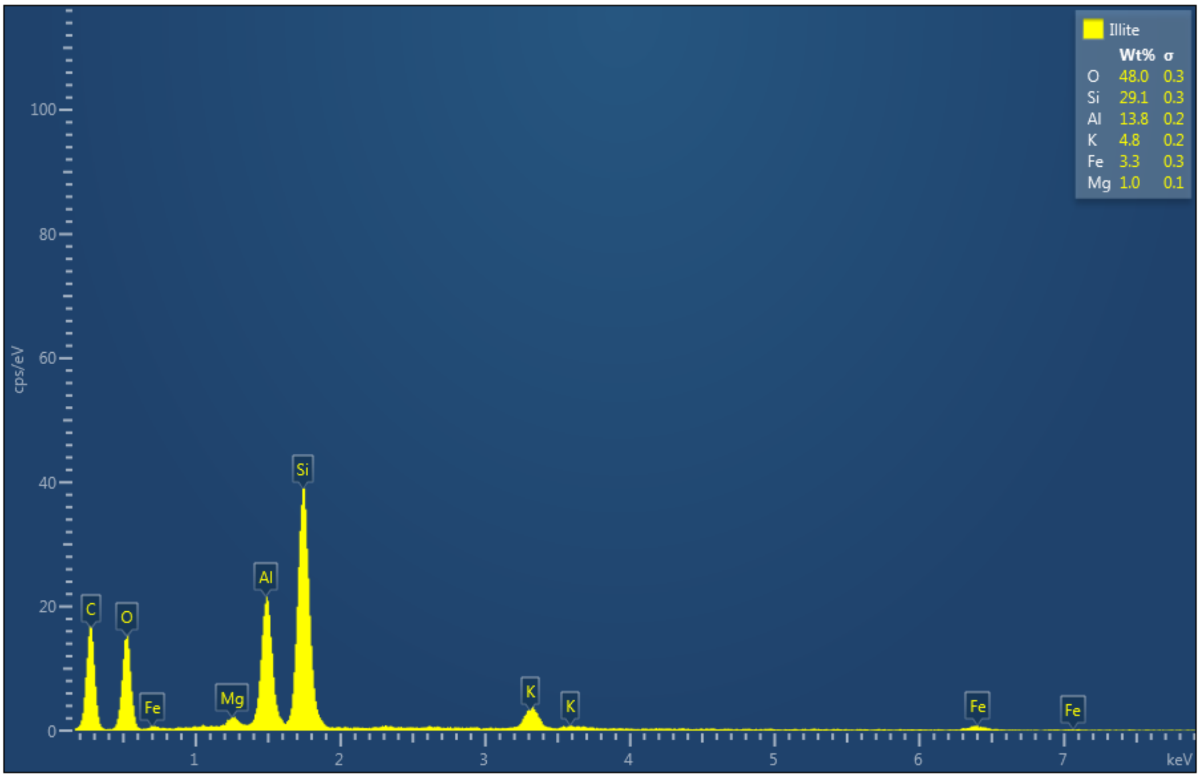
Illite
Wt% σ
O 48.0 0.3
Si 29.1 0.3
Al 13.8 0.2
K 4.8 0.2
Fe 3.3 0.3
Mg 1.0 0.1
cps/eV
100
80
60
40
20
0
C
O
Fe
Mg
Al
Si
K
K
Fe
Fe
1
2
3
4
5
6
7
keV

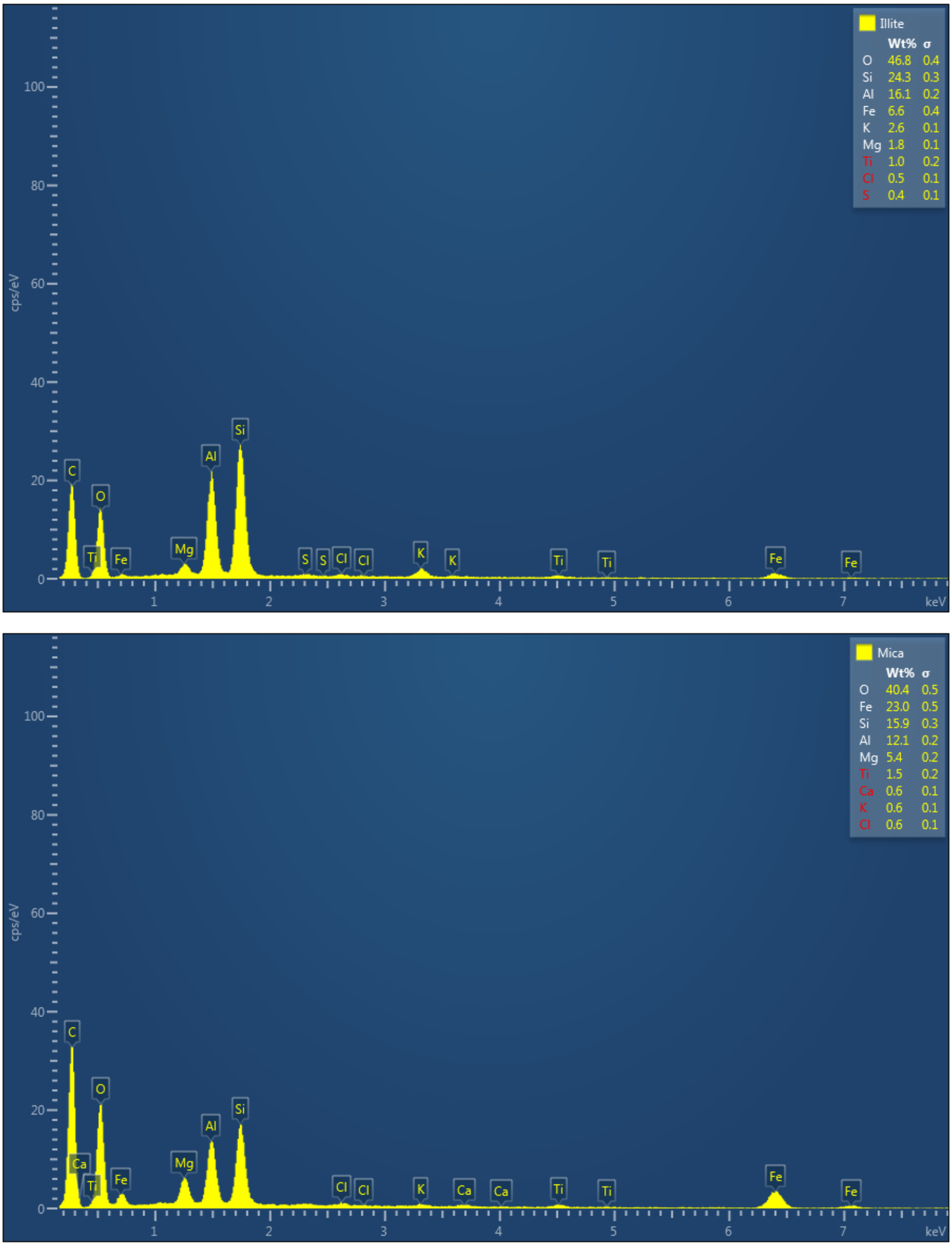

Illite

	Wt%	σ
O	46.8	0.4
Si	24.3	0.3
Al	16.1	0.2
Fe	6.6	0.4
K	2.6	0.1
Mg	1.8	0.1
Ti	1.0	0.2
Cl	0.5	0.1
S	0.4	0.1

Mica

	Wt%	σ
O	40.4	0.5
Fe	23.0	0.5
Si	15.9	0.3
Al	12.1	0.2
Mg	5.4	0.2
Ti	1.5	0.2
Ca	0.6	0.1
K	0.6	0.1
Cl	0.6	0.1

Figure II. SEM-EDS analysis of grain-coating and pore-filling illite, partly dissolved/altered mica, and mica-replacing ferroan dolomite, and their EDS spectra. Sample from Nelson field, well 22/11-6, 2219 m TVDSS.

Electron Image 28

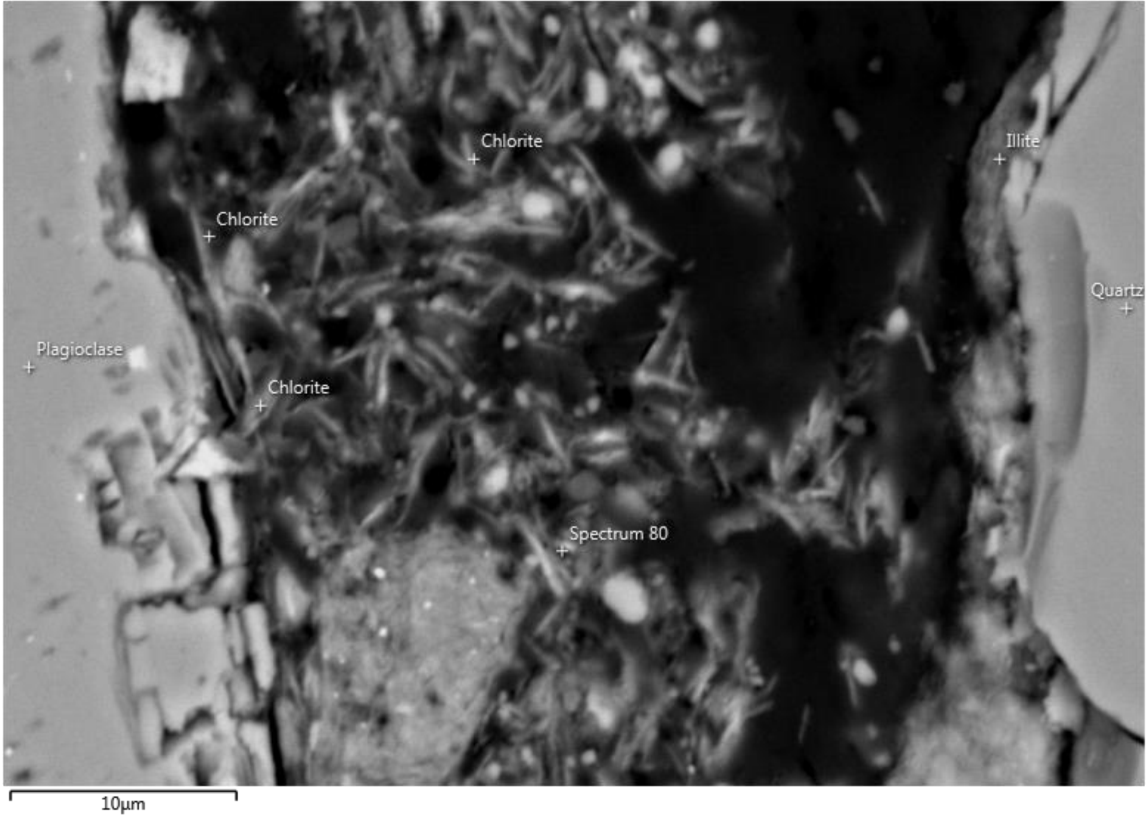

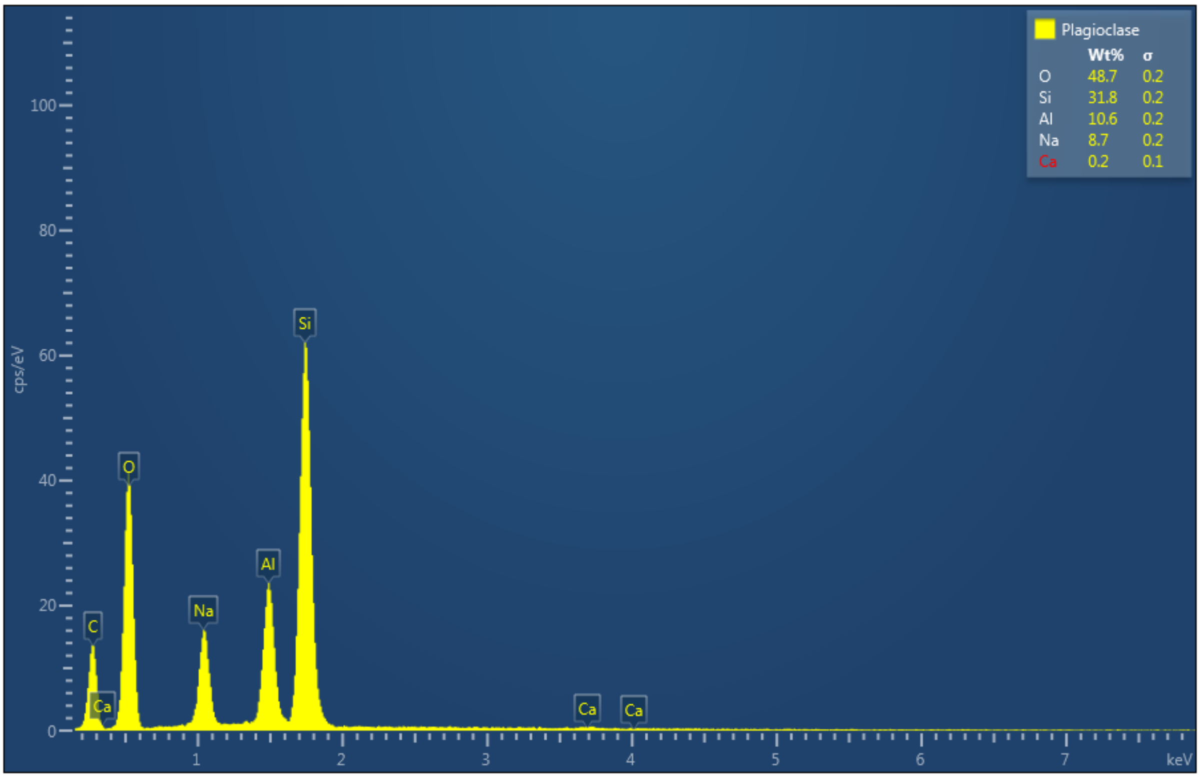

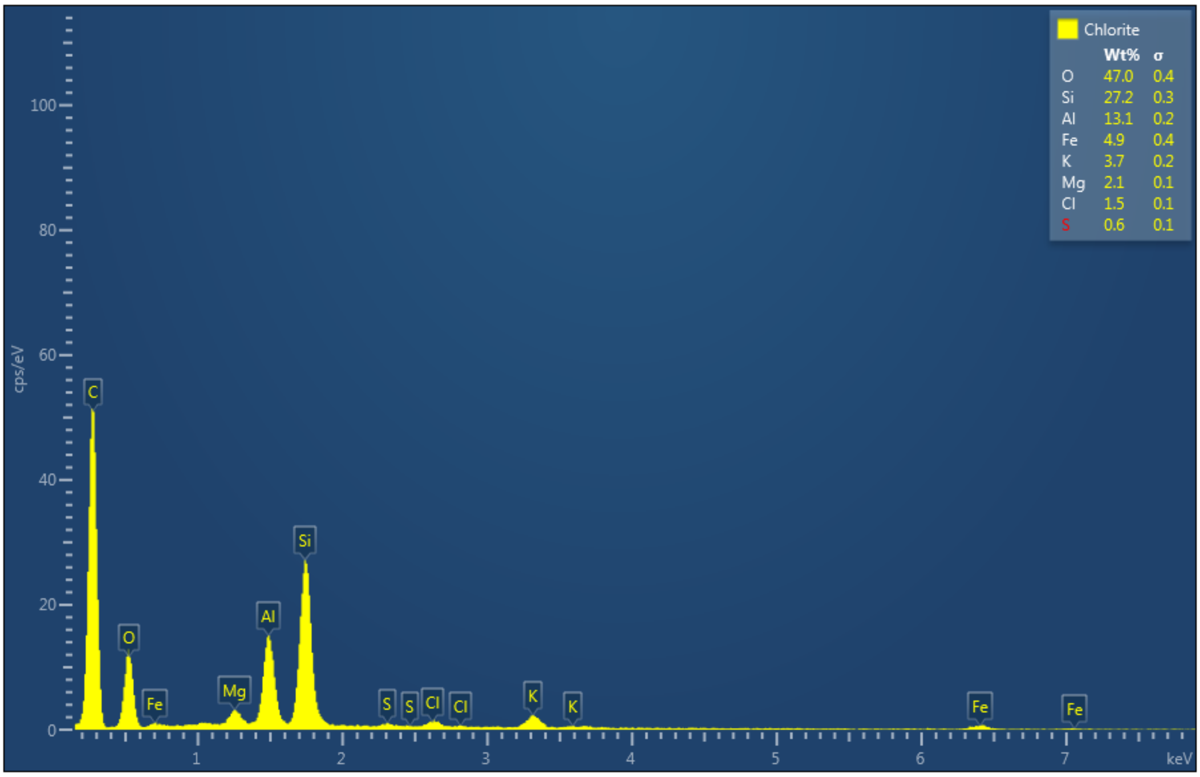
Chlorite
Wt% σ
O 47.0 0.4
Si 27.2 0.3
Al 13.1 0.2
Fe 4.9 0.4
K 3.7 0.2
Mg 2.1 0.1
Cl 1.5 0.1
S 0.6 0.1
cps/eV
100
80
60
40
20
0
C
O
Fe
Mg
Al
Si
S
S
Cl
Cl
K
K
Fe
Fe
1
2
3
4
5
6
7
keV

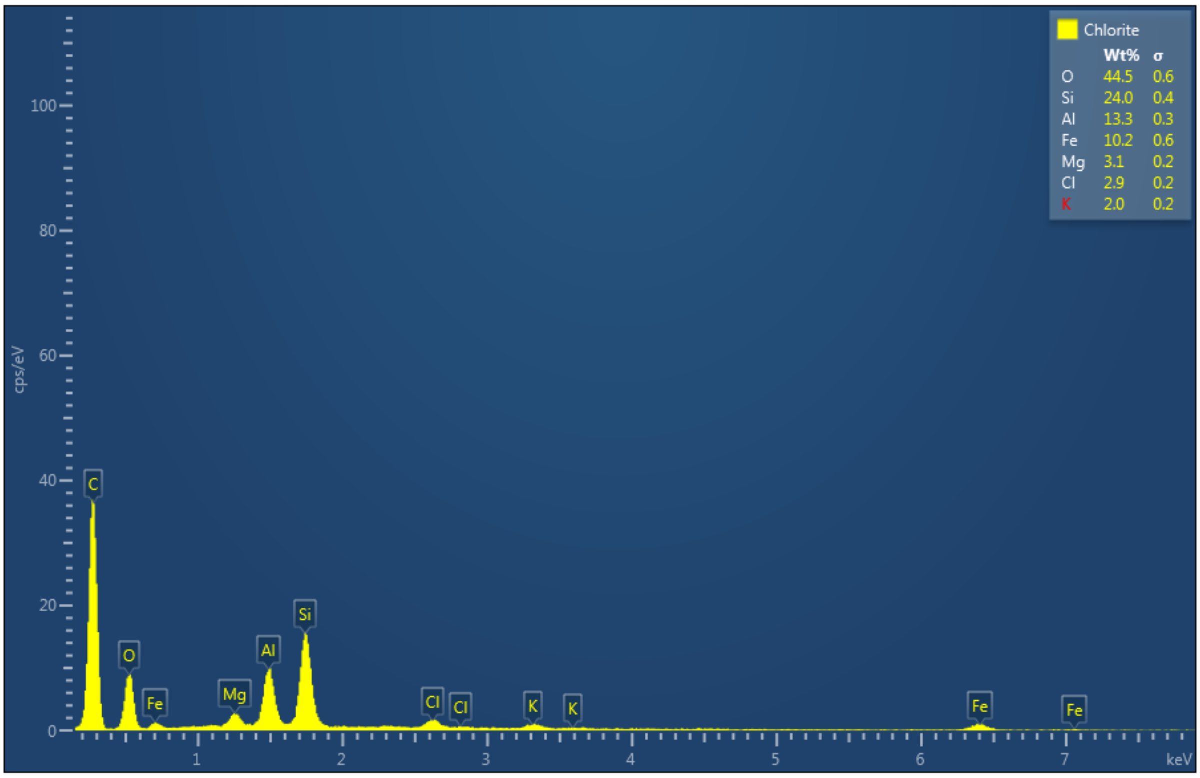
Chlorite
Wt% σ
O 44.5 0.6
Si 24.0 0.4
Al 13.3 0.3
Fe 10.2 0.6
Mg 3.1 0.2
Cl 2.9 0.2
K 2.0 0.2
cps/eV
100
80
60
40
20
0
C
O
Fe
Mg
Al
Si
Cl
Cl
K
K
Fe
Fe
1
2
3
4
5
6
7
keV

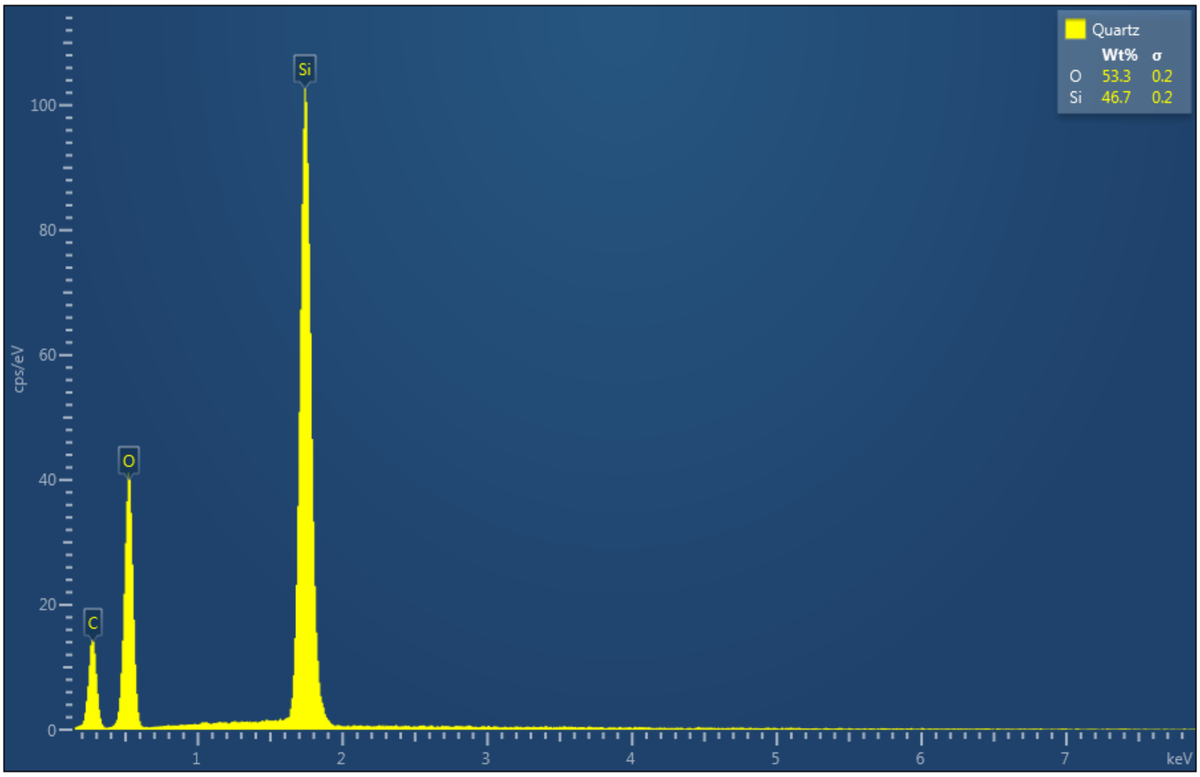

	Wt%	σ
O	53.3	0.2
Si	46.7	0.2

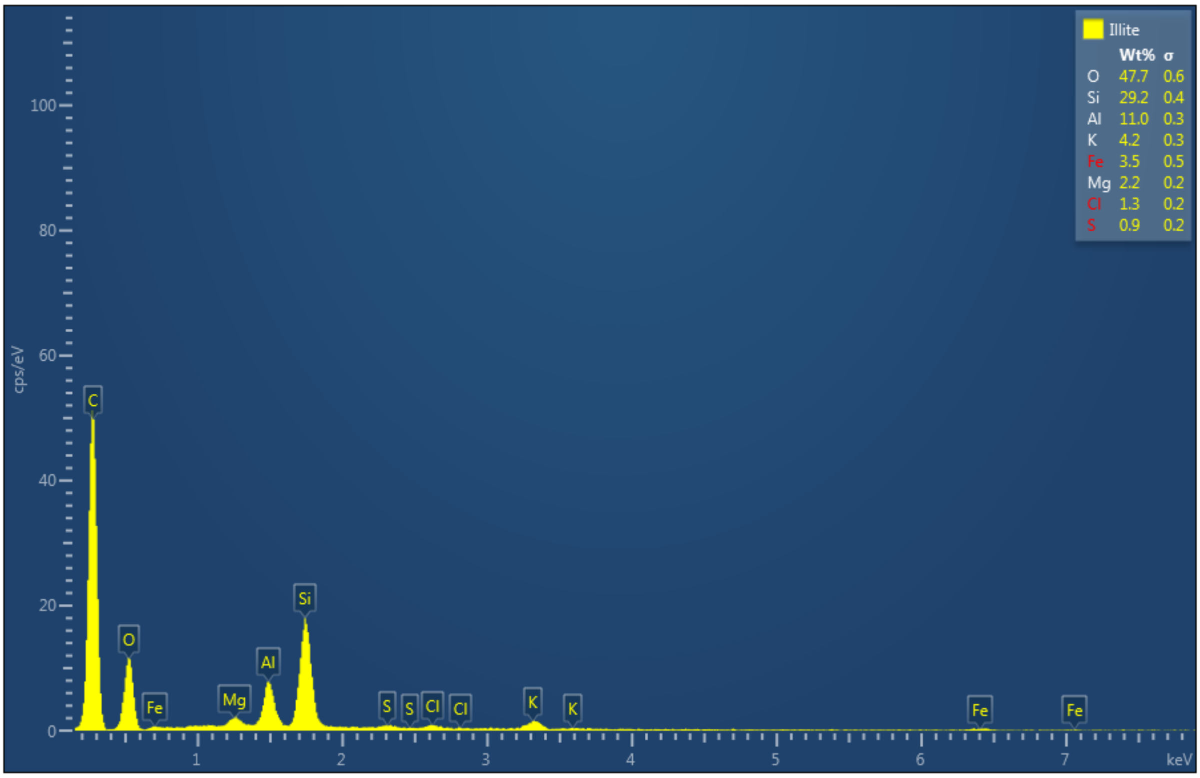

	Wt%	σ
O	47.7	0.6
Si	29.2	0.4
Al	11.0	0.3
K	4.2	0.3
Fe	3.5	0.5
Mg	2.2	0.2
Cl	1.3	0.2
S	0.9	0.2

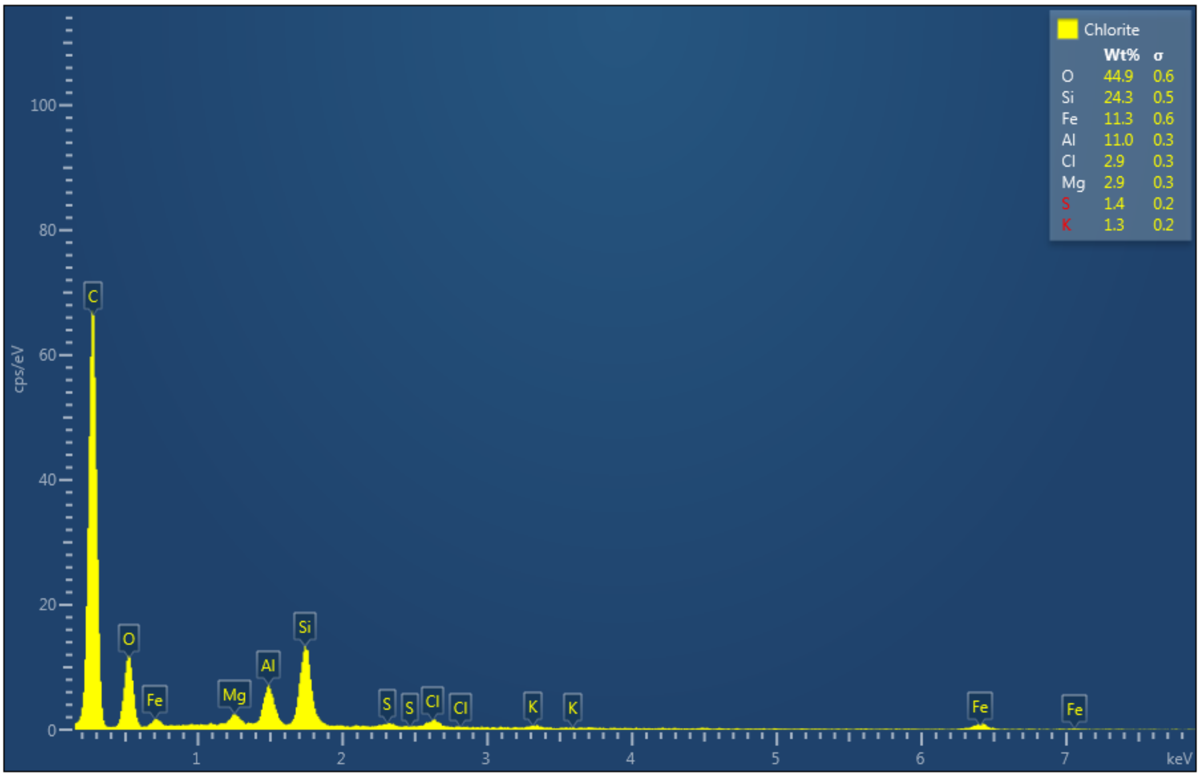

Figure II. SEM-EDS analysis of detrital plagioclase, quartz, authigenic grain-coating illite, and pore-filling chlorite and their EDS spectra. Sample from Everest field, well 22/14a-2, 2216 m TVDSS.

Electron Image 8

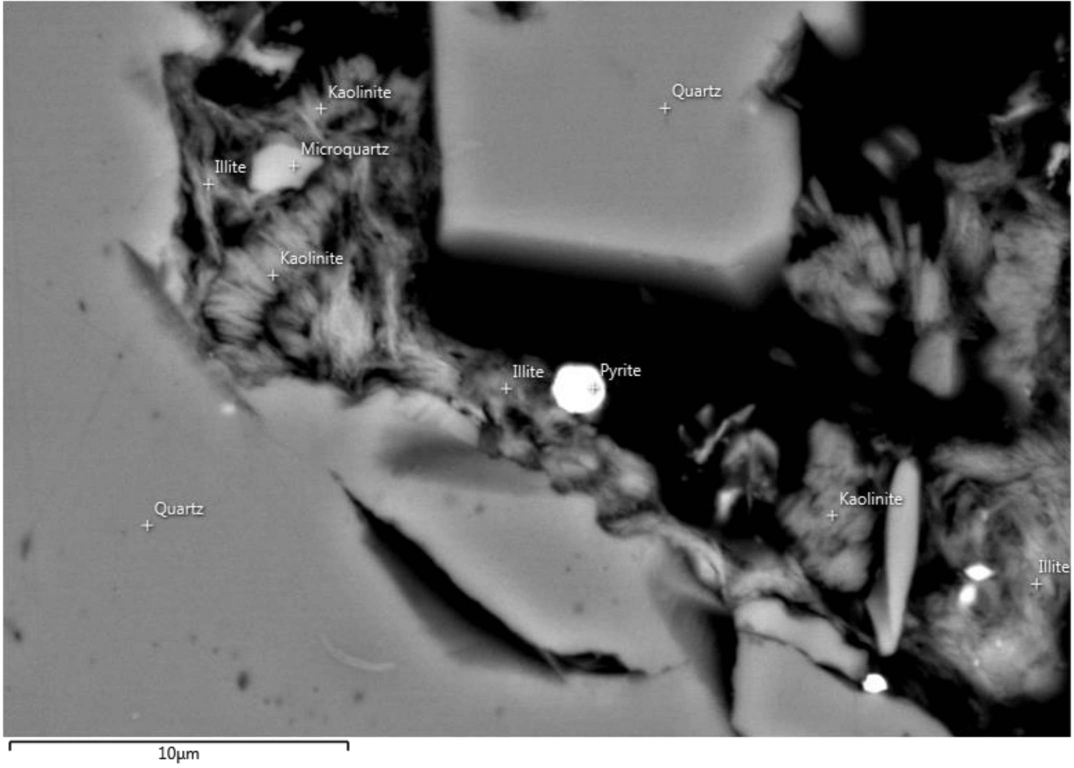

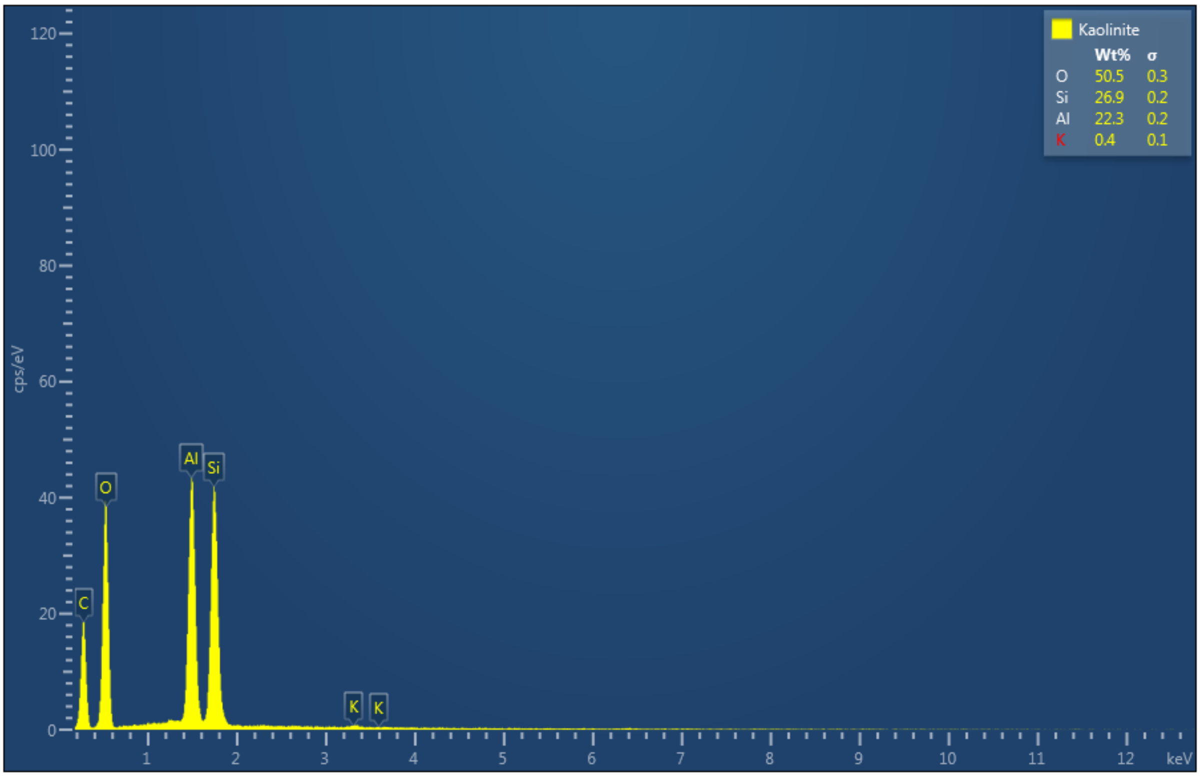

Kaolinite

	Wt%	σ
O	50.5	0.3
Si	26.9	0.2
Al	22.3	0.2
K	0.4	0.1

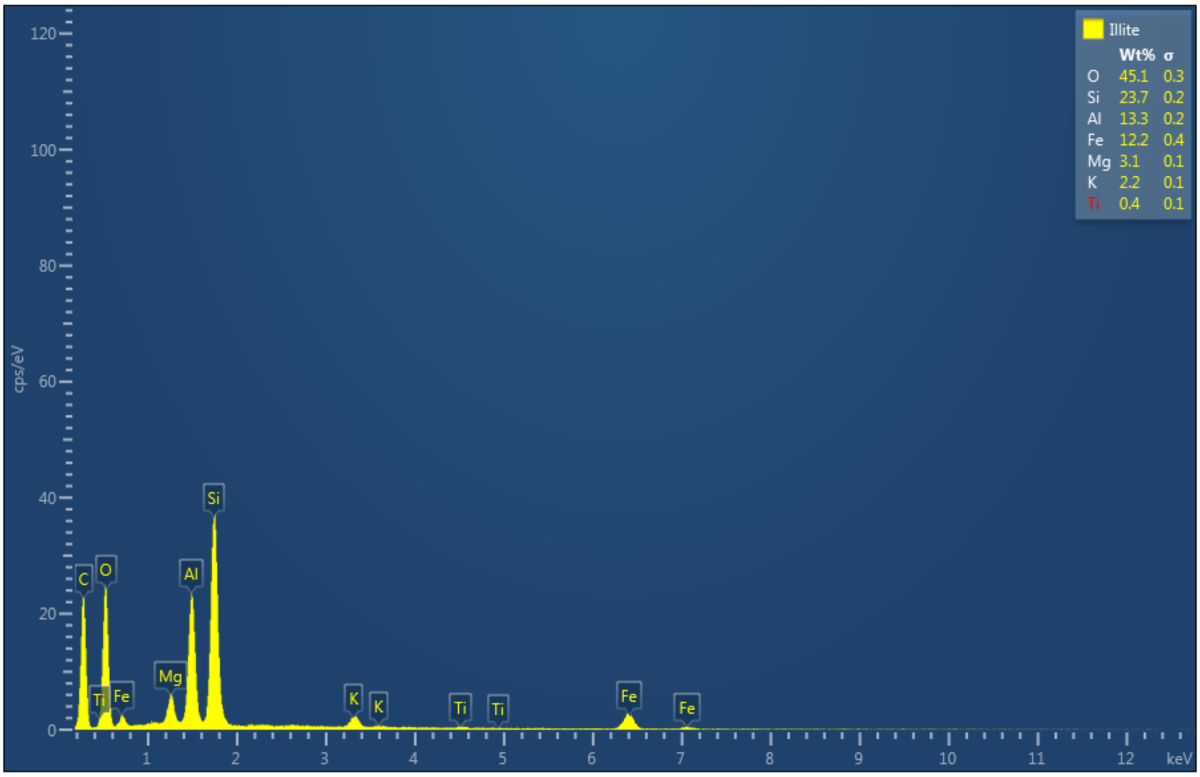
Illite
Wt% σ
O 45.1 0.3
Si 23.7 0.2
Al 13.3 0.2
Fe 12.2 0.4
Mg 3.1 0.1
K 2.2 0.1
Ti 0.4 0.1
cps/eV
0
20
40
60
80
100
120
C
O
Ti
Fe
Mg
Al
Si
K
K
Ti
Ti
Fe
Fe
1
2
3
4
5
6
7
8
9
10
11
12
keV

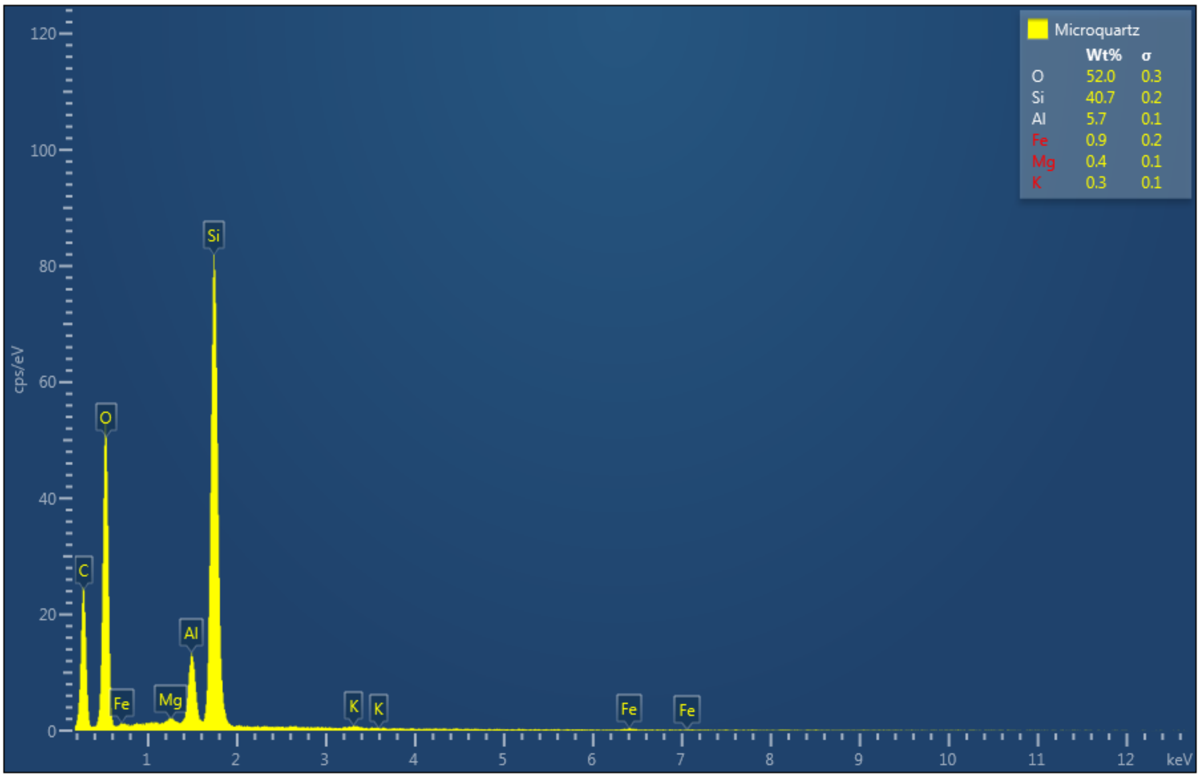
Microquartz
Wt% σ
O 52.0 0.3
Si 40.7 0.2
Al 5.7 0.1
Fe 0.9 0.2
Mg 0.4 0.1
K 0.3 0.1
cps/eV
0
20
40
60
80
100
120
C
O
Fe
Mg
Al
Si
K
K
Fe
Fe
1
2
3
4
5
6
7
8
9
10
11
12
keV

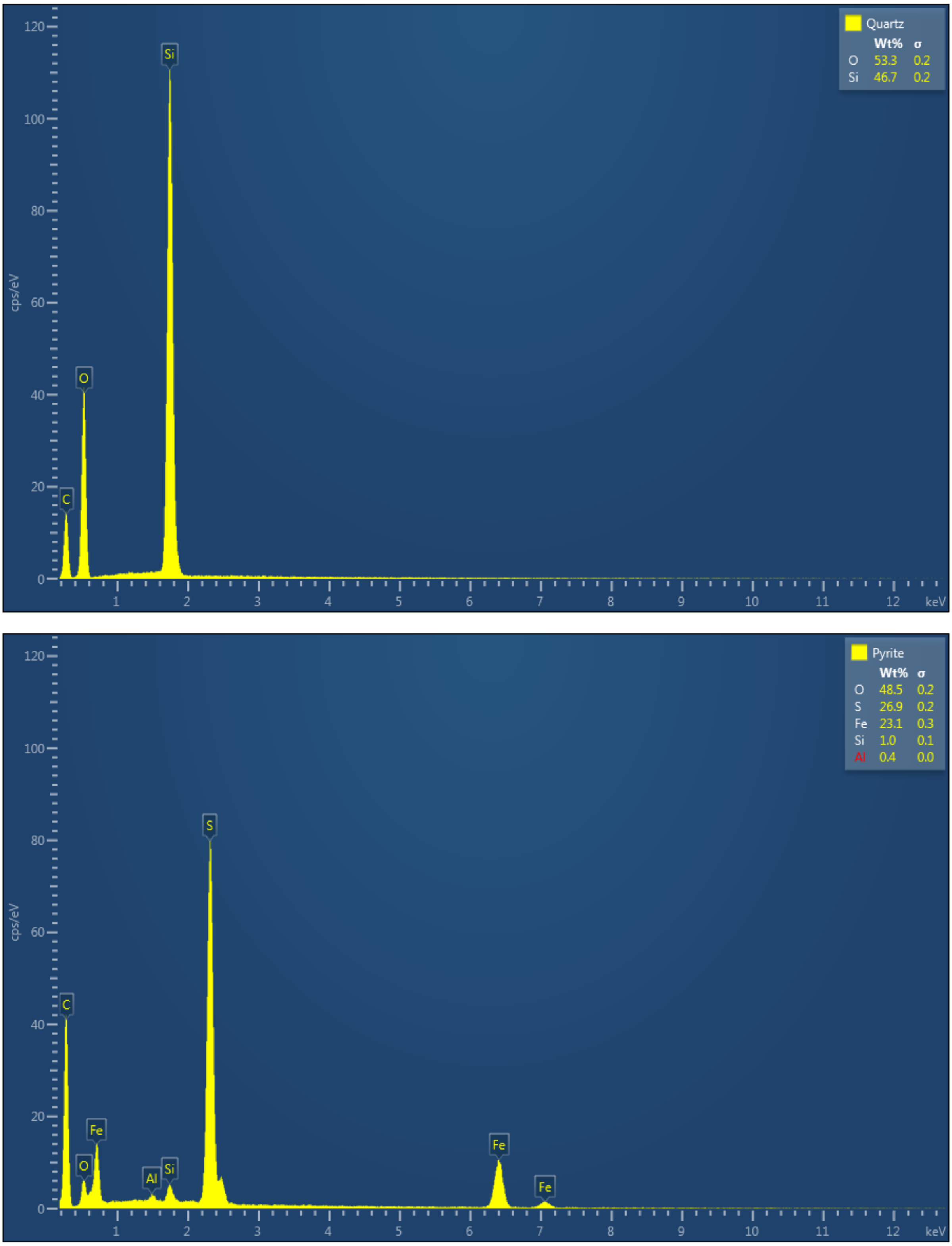

Figure II. SEM-EDS analysis of detrital quartz grains, authigenic microquartz, pyrite, kaolinite, and illitized kaolinite and their EDS spectra. Sample from Blane field, well 30/03a-1, 3096 m TVDSS.

Appendix II: CL data

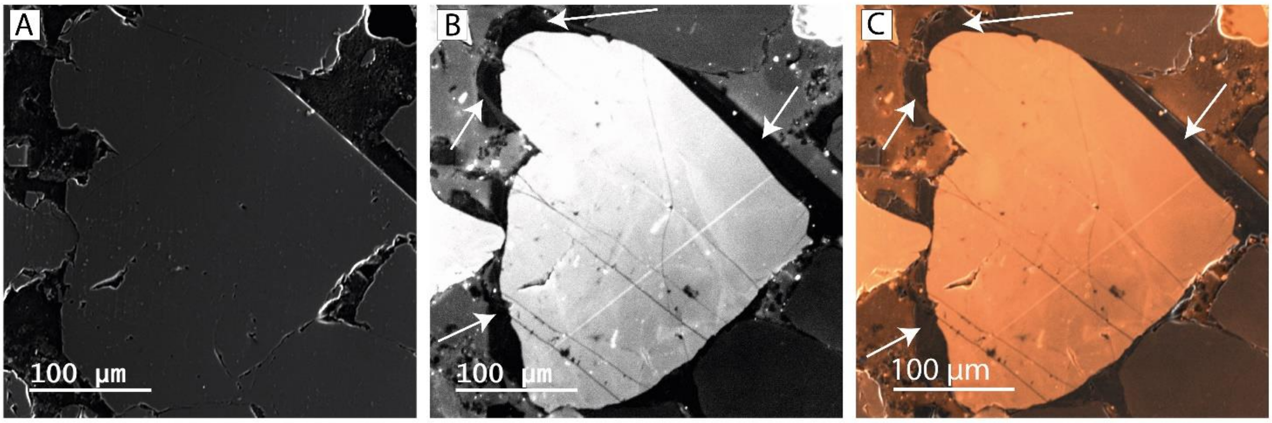

Figure II. Extent of quartz overgrowth in the studied Forties Sandstone Member. (A) SEM image showing detrital quartz (centre); (B) CL image showing quartz overgrowth (black outline; white arrows). Note the sub-vertical, healed fractures on the detrital quartz (centre). (C) Coloured SEM-CL composite image of detrital quartz (centre; light brown) and quartz overgrowth (black outline; white arrows). Sample from Blane field, well 30/03a-1, 3097 m TVDSS.

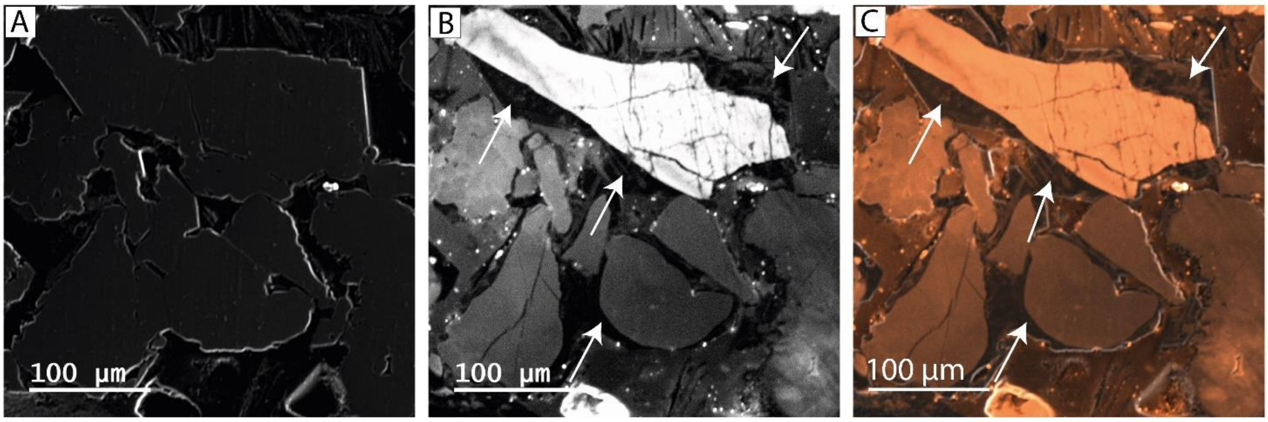

Figure II. Development of quartz overgrowths on detrital quartz grains in the Forties Sandstone Member. (A) SEM image showing detrital quartz grains (top and centre); (B) CL image showing quartz overgrowths on detrital quartz grains (black outlines; white arrows). Notice the horizontal and sub-vertical, healed fractures on the detrital quartz grains (top and centre). (C) Coloured SEM-CL composite image of detrital quartz grains (centre and top; light brown) and quartz overgrowths (black outlines; white arrows). Sample from Blane field, well 30/03a-1, 3097 m TVDSS.

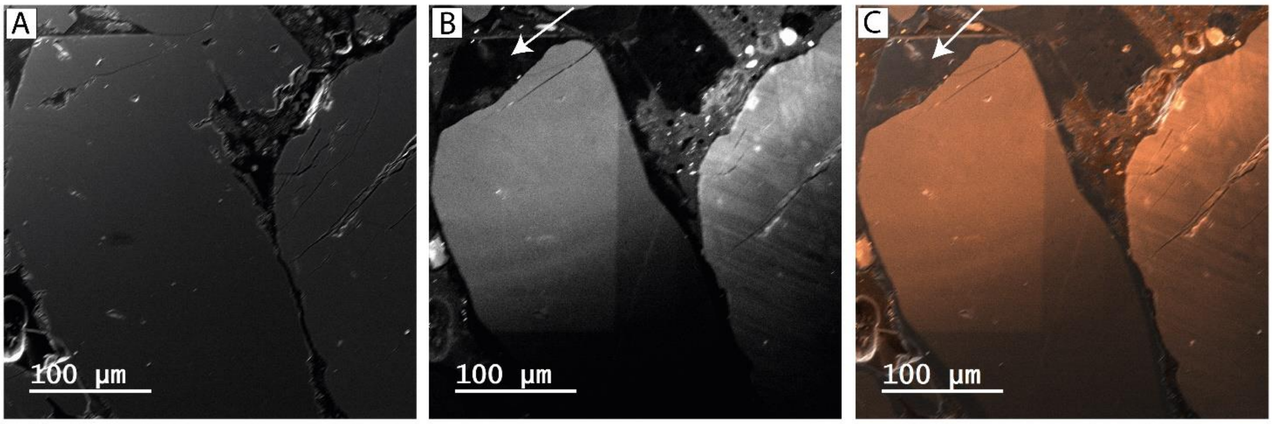

Figure II. Quartz cementation in the Forties Sandstone Member. (A) SEM image showing detrital quartz grain (left); (B) CL image showing quartz overgrowth on the detrital quartz (black outline; white arrow). (C) Coloured SEM-CL composite image of detrital quartz grain (left; light brown) and quartz overgrowth (black outline; white arrow). Sample from Everest field, well 30/03a-1, 3097 m TVDSS.